Pressure and flow within the umbilical vessels

David John Wilke

October 5, 2016

Thesis submitted for the degree of
Doctor of Philosophy
in
Mathematical Sciences
at The University of Adelaide
Faculty of Engineering, Computer and Mathematical Sciences
School of Mathematical Sciences

THE UNIVERSITY
of ADELAIDE

Contents

List of Tables

List of Figures

Abstract

This thesis considers a fluid dynamic study of blood flow within the umbilical vessels of the human maternal-fetal circulatory system. In particular it evaluates the efficacy of the umbilical coiling index (UCI) in predicting the blood vessel pressure drop, and develops clinically viable indices for the quantification of umbilical cord flow resistance. A numerical approach is developed employing the finite element method via the open-source `c++` code `oomph-lib`, available from the University of Manchester. This permits the description of an umbilical vessel geometry as a fully three-dimensional rigid tube in order to consider a wide range of cords subject to steady and unsteady boundary conditions.

The thesis is composed of three main studies. The first concerns steady incompressible Newtonian flow through model geometries representative of the umbilical vessels. It is found that the UCI is unable to distinguish between cords of significantly varying pressure and flow characteristics, which are typically determined by the vessel curvature, torsion and length. Larger scale geometric non-uniformities superposed over the inherent coiling, including cords exhibiting width and/or local UCI variations as well as loose true knots, typically produce a small effect on the total pressure drop. Crucially, this implies that a helical geometry of mean coiling may be used to determine the steady vessel pressure drop through a more complex cord. The presence of vessel constriction, however, drastically increases the steady pressure drop and alters the flow profile.

The second study provides an analysis of pulsatile incompressible Newtonian flow through arterial geometries. The steady pressure drop is found to approximate the time-averaged value with high accuracy over a wide range of arteries. Furthermore, the relative peak systolic pressure measured over the period is found to remain virtually constant and approximately 25% below the equivalent straight pipe value for a large range of non-straight vessels. Interestingly, this suggests that the coiled structure dampens extreme pressures within the arterial cycle and may provide another possible evolutionary benefit to the coiled structure of the cord.

Having shown the UCI ineffective at predicting the vessel pressure drop, the third and final study presents two alternative indices for the diagnosis of cord pathology based on steady calculations. The umbilical pressure index, PX, and flow index, QX, quantify the deviation of a cord geometry from typical conditions by considering the steady pressure and flow-rate, respectively. These indices are calculated based on a combination of empirical and interpolated numerical data and require only one additional geometric measurement to the calculation of the UCI; namely the cord width. Together the indices provide a non-invasive measure of the flow-resistance inherent to a particular cord geometry, and allow comparison with typical values in pregnancy. Further testing of the indices is required to determine their efficacy in a clinical setting, however, their simple and robust nature ensures that they are promising candidates.

Signed Statement

I certify that this work contains no material which has been accepted for the award of any other degree or diploma in my name, in any university or other tertiary institution and, to the best of my knowledge and belief, contains no material previously published or written by another person, except where due reference has been made in the text. In addition, I certify that no part of this work will, in the future, be used in a submission in my name, for any other degree or diploma in any university or other tertiary institution without the prior approval of the University of Adelaide and where applicable, any partner institution responsible for the joint-award of this degree. I give consent to this copy of my thesis, when deposited in the University Library, being made available for loan and photocopying, subject to the provisions of the Copyright Act 1968.

I also give permission for the digital version of my thesis to be made available on the web, via the Universitys digital research repository, the Library Search and also through web search engines, unless permission has been granted by the University to restrict access for a period of time.

Signed: ..... Date: .....

Acknowledgements

I wish to extend my gratitude to those that have supported me throughout my study and in particular, through the completion of this thesis. Firstly, to Dr. Trent Mattner, for unwavering technical and personal support over the years. To Prof. Jim Denier, for providing an interesting research topic as well as the freedom to explore it independently. To Prof. Yee Khong, for enthusiasm, guidance and direction in an unknown medical world. To Dr. Phil Haines, for countless meetings on `oomph-lib` without which this study may well have taken a decade. To Prof. Matthias Heil and Dr. Andrew Hazel for developing, and their personal correspondence regarding `oomph-lib`. To my fellow Ph.D students, in particular Dr. Wade and Dr. Stanford, for providing a welcoming office and some respite in difficult times. To my family; my father Ray, and my two sisters Susannah and Eve, for support throughout my study and beyond. To Mr. Fahy, Mr. Robertson, Mr. Griffith and Dr. Ugalov for providing a comfortable home. Finally, to Amelia, for your love, support and patience.

Dedication

For my mother, Rosemary.

Chapter 1

Introduction

In humans, the umbilical cord is the lifeline between the developing embryo or fetus and the placenta throughout gestation. It facilitates the supply of oxygen and nutrient-rich blood from the placenta via the single umbilical vein, in addition to the return of deoxygenated blood from the fetus through two umbilical arteries (Cunningham et al., 2009). These blood vessels lie within a gelatinous substance called Whartons Jelly, with the entire cord suspended in the amniotic fluid (Ferguson and Dodson, 2009). Key to the structure of the umbilical cord is the coiling; in a normal pregnancy the whole cord and its vasculature intertwine in a helical pattern thought to provide many benefits to the development of the fetus. These include a level of strength and distensibility to fetal movement in-utero (de Laat et al., 2005), as well as a necessary flow resistance to strengthen the developing fetal heart (Kaplan et al., 2010). Despite the importance of this structure, and more broadly, of the umbilical cord itself, there is currently only a single geometrically derived diagnostic measure used to quantify coiling and attempt to identify adverse outcomes. The umbilical coiling index, or UCI, is a ratio of the number of coils of the cord to its length (in cm), and aims to describe the level of coiling of a particular cord. In this context, an umbilical coil is defined as one complete 360° helix of the cord (including the blood vessels) around itself. While there is some debate concerning the values of the UCI expected for a normal pregnancy, most sources agree that undercoiling, or *hypocoiling*, should correspond to an UCI $\leq 10^{th}$ percentile while cords exhibiting overcoiling, or *hypercoiling*, are those with an index $\geq 90^{th}$ percentile (de Laat et al., 2005). Cords exhibiting these severe coiling characteristics have been observed by some authors to correlate with adverse perinatal outcomes and obstetrical complications, including fetal demise (de Laat et al., 2005).

Within the field of pathology, however, there is an inconsistency in measuring both the length of the umbilical cord and the number of coils, which

may lead to the presence of errors in the calculation of the UCI and the aforementioned discrepancy in standard UCI values (Khong, 2010). It also means that while a cord may be considered normal with respect to one data set, it may in fact be hypercoiled or hypocoiled with respect to another, and hence the classification is ambiguous. Moreover, many umbilical cords exhibit non-uniform coiling characteristics. For example, an umbilical cord may exhibit localised regions of intensive hypercoiling with normocoiling or hypocoiling in other areas. These cases are improperly described by the UCI system. Similarly, structural abnormalities such as the presence of 'true' or 'false' knots, which represent a whole-knotting of the cord or a localised exaggerated looping of the umbilical vessels, respectively, are entirely unaccounted for in the calculation of the UCI (Khong, 2010).

In order to properly assess the umbilical cord for pathology a knowledge of the blood flow within the vessels is required. The UCI, which is simply a ratio of two cord measurements, is not theoretically linked to any underlying properties of the blood flow and has been shown by some authors to lack any correlation with the remaining diagnostics, such as the arterial doppler indices (Degani et al., 1995). Hobbins (2008) go as far as to state that,

> *"... to attempt to quantify how many coils there are per centimetre is not worth the effort and is, at best, a very weak reflector of fetal condition that can be far better appreciated by Doppler's or biophysical testing."*

To this end, this thesis explores the efficacy of the UCI as a diagnostic indicator for the flow resistance associated with a particular cord geometry, as well as the effect of cord non-uniformities on the blood flow. The aim is to use a fluid dynamic analysis in order to provide an improved description of umbilical cord flow resistance that, however, may still be employed in a clinical environment.

Throughout the following chapter the literature relevant to the mathematical modelling of blood flow in the umbilical cord is presented. Initially a general discussion of the physiology and pathology of the umbilical cord is given in section 1.1, focusing on the motivation behind a fluid dynamic analysis. A full parameter survey is then presented in section 1.2 to describe the flow within the umbilical cord. The properties of blood flow including the constitutive equations are addressed in section 1.3 followed by a review of the literature concerning fluid flow in curved and helical pipes in section 1.4. A review of the previous mathematical and biomechanical analyses of umbilical cord processes is then presented in section 1.5 to highlight the need for further research. Finally, section 1.7 outlines the aims of this study and the thesis structure.

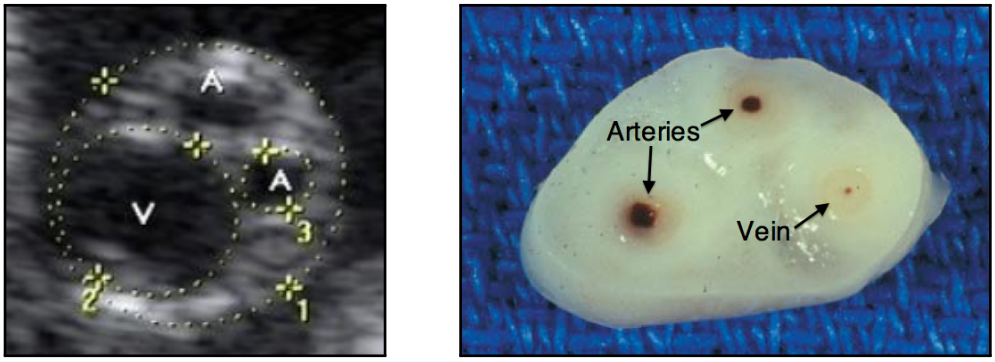

(a) (b)

Figure 1.1: a) A pre-natal umbilical cross-section used with permission from (Barbieri et al., 2011); b) post-natal cross-section used with permission from (Kaplan, 2007).

1.1 The umbilical cord

The fetal circulatory system differs from the circulatory system of a newborn, as prior to birth the lungs are not functional and hence the fetus is dependent upon the the mother for its necessary oxygen. To this end, two organs, namely the placenta and umbilical cord, act to provide the required nutrients and also to allow for the discharge of waste products from the fetus. In humans, deoxygenated fetal blood flows to the placenta via two umbilical arteries (Cunningham et al., 2009) where a gas and nutrient exchange takes place between the fetal and maternal circulatory systems. The oxygen rich blood then flows from the placenta to the fetus via the single umbilical vein, and is eventually distributed into the fetal systemic circulation. In a normal pregnancy the umbilical cord consists of these three umbilical vessels, the two umbilical arteries and a single umbilical vein (Cunningham et al., 2009), which lie within a porous connective tissue called Whartons Jelly, shown in figures 1.1(a) and (b). This is in turn covered by an outer layer of amnion (Ferguson and Dodson, 2009), and the entire cord is suspended between the placenta and fetus within the amniotic fluid.

One of the most striking characteristics of the umbilical cord is its coiled structure, which is shown in figure 1.2. The coiling of the umbilical cord is most often in a counterclockwise sense (approximately forming a left-handed helix) which can be detected via ultrasonographic examination as early as the first trimester during pregnancy (Dudiak et al., 1995). An image of three umbilical cords exhibiting left, right and no twisting is shown in figure 1.3. Ordinarily there may be up to 40 of these coils, however as many as 380 have

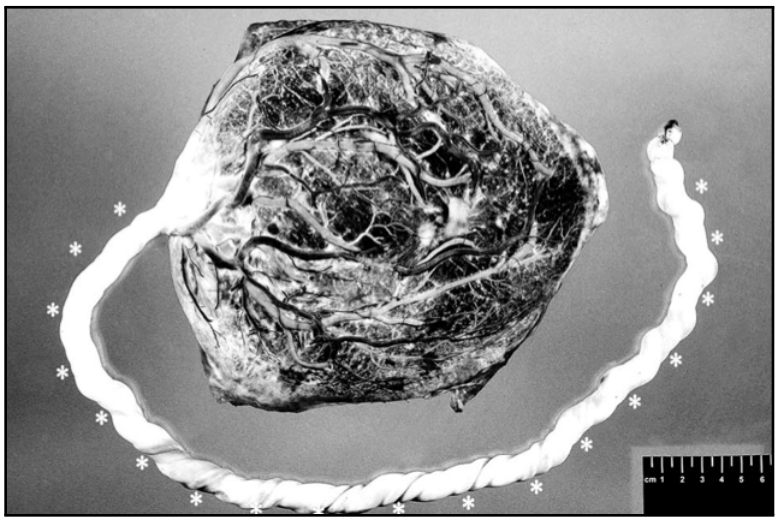

Figure 1.2: A normocoiled umbilical cord with placenta attached. The UCI for this case was calculated as 0.24 coils/cm from the 18 complete coils and 75cm length. The coils are designated with asterisks (de Laat et al., 2006).

been reported in a single umbilical cord (Benirschke et al., 2006). Strong et al. (1994) state that a typical normally-coiled cord is around 50-60 cm long, with approximately 11 coils along its length. The mechanisms underlying the coil formation, however, are still a matter of debate. Benirschke et al. (2006) state that the spiralling of the cord is usually attributed to fetal activity, and hence a lack of this characteristic may be indicative of fetal inactivity and possibly of central nervous system disturbances. However, active or passive torsion of the embryo, fetal hemodynamic forces, differential umbilical vascular growth rates as well as the presence of muscular fibers in the wall of the arteries have been suggested as several other factors fuelling this configuration (de Laat et al., 2005).

Despite the uncertainty of its origins, the coiling is known to ensure that the umbilical cord is both strong and flexible, and able to resist external forces which would otherwise compromise blood flow (de Laat et al., 2005). Cords therefore exhibiting abnormal coiling characteristics have been reported to exist more frequently in cases of adverse perinatal outcome (de Laat et al., 2005). Cords with a below average amount of coiling, or *hypocoiling*, are associated with fetal demise and chorioamnionitis[1] while cords exhibiting overcoiling, or *hypercoiling*, are associated with fetal demise, stenosis[2], thrombo-

[1] An inflammation of the fetal membranes (Youngson, 1992)

[2] A narrowing of the diameter of a bodily passage or orifice (Youngson, 1992)

Figure 1.3: Umbilical cords with left (L), untwisted (U) and right (R) twisting. Used with permission from (Kaplan, 2007).

sis[3], iatrogenic preterm delivery[4], aneuploidy[5] and structural anomalies (Kaplan et al., 2010). For this reason, a methodology quantifying the amount of coiling is desirable. Edwards (1954) was the first to develop such a system, termed the 'index of twist', which represents a ratio of the number of twists of the umbilical cord to its length. A twist here is defined as one complete 360° helix of the cord (including the blood vessels) around itself, with a change in direction corresponding to a negative 'twist'. This method was later simplified by Strong et al. (1994) to the method in use today which ignores the direction of the coils and is termed the umbilical coiling index or UCI.

Ideally, this system should be used to determine which umbilical cords exhibit an abnormal amount of coiling, and hence to diagnose or predict abnormal fetal outcomes. However, within the field of pathology there is an inconsistency in measuring both the length of the umbilical cord and the number of coils, which leads to the presence of errors in the calculation of the UCI and hence to a large variance in what are considered 'normal' values (Khong, 2010). It is generally agreed that cords with hypocoiling should be

[3]The formation or presence of a blood clot within a blood vessel (Youngson, 1992)

[4]Preterm delivery induced inadvertently by a physician or surgeon or due to medical treatment or diagnostic procedures (Youngson, 1992)

[5]Having an irregular number of chromosomes (Youngson, 1992)

defined as those cords with an UCI $\leq 10^{th}$ percentile while cords exhibiting hypercoiling are those with an index $\geq 90^{th}$ percentile (de Laat et al., 2005). However, depending on the data set used, the mean value of UCI may vary between 0.05 and 0.36, with the cut-off value for hypocoiling varying between 0.03 and 0.17 and that for hypercoiling between 0.25 and 0.54 (Khong, 2010). This factor ensures that the classification of a cord as hypo-, normo-, or hypercoiled is dependent on the data sample used and a completely different classification may be obtained by conducting the test with respect to a different sample. There is also some confusion in the literature regarding the measurement taken in determining the length of the cord. de Laat et al. (2005) describe the length measured as the 'length of the cord' while Khong (2010) reports various lengths being excised from the fetal end, which can purportedly range from 2 to 10 cm. This practice will affect the calculation of the UCI and potentially alter the cord classification. Kaplan et al. (2010) calculate this length as the true arclength of the coiled section of the cord, which twists and turns along its length, disregarding straight portions. They cite Strong et al. (1994) for this particular methodology, however, this paper describes the length as: *"measured in its entirety, including any segments removed for blood gas analysis"*. In a clinical setting, it is unlikely that the true arclength of the cord is being measured, and indeed the 'straightened' length may refer only to a large-scale straightening rather than to the removal of the helical character, as suggested by Kaplan et al. (2010). Regardless, the ambiguity in the literature results in wide variances to the calculated UCI. The number of coils, N, is also subject to some interpretation. Various authors such as de Laat et al. (2005) and Kaplan et al. (2010) take N as the number of complete coils of the cord, disregarding fractional turns. As Khong (2010) describes, this can lead to discrepancies in the calculation of the UCI, and potentially alter classification.

In addition to these issues, umbilical cords are not perfect helices and many will exhibit non-uniform coiling characteristics, as shown in figure 1.4. It is therefore possible that an umbilical cord may exhibit localised regions of intensive hypercoiling with normocoiling or hypocoiling in other areas. This information is effectively removed in the calculation of the UCI, which in essence describes the average length of one coil. Similarly, the appearance of structural abnormalities such as the presence of a 'false knot', which represents a localised exaggerated looping of the umbilical vessels, or a 'true knot', which are both shown in figure 1.5, are left completely unaccounted for in the calculation of the UCI (Khong, 2010). It is also not necessarily true that the large scale coiling of the cord be reflective of the coiling of the vessels. Figure 1.6 shows a cord which exhibits a highly coiled vasculature with a much lower coiling of the whole cord. The UCI calculated based on

Figure 1.4: An umbilical cord showing regions with non-constant twist. Here a right twisted cord becomes untwisted. Used with permission from (Kaplan, 2007).

the latter is therefore a poor approximation of the UCI of the vessels.

Ultimately the UCI represents a ratio of two measurable quantities which do not have any theoretical basis in pathology. Degani et al. (1995) found that the UCI did not correlate with any Doppler characteristics in the artery, though it correlated linearly to venous flow rate, increasing with index. Blood pressure is a common diagnostic for pathology within the systemic human circulation and is likewise believed to be important within the fetal circulatory system (Kaplan et al., 2010). Umbilical pressure measurements, however, are associated with a high level of risk and are typically replaced by less invasive Doppler measurements (Kiserud, 2005). As such a quantitative link between vessel pressure and pathology remains elusive. It is well known that the mean blood pressure drop within a vessel varies linearly with vessel length (Poiseuille, 1840). The UCI, which represents the average number of coils per unit (cm) length, critically removes any reference to the total vessel length and therefore the total vessel pressure drop. It is proposed that this renders the UCI ineffective as a diagnostic indicator.

1.2 Umbilical parameter survey

In order to model blood flow within the umbilical vessels, reference ranges for a number of physically important parameters must be developed. This is particularly relevant to the calculation of the Reynolds number, Re, and the reduced velocity, U_{red} (detailed in section 1.3) as well as to the geometric description of the cord.

Figure 1.5: An umbilical cord with true and false knots in a live infant. The arteries wind around the vein (indicated by the left arrow); a false knot with the vessels (top arrow) and another false knot with only the Wharton's jelly (central arrow), which is itself on a true knot. Used with permission from (Benirschke et al., 2006).

Figure 1.6: An umbilical cord for which the vessel coiling differs significantly from the whole cord coiling, courtesy of SA Pathology.

1.2.1 Vessel radius (R)

To an approximation the cross-section of each of the umbilical vessels may be assumed circular. In general, studies quantifying the typical reference ranges of the umbilical cross-section quote ranges for the radius, diameter or cross-sectional area. In this section a summary of the literature is presented in terms of the vessel radius alone, with the remaining parameters suitably converted. As will be further discussed, the distensibility of the umbilical vessel wall is ignored throughout this thesis and the cross-section is likewise assumed constant.

Many authors provide data on the cross-section using antenatal ultrasound imaging. Barbieri et al. (2012) examined 2310 low-risk pregnancies between 12 and 40 weeks' gestation. The arterial and venous radius were found to increase approximately linearly throughout the first 32 weeks of gestation, after which time they remained relatively constant until birth. Using 10^{th} and 90^{th} percentiles, the arterial diameter at 40 weeks gestation was found to vary between 0.32 cm and 0.68 cm. The arterial radius therefore varies such that, typically,

$$0.16 \text{ cm} < \hat{R}_A < 0.34 \text{ cm}.$$

The umbilical vein was likewise found to vary between approximately 0.65 cm and 1.3 cm in diameter,

$$0.33 \text{ cm} < \hat{R}_V < 0.65 \text{ cm}.$$

Flo et al. (2010) examined the umbilical vein diameter as well as volume blood flow-rates in 53 low-risk pregnancies between 22 and 39 weeks' gestation. At 39 weeks the diameter was found to vary between 0.66 cm (5^{th} percentile) and 0.9 cm (95^{th} percentile),

$$0.33 \text{ cm} < \hat{R}_V < 0.45 \text{ cm}.$$

Boito et al. (2002) examined the venous volume flow and cross-sectional area in a number of appropriate for gestational age (AGA) and intrauterine growth-restricted (IUGR) fetuses. For the AGA fetuses, the venous vessel area varied between 40 mm^2 (5^{th} percentile) and 66 mm^2 (95^{th} percentile) at approximately the 36^{th} week,

$$0.36 \text{ cm} < \hat{R}_V < 0.46 \text{ cm}; \qquad \bar{R}_V = 0.41 \text{ cm}.$$

For the growth restricted fetuses, the cross-sectional area could be as low as 27.5 mm^2 ($\hat{R}_V = 0.30$ cm). Togni et al. (2007) examined 312 women

between the 24^{th} and 39^{th} weeks of a normal pregnancy, and determined correlations between fetal anthropometric parameters and cross-sectional areas. For the umbilical vein, the cross-sectional area varied between 26.2 mm^2 (5^{th} percentile) and 87.9 mm^2 (95^{th} percentile) with a mean of 57.1 mm^2 at approximately the 39^{th} week,

$$0.29 \text{ cm} < \hat{R}_V < 0.53 \text{ cm}; \qquad \bar{R}_V = 0.43 \text{ cm}.$$

For the umbilical artery, the cross-sectional area varied between 5.8 mm^2 (5^{th} percentile) and 19.9 mm^2 (95^{th} percentile) with a mean of 12.8 mm^2 at approximately the 39^{th} week,

$$0.14 \text{ cm} < \hat{R}_A < 0.25 \text{ cm}; \qquad \bar{R}_A = 0.20 \text{ cm}.$$

Di Naro et al. (2002) compared umbilical vein blood flow in 15 growth-restricted fetuses with the same properties in 30 normal pregnancies. For the normal pregnancies, the mean cross-sectional arterial area was found to be 11.1 $\pm$ 3.8 mm^2, while the corresponding area for the vein was 43.1 $\pm$10.2 mm^2. For the growth-restricted fetuses, these were recorded as 10.3 $\pm$ 2.2 mm^2 and 35.5 $\pm$ 6.9 mm^2, respectively. The corresponding mean radii are therefore,

$$\begin{aligned} \bar{R}_A &= 1.9 \pm 1.1 \text{ cm}, \\ \bar{R}_{A,IUGR} &= 1.8 \pm 0.8 \text{ cm}, \\ \bar{R}_V &= 3.7 \pm 0.6 \text{ cm}, \\ \bar{R}_{V,IUGR} &= 3.4 \pm 1.5 \text{ cm}. \end{aligned}$$

Kaplan et al. (2010) use an umbilical arterial radius of 0.2 cm for their computational study while Waters and Guiot (2001) quote a radius of 0.35 cm for the umbilical vein in their elastic tube calculations. These values are consistent with the above survey and are used throughout this thesis.

1.2.2 Blood flow-rate (Q)

Knowledge of the blood flow-rate is important for developing bounds on the Reynolds number (Re) within each of the umbilical vessels. Due to the sensitivity of the environment, the flow-rate must be measured indirectly using Doppler ultrasound techniques. This method involves measuring the maximum velocity, or the time-averaged equivalent for the arteries, and assumes a simple Poiseuille flow distribution within both vessels. The flow-rate may then be computed using the average cross-sectional area. In this section flow-rate data for both vessels is presented. Information regarding the arterial

flow-rate, however, is less prevalent as parameters such as the pulsatility index (PI), are more commonly measured in practice. As will be discussed, the mean arterial flow-rate (Q_A) chosen for the purpose of this study is roughly half the value quoted within several similar studies. This has an important implication for the flow Re, which depends linearly on the flow-rate.

In addition to the cross-sectional measurements discussed, Flo et al. (2010) also examined the venous volume blood flow-rate in 53 low-risk pregnancies. At 39 weeks the blood-flow rate based on the time-averaged maximum velocity (TAMXV) was found to vary between 200 mL/min (5^{th} percentile) and 525 mL/min (95^{th} percentile),

$$3.33 \times 10^{-6}\ \text{m}^3/\text{s} < \hat{Q}_V < 8.75 \times 10^{-6}\ \text{m}^3/\text{s}; \qquad \bar{Q}_V = 6.04 \times 10^{-6}\ \text{m}^3/\text{s}.$$

Boito et al. (2002) examined the venous volume flow and cross-sectional area in a number of normal and growth-restricted fetuses. For the normal fetuses, the umbilical venous blood flow varied between 176 mL/min (5^{th} percentile) and 280 mL/min (95^{th} percentile) at approximately the 36^{th} week,

$$2.93 \times 10^{-6}\ \text{m}^3/\text{s} < \hat{Q}_V < 4.67 \times 10^{-6}\ \text{m}^3/\text{s}; \qquad \bar{Q}_V = 3.80 \times 10^{-6}\ \text{m}^3/\text{s}.$$

For the growth restricted fetuses, the flow-rate could be as low as 90 mL/min (1.5×10^{-6} m^3/s). Di Naro et al. (2002) compared umbilical vein blood flow in 15 growth-restricted fetuses with the same properties in 30 normal pregnancies in order to determine changes in the flow with gestational age. The absolute vein flow in the IUGR fetuses was found to be significantly lower than the AGA fetuses. In one particular case, the flow-rate was found to be lower than 100 mL/min (2.93×10^{-6} m^3/s).

While arterial flow-rate data is relatively scarce, Lees et al. (1999) presents a study which compares umbilical venous and arterial blood flow in 129 pregnancies between 23 and 33 weeks' gestation. They quote the total arterial flow-rate (from figure 5 of that paper) as varying between 175 mL/min (5%) and 400 mL/min (95%) with a mean of 287.5 mL/min. For a single umbilical artery the flow-rate is half the total, hence appropriate ranges on the flow-rate within a single artery are,

$$1.46 \times 10^{-6}\ \text{m}^3/\text{s} < \hat{Q}_A < 3.33 \times 10^{-6}\ \text{m}^3/\text{s}; \qquad \bar{Q}_A = 2.40 \times 10^{-6}\ \text{m}^3/\text{s}.$$

where the mean is approximately 144 mL/min. Several fluid dynamic studies of the umbilical arteries quote the total arterial flow-rate measured by Lees et al. (1999) as the value for a single vessel. Gordon et al. (2007), which examined blood-flow through a Hyrtl anastomosis[6], use a value of 250 mL/min

[6]A connection between the umbilical arteries near the placenta (Youngson, 1992)

for the inlet boundary condition to a single artery. This study is in-turn referenced by Kaplan et al. (2010) for their computational analysis of umbilical arterial flow. The flow-rate used for this study is chosen as 265 mL/min, citing Gordon et al. (2007), Kiserud (2005) and Acharya et al. (2005*b*). The latter of these studies concerns only venous flow, while Kiserud (2005) states the figure as referring to 'umbilical blood flow' and cites the venous study of Acharya et al. (2005*b*). It is therefore likely that the value quoted is too large for a single umbilical artery.

Aside from Lees et al. (1999), arterial flow-rate data is scarce. However, Acharya et al. (2005*a*) measured the time-averaged maximum velocity (TAMXV), in addition to a number of other arterial parameters, from which an estimate of the arterial flow-rate can be determined. Using the Poiseuille flow assumption and an arterial radius of 0.2 cm, the arterial flow-rate quoted in Acharya et al. (2005*a*) varies so that,

$$1.00 \times 10^{-6} \text{ m}^3/\text{s} < \hat{Q}_A < 4.21 \times 10^{-6} \text{ m}^3/\text{s}; \qquad \bar{Q}_A = 2.42 \times 10^{-6} \text{ m}^3/\text{s}.$$

This mean flow-rate agrees well with the figure adapted from Lees et al. (1999). Additionally, it is intuitive that the arterial flow-rate in a normal three vessel cord should measure half the flow-rate within the vein. For these reasons the mean arterial flow-rate used within this study is 2.42×10^{-6} m^3/s, or 145 mL/min.

1.2.3 Pulsatility characteristics

In addition to the time-averaged maximum velocity, a number of other parameters are routinely measured to quantify the pulsatility within the umbilical arteries. Acharya et al. (2005*a*) examined 130 normal pregnancies and recorded arterial velocity parameters at three locations; the intra-abdominal, fetal and placental ends. The measured parameters were the peak systolic velocity (PSV), the end diastolic velocity (EDV), the time-averaged maximum velocity (TAMXV) and the pulsatility index (PI), which is defined as,

$$\text{PI} = \frac{\text{PSV} - \text{EDV}}{\text{TAMXV}}.$$

The evolution of the measured velocities with gestation was found to depend on the measurement location. At the fetal end the velocities typically increased with gestational age. At the intra-abdominal portion the gestation curves took on a less simple relation with the PSV and TAMXV typically attaining their maximum value at around 30 wks gestation with EDV increasing throughout. At the placental end the same general trends as for the

	PSV	EDV	TAMXV	PI	$\frac{2\text{PSV}}{\text{TAMXV}}$
20 wks	40.0	7.50	22.5	1.42	3.56
30 wks	52.0	16.0	35.0	1.05	2.97
40 wks	58.5	24.5	38.0	0.80	3.10

Table 1.1: Values of the peak systolic velocity (PSV), end diastolic velocity (EDV), time-averaged maximum velocity (TAMXV) and the pulsatility index (PI) read from Acharya et al. (2005*a*) at 20, 30 and 40 wks gestation. Velocity measurements are quoted in cm/s. The ratio of the peak velocity (PSV) to the temporally and cross-sectionally averaged velocity (TAMXV/2) is relevant to the pulsatile inlet boundary condition.

fetal end were present. The PI, however, was found to reduce with gestational age at each of the three measurement locations. For the purpose of developing an inflow boundary condition the fetal end measurements are the most relevant to this study and hence the mean values recorded at 20, 30 and 40 wks gestation are presented in table 1.1.

Tejada-Martínez et al. (2011) conducted a two-dimensional analysis of umbilical artery flow in which they used a PSV of 24.0 cm/s and an EDV of 2.0 cm/s, based upon the work of Acharya et al. (2005*a*). These values are quoted from Table 4 of this paper which is a table of differences and does not list the measured velocities. The PSV and EDV recorded in Acharya et al. (2005*a*), shown in table 1.1, are roughly 60 and 25 cm/s, respectively. The values quoted by Tejada-Martínez et al. (2011) are therefore lower than typically observed at gestation.

The ratio of the PSV to the temporally and cross-sectionally averaged velocity is important for the prescription of the pulsatile inlet boundary condition. A ratio of 3.1 is typical at birth (Acharya et al., 2005*a*) and is used in the unsteady analysis of chapter 4.

1.2.4 Fetal heart-rate (f)

The fetal heart-rate in a healthy pregnancy is substantially higher than recorded in an adult human. Kaplan et al. (2010) use a nominal fetal heart-rate of 140 bpm which agrees with the study conducted by Pildner von Steinburg et al. (2013) where the fetal heart-rate was found to vary between 110

and 160 bpm in a normal pregnancy. Liao et al. (2000) describe the fetal heart-rate as typically increasing from 110 bpm at 5 weeks gestation to 170 bpm at 9 weeks before gradually decreasing to 150 bpm at 14 weeks. Values outside these limits are usually indicative of pathology and bradycardia (or a reduced heart-rate) is defined as a heart-rate less than 100 bpm, while tachycardia (or an elevated heart-rate) occurs at fetal heart-rates exceeding 160 bpm. For the pulsatile analysis of chapter 4 a nominal heart-rate of 140 bpm is used.

1.2.5 Kinematic viscosity (ν)

Blood viscosity is primarily controlled by the level of haematocrit, erythrocyte deformability, total serum protein and plasma fibrinogen (Jouppila et al., 1986). In the context of a fluid dynamic study, it has important implications for the flow Re. Data for the blood viscosity specific to the umbilical cord, however, is quite rare. Jouppila et al. (1986) performed measurements on the vein shortly after birth in a number of normal and irregular pregnancies. They found a mean dynamic viscosity of $\hat{\mu} = 4.2 \pm 0.6$ cP ($4.2 \times 10^{-3} \pm 6 \times 10^{-4}$ kg/ms) for the normal pregnancies, however, for irregular pregnancies this could be as high as $\hat{\mu} = 5.0$ cP (5.0×10^{-3} kg/ms). Assuming a blood density of $\hat{\rho} = 1060$ kg/m^3, the normal venous blood kinematic viscosity could be expected to vary between,

$$3.4 \times 10^{-6} \text{ m}^2/\text{s} < \hat{\nu}_V < 4.72 \times 10^{-6} \text{ m}^2/\text{s}.$$

Many fluid dynamic studies, including Gordon et al. (2007), Kaplan et al. (2010) and Guettouche et al. (1992), simply use the standard human blood viscosity values measured elsewhere in the body. Guettouche et al. (1992) quote a blood density of $\hat{\rho} = 1060$ kg/m^3 and blood dynamic viscosity $\hat{\mu} = 0.052$ dyn.s/cm^2 (5.2×10^{-3} kg/ms) which results in a kinematic viscosity of,

$$\hat{\nu} = 4.91 \times 10^{-6} \text{ m}^2/\text{s}.$$

Thompson and Trudinger (1990) cite Caro et al. (1978) and use $\hat{\mu} = 4 \times 10^{-3}$ kg/ms while Womersley (1955) quote 1056 kg/m^3 for the blood density and allow the viscosity to vary such that 1×10^{-3} kg/ms $< \hat{\mu} < 8 \times 10^{-3}$ kg/ms,

$$9.5 \times 10^{-7} \text{ m}^2/\text{s} < \hat{\nu} < 7.6 \times 10^{-6} \text{ m}^2/\text{s}.$$

This is quite a significant range and typically, the kinematic viscosity can be expected to lie around 4.0×10^{-6} m^2/s. In this study a blood density of $\hat{\rho} = 1060$ kg/m^3 coupled with a dynamic viscosity of $\hat{\mu} = 4.0 \times 10^{-3}$ kg/ms is used which results in a kinematic viscosity of $\hat{\nu} = 3.77 \times 10^{-6}$ m^2/s.

1.2.6 Cord vessel pressure (P)

Direct measurement of the umbilical blood pressure is possible, though non-standard, through a process known as cordocentesis. The procedure, in which a needle is used to penetrate the cord, carries a significant likelihood of complication and is only performed in pregnancies considered high-risk. Kiserud (2005) state that the umbilical venous pressure measured in this way increases from 4.5 mmHg (approximately 600 Pa) at 18 weeks to 6 mmHg (approximately 800 Pa) at term, when corrected for amniotic pressure. The mean arterial pressure was similarly found to measure 15 mmHg (approximately 2000 Pa) between the 19th and 21st week of gestation. Reynolds (1978) notes that the pressure drop over the length of the umbilical artery (from umbilicus to placental cotyledon) in lambs is typically around 10 mmHg, however, at the time of writing there is no comparable data for the human umbilical cord. If a similar pressure gradient of approximately 0.48 mmHg per cm of artery were observed within the human umbilical cord, the pressure within the placenta would quickly drop to less than zero yielding an unphysical situation. This suggests that the mean arterial pressure gradient in humans is less severe than in lambs. The analysis of the Hyrtl anastomosis conducted by Gordon et al. (2007) prescribed an inlet pressure of 38.6 mmHg (5150 Pa) coupled with an outlet pressure of 9 mmHg (1200 Pa), described as the pressure at the cotyledons. This yields an arterial pressure drop of 29.6 mmHg, or 3950 Pa. The mean arterial pressure in this paper is quoted to lie between 20 and 80 mmHg.

1.2.7 Umbilical coiling index (UCI)

The umbilical coiling index is calculated based on measurement of the cord length, $\hat{L}$, and the number of coils, N. The ambiguity in the literature regarding the definition of each of these parameters has resulted in a corresponding variance in the typical reference ranges. The first paper to suggest the potential of the UCI as a diagnostic indicator, Strong et al. (1994), found that a mean of 0.21 ± 0.07 (SD) coils/cm was typical in a normal pregnancy. de Laat et al. (2005) state that the normal UCI is typically 0.17 coils/cm with hypocoiling present for UCI < 0.07 coils/cm and hypercoiling for UCI > 0.3 coils/cm. Machin et al. (2000) report a mean of 0.2 ± 0.1 coils/cm while Kaplan et al. (2010) state that the normal UCI lies between 0.18 and 0.22 coils/cm, equivalent to 10-11 coils in a 50 cm long cord. Tahmasebi and Alighanbari (2011) measured a mean prenatal UCI of 0.4 coils/cm, for pregnancies greater than 20 wks gestation. The index was calculated sonographically and was only measured in an average sense as the reciprocal of one

coil length at several cord positions. The UCI, which is typically measured postpartum, should ideally represent the cord geometry in-utero. However, Degani et al. (1995) found a reduction of the mean coiling index from 0.44 $\pm$ 0.11 coils/cm measured sonographically within 24 hrs of birth, to 0.28 $\pm$ 0.08 cm measured after birth. This same study also found a higher incidence of coils at the fetal end and reported 12% of cords to have mixed helical direction.

1.2.8 Cord thickness (w)

A knowledge of the cord thickness is important to fully describe the helical nature of the vessels. Barbieri et al. (2012) found the cord thickness to increase throughout pregnancy until around 32 wks, with a mean of 1.78 $\pm$ 0.22 cm. The measured vein and artery diameter in each of these cases was larger than standard with a mean of 0.91 and 0.46 cm at 40 wks, respectively. Raio et al. (1999) found a similar increase in cord thickness of 1.672 cm to 32 wks, however, this was followed by a reduction in mean thickness to 1.442 cm at 41 wks. The cord thickness at birth varied in-utero after 20 wks gestation between 0.36 and 2.36 cm with a mean of 1.54 cm in the study conducted by Tahmasebi and Alighanbari (2011). The Wharton's jelly, which encases the umbilical vasculature, was also found to increase throughout pregnancy by Barbieri et al. (2011). In this study, the nominal width is taken as $\hat{w} = 1.6$ cm.

1.2.9 Summary

A summary of the important parameters from the literature is compiled in table 1.2. The minimum and maximum shown represent extreme bounds, however, are useful in devising reference ranges for the dynamical parameters relevant to a three-dimensional numerical study.

1.3 Modelling blood flow

While experimental results are invaluable to the study of physiological flow processes, this understanding can be supplemented by a theoretical analysis utilising mathematical techniques. There are many complexities involved in modelling blood flow from a mathematical perspective. Firstly, blood is not a homogenous fluid and is instead a suspension of particles in an aqueous solution (Mazumdar, 1992). It is known to exhibit non-Newtonian behaviour at low-shear rates (Pedley, 1980) and hence care must be taken

	min.	max.	nominal
Arterial radius, $\hat{R}_A$ (cm)	0.14	0.34	0.2
Venous radius, $\hat{R}_V$ (cm)	0.29	0.75	0.35
Arterial flow-rate, $\hat{Q}_A$ (10^{-6} m^3/s)	1.00	4.21	2.4
Venous flow-rate, $\hat{Q}_V$ (10^{-6} m^3/s)	1.45	8.75	4.4
Blood viscosity, $\hat{\nu}$ (10^{-6} m^2/s)	3.40	4.72	3.77
Fetal heart-rate, f (bpm)	110	160	140

Table 1.2: Summary of the umbilical parameters relevant to a dynamical analysis, surveyed from the literature.

to ensure that these effects are duly considered. Arterial blood flow is also pulsatile (Pedley, 1980), exhibiting a time-dependence which affects the flow field throughout the cycle. This factor, coupled with the distensibility of the arterial wall, ensures that the diameter of the artery is not necessarily constant (Mazumdar, 1992). Moreover, the three-dimensional structure of the vasculature in the umbilical cord is non-trivial and will significantly affect the pressure drop, wall shear stress, as well as the formation of secondary velocity fields (Fung, 1997). In practice, however, it is necessary to isolate the defining aspects of a given flow, and to ignore issues considered of limited or reduced consequence. These assumptions are dependent on the region of the circulatory system considered, as well as on the particular aspects of the flow under examination. In this study the distensibility of the arterial wall is ignored in order to allow for the analysis of complex three-dimensional geometries without signifcant numerical cost.

1.3.1 The nature of blood

Blood itself is composed of a number of formed elements suspended within a plasma (Pedley, 1980). The formed elements include red blood cells, white blood cells and platelets, and occupy approximately 45% by volume of the blood (Pedley, 1980). The red blood cells are the most numerous and hence dominate the mechanical properties of the blood, while the platelets and white blood cells have a lower concentration and are essentially dynamically unimportant (Pedley, 1980). For flow in the larger arteries, the multi-phase nature of blood must often be ignored in order to yield a tractable solution.

This assumption, however, is not valid in the smallest blood vessels, where the capillary diameters are of comparable size to the red cells (Pedley, 1980). The non-Newtonian nature of the blood is another feature which, provided the flow meets certain requirements, can be ignored in order to aid in the solution of the problem. For an incompressible Newtonian fluid, the deviatoric stress tensor, $\tau_{i,j}$, may be related to the rate-of-strain tensor by a constant of proportionality, μ, the dynamic viscosity (Batchelor, 1967),

$$\tau_{i,j} = 2\mu \left(\frac{\partial u_i}{\partial x_j} + \frac{\partial u_j}{\partial x_i} \right), \tag{1.1}$$

where u_i represent the three Cartesian components of velocity, μ has units kg/ms and Einstein summation notation is used. It has been determined experimentally that the viscosity, μ, of blood is approximately independent of the rate-of-strain, S, for $S > 100$ s^{-1} (Whitmore, 1968). The average shear-rate at the artery walls is substantially greater than this threshold (Pedley, 1980), and hence it is often acceptable to assume that the blood behaves as a Newtonian fluid. It should, however, be noted that the shear-rate will have a lower value in separated and recirculating regions of the flow, as well as within the core of the flow in a straight blood vessel. Moreover, if flow reversal is present the wall shear will become zero, and hence the above condition on S is not satisfied at all times within the flow field. While this temporary non-Newtonian behaviour is not yet fully understood, blood flow in the larger arteries is often, for the sake of a solution, treated as a homogenous, Newtonian fluid (Pedley, 1980).

The unsteady nature of arterial blood flow introduces and affects a number of important flow processes, such as the transition from a laminar (smooth) flow to a turbulent (or more chaotic) flow (Fung, 1997). For this reason, the unsteady nature of blood flow should be accounted for if a more rigorous analysis of the flow regime is to be sought. Likewise, the variable vessel diameter provides a feedback system between fluid and structure which is important in some arterial networks in order to obtain a precise understanding of the biological system (Formaggia et al., 2009). The three-dimensional nature of the flow-field also has a large effect on flow properties (Doorly and Sherwin, 2009) and any complete flow-field analysis will account for geometric effects appropriately. These aspects are further discussed in section 1.4.

1.3.2 The constitutive equations

When treated as a continuous fluid, blood flow is described by the three-dimensional Navier-Stokes equations. Provided a solution exists, this system

forms a set of non-linear partial differential equations yielding the velocity field for a given flow,

$$\hat{\rho}\left(\frac{\partial \hat{u}_i}{\partial \hat{t}} + \hat{u}_j \frac{\partial \hat{u}_i}{\partial \hat{x}_j}\right) = -\frac{\partial \hat{P}}{\partial \hat{x}_i} + \hat{B}_i(\hat{x}_j, \hat{t}) + \hat{\rho}\hat{G}_i + \frac{\partial}{\partial \hat{x}_j}\left(\mu\left(\frac{\partial \hat{u}_i}{\partial \hat{x}_j} + \frac{\partial \hat{u}_j}{\partial \hat{x}_i}\right)\right). \quad (1.2)$$

Here $\hat{\rho}$ is the fluid density, $\hat{t}$ represents time, $\hat{P}$ is the fluid pressure, and the body force has been split into a variable force, $\hat{B}_i(\hat{x}_j, \hat{t})$, and a constant vector, $\hat{\rho}\hat{G}_i$, which is representative of gravitational forces. The hatted quantities are dimensional, however, problem-specific reference quantities can be used to produce the non-dimensional equations,

$$\begin{aligned} R_\rho Re\left(St\frac{\partial u_i}{\partial t} + u_j\frac{\partial u_i}{\partial x_j}\right) = &-\frac{\partial P}{\partial x_i} + B_i(x_j, t) + R_\rho \frac{Re}{Fr} G_i \\ &+ \frac{\partial}{\partial x_j}\left(R_\mu\left(\frac{\partial u_i}{\partial x_j} + \frac{\partial u_j}{\partial x_i}\right)\right). \end{aligned} \quad (1.3)$$

where Re is the Reynolds number, St is the Strouhal number and Fr is the Froude number,

$$Re = \frac{\mathcal{U}\mathcal{L}\rho_{ref}}{\mu_{ref}}, \quad St = \frac{\mathcal{L}}{\mathcal{U}T}, \quad Fr = \frac{\mathcal{U}^2}{g\mathcal{L}}.$$

Here $\mathcal{U}$, $\mathcal{L}$, ρ_{ref}, μ_{ref}, T and g are the reference quantities for the velocity, length, density, viscosity, time and gravity scales, respectively. Unless stated these scales are taken as the cross-sectionally (and temporally) averaged fluid velocity, the vessel radius, the nominal fluid density and viscosity (see table 1.2), the period of the fetal heart-beat and the standard gravity scale (which is irrelevant to this study), respectively.

Physically, Re is an important parameter used in the description of a flow-field. It represents a ratio of the inertial and viscous forces and can therefore be used to predict turbulent transition. For flow in a straight pipe, a lower Reynolds number flow (Re less than approximately 2000) is associated with laminar, or stable flow, while Re in excess of 4000 usually indicates that the flow is turbulent (Ward-Smith, 1980). Using the vessel radius, R, as the length scale and the average cross-sectional velocity, w_m, as the velocity scale in combination with the parameter ranges given in table 1.2, the Re within each of the umbilical vessels typically lie within the range,

$$20 < Re_A < 280,$$

$$10 < Re_V < 280.$$

These are extreme bounds and the Reynolds number in each vessel is nominally around 100 based on the typical values from the study of section 1.2. According to Quarteroni et al. (2009) the Reynolds number is approximately 50 for small arteries of radius 0.1 cm in the systemic circulation of an adult human. For an umbilical artery twice the size at 0.2 cm radius it is reasonable to expect a Re of 100 based on induction and the definition of Re stated above. Kaplan et al. (2010) quote the normal Re (based on the arterial diameter) within the umbilical arteries as between 420 and 430, however this is due to the larger arterial blood flow rate used in this study, discussed previously in section 1.2.2.

Equation (1.3), together with the equation of continuity which for an incompressible fluid is given by,

$$\frac{\partial u_i}{\partial x_i} = 0, \tag{1.4}$$

form a system of four equations in the four unknowns, u_i for $i = 1, 2, 3$ and P. This system permits analytic solutions in only a few, simplified cases. In order to solve more general flow problems such as blood flow through complex geometries, numerical methods, discussed further in chapter 2, may be used to provide approximations to the velocity and pressure field. However, for the simplified case of steady, fully developed laminar flow in a straight pipe a formula relating the velocity field and pressure drop was initially formulated by both Hagen (1839) and Poiseuille (1840) while investigating the flow of blood in capillary tubes. They showed that the fully developed axial velocity profile, $w = W(r)$, in a straight tube assumes a parabolic dependence on the radial distance, r, from the centre, i.e. $W(r) \propto 1 - r^2$. Flows which satisfy this relationship are termed Poiseuille flow, and represent the equilibrium flow regime attained in steady, low Reynolds number straight pipe flow. Using this result, flow fields within more complex geometries may be approximated using perturbation methods which offer insight not available through computational means. Application of this particular method to fluid flow in curved and helical pipes is discussed in section 1.4.

1.3.3 Pulsatile flow

Blood flow within the umbilical arteries is inherently unsteady, exhibiting a pulsatile waveform dependent on the pressure pulse developed by the fetal heart. Womersley (1955) developed a closed-form analytic solution for the axial velocity within an infinite circular pipe, consisting of periodic laminar

flow, with the velocity at each temporal harmonic given by,

$$w_n(r,t) = \Re\left(\frac{P_n i}{\rho\omega_n}\left(\frac{J_0(i^{3/2}\alpha_n r/R)}{J_0(i^{3/2}\alpha_n)} - 1\right)e^{i\omega_n t}\right). \tag{1.5}$$

Here $\Re(x)$ denotes the real component of x, P_n are complex pressure coefficients related to the axial pressure gradient,

$$\frac{\partial P}{\partial Z} = \Re\left(\sum_{n=0}^{N} P_n e^{i\omega_n t}\right), \tag{1.6}$$

$\omega_n = 2\pi n/T$ is the circular frequency at the n-th harmonic with period T, $i = \sqrt{-1}$, J_0 is the zeroth-order Bessel function of complex argument and α (sometimes Wo) is the Womersley number given by,

$$\alpha_n = R\sqrt{\frac{\omega_n}{\nu}} = \sqrt{\frac{2\pi Re}{U_{red}}}.$$

Here ν is the kinematic viscosity of the fluid, Re is the Reynolds number based on the temporally and cross-sectionally averaged axial velocity, $\overline{w}_m$, and the vessel radius, R, and U_{red} is the reduced velocity which relates the physical velocity, time and length scales,

$$U_{red} = \frac{\overline{w}_m T}{R} = \frac{\text{distance travelled by mean flow}}{\text{pipe radius}}.$$

The reduced velocity is the reciprocal of the Strouhal number, St, and is sometimes favoured over the Womersley parameter which can be interpreted as a ratio of cross-sectional length scales only,

$$\alpha = R\sqrt{\frac{\omega}{\nu}} \propto \frac{R}{\nu T} = \frac{\text{vessel radius}}{\text{boundary length growth in time } T}.$$

The velocity scale used in pulsatile flow problems is typically taken as $\overline{w}_m$, the temporally averaged velocity given by,

$$\overline{w}_m = \frac{1}{T}\int_0^T w_m(t)\mathrm{d}t, \tag{1.7}$$

where $w_m(t)$ is the sectional average given by,

$$w_m(t) = \frac{2}{R^2}\int_0^R w(r,t) r \mathrm{d}r. \tag{1.8}$$

From Womersley (1955) the axial velocity profile for axisymmetric flow is given by,

$$w(r,t) = w_0(r) + \sum_{n=1}^{N} \Re\left(\frac{P_n i}{\rho \omega_n} \left(\frac{J_0(i^{3/2}\alpha_n r/R)}{J_0(i^{3/2}\alpha_n)} - 1 \right) e^{i\omega_n t} \right), \tag{1.9}$$

where the steady solution, $w_0(r)$, is given by the Poiseiulle flow solution,

$$w_0(r) = 2w_{m,s}\left(1 - \left(\frac{r}{R}\right)^2\right). \tag{1.10}$$

Here $w_{m,s}$ is the sectional mean for the steady flow. The real part of each of the harmonic terms corresponding to the prescribed pressure gradient in equation (1.6) are taken, however this could equally be performed for the imaginary components.

1.4 Flow in curved and helical pipes

The umbilical cord exhibits a coiled structure which can be thought of as a pipe that twists and turns in space, with the centreline not constrained within a plane. In mathematical terms, this centreline exhibits both non-zero curvature, κ, and torsion, τ. For a simple helical curve, these parameters are defined as,

$$\kappa = \frac{R_h}{(P_h/2\pi)^2 + R_h^2} \qquad \tau = \frac{P_h/2\pi}{(P_h/2\pi)^2 + R_h^2} \tag{1.11}$$

where the radius of the helix is given by R_h and P_h is the pitch. This simple characteristic presents several challenges from a mathematical stand-point. As stated previously, a general solution to the system of equations (1.3) and (1.4), does not exist in three dimensions. As such, several techniques have been developed within the last century in order to approximate flow in curved pipes, and more recently flow in pipes exhibiting torsion. One of the first of these studies began with the pioneering work of Dean (1927, 1928), who examined fluid flow in a loosely-coiled torus where $\tau = 0$. Here a perturbation about Poiseuille flow was used in order to arrive at the famous Dean equations. The non-dimensional Dean number, Dn, is a dimensionless parameter which arises naturally in such an analysis and can be viewed as a Reynolds number modified for curved pipes (Doorly and Sherwin, 2009). It is defined as,

$$Dn = 8Re\sqrt{\frac{2R}{R_c}},$$

where R_c is the radius of curvature of the bend. The curvature of a toroidal pipe develops a centrifugal force which skews the parabolic axial velocity profile toward the outside of the pipe. A cross-pipe secondary flow is created which, for a sufficiently low Dn, consists of two counter-rotating vortices, symmetric about the pipe normal axis.

1.4.1 Coordinate systems

Following Dean (1927, 1928) similar methods have been employed in order to extend this analysis to helical pipes and the complex secondary motions that evolve as a result. To facilitate these studies an orthogonal coordinate system was developed by Germano (1982) based on the Frenet triad of unit vectors associated with a generic spatial curve. Recognising that the system previously defined by Wang (1981) was not orthogonal, Germano (1982) allowed the coordinate axes within the normal plane defined by the normal, $\boldsymbol{N}$, and binormal, $\boldsymbol{B}$, vectors to vary according to the torsion, essentially rotating with precession through the helix. This system was modified slightly by Kao (1987) to measure the angle from the line parallel to $-\boldsymbol{N}$, where a point in the pipe, $\vec{R}$, is given by its arclength along the pipe centreline, s, the radial distance within the pipe, r, and the angular position, θ, within the cross-section,

$$\vec{R}(s) = \vec{R}_0(s) - r\cos(\theta + \phi(s) + \phi_0)\boldsymbol{N} + r\sin(\theta + \phi(s) + \phi_0)\boldsymbol{B}. \qquad (1.12)$$

Here $\vec{R}_0(s)$ is the arclength parameterisation of the pipe centreline curve and $\phi(s)$ varies with torsion by,

$$\phi(s) = \int_0^s \tau(s)\,\mathrm{d}s. \qquad (1.13)$$

This description has the advantage that it is orthogonal and applicable to a large range of pipes, however, for a helical pipe it has the disadvantage of referring to the pipe centreline. As a result, the basis does not contain the tangent vector field to the line congruence of helices with the same pitch which provides a natural means of distinguishing between the primary and secondary flow-fields (Gammack and Hydon, 2001). This factor highlights the truly three-dimensional nature of helical flows. Zabielski and Mestel (1998*a*,*b*) proposed an alternative, helically symmetric coordinate system for the analysis of steady and unsteady blood flow in a helix. This system is based on the helical symmetry direction, $\boldsymbol{H}$, and is computationally efficient as it reduces the problem to essentially two dimensions. However, for an analysis of fluid-flow within pipes of variable torsion the system is unsuitable

as these pipes lack helical symmetry (Gammack and Hydon, 2001). The umbilical blood flow analysis considered here must account for variable torsion cords and should therefore utilise the system introduced by Germano (1982). However, care must be taken in order to appropriately distinguish between primary and secondary flow components.

1.4.2 Characteristics of helical flow

Analytical studies of helical pipe flow in uniform geometries have been provided by Germano (1982, 1989), Kao (1987), Wang (1981) and Tuttle (1990) to name only a few. For flow within a circular cross-section the effect of small torsion is to skew the Dean vortices in the direction of increasing torsion (Kao, 1987), i.e. with greater incline to the pipe normal axis. As the torsion increases at constant Dean number, the angle increases further until only a single recirculating region is formed (Yamamoto et al., 2002). This transition is demonstrated in the experimental tests conducted by Yamamoto et al. (2002), which are shown in figure 1.7. Note that while the Reynolds number varies slightly throughout these tests the images display the qualitative effect of increasing torsion on the cross-pipe flow as the curvature is held constant. For lower Reynolds number flow at low torsion and curvature, a single-vortex solution also exists (Wang, 1981) which could be seen in the experimental work of Yamamoto et al. (2002).

Fluid flow within pipes of non-constant pitch and helical radius are of interest in the study of umbilical cord blood flow as it is unlikely that the cord will form a regular helix. Gammack and Hydon (2001) considered steady and unsteady fluid flow within pipes of variable curvature and torsion. They found that in the pulsatile case, flow reversal occurs for pipes of non-uniform curvature provided the frequency of oscillation is low enough. This flow reversal was found to differ from that previously described as it is due to an inversion of the perturbed pressure profile.

1.4.3 The pressure drop and flow friction factor

The pressure drop measured along the length of a straight pipe is typically stated in the form of the so-called 'flow friction factor' often written as f and not to be confused with the flow frequency. This quantity relates to the pipe longitudinal pressure gradient by,

$$fRe = -\frac{2RRe}{\rho w_m^2}\frac{\Delta \hat{P}}{\Delta \hat{Z}}. \tag{1.14}$$

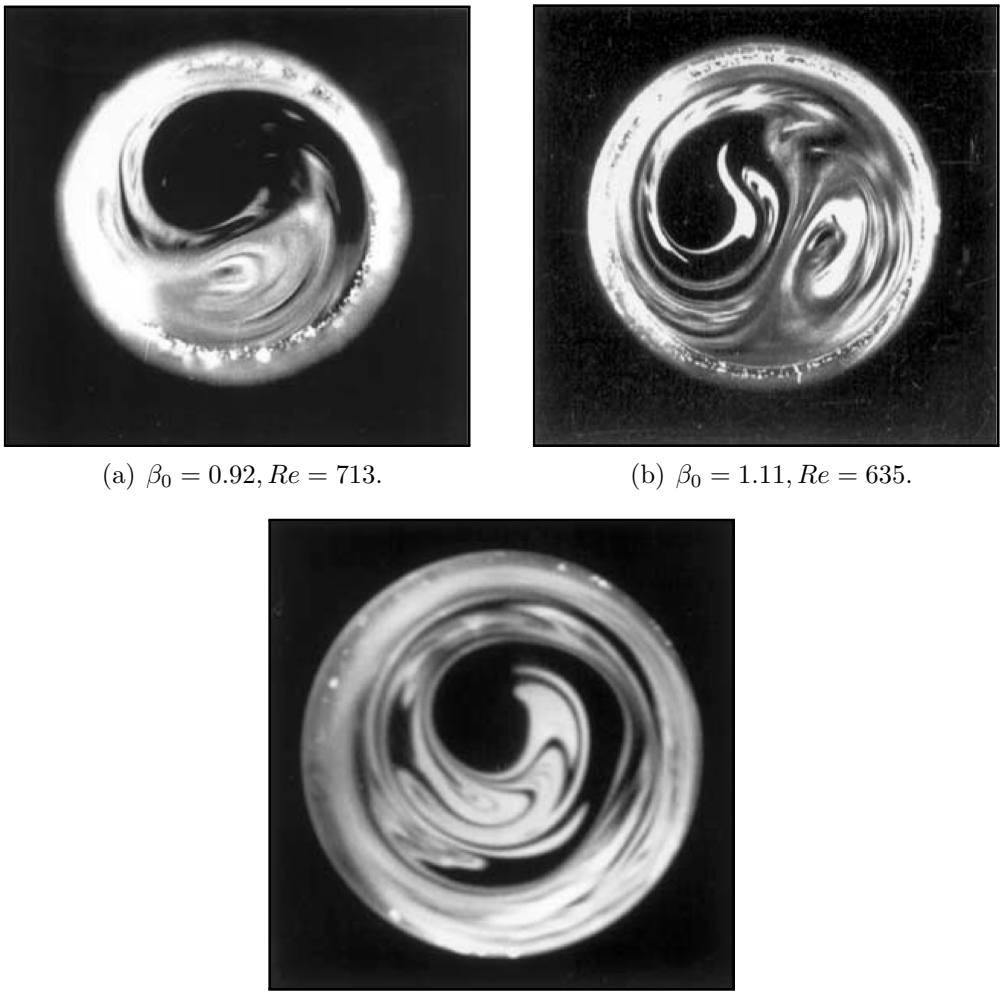

(a) $\beta_0 = 0.92, Re = 713.$

(b) $\beta_0 = 1.11, Re = 635.$

(c) $\beta_0 = 1.60, Re = 641.$

Figure 1.7: Experimental flow visualisation in a helical pipe of circular cross-section obtained from Yamamoto et al. (2002). Note here that $\beta_0 = \tau/(2\kappa^{3/2})$. Torsion increases clock-wise from top-left.

The pressure drop, $\Delta\hat{P}$, which is here written in dimensional units, can be written in non-dimensional terms on both the inertial and viscous scales. For the purpose of this study the viscous scale is the most appropriate,

$$\Delta P = \frac{\hat{\rho}\hat{R}^2\Delta\hat{P}}{\hat{\mu}^2 Re}. \tag{1.15}$$

Using this relation the pressure gradient can be determined from the friction factor by,

$$\frac{dP}{dZ} = -\frac{fRe}{2}. \tag{1.16}$$

Empirical estimates of the friction factor have been determined by various authors for different curved and helical pipes throughout the past century, with varying accuracy and applicability. Ali (2001) provide an overview of the literature as well as some empirical formulae obtained through experimental analysis of helical flow. Dean (1928) and Van Dyke (1978) provide an analytical expression for the flow friction factor through a curved tube, while helical correlations were provided by Mishra and Gupta (1979), Hasson (1955), Manlapaz and Churchill (1980) and Liu and Masliyah (1993). Liu and Masliyah (1993) give a correlation for fRe for helical pipes of finite pitch, where the previous work had concerned helical pipes in the limit of small curvature and/or torsion. The correlation is,

$$\begin{aligned} fRe = &\left(16 + \left(\sqrt{2}\times 0.378 Re^{1/2} + 12.1\kappa^{-1/2}Dn^{-1/2}\right)\tau^2\right) \\ &\times\left(1 + \frac{\left(0.0908 + 0.0233\kappa^{1/2}\right)Dn^{1/2} - 0.132\kappa^{1/2} + 0.37\kappa - 0.2}{1 + 49/Dn}\right), \end{aligned} \tag{1.17}$$

which requires,

$$Dn \leq 5000, \quad \gamma = \frac{Gn}{Dn^{3/2}} = \frac{\tau}{\sqrt{2Re}\kappa^{3/4}} < 0.1,$$

where Gn is the Germano number, $2Re\tau$. The relative magnitude of the Germano number with respect to the Dean number is measured by the parameter γ, which implicitly describes the importance of the torsion on the flow-field. This empirical relation performs well over a large range of helical geometries, however, the correlation breaks down for flows with $Dn > 5000$ and, more importantly for umbilical blood flow, $\gamma \geq 0.1$.

1.5 Biomechanical studies of the cord

While the umbilical cord has received attention from pathologists for many years, mathematical or biomechanical analyses of the underlying physical processes have only recently been pursued. A mathematical investigation of the coiling effect on blood flow in the umbilical cord is limited to Kaplan et al. (2010), which employed a computational study of arterial blood flow, neglecting effects due to the distensible arterial walls, non-uniform coiling, non-Newtonian nature of the blood as well as pulsatile characteristics. This analysis examined flow in uniform helical tubes and computed the pressure gradient between the umbilicus (fetal end) and the placental insert, which was assumed to be a constant, zero pressure outlet. The arterial diameter and length were assumed constant, as was the length and pitch of each coil. The helical pitch, diameter and number of coils were altered in order to provide cases with different UCI. It was shown that the pressure gradient along the length of the cord increased with an increasing number of coils and decreased with an increasing pitch of the helix. The increase in the pressure gradient due to the number of coils causes an attendant decrease to the flow-rate through the arteries. Hence, as the maximum driving pressure at the umbilicus is constrained by the maximal forces the fetal heart can develop, the amount of arterial blood flow to the placenta will decrease with an increase to the UCI (Kaplan et al., 2010). It was also shown that the wall shear stress (WSS) increases with reduced pitch of the helix (i.e. increased UCI), and exhibits large spatial gradients within the cross-section of the tube. This factor may have adverse effects as it is known that WSS play an important role in the pathogenesis of artherosclerosis (Cunningham and Gotlieb, 2005). Hypocoiled cords were also examined and it was found that the pressure gradient developed in this case was significantly lower, which would physically ensure that the fetal heart is loaded less severely and hence may develop abnormally.

A number of other analyses have been conducted in order to better understand some of the important umbilical flow processes. Gordon et al. (2007) conducted a computational study of blood flow through a Hyrtl Anastomosis; a common 'bridging' between the two umbilical arteries immediately prior to placental insertion. The Hyrtl Anastomosis was modelled in `FLUENT` as an H-type junction between two parallel rigid, straight tubes representative of the arteries. As such, the coiled nature of the cord as well as the wall distensibility were not investigated. Tejada-Martínez et al. (2011) produced an unsteady, two-dimensional computational analysis of umbilical artery blood flow in order to investigate the effect of a constriction on the flow. The artery walls were assumed rigid and straight and the asymmetric constriction was

used to represent some structural abnormality, such as a true knot. Arterial umbilical blood flow was also examined by Kleiner-assaf et al. (1999), where the arteries were modelled as straight, isotropic, thin-walled elastic pipes, with the blood flow assumed axisymmetric, pulsatile, incompressible and Newtonian. Fewer papers have examined venous umbilical blood flow from a biomechanical perspective. Waters and Guiot (2001) investigated fluid flow in a straight, axisymmetric tube with an elastic wall subject to a prescribed external pressure or motion, while Hellevik et al. (2000) considered umbilical venous pulsation.

1.6 Summary

The umbilical cord is a complex structure which facilitates oxygen and nutrient transport between the mother and developing fetus (de Laat et al., 2005). Despite the importance of the cord, the current diagnostic measure, the umbilical coiling index (UCI) has several measurement ambiguities (Khong, 2010) and has been found to unreliably correlate with other diagnostic indices (Degani et al., 1995). In essence the index represents the average number of coils (per cm) length, and is not based on any theoretical methodology related to the umbilical blood flow or the development of the fetus.

With the advent of advanced computing, numerical methods have been increasingly utilised to solve blood flow problems. While the biological structure of the umbilical cord has received significant attention in the literature, little work concerning the effect of the geometry on the blood flow exists. Furthermore there has been no critical fluid dynamic evaluation of the UCI as a diagnostic index. Of the studies to model umbilical blood flow, several use a flow Reynolds number calculated based on an arterial blood flow-rate which is higher than typically found in the vessels. The remaining studies concern cord abnormalities and focus on specific attributes such as flow velocity waveform notching and the effects of a Hyrtl Anastamosis.

There is therefore a lack of fluid dynamic research on the effect of the cord geometry on umbilical blood flow and the efficacy of the UCI as a diagnostic index. Additionally, there are few alternative indices capable of quantifying pathology in both vessels. There is therefore a need for the development of a more robust, theoretically derived methodology based on tangible characteristics of the blood flow.

1.7 Aims and objectives

Motivated by a lack of research on the efficacy of the UCI and more generally, on the effect of geometric cord variations, this thesis presents a fluid dynamic study of blood flow within the umbilical vessels. The key questions posed are; does the UCI predict pressure variations among cords of varying geometry? Do geometric irregularities play a significant role in blood flow processes? Finally, if the UCI cannot predict blood vessel pressure, is there another, clinically suitable method for estimating the flow resistance? To answer these questions, four key aims are specified;

i) To determine the efficacy of the UCI for predicting the mean cord vessel pressure drop and variations to the flow field;

ii) To quantify the effect of geometric irregularities including variable coiling, twist reversal and knots;

iii) To determine the effect of pulsatility within the umbilical arteries, and;

iv) To develop new indices for the prediction of mean umbilical vessel blood pressure and flow-rate based on simple, non-invasive geometric cord measurements.

This thesis is composed of a further five chapters in order to address (i)-(iv), above. The analysis centres around a numerical study of incompressible Newtonian fluid flow in rigid three-dimensional tubes approximating the flow of blood within the umbilical vessels. Chapter 2 presents the details of the method used; in particular the assumptions, dimensional scalings and vessel geometric models used to analyse umbilical blood flow. This chapter also presents the results of two validation studies; a first considering steady entry flow into a curved pipe, and a second considering pulsatile flow into a straight, stenosed vessel. This study allows the derivation of problem specific parameters and verifies that the numerical scheme is suitably accurate. Some basic details of the finite element method, chosen for the analysis and implemented using the open-source `c++` code `oomph-lib` available from the University of Manchester, are also included in appendix A.

The main structure of the thesis composes three results chapters which link together to demonstrate that a new diagnostic method is necessary. Furthermore, they show that this diagnostic method can be derived using steady results through idealised helical tubes. Chapter 3 addresses (i) and (ii), above, by considering the steady flow of blood through model geometries representative of the umbilical vessels. A number of models are defined in order to examine the effect of varying the geometry on the blood flow. It

is found that the UCI is unable to distinguish between cords of significantly varying pressure and flow characteristics, which are typically determined by the vessel curvature, torsion and length. Crucially, the UCI removes any reference to the latter in its calculation. Larger scale geometric non-uniformities superposed over the inherent coiling, including cords exhibiting width and/or UCI variations as well as loose true knots, typically produce a small effect on the total pressure drop. This illustrates that a helical geometry of mean coiling may be used to determine the steady vessel pressure drop through a more complex cord. The presence of vessel constriction, however, drastically increases the pressure drop and alters the flow profile.

While the flow is reasonably steady in the umbilical vein, unsteadiness is present within the arteries due to the forcing of the fetal heart. Chapter 4 addresses (ii) and (iii) by considering pulsatile flow through a selection of arterial geometries. The temporally averaged results are predicted to a high accuracy by the corresponding steady calculations validating the steady analysis as relevant to both vessel types. The peak systolic pressure ratio within the non-straight arteries is also found to remain virtually constant and approximately 25% below the equivalent straight pipe value for a large range of cords within pregnancy. This suggests another possible benefit to the helical cord geometry; the coiled structure dampens extreme pressures within the cycle.

Having shown that the UCI is unable to describe pressure variations due to the geometry, an alternative method for the description of the flow resistance inherent to a particular cord is necessary. Chapter 3 shows that unconstricted cords can be approximated by a helical tube with the mean curvature and torsion of the full geometry. Additionally, chapter 4 shows that pulsatile fluctuations within the arteries result in a fairly uniform pressure profile which oscillates about the steady pressure drop. Chapter 5 therefore addresses (iv) to develop a new methodology for the description of the flow resistance within a cord. The umbilical pressure index, PX, and flow index, QX, quantify the deviation of a cord geometry from the typical conditions by considering the steady pressure and flow-rate, respectively. These indices are calculated based on a combination of empirical and interpolated numerical data and require only one additional geometric measurement to the calculation of the UCI; namely the cord width. Together the indices provide a non-invasive measure of the flow-resistance inherent to a particular cord geometry, and allow comparison with typical values in pregnancy.

Finally, chapter 6 presents a concatenation of the results of the preceding work and a discussion of the further analysis required. In answer to the initial questions posed, the UCI does not predict pressure variations among cords of varying geometry. The pressure drop over the length of an umbilical vessel

depends on many factors including the torsion, curvature, flow Reynolds number and crucially, the length of the cord. The UCI is a ratio of the number of coils of the cord to its length and therefore represents the length of a single coil only. It also lacks a reference to the transverse cord measurement, the cord width, which is important in determining the total vessel arclength as well as the curvature and torsion. Geometric irregularities typically play an insignificant role in blood flow processes at the Reynolds numbers present within the umbilical cord. However, vessel constrictions, such as may occur as a result of a tight true knot, can significantly affect flow and pressure characteristics. Finally, the pressure and flow indices developed represent a clinically suitable method for estimating flow resistance, however, require further validation to determine their efficacy.

Chapter 2

Methods

The Navier-Stokes equations in three-dimensions are generally unsolvable by analytic means. However, with the advent of advanced computing systems numerical methods have been increasingly utilised to solve fluid dynamics problems. Numerical methods are particularly necessary for flows within complex geometries, or flows for which the Reynolds number is large and nonlinear effects have substantial bearing. While results obtained through the perturbation analyses listed in section 1.4 are useful in understanding some helical pipe flows, the limiting assumptions of low Re, small torsion and small curvature ensure that this method is not as flexible as a computational study. It is for this reason that the primary method of umbilical blood flow analysis within this document is a computational study. There are many computational methods available for the solution of fluid flow problems, and accordingly there are many open-source and commercial packages available which implement these methods. An open-source library of finite elements designed for the solution of multi-physics problems named `oomph-lib`, the object-oriented multi-physics library (Heil et al., 2008), is available from the University of Manchester and is specifically designed for biological flow problems. Throughout the following chapter the assumptions and methods used within the work of this thesis are listed in addition to a detailed problem formulation. Finally, two relevant code validation studies are presented in order to assess the performance of the numerical solvers. The first study, included in section 2.5, concerns steady flow through a curved pipe, while the second considers pulsatile flow in a straight pipe stenosis modelled as a simple constriction and is presented in section 2.6.

Details of the implementation of the finite element method within `oomph-lib` are contained within appendix A in addition to an overview of the iterative linear solvers used to perform numerical calculations on problems with a high degree of freedom.

2.1 Assumptions

A number of assumptions are necessary in order to yield a tractable problem fit for numerical solution. Based on the literature review of chapter 1 the following assumptions are used:

i) The umbilical blood vessels are rigid, non-deforming tubes with a circular cross-section.

ii) There are three umbilical blood vessels; a single vein and two arteries, contained within the nominal umbilical cord.

iii) The flow of blood is steady within the vein.

iv) The flow of blood is pulsatile within the arteries, and;

v) The flow in both vessels is governed by the incompressible, three-dimensional Navier-Stokes equations.

2.2 Dimensional scaling and flow regime

The dimensional length scale, $\mathcal{L}$, is based on the vessel radius, $\hat{R}$,

$$\mathcal{L} = \hat{R}.$$

The velocity reference scale, $\mathcal{U}$, is derived from the mean cross-sectional flow-rate, $\hat{Q}$, so that,

$$\mathcal{U} = \frac{\hat{Q}}{\pi \hat{R}^2}.$$

For unsteady problems the time scale is chosen as the period of the fetal heart-beat, $\hat{T}$,

$$\mathcal{T} = \hat{T}.$$

The non-dimensional pressure can be calculated on the viscous or inertial scales. For the work within this thesis the viscous scale is used so that,

$$\Delta P = \frac{\rho \hat{R}^2 \Delta \hat{P}}{\hat{\mu}^2 Re},$$

where Re is the flow Reynolds number written,

$$Re = \frac{\mathcal{U}\mathcal{L}}{\hat{\nu}} = \frac{\hat{Q}}{\pi \hat{R} \hat{\nu}}.$$

Here $\hat{\nu}$ is the blood kinematic viscosity. For unsteady flow, the reduced velocity is calculated by,

$$U_{red} = \frac{\mathcal{U}\mathcal{T}}{\mathcal{L}} = \frac{\hat{Q}\hat{T}}{\pi\hat{R}^3}.$$

Nominal values for each of the parameters are summarised in table 2.1 for both the artery and vein. The blood kinematic viscosity is computed taking $\hat{\rho} = 1060$ kg/m^3 with $\hat{\mu} = 4 \times 10^{-3}$ kg/ms.

Blood flow within the umbilical cord is examined over a range of physiologically applicable Re and U_{red}. The umbilical parameter study conducted in chapter 1 provides references ranges for each of the constituent parameters in table 1.2. Nominally, each vessel has a roughly equivalent Re, which is approximately 100. By considering variations in each of the constituent parameters, it is theoretically possible that Re varies such that,

$$10 < Re < 280.$$

Of course these extreme values are obtained by taking extreme values in each of $\hat{Q}, \hat{R}, \hat{\nu}$, and will likely not exist in a realistic physiological setting. Similarly, with a fetal heart-rate of 140 bpm (Kaplan et al., 2010) the typical period of an arterial pulsation is approximately $T \approx 0.43$ s. The reduced velocity within the umbilical arteries is therefore approximately 41, which corresponds to a Womersley parameter of $\alpha = 3.92$. Considering the variation of the fetal heart-rate stated in table 1.2, the reduced velocity will typically vary between 30 and 50. The larger variation of,

$$30 < U_{red} < 70,$$

is considered in the work of chapter 4.

2.3 UCI calculation

As described in chapter 1, there has been some confusion in the literature regarding the calculation of the umbilical coiling index. Specifically, this ambiguity concerns measurement of both the length of the cord, and the number of coils. In order to examine the efficacy of the index, two definitions are provided here. An example cord vessel is shown in figure 2.1 with the relevant measurements annotated.

> The **clinical** UCI ($\hat{U}_c$) which is computed using the pitch-length of the cord ($\hat{L}_p$) and the total number of coils (N) fractional turns included.

	A	V
Vessel radius, $\hat{R}$ (cm)	0.20	0.35
Flow-rate, $\hat{Q}$ (10^{-6} m^3/s)	2.42	4.42
Blood viscosity, $\hat{\nu}$ (10^{-6} m^2/s)	3.77	3.77
Flow period, $\hat{T}$ (s)	0.43	N/A
Reduced velocity, U_{red}	41	N/A
Reynolds number, Re	100	100

Table 2.1: Nominal parameters used throughout the flow analysis for the artery, A, and vein, V.

The **theoretical** UCI ($\hat{U}_t$) which is computed based on the total cord arclength ($\hat{L}_Z$) and the number of complete coils (N_c) disregarding fractional turns. The relationship between the two is described by the ceiling function, $N_c = \lfloor N \rfloor$.

In practice the clinical UCI is likely the most prevalent calculation as it is easier to measure in a clinical setting. For this reason, the bulk of the work within this thesis concerns this form of the index. The following section presents a brief description of the calculation of each index as well as their associated limitations. Generally, the UCI will be quoted in non-dimensional terms with $U_c = (100\hat{R})\hat{U}_c$, where $\hat{R}$ is the vessel radius and the factor of 100 is used to convert to cm. The geometries used to describe the UCI calculation are based on the work of Kaplan et al. (2010) and comprise a straight inlet/outlet in addition to the main coiled body, as per figure 2.1.

2.3.1 Clinical UCI, $\hat{U}_c$

Excluding the straight section, the pitch-length ($\hat{L}_p$) is determined by the helical pitch ($\hat{P}_h$) of the cord and the total number of coils, fractional turns included (N),

$$\hat{L}_p = \hat{P}_h N = \frac{2\pi\hat{\tau}N}{\hat{\tau}^2 + \hat{\kappa}^2}.$$

The clinical UCI is then simply the reciprocal of the pitch,

$$\hat{U}_c = \frac{1}{\hat{P}_h} = \frac{\hat{\tau}^2 + \hat{\kappa}^2}{2\pi\hat{\tau}}. \tag{2.1}$$

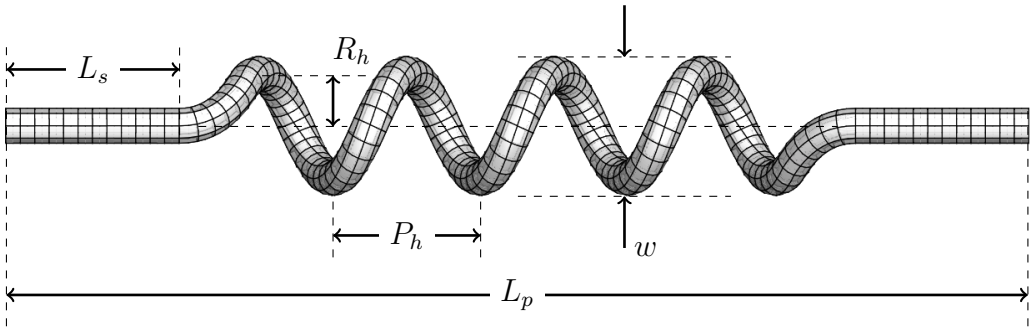

Figure 2.1: A regularly coiled vessel modelled on the work of Kaplan et al. (2010) showing the pitch length of the entire vessel (L_p), the helical radius (R_h), the helical pitch (P_h), straight section length (L_s), and the coil width (w). The arclength (L_Z) is measured along the tube centreline.

This description lacks any reference to the helical radius of the cord ($\hat{R}_h$) and hence all cords with the same pitch and varying width will have identical $\hat{U}_c$. This fact is examined in section 3.2.2 where a selection of vessels with varying R_h are considered. For the regularly coiled geometries, shown in figure 2.1 and to be further described in section 2.4.1, the work of Kaplan et al. (2010) is followed with two straight inlet/outlets appended via a physiologically curved tube. The clinical UCI is then found from,

$$\hat{U}_c = \frac{N}{\hat{L}_p},$$

where $\hat{L}_p$ here refers to the total cord pitch length, including straight and curved sections. The additional uncoiled length acts to reduce the calculated $\hat{U}_c$.

2.3.2 Theoretical UCI, $\hat{U}_t$

The total arclength of a helical curve ($\hat{L}_h$) is determined by $\hat{P}_h$, N and $\hat{R}_h$,

$$\hat{L}_h = 2\pi N\sqrt{\hat{R}_h^2 + (\hat{P}_h/(2\pi))^2} = \frac{2\pi N}{\sqrt{\hat{\tau}^2 + \hat{\kappa}^2}}.$$

The theoretical UCI for a helical section ($\hat{U}_t$) is therefore,

$$\hat{U}_t = \frac{1}{2\pi\sqrt{\hat{R}_h^2 + (\hat{P}_h/(2\pi))^2}} = \frac{\sqrt{\hat{\tau}^2 + \hat{\kappa}^2}}{2\pi}, \tag{2.2}$$

which unlike $\hat{U}_c$ contains a reference to $\hat{R}_h$. The regularly coiled geometries to be studied in sections 3.2.1 and 3.2.2, comprise additional, uncoiled sections and the total cord arclength is therefore,

$$\hat{L}_Z = 2\hat{L}_s + 2\hat{L}_c + \hat{L}_h,$$

where $2\hat{L}_s$ is the arclength of the (combined) straight sections and $2\hat{L}_c$ is the length of the (combined) curved joins. For the calculation of the theoretical UCI in section 3.2.1 the number of complete coils are used. That is,

$$\hat{U}_t = \frac{N_c}{\hat{L}_Z}, \tag{2.3}$$

This has the effect of further reducing the computed UCI. Intuitively, $\hat{U}_c \geq \hat{U}_t$, with equality holding in the case that $\kappa = 0$, i.e. the vessel is straight.

2.4 Vessel models

In the current work, the vessel geometry is prescribed using the centreline method, whereby the artery or vein is taken to be a tube of constant cross-sectional radius (except in the work relating to constricted true knots), with the centreline curve dependent upon arclength, Z, in a physiologically realistic manner. A general three-dimensional space-curve can be written as

$$\vec{L_c}(t) = x_c(t)\mathbf{i} + y_c(t)\mathbf{j} + z_c(t)\mathbf{k} \quad \text{for} \quad t \in [t_0, t_1], \tag{2.4}$$

where we seek x_c, y_c and z_c which depend continuously on the parameter $t = t(Z)$, not to be confused with time. Local coordinates within the tube then consist of the centreline arclength measured from the inlet in addition to the relative coordinates within the corresponding normal plane (X, Y), spanned by the centreline curve normal, $\boldsymbol{N}(Z)$ and binormal, $\boldsymbol{B}(Z)$. The global Cartesian coordinates of any point within the tube can then be determined using this information and the coordinates of the centreline curve,

$$(x, y, z)(Z) = \vec{L_c}(Z) + X\boldsymbol{N}(Z) + Y\boldsymbol{B}(Z) \quad \text{for} \quad Z \in [0, L_Z]. \tag{2.5}$$

For a given curve, $\boldsymbol{N}$ is determined using the Frenet-Serret formula,

$$\boldsymbol{N} = \kappa \frac{\mathrm{d}\boldsymbol{T}}{\mathrm{d}Z}, \tag{2.6}$$

where κ is the curvature of the centreline, and the tangent is related to $\vec{L_c}$ by,

$$\boldsymbol{T} = \frac{\mathrm{d}\vec{L_c}}{\mathrm{d}Z}. \tag{2.7}$$

The binormal, $\boldsymbol{B}$, may then be determined using the orthogonality condition,

$$\boldsymbol{B} = \boldsymbol{T} \times \boldsymbol{N}. \tag{2.8}$$

For complex geometries, namely the regularly coiled cords described in section 2.4.1, the vessel centreline may be approximated by the concatenation of N distinct segments joined in serial. The composite centreline is then simply the union of these segments, where continuity of the normal, binormal and tangents at each of the joins is required. The generic curve parameter t is used for all geometric descriptions herein though its relation to the vessel arclength as well as the appropriate boundary values will vary.

A limitation of coordinate systems based upon the centreline curve is that the geometry is constrained by the permissible curvature. For a tube with planar centreline,

$$\hat{\kappa} < \frac{1}{\hat{R}}, \tag{2.9}$$

where $\hat{R}$ is the (dimensional) vessel radius and $\hat{\kappa}$ is the (dimensional) curvature of the vessel centreline. This is equivalent, in non-dimensional terms, to $\kappa < 1$, where κ is found from the centreline tangent by,

$$\kappa(t) = \left\| \frac{\mathrm{d}\boldsymbol{T}}{\mathrm{d}Z} \right\| = \left\| \frac{\mathrm{d}\boldsymbol{T}}{\mathrm{d}t} \frac{\mathrm{d}t}{\mathrm{d}Z} \right\|. \tag{2.10}$$

This constraint restricts the permissible cords for which steady and unsteady numerical solutions can be determined. Throughout the following sections a number of cord geometries are presented which each examine an aspect of umbilical blood flow. Regularly coiled geometries based on the work of Kaplan et al. (2010) are presented in section 2.4.1. These models represent typical umbilical vessels and are used in an initial demonstration of the inability of the UCI (in either clinical or theoretical form) to predict the vessel pressure drop. The effect of varying the blood flow-rate, viscosity, vessel radius and coil width is also examined using these models. Cords with a nominally identical clinical UCI (of 0.2 coils/cm), but with linearly varying coil spacing (the reciprocal of the local UCI) and/or width are then described in section 2.4.2. Knotted cords are considered to fall within three classifications; loose true knots for which the geometric knotting of the cord is the dominant feature, tight true knots for which vessel constriction dominates, and false knots, which represent a localised deviation from the helical character with or without twist reversal. These geometries are discussed in section 2.4.3.

2.4.1 Regularly coiled vessels

The regularly coiled vessel geometries comprise a simple helical structure between the umbilicus and placental insertion based on the work of Kaplan et al. (2010). This model consists of three unique sections;

i) Straight tubes which join the cord to the fetus (at the umbilicus) and the placenta (at the placental insertion),

ii) A helically coiled tube which represents the bulk of the cord,

iii) Two 'physiologically smooth' transition sections between the straight inlet/outlet and the coiled region.

This model is used in Kaplan et al. (2010) to investigate arterial flow, however as the vein and arteries have roughly equivalent Reynolds number, a simple scaling of the computed (non-dimensional) results by the appropriate $\hat{R}$ and $\hat{Q}$ (see table 2.1) will represent the flow within a vein.

Centrelines for the straight ($\vec{L_c^1}$,$\vec{L_c^5}$) and helical ($\vec{L_c^3}$) sections have standard centreline parameterisations, however, the curved join between them ($\vec{L_c^2}$,$\vec{L_c^4}$) is somewhat more arbitrary. The total centreline description is then the union of these sections. An example regularly coiled geometry is shown in figure 2.1.

Straight section

The straight inlet/outlet in the $z-$direction is chosen to have centreline parameterisation,

$$\vec{L_c^1}(t) = R_h\mathbf{i} - R_h\mathbf{j} + t\mathbf{k} \quad \text{for} \quad t \in [0, L_s], \tag{2.11}$$

where here $t = Z$, the desired length of the section is L_s and the (x, y)-coordinate is chosen such that the tube lie on the radius of the helix, R_h. This final condition simplifies the nature of the curved join described in section 2.4.1. The outlet, $\vec{L_c^5}$, is described similarly.

Helical section

The helical centreline has a standard parameterisation based on a left-handed helix of radius R_h and pitch P_h,

$$\vec{L_c^3}(t) = R_h \cos\left(t + \frac{\pi}{2}\right)\mathbf{i} - R_h \sin\left(t + \frac{\pi}{2}\right)\mathbf{j} + \left(\frac{P_h}{2\pi}t + z_2\right)\mathbf{k}, \tag{2.12}$$

for $t \in [0, 2\pi N]$. The number of complete coils of the cord, N_c, is related to N by, $N = N_c + 3/4$. The additional $3/4$ is related to the choice of curved transition which occurs over a range of $\pi/2$ in t. The centreline arclength Z is related to t by,

$$Z = t\sqrt{R_h^2 + (P_h/(2\pi))^2} + Z_2 = \frac{t}{\sqrt{\tau^2 + \kappa^2}} + Z_2,$$

where Z_2 is the arclength at the outlet of the first curved section (the inlet to the helix).

Curved section

The curved section is required to join the straight inlet to the start of the helical section, and likewise, the end of the helical section to the straight outlet in a way that ensures the local coordinate description remains suitably smooth. As the helix centreline varies sinusoidally in both the x and y coordinate directions, a simple planar curved transition section may be defined by removing dependence on the required coordinate. Restricting the sinusoid to vary over an angle of $\pi/2$ ensures that the first derivative is zero at the connection to the straight inlet ($t = 0$) and equal to the centreline tangent at the helix connection ($t = 1$). The curved section therefore traverses a z (or pitch) distance of $P_h/4$ with the inlet given by,

$$\vec{L_c^2}(t) = R_h \cos\left(\frac{\pi}{2}t\right)\mathbf{i} - R_h\mathbf{j} + \left(\frac{P_h}{4}t + L_s\right)\mathbf{k} \quad \text{for} \quad t \in [0, 1] \tag{2.13}$$

while the outlet can be defined in a similar way,

$$\vec{L_c^4}(t) = R_h\mathbf{i} - R_h \sin\left(\frac{\pi}{2}t\right)\mathbf{j} + \left(\frac{P_h}{4}t + z_3\right)\mathbf{k} \quad \text{for} \quad t \in [0, 1]. \tag{2.14}$$

Here z_3 is the z-coordinate at the end of the helical section, which depends on the number of coils and the pitch,

$$z_3 = L_s + P_h/4 + P_h N.$$

For the curved inlet given above in equation (2.13), the curvature is,

$$\kappa(t) = \left|\left(\frac{2\pi}{P_h}\right)^2 R_h \cos\left(\frac{\pi}{2}t\right)\right| \left(1 + \left(\frac{2\pi}{P_h}\right)^2 R_h^2 \sin^2\left(\frac{\pi}{2}t\right)\right)^{-3/2}.$$

A plot of κ over the inlet length is shown in figure 2.2(a) for cord U_{t1}, to be described in section 2.4.1. In all cords the curvature is greatest at $t = 0$

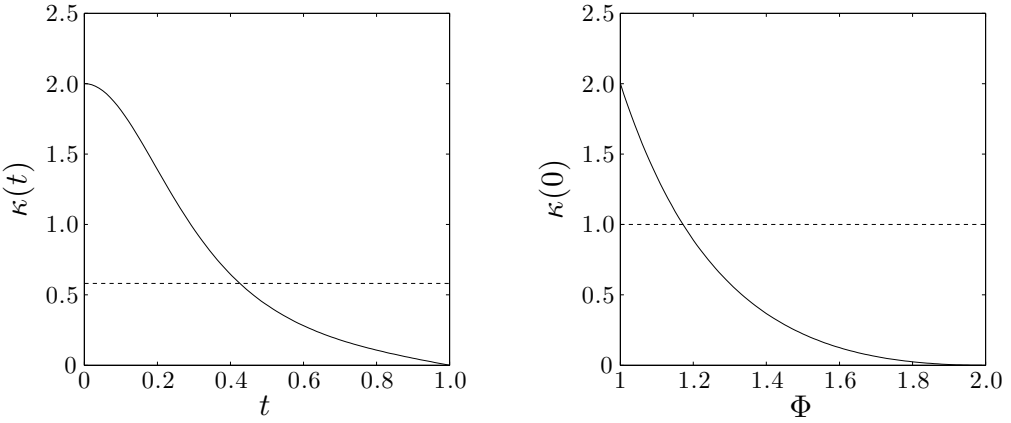

Figure 2.2: a) Curvature of the curved inlet centreline for cord U_{t1}. The helical section of this cord has $P_h = 4.905, R_h = 1.219$, with the dashed line showing the helix curvature; b) the curvature of the curved inlet centreline at the join to the straight section ($t = 0$) vs. the smoothing parameter (Φ) for the same cord. Here the dashed line indicates $\kappa = 1$.

where the join to the straight section occurs. The curvature then reduces to zero when it meets the helix. For this particular cord, the curvature at $t = 0$ is larger than unity and the tube will therefore intersect itself as per equation (2.9). In order to reduce the curvature at this location the 'pitch' of the curved section is re-defined.

Physiological inlet/outlet

The curvature at the join from the straight inlet to the curved section (and likewise the curved section to the outlet) may be reduced by allowing the 'pitch' of the curved section to vary with the parameter t. A simple approach is to allow this effective pitch to vary linearly with t, so that $z_c^2(t)$ is now quadratic,

$$z_c^2(t) = \frac{P_h}{4} t \left(\frac{(1-\Phi)t + \Phi}{2 - \Phi} \right), \tag{2.15}$$

where the smoothing parameter Φ ($1 \leq \Phi < 2$) is determined by the helical pitch, P_h, and the 'pitch' at the join ($t = 0$),

$$P(t = 0) = \Phi P_h.$$

Note that for the case $\Phi = 1$, equation (2.15) reduces to the form used in equation (2.13). Increasing Φ therefore elongates the inlet section in the z-coordinate. The effect on the curvature at the straight join ($t = 0$) is shown

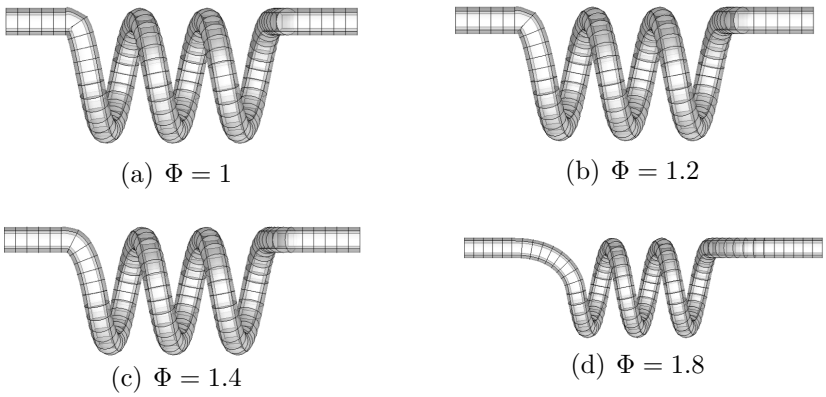

(a) $\Phi = 1$ (b) $\Phi = 1.2$

(c) $\Phi = 1.4$ (d) $\Phi = 1.8$

Figure 2.3: Smoothing the inlet with varying Φ for a regularly coiled vessel.

in figure 2.2(b), where the curvature is,

$$\kappa(0) = \frac{4\pi^2 R_h (2-\Phi)^2}{\Phi^2 P_h^2}. \tag{2.16}$$

For cord U_{t1}, $\Phi > 1.17$ produces a non-intersecting join ($\kappa < 1$), while increasing further produces 'smoother', and longer transitions. This effect is shown in figure 2.3. Using equation (2.15) the centreline for the inlet then becomes,

$$\vec{L_c^2}(t) = R_h \cos\left(\frac{\pi}{2}t\right)\mathbf{i} - R_h\mathbf{j} + \frac{P_h}{4}t\left(\frac{(1-\Phi)t+\Phi}{2-\Phi}\right)\mathbf{k}. \tag{2.17}$$

The Frenet-Serret formulae in equations (2.6)-(2.8) are used to determine $\boldsymbol{T}$, $\boldsymbol{N}$ and $\boldsymbol{B}$ and hence construct the mesh. The arclength is determined via

$$Z = \int_0^t \sqrt{\left(\frac{\pi}{2}R_h \sin\left(\frac{\pi}{2}t'\right)\right)^2 + \left(\frac{P_h\Big((1-\Phi)t' + \Phi/2\Big)}{2(2-\Phi)}\right)^2}\,\mathrm{d}t', \tag{2.18}$$

which requires numerical evaluation achieved using the trapezoidal rule. The outlet description is very similar and so is not included here. The regularly coiled cords necessarily have discontinuities in the centreline curvature; first at the straight/curved join where κ jumps from zero to some finite value and then at the curved/helix interface where κ again jumps from zero to some finite (constant) value for the helix, determined by P_h and R_h. This trend is reversed at the outlet.

Constant U_t study

To examine the efficacy of the theoretical UCI, U_t, a number of regularly coiled vessel geometries are considered which have varying N, τ and κ but which have identical U_t. Kaplan et al. (2010) state that the UCI normally falls within the range, $0.18 < \text{UCI} < 0.22$ coils/cm, and hence the nominal value throughout this study is taken as 0.2 coils/cm. The vessel geometries in this study are chosen to replicate arterial characteristics; a radius of $\hat{R} = 0.2$ cm gives a non-dimensional theoretical UCI of $U_t = 0.04$, and hence all vessels considered in this study satisfy $N_c/L_Z = 0.04$. While the vessels are nominally arterial, the corresponding (dimensional) venous geometries have a UCI of $\hat{U}_t = 0.11$ coils/cm, which is low but not hypocoiled according to Kaplan et al. (2010). The geometries examined may therefore also be used to analyse normal venous flow. The (non-dimensional) straight entrance/exit length is chosen as $L_s = 10$ and the curved smoothing parameter, Φ, is fixed at 1.4. The pitch, P_h, helical radius, R_h, and complete number of coils, N_c, are then allowed to vary so that the theoretical UCI is held constant. The vessel geometries detailed in table 2.2 and shown to scale in figure 2.4 are selected such that a range of τ and κ be represented in the study. This is shown diagrammatically in figures 2.5(a) and (b). It is clear from inspection that the vessels in figure 2.4 will exhibit differing flow and pressure patterns, if only because of the significantly increased length associated with, for example, cord U_{t6} compared to U_{t1}. Comparing with the clinical UCI calculation, the helical section of each vessel has $U_c > 0.06$ and so each model is clinically hypercoiled. The steady numerical simulations for these geometries are presented in section 3.2.1, while the pulsatile results are documented in section 4.2.1.

Constant U_c study

To examine the clinical UCI, U_c, a number of regularly coiled vessel geometries are created which have equivalent P_h, N and hence identical U_c. The curvature and torsion are therefore altered through variation of R_h alone, a process which highlights two issues with the UCI as a diagnostic index. Firstly, as $R_h \to 0$ the vessel becomes straight, but still retains its coiled structure. There is therefore the potentially paradoxical effect of jumping from a vessel which is hypercoiled, to one which is straight and by definition, hypocoiled, as R_h moves from some finite positive value to zero. This procedure can be better visualised by comparing geometries in figure 2.6, as well as the magnified vessel, U_{c1}, in figure 2.7. Here the vessel becomes highly twisted with low curvature and high torsion. The second paradoxical effect

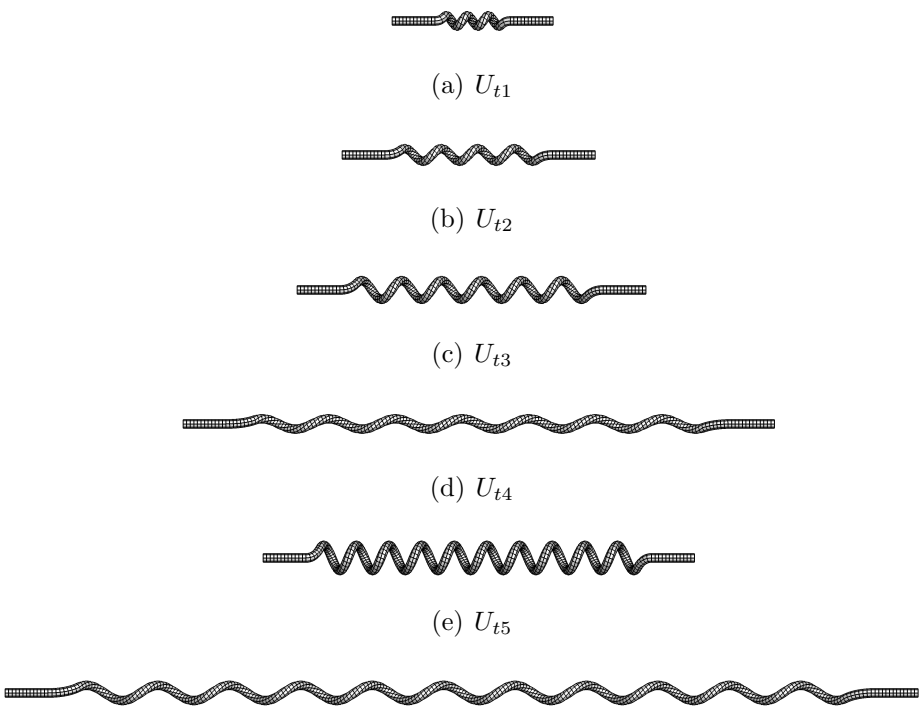

(a) U_{t1}

(b) U_{t2}

(c) U_{t3}

(d) U_{t4}

(e) U_{t5}

(f) U_{t6}

Figure 2.4: Regularly coiled vessels with constant U_t.

	N_c	R_h	P_h	τ	κ	L_Z	U_c ($\hat{U}_c$ coils/cm)
U_{t1}	2	1.219	4.905	0.3725	0.5818	50	0.20 (1.02)
U_{t2}	3	1.467	8.523	0.3397	0.3675	75	0.12 (0.59)
U_{t3}	5	2.193	9.327	0.2167	0.3127	125	0.11 (0.54)
U_{t4}	6	1.2	15.56	0.3271	0.1585	150	0.06 (0.32)
U_{t5}	9	2.957	7.618	0.1187	0.2895	225	0.13 (0.66)
U_{t6}	10	1.773	16.66	0.2606	0.1742	250	0.06 (0.30)

Table 2.2: Geometric parameters for the constant U_t geometries shown in figure 2.4. Here U_c is the clinical UCI based on the helical section alone, calculated using equation (2.1) on page 36 with an arterial radius of 0.2 cm.

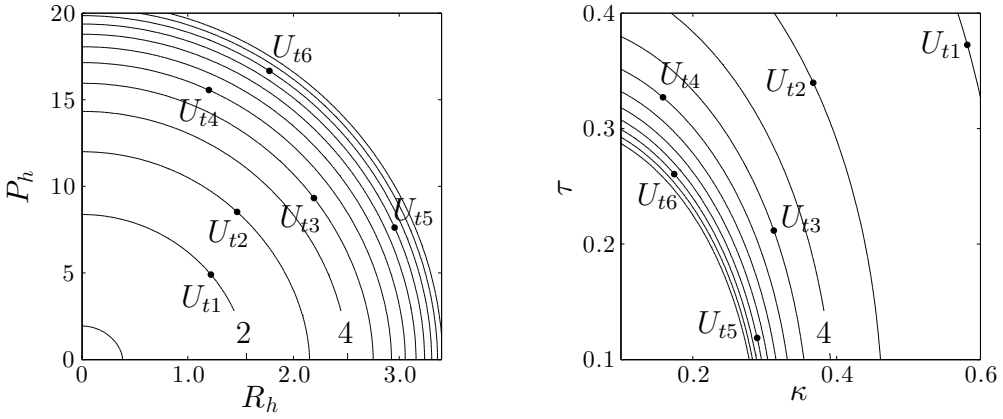

Figure 2.5: The collection of vessels studied with constant theoretical UCI, $U_t = 0.04$. The contour levels are at constant N_c, drawn at increments of one coil. a) The vessels shown against P_h and R_h, and; b) shown against τ and κ.

is related to the increasing arclength associated with increases to R_h. As the number of coils is held constant, a decrease in U_t is measured as R_h increases and hence vessels which 'appear' more coiled are in fact less coiled in terms of their theoretical UCI.

To examine these issues seven cords which each have $P_h = 9.5$, $N = 6$, $\Phi = 1.6$ and varying R_h are detailed in table 2.3 and shown in figure 2.6. These cords have an identical clinical UCI of $U_c = 0.0625$, or $\hat{U}_c = 0.31$ coils/cm based on the arterial radius, and are therefore clinically hypercoiled. However as shown in figure 2.8(a), the theoretical UCI and hence theoretical classification will vary with R_h. This particular collection of vessels is chosen to represent a spread of such classifications, ranging from (theoretically) hypercoiled in case U_{c1} to hypocoiled in U_{c7}. Increasing R_h in this way reduces the torsion and produces a maximum curvature when $R_h = P_h/2\pi \approx 1.512$, shown in figure 2.8(b). The steady numerical simulations for these geometries are presented in section 3.2.2, while the pulsatile results are documented in section 4.2.2.

2.4.2 Irregularly coiled cords

The effect of non-uniform coiling on the pressure and flow within the umbilical vessels is considered here. A selection of cords with variable R_h and P_h, set as functions of arclength, are designed in order to maintain identical clinical UCI, U_c, computed over the full cord length. For these models the

(a) U_{c1}: $R_h = 0.2$, $U_t = 0.062$ (theoretically hypercoiled)

(b) U_{c2}: $R_h = 0.5$, $U_t = 0.060$ (theoretically hypercoiled)

(c) U_{c3}: $R_h = 1.512$, $U_t = 0.049$ (theoretically normo-coiled)

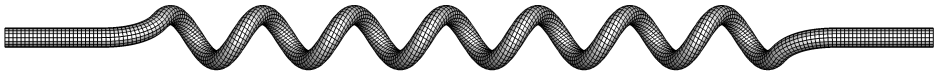

(d) U_{c4}: $R_h = 2.33$, $U_t = 0.040$ (theoretically normo-coiled)

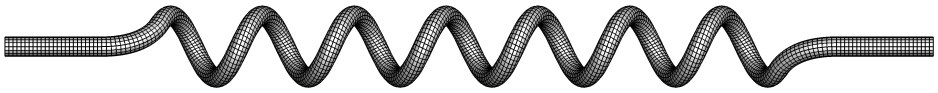

(e) U_{c5}: $R_h = 3.2$, $U_t = 0.033$ (theoretically normo-coiled)

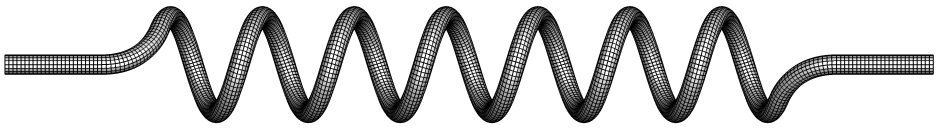

(f) U_{c6}: $R_h = 5$, $U_t = 0.023$ (theoretically normo-coiled)

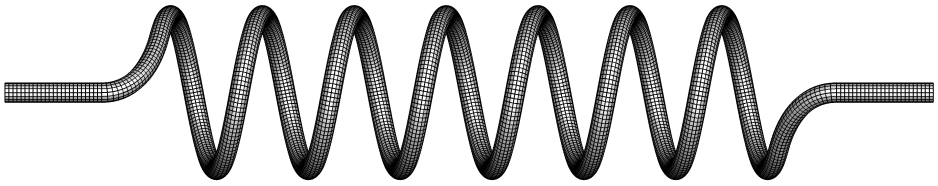

(g) U_{c7}: $R_h = 8$, $U_t = 0.016$ (theoretically hypocoiled)

Figure 2.6: Regularly coiled vessels with constant U_c ($= 0.0625$), with $P_h = 9.5$, $N = 6$, $\Phi = 1.6$. Each of these vessels are clinically hypercoiled.

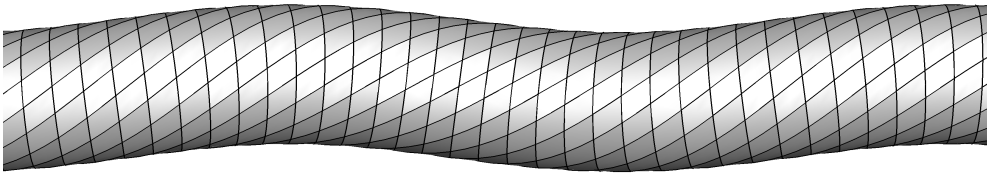

Figure 2.7: A magnified view of cord U_{c1} which has large torsion, low curvature.

	R_h	τ	κ	L_Z	U_t ($\hat{U}_t$ coils/cm)
U_{c1}	0.2	0.6500	0.0860	96.57	0.062 (0.31)
U_{c2}	0.5	0.5962	0.1972	99.49	0.060 (0.30)
U_{c3}	1.512	0.3307	0.3307	123.2	0.049 (0.24)
U_{c4}	2.33	0.1960	0.3020	151.1	0.040 (0.20)
U_{c5}	3.2	0.1207	0.2555	184.4	0.033 (0.16)
U_{c6}	5	0.0554	0.1832	258.3	0.023 (0.12)
U_{c7}	8	0.0228	0.1207	386.9	0.016 (0.08)

Table 2.3: Geometric parameters for the constant U_c geometries, shown in figure 2.6. $\hat{U}_t$ is calculated using an arterial radius of 0.2 cm.

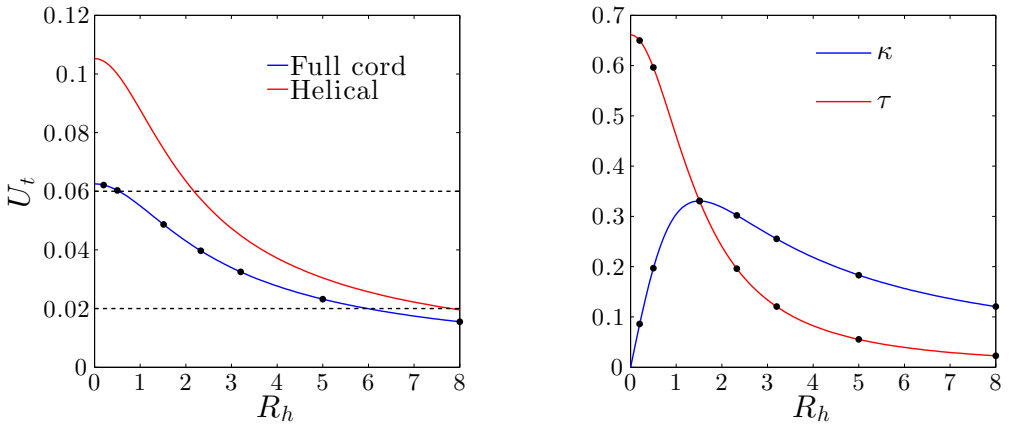

Figure 2.8: Variation of the theoretical UCI, curvature and torsion for the U_c geometries. a) Variation of the theoretical UCI with R_h. The blue line shows U_t calculated for the whole vessel using equation (2.3) on page 38, while the red line is calculated over the helical section alone, using equation (2.2). The dashed black lines denote the hypercoiled (upper) and hypocoiled (lower) boundaries; b) variation of the curvature and torsion with R_h. In both plots the solid black circles indicate the vessels studied.

straight or planar curved sections used in the regularly coiled studies are omitted and the geometry instead comprises only the coiled section,

$$\vec{L_c}(t) = R_h(t)\cos\left(t+\frac{\pi}{2}\right)\mathbf{i} + R_h(t)\sin\left(t+\frac{\pi}{2}\right)\mathbf{j} + \frac{tP_h(t)}{2\pi}\mathbf{k}, \tag{2.19}$$

where R_h and P_h now vary linearly with the parameter $t \in [0, 2\pi N]$ and the handedness has been reversed. This description allows specification of the relative variation, χ, in the coil spacing, S, which is akin to the pitch distance between coils, and the coil width, w, along the cord length,

$$\chi_S = \frac{S_u - S_p}{S_m}, \tag{2.20}$$

$$\chi_w = \frac{w_u - w_p}{w_m}, \tag{2.21}$$

where subscripts m, u and p refer to the mean, umbilicus and placental insertion values, respectively. The (dimensional) coil width depends on the helical radius via the relation,

$$\hat{w} = 2(\hat{R}_h + \hat{R}), \tag{2.22}$$

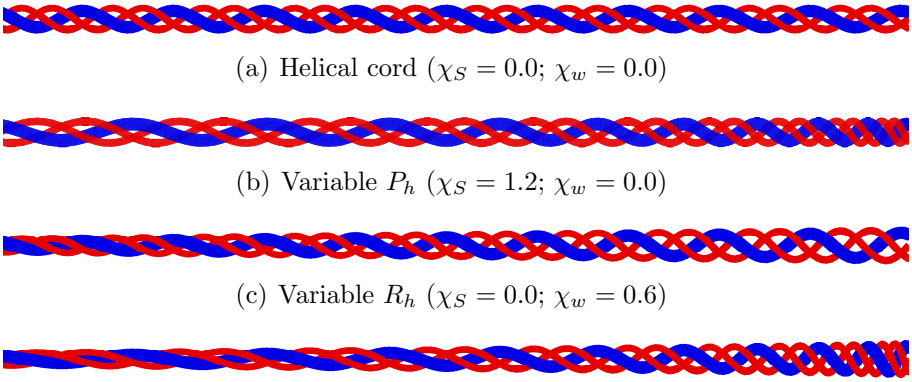

(a) Helical cord ($\chi_S = 0.0$; $\chi_w = 0.0$)

(b) Variable P_h ($\chi_S = 1.2$; $\chi_w = 0.0$)

(c) Variable R_h ($\chi_S = 0.0$; $\chi_w = 0.6$)

(d) Variable P_h, R_h ($\chi_S = 1.2$; $\chi_w = 0.6$)

Figure 2.9: Schematic diagram of the irregular cord types considered with $\hat{S}_m = 5.0$ cm, $\hat{w}_m = 1.6$ cm. The red tubes indicate the arteries while the blue tube is the vein. The nominal cord is shown in (a).

and represents the 'width' of a coil; the extent that the tube occupies in the transverse direction to the helical axis, shown in figure 2.1. $\hat{P}_h$ has a more complex relation to the coil spacing, $\hat{S}$, which is described in the discussion on variable coil spacing, below.

In the studies detailed throughout the following sections realistic cords of equal length ($\hat{L}_p = 50$ cm) and number of coils ($N = 10$) are considered, ensuring that the mean coil spacing for each model is set at $\hat{S}_m = 5$ cm with a mean coil width of $\hat{w}_m = 1.6$ cm. The relative variations in each of S and w as defined in equations (2.20) and (2.21) are then altered either separately or in tandem in order to examine the resulting changes to the flow and pressure profile. The majority of the vessels considered here are vein models however four corresponding arterial geometries are also examined for which steady and pulsatile solutions are sought. These models differ slightly from their venous counterparts in that R_h depends on the length scale $\hat{R}$ according to equation (2.22) and so the arterial R_h is larger, though the non-dimensional κ is lower than the vein in the same cord. To be consistent flow is also in the reverse sense in these models (i.e. from umbilicus to placenta), a factor which is investigated further in section 3.2.3. Schematic diagrams of the full cord geometries in figure 2.9 show the four main combinations of χ_w and χ_S. The variable P_h venous geometries considered are shown in figure 2.10, the variable R_h venous geometries are shown in figure 2.11 while veins with varying R_h and P_h are shown in figure 2.12. The variation of the curvature and torsion with pitch length is included for each of these geometries in figure 2.13.

Variable coil spacing

The pitch, P_h, is chosen to vary linearly with the rotational parameter, t, by

$$P_h(t) = \left(\frac{P_{h,u} - P_{h,p}}{2\pi N}\right) t + P_{h,p} = P_{h,u}\left(\frac{t}{2\pi N}\left(1 - \Phi_n\right) + \Phi_n\right) \tag{2.23}$$

where Φ_n ($= P_{h,p}/P_{h,u}$) is a ratio of the prescribed variation in P_h along the cord and N is the total number of coils. The actual distance, S, between successive coils at a given t is not equal to P_h as the z-coordinate of the cord centreline now depends quadratically on t and hence n ($= t/2\pi$). The z-coordinate of the centreline is,

$$z_c = \frac{tP_h(t)}{2\pi} = nP_{h,u}\left(\frac{n}{N}\left(1 - \Phi_n\right) + \Phi_n\right).$$

The true pitch distance between successive coils at the n-th coil is then

$$S(n) = z(n+1) - z(n) = P_{h,u}\left(\frac{2n+1}{N}(1 - \Phi_n) + \Phi_n\right), \tag{2.24}$$

where $n < N \in \mathbb{Z}$. The coil separation at the placental end (for the vein) is then $S(0)$ while the coil separation at the umbilicus is $S(N-1)$. Intuitively a vessel for which the pitch is constant ($\Phi_n = 1$) will have constant coil spacing $S = P_{h,u} = P_h$ over the entire cord. The total pitch length of such an irregular cord then depends only on the total number of coils and the pitch at the umbilicus,

$$L_p = \int_0^{2\pi N} \frac{\mathrm{d}z_c}{\mathrm{d}t}\mathrm{d}t = \frac{1}{2\pi}\int_0^{2\pi N} tP_h(t)\mathrm{d}t = NP_{h,u}. \tag{2.25}$$

As $S_m = L_p/N$ it follows from equation (2.25) that $S_m = P_{h,u}$, i.e. that the prescribed pitch at the umbilicus is equal to the mean coil spacing. Using equation (2.24) the relative variation in the coil spacing, χ_S is,

$$\chi_S = \frac{S(N-1) - S(0)}{S_m} = \frac{2(N-1)}{N}\left(1 - \Phi_n\right),$$

with corresponding Φ_n,

$$\Phi_n = 1 - \frac{\chi_S N}{2(N-1)}. \tag{2.26}$$

Figure 2.10 shows five variable P_h venous geometries constructed using equation (2.23) for which steady solutions are presented in section 3.2.3. Larger coil separation is prescribed at the placental insertion as the measured UCI is typically lower at this location (Baergen, 2005).

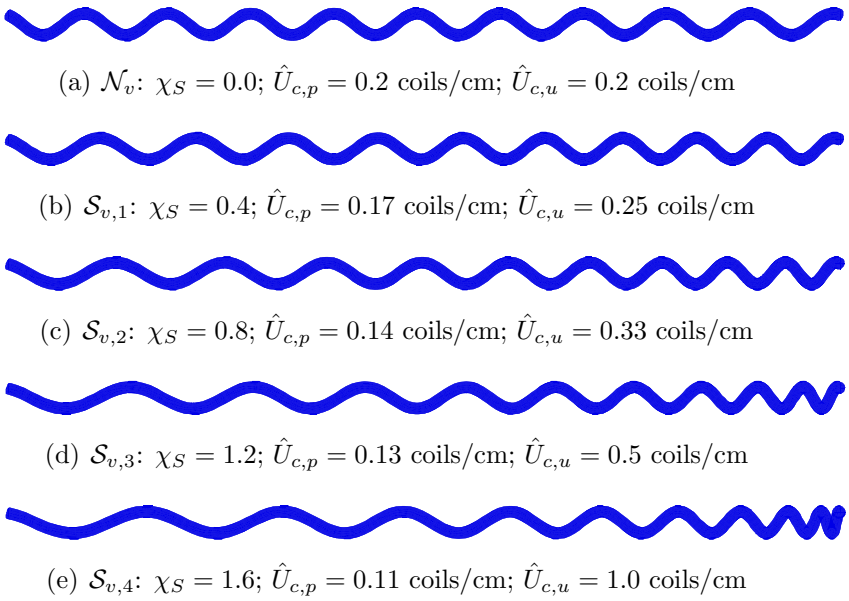

(a) $\mathcal{N}_v$: $\chi_S = 0.0$; $\hat{U}_{c,p} = 0.2$ coils/cm; $\hat{U}_{c,u} = 0.2$ coils/cm

(b) $\mathcal{S}_{v,1}$: $\chi_S = 0.4$; $\hat{U}_{c,p} = 0.17$ coils/cm; $\hat{U}_{c,u} = 0.25$ coils/cm

(c) $\mathcal{S}_{v,2}$: $\chi_S = 0.8$; $\hat{U}_{c,p} = 0.14$ coils/cm; $\hat{U}_{c,u} = 0.33$ coils/cm

(d) $\mathcal{S}_{v,3}$: $\chi_S = 1.2$; $\hat{U}_{c,p} = 0.13$ coils/cm; $\hat{U}_{c,u} = 0.5$ coils/cm

(e) $\mathcal{S}_{v,4}$: $\chi_S = 1.6$; $\hat{U}_{c,p} = 0.11$ coils/cm; $\hat{U}_{c,u} = 1.0$ coils/cm

Figure 2.10: Venous models with linearly varying P_h and identical mean coil spacing, S_m (or average UCI). Flow is from the left (placenta) to right (umbilicus).

Variable coil width

The same procedure as for P_h can be applied to the helical radius, R_h,

$$R_h(t) = \left(\frac{R_{h,u} - R_{h,p}}{2\pi N}\right) t + R_{h,p},$$

where $R_{h,u}$ is the non-dimensional helical radius at the umbilicus, and $R_{h,p}$ is the equivalent value measured at the placenta. These are related to the mean cord width, w_m, and the relative variation in the width, χ_w, by

$$R_{h,p} = \left(1 - \frac{\chi_w}{2}\right)\left(\frac{w_m}{2}\right) - 1,$$

$$R_{h,u} = \left(1 + \frac{\chi_w}{2}\right)\left(\frac{w_m}{2}\right) - 1,$$

where χ_w is as defined in equation (2.21). Five venous geometries with varying χ_w are shown in figure 2.11. As the clinical UCI is independent of the cord width these cords each have identical UCI.

2.4.3 Umbilical knots

The presence of knots in the umbilical cord has been discussed previously in chapter 1. In pathological terms, knots are classified as being either *true*

(a) $\mathcal{N}_v$: $\chi_w = 0.0$; $\hat{w}_p = 1.6$ cm; $\hat{w}_u = 1.6$ cm

(b) $\mathcal{W}_{v,1}$: $\chi_w = 0.2$; $\hat{w}_p = 1.44$ cm; $\hat{w}_u = 1.76$ cm

(c) $\mathcal{W}_{v,2}$: $\chi_w = 0.4$; $\hat{w}_p = 1.28$ cm; $\hat{w}_u = 1.92$ cm

(d) $\mathcal{W}_{v,3}$: $\chi_w = 0.6$; $\hat{w}_p = 1.12$ cm; $\hat{w}_u = 2.08$ cm

(e) $\mathcal{W}_{v,4}$: $\chi_w = 1.0$; $\hat{w}_p = 0.80$ cm; $\hat{w}_u = 2.40$ cm

Figure 2.11: Venous models with linearly varying R_h and identical mean coil spacing, S_m (or average UCI). Flow is from the left (placenta) to right (umbilicus).

(a) $\mathcal{C}_{v,1}$: $\chi_w = 0.6$, $\chi_S = 1.2$

(b) $\mathcal{C}_{v,2}$: $\chi_w = -0.6$, $\chi_S = 1.2$

Figure 2.12: Venous models with linearly varying R_h and P_h, and identical mean coil spacing, S_m (or average UCI). Flow is from the left (placenta) to right (umbilicus).

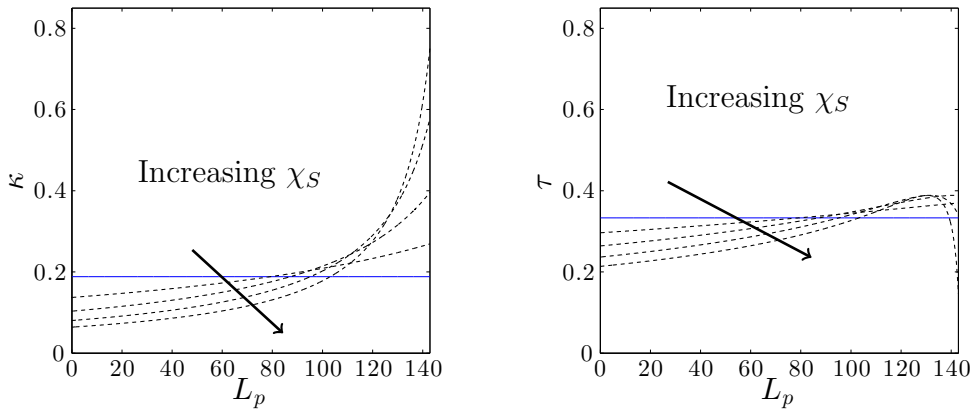

(a) Variable P_h veins

(b) Variable P_h veins

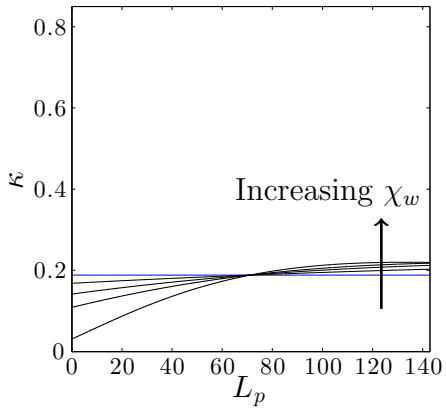

(c) Variable R_h veins

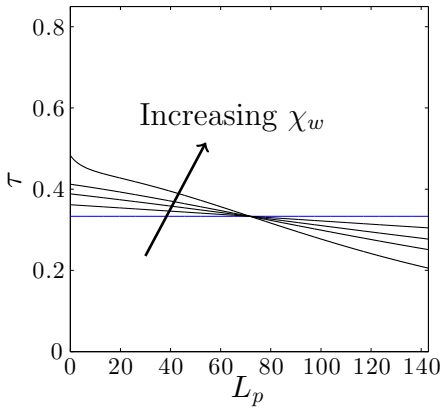

(d) Variable R_h veins

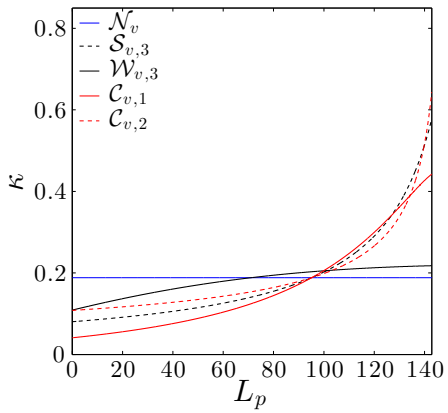

(e) Variable P_h, R_h veins

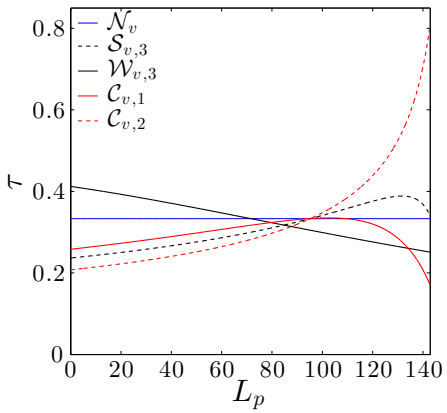

(f) Variable P_h, R_h veins

Figure 2.13: Variation of the curvature and torsion for each of the veins studied. Top: Variable P_h curvature (a) and torsion (b); Middle: Variable R_h curvature (c) and torsion (d); Bottom: Variable P_h, R_h curvature (e) and torsion (f). The blue line in each figure is the nominal vein ($\mathcal{N}_v$) with $\chi_S = 0$, $\chi_w = 0$.

or *false*. A true knot occurs when the complete geometry of the umbilical cord becomes knotted through itself, typically caused by fetal movement in-utero (Baergen, 2005). True knots are associated with adverse outcomes in pregnancy as well as measurable disturbances to the flow velocity waveform, such as the presence of 'notching'. Conversely, false knots are defined as an exaggerated looping of one or more of the umbilical vessels, causing a knot-like dilatation of the cord. They are generally treated as a benign feature thought to have little effect on the umbilical flow characteristics (Benirschke et al., 2006). For the purpose of this study, three broad knot classifications are defined here,

i) **Loose true knots** (LK); where constriction is insignificant but the vessels exhibit a simple geometric knotting,

ii) **Tight true knots** (TK); where constriction of the vessel is assumed significant compared to the geometric knotting.

iii) **False knots** (FK); where the cord structure briefly deviates from a helical description without constriction or geometric knotting.

To examine the effect of each of these structures three geometric descriptions are developed and outlined throughout the following sections. In each case a fully-developed helical flow is established before the inclusion of the knot feature.

Loose true knots

Loosely-knotted cords (LK) for which constriction is insignificant typically have less severe outcomes than tight true knots (Baergen, 2005). Geometrically, the whole-cord structure is assumed to take the form of an overhand-knot; a simple knot topologically equivalent to a trefoil curve when the cord ends are joined. The whole-cord centreline through a loose knot can therefore be approximated using a truncated section of a trefoil, appended to appropriate end-curves. The vessel geometry will then vary in a more complex sense about this knot centreline. Using expressions for the $\boldsymbol{N}$ and $\boldsymbol{B}$ vectors associated with this curve a helical centreline of prescribed P_h and R_h may then be 'wound' around the knot centreline to approximate the vessels.

In this section a description of the underlying knot geometry; a simple three-dimensional curve composed of five sections continuously joined in an analogous manner to the regularly coiled geometries of section 2.4.1, is presented. The procedure used to construct the vessels around this knot centreline is then discussed, as are the three loose knots analysed later under steady conditions in section 3.2.4 and then with pulsatile inflow in section 4.4.1.

Knot centreline

The underlying definition of the knot is based around a truncated trefoil curve ($\vec{L}^3_k$) with planar cubic transitions ($\vec{L}^2_k$, $\vec{L}^4_k$) and a straight inlet and outlet ($\vec{L}^1_k$, $\vec{L}^4_k$) appended to form a simple overhand knot in a similar way to the regularly coiled geometries. The trefoil curve has centreline description,

$$\vec{L}^3_k(t) = A\Big(\sin(t)+2\sin(2t)\Big)\mathbf{i} + A\Big(\cos(t)-2\cos(2t)\Big)\mathbf{j} + A\sin(3t)\mathbf{k}, \quad (2.27)$$

where A is a constant used to control the size of the knot and the parameter t is restricted such that $t \in [0, 4\pi/3]$ in order to avoid the knot closing (as in the case of a full trefoil). This trefoil curve is shown in figure 2.14(a), with the final overhand knot centreline shown in figure 2.14(b). For simplicity, the inlet and outlet of the overhand knot lie in the respective planes spanned by $\boldsymbol{T}^3_k$ and $\boldsymbol{B}^3_k$ (the knot tangent and binormal to the trefoil section, respectively) which are calculated at the truncated trefoil end-points, $t = 0$ and $t = 4\pi/3$. Within these two planes cubic polynomials are described which have the desired tangent at each end point (in order to satisfy first derivative continuity) as well as an appropriate width and length (C_l, C_w), which can be altered to smooth the transition. For the outlet plane the cubic is,

$$\vec{L}^4_k(t') = t'\boldsymbol{T}^3_{k,e} + \left(\beta_2 t'^2 + \beta_3 t'^3\right)\boldsymbol{B}^3_{k,e} + \vec{L}^3_{k,e}, \quad (2.28)$$

where $t' \in [0, C_l]$, the e subscript denotes the value computed at the end of the trefoil, $t = 4\pi/3$, and β_2 and β_3 are constants which depend on C_l, C_w and the end point tangents. To satisfy continuity, the outlet cubic tangent at $t' = 0$ must align with the trefoil tangent at $t = 4\pi/3$,

$$\boldsymbol{T}^4_k(t'=0) = \boldsymbol{T}^3_{k,e}.$$

Additionally, the cubic tangent at $t' = C_l$ must lie within both the inlet and outlet planes in order for the overhand knot to resume its original path. It therefore follows that the tangent must be orthogonal to both knot-end normals,

$$\boldsymbol{T}^4_k(t'=C_l) = \frac{\boldsymbol{r}}{|\boldsymbol{r}|}, \quad \boldsymbol{r} = \boldsymbol{N}^3_{k,s} \times \boldsymbol{N}^3_{k,e}$$

where the s subscript here denotes the value computed at the *start* of the trefoil, $t = 0$. The cubic coefficients are then given by,

$$\beta_2 = \frac{3C_w - C_l D_0}{C_l^2},$$
$$\beta_3 = \frac{-2C_w + C_l D_0}{C_l^3},$$

where,

$$D_0 = -\sqrt{\frac{1}{\boldsymbol{T}_k^4(t' = C_l) \cdot \boldsymbol{T}_{k,e}^3} - 1}.$$

A planar view of this curve is shown in figure 2.15. To complete the outlet of the overhand knot a straight section of variable length is appended parallel to $\boldsymbol{r}$ at $\vec{L}_k^4(t' = C_l)$. This length can be altered in order to achieve fully developed helical flow (as a vessel wrapped around a straight section is simply a helix) at the start of the cubic section and remove exit effects at the outlet. An analogous procedure is used for the definition of the inlet and so it is not specified here. The full overhand centreline is shown in figures 2.14(b) and 2.16.

Vessel centreline

The vessel centreline for the vein and each of the arteries is then 'wound' around the knot centreline $\vec{L}_k$ using $\boldsymbol{N}_k$ and $\boldsymbol{B}_k$. An example of the vessel description within the trefoil section is,

$$\vec{L}_c^3 = \vec{L}_k^3 + R_h \sin\left(\frac{2\pi s_k}{P_h}\right) \boldsymbol{N}_k^3 + R_h \cos\left(\frac{2\pi s_k}{P_h}\right) \boldsymbol{B}_k^3, \tag{2.29}$$

where s_k is the arclength along the knot curve (in this case measured from the trefoil start) and R_h, P_h are as defined previously. Through the rest of the cord expressions for $\boldsymbol{N}_k$ and $\boldsymbol{B}_k$ may be negated (or switched) in order to ensure mesh continuity. The geometry of the vessel centreline is implemented using splines, which facilitate computation of the vessel geometric parameters, such as the normal, tangent, binormal and arclength. An example `oomph-lib` script is included in appendix C.1. The full vessel centreline is shown with the underlying knot curve in figures 2.14(c) and 2.16. A comparison of the LK model with a physical umbilical knot is shown in figure 2.17. Here the vessel centrelines are separated by a rotation of $2\pi/3$.

LK Study

The LK study examines the effect of varying coil spacing through a prescribed loose knot geometry with nominal width, $\hat{w} = 1.6$ cm. The parameters common to each knot are given in table 2.4 where the scale, A, is chosen to create the tightest non-intersecting knot for the given width. The parameters C_l and C_w differ slightly to avoid large gradients in the local vessel coordinate description which occurs for cubics defined as in equation (2.28). Three coil spacings are chosen which categorise the cords as hypo-, normo-

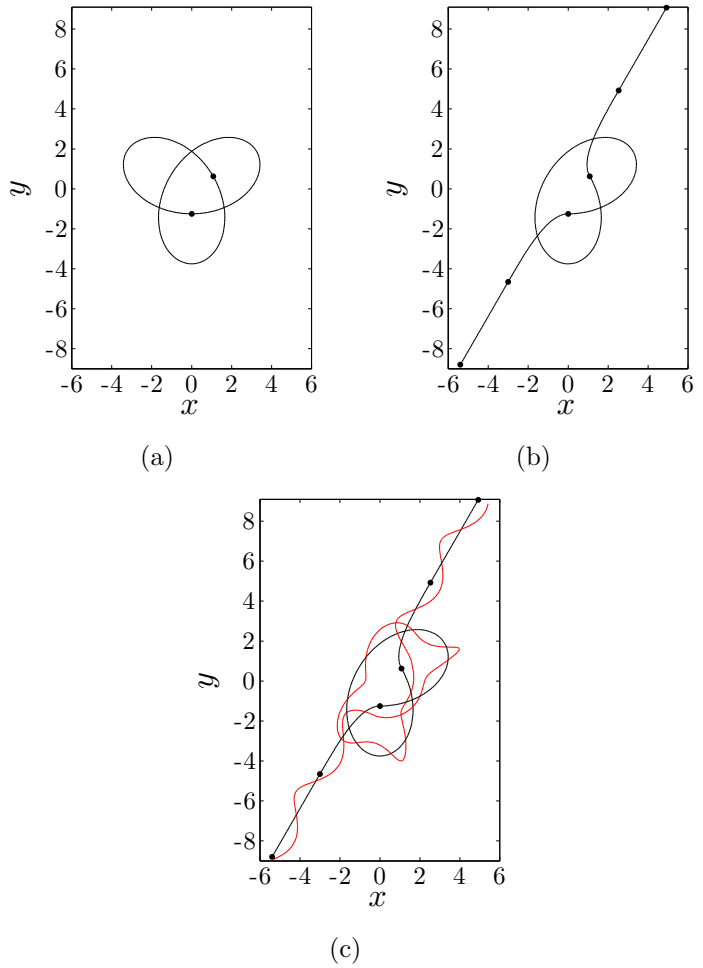

Figure 2.14: Construction of the loose knot (LK) centreline geometry in the (x, y)-plane; a) simple trefoil curve with end-points indicated by the black dots; b) the overhand knot with joins denoted, and; c) the overhand knot with vessel centreline (red).

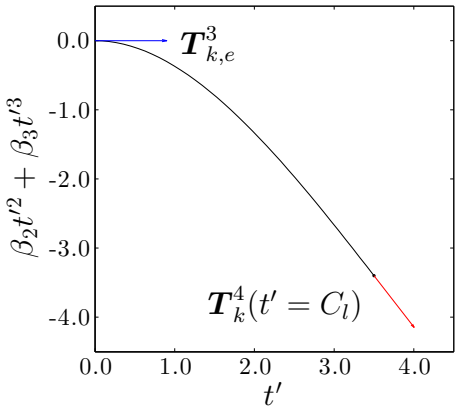

Figure 2.15: The outlet cubic shown in-plane for the loose knot centreline. The t'-axis here aligns with the tangent to the knot end ($t = 4\pi/3$) allowing the width (C_l), length (C_w) and cubic outlet tangent ($\boldsymbol{r}/|\boldsymbol{r}|$) to be set. Here $C_l = 3.5$, $C_w = -3.4$.

and hypercoiled and are labelled UC, NC and OC, respectively. Geometric properties of these cords are given in table 2.5 with comparative diagrams of the cords shown in figure 2.18. For simplicity all vessels were chosen to have the same (angular) position within the cord, unlike the schematic diagrams of figure 2.18. The slightly non-standard choice of P_h is reflective of the complex geometry; as in the regularly coiled vessels the underlying knot and vessel centrelines exhibit discontinuities in the curvature and torsion which are highlighted in figure 2.19. The angular position of the vessel within the cord at each of the knot centreline joins can therefore significantly affect the flow and pressure within the vessel. As a result values of $\hat{P}_h$ were chosen to avoid exceedingly high curvature at the joins. This is justified on the basis that these features are unlikely to exist in a physiological setting and detract from the key purpose of the study; to examine the effect a similar knot has on cords of different UCI. The `gsl` spline package is used to determine $\boldsymbol{T}, \boldsymbol{N}$ and $\boldsymbol{B}$ for each of the vessels with additional smoothing for the NC and OC geometries achieved via the `matlab` package `csaps` in order to reduce the observed ringing around the curvature discontinuities. The straight section lengths differ for each geometry and are selected in order to ensure fully-developed helical flow at the inlet to the cubic. Steady results for these cords are presented in section 3.2.4 while the corresponding pulsatile results for the arterial geometries are in section 4.4.1.

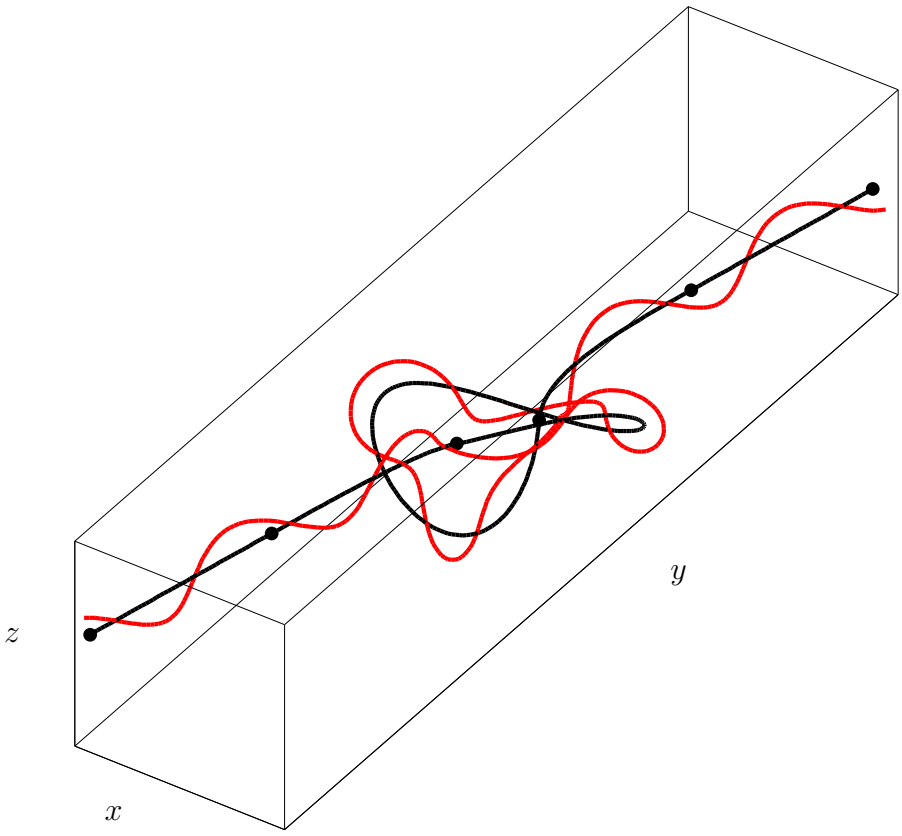

Figure 2.16: The loose, overhand knot (solid black) with vessel centreline (red) wound around it.

$\hat{w}$	1.6	Cord width
A	1.25	Scale factor
C_l	3.5	Cubic inlet/outlet width
C_w	-3.4	Cubic inlet/outlet length
$\hat{L}_{knot}/\hat{w}$	21.3	Length to width ratio

Table 2.4: Characteristics of the nominal loose knot. Note that $\hat{L}_{knot}$ is based on the knot centreline distance between the inlet to the first cubic section and the outlet to the second.

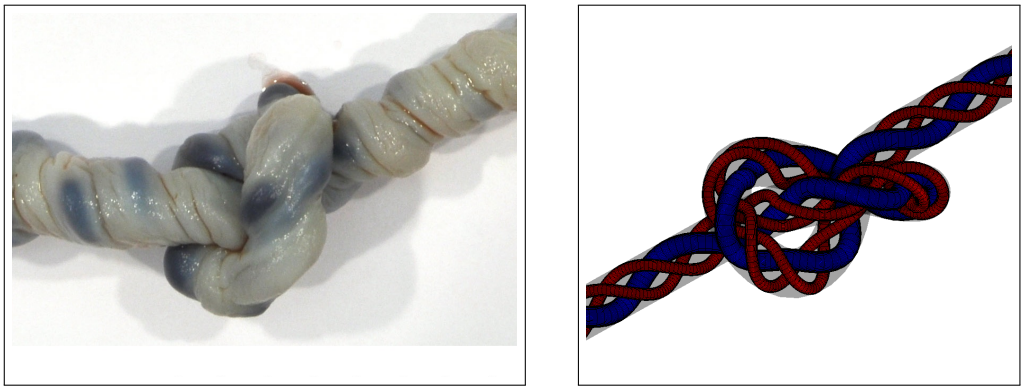

(a) (b)

Figure 2.17: Knots in the umbilical cord. a) A true knot (courtesy SA Pathology); b) A loose true knot model with normo-coiling and $\hat{w} = 1.6$ cm. The blue tube indicates the vein while the red tubes are the arteries. The grey region is the Wharton's Jelly.

	$\hat{P}_h$ (cm)	$\hat{U}_c$ (cm)	$R_{h,V}$	$R_{h,A}$	$L_{Z,V}$	$L_{Z,A}$	N
UC	10.8	0.09	1.29	3.00	102.2	184.0	3.16
NC	4.8044	0.21	1.29	3.00	112.8	216.0	7.09
OC	2.6691	0.37	1.29	3.00	140.2	290.5	12.77

Table 2.5: Knot geometries used in this study. $R_{h,i}$ is the non-dimensional helical radii for each of the distinct vessels, $L_{Z,i}$ is the corresponding vessel arclength and N is the total number of coils throughout the knot (excluding the straight sections).

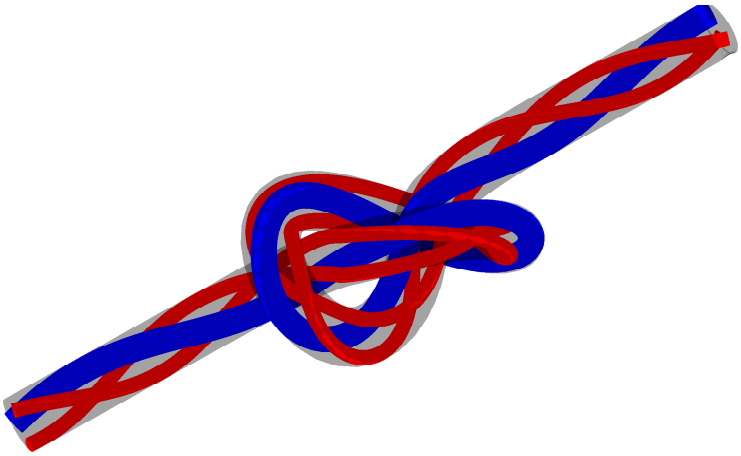

(a) UC ($\hat{U}_c = 0.09$ coils/cm)

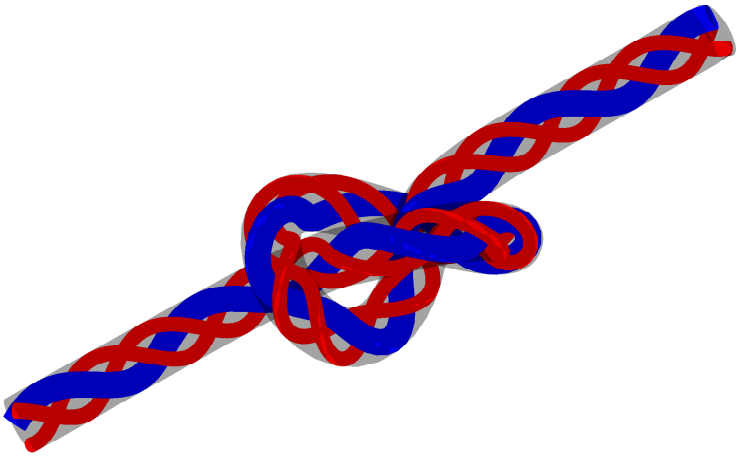

(b) NC ($\hat{U}_c = 0.21$ coils/cm)

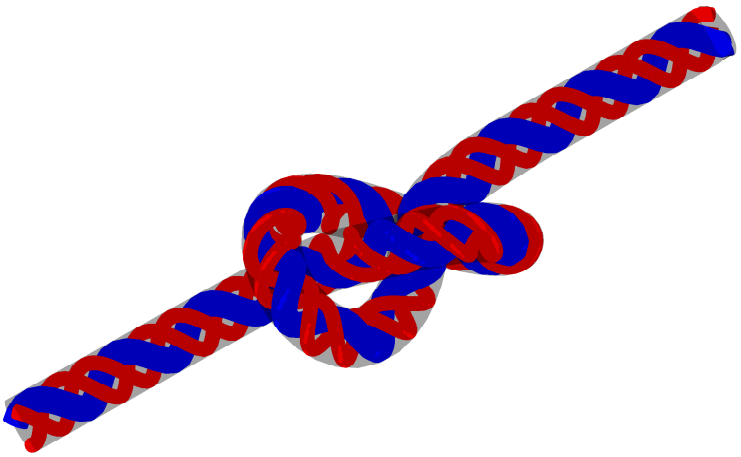

(c) OC ($\hat{U}_c = 0.37$ coils/cm)

Figure 2.18: Schematic of the loose-knots investigated in the LK study. Each cord has nominal width ($\hat{w} = 1.6$ cm) and identical knot centreline.

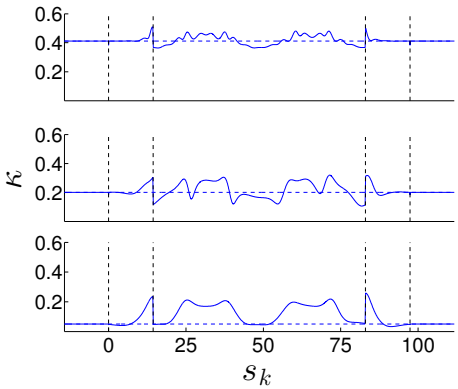

(a) Venous curvature: Top - OC; Middle - NC; Bottom - UC.

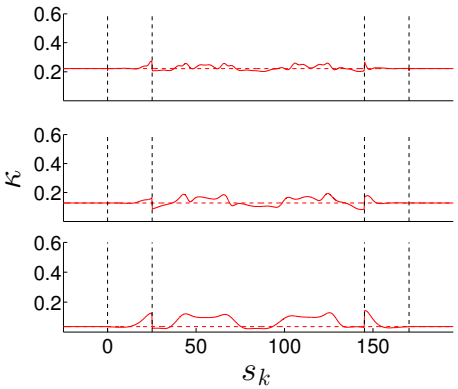

(b) Arterial curvature: Top - OC; Middle - NC; Bottom - UC.

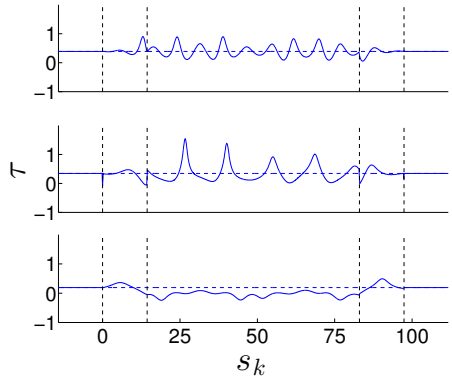

(c) Venous torsion: Top - OC; Middle - NC; Bottom - UC.

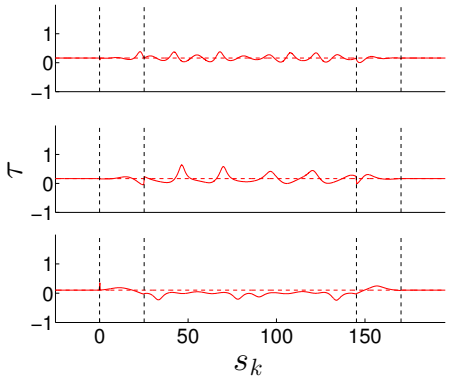

(d) Arterial torsion: Top - OC; Middle - NC; Bottom - UC.

Figure 2.19: Curvature and torsion along knot centreline, s_k, for each of the UC, NC and OC veins and arteries from the LK study. The black-dashed lines indicate the knot centreline section boundaries which were previously denoted by solid black circles in figure 2.16. The dashed blue and red lines indicate the value for the purely helical cord (i.e. without the knot) for the vein and artery, respectively.

	$\overline{\kappa}$	κ_h	δ_κ	$\overline{\tau}$	τ_h	δ_τ	var(κ)	var(τ)
UCV	0.129	0.050	1.586	0.021	0.191	0.891	0.0042	0.0210
NCV	0.223	0.200	0.116	0.355	0.340	0.045	0.0031	0.0875
OCV	0.422	0.411	0.675	0.399	0.388	0.029	0.0010	0.0388
UCA	0.073	0.036	1.029	0.007	0.104	0.928	0.0013	0.0084
NCA	0.140	0.127	0.101	0.171	0.162	0.058	0.0007	0.0189
OCA	0.228	0.222	0.029	0.162	0.157	0.031	0.0002	0.0076

Table 2.6: Curvature and torsion of the loose knot, LK, geometries. The overline indicates the mean value computed over the knot while the h subscript indicates the helical value (without the knot). The parameter δ is the relative difference between the mean and helical vessel values and the variance is denoted var().

Tight true knots, false knots and twist reversal

The effect of tight true knots, false knots and twist reversal are all examined using the same geometric basis as the regularly coiled models of section 2.4.1. The geometry of the knot models, however, is defined by truncating a regularly coiled geometry at the end of the curved outlet and appending another such vessel (sans straight inlet), as shown in figure 2.20. The centreline through the 'knot' section is then simply the curved outlet ($\vec{L}_c^4$) adjoined to a curved inlet ($\vec{L}_c^2$), which have been described previously in section 2.4.1. This local deviation of the geometry from a helical centreline alone can be used to model the presence of a false knot, FK, shown in figure 2.20(a), while geometries for which the handedness of the helical section changes can be used to investigate twist reversal, TR, shown in figure 2.20(b). To model a tight true knot an axisymmetric constriction of variable severity is prescribed which reaches its minimum point at the junction between the outlet and the inlet. This is prescribed following Sherwin and Blackburn (2005) as in the pulsatile stenotic validation of section 2.6, shown in equation (2.43).

Tejada-Martínez et al. (2011) have previously investigated two-dimensional flow of arterial umbilical blood past an asymmetrical constriction. At its apex the largest constriction considered occupied 85% of the diameter of the artery. In the present study we consider four constriction sizes; $R_{min} = 0.5R$ (resulting in a 75% reduction in cross-sectional area), $0.625R$ (61%), $0.75R$ (44%) and $0.875R$ (23%). The models have three complete coils on either

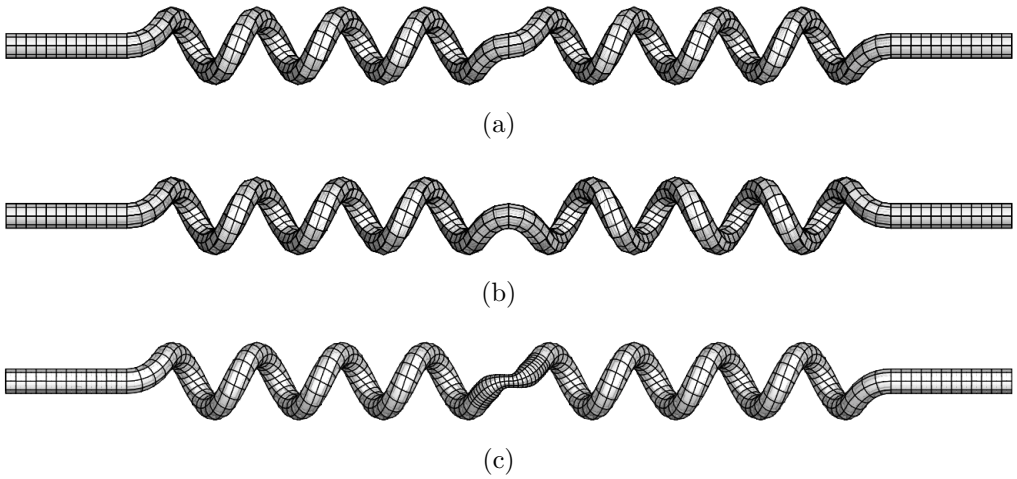

Figure 2.20: The false knot, twist reversal and tight true knot geometries. a) A vessel exhibiting a false knot, FK; b) a vessel with twist reversal, TR, and; c) a vessel with a tight true knot, TK, with constriction to $R_{min} = 0.5R$. Three complete coils are designated either side of the 'knot' feature.

side of the constriction in order to promote the development of fully developed helical flow before the knot as well as the resumption of helical flow downstream of it. This ensures that each vessel has the same U_c and U_t with the latter identical to case U_{t4} described in section 2.4.1. The junction at the centre has a more severely varying curvature than the inlet and outlet with $\Phi = 1.3$ (as opposed to 1.6). The helical sections have $R_h = 2.16$, $P_h = 7$, $\kappa = 0.37$, $\tau = 0.19$ with a total vessel length of 150. Steady results for these models are presented in section 3.2.4 while the pulsatile results are computed for smaller geometries of only 1 coil either side of the constriction in section 4.4.2.

2.5 Steady validation

As validation of the steady `oomph-lib` solvers, entrance flow into a 90° curved tube is considered. This problem has been investigated previously by a number of authors, however, for the purpose of code validation the two studies by Bovendeerd et al. (1987) and Van de Vosse et al. (1989) are used for comparison. Each of these works examine the upstream effects of a planar bend on steady, laminar flow, motivated by a study of blood flow within the human carotid bifurcation. As such the problem is highly suitable as a validation case for umbilical blood flow.

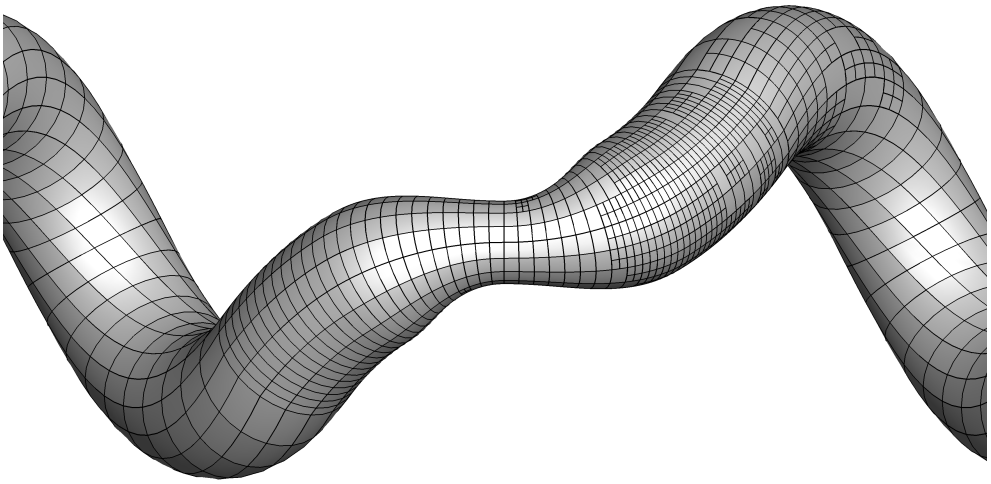

Figure 2.21: A magnified view of a tight true knot on a helical geometry showing mesh refinement. The constriction in this case is to $R_{min} = 0.5R$.

2.5.1 Background

Flow into a curved tube has attracted attention within the literature as a problem readily investigated via experimental and numerical methods. Bovendeerd et al. (1987) experimentally analysed steady laminar flow in a curved pipe for $Re = 350$ with Van de Vosse et al. (1989) continuing this investigation with experimental results at $Re = 150$ as well as numerical results at $Re = 50$, 150 and 250. As with fully developed flow in a toroidal pipe, a vortex pattern is observed as a result of an interaction between inertial, centrifugal and viscous forces within the fluid. On entering the bend the fluid experiences a centrifugal force due to the change in geometry which results in a pressure gradient force toward the centre of curvature. The centrifugal force dominates the pressure gradient force in the centre of the pipe where the axial velocities are high, resulting in an outward motion of the fluid. At the pipe wall, however, the lower axial velocities result in a comparatively larger pressure gradient force which induces a circumferential inward motion of the fluid. Interestingly, an upstream influence of the bend was noted by both Bovendeerd et al. (1987) and Van de Vosse et al. (1989), whereby the secondary velocity at the inlet to the bend is directed entirely toward the centre of curvature.

The experimental apparatus in each of the above studies consisted of two halves of perspex split at the plane of symmetry, with the 90° bend machined out. The (non-dimensional) curvature of the bend in both cases was $\kappa = 1/6$. Laser-Doppler velocity measurements were obtained for the three components of velocity at five axial stations within the bend. In order to ensure fully developed flow at the entrance to the bend, a straight inlet section of length $100R$, where R is the internal pipe radius, was placed before the curved section. Another straight section was adjoined to the bend outlet which led to the reservoir through a rotameter. The axial location measurement was considered accurate up to an estimated relative error of 0.03 while the axial and secondary velocities had estimated errors of 1 and 5%, respectively. Misalignment of the plane of the laser beams could incur a 2% contribution of the axial velocity to the measured secondary velocities. It is also likely that some velocity 'smearing' and averaging occurred over the probe volume. The numerics of Van de Vosse et al. (1989) employed a Galerkin finite element penalty function method. The elements used were 27-noded hexahedral (Q2 - P1), and the mesh consisted of 220 elements (2205 nodes) over half a cross-section.

2.5.2 The computational model

The computational domain defined by the `GeomObject` in `oomph-lib` consists of a straight inlet and outlet of non-dimensional length $L_s = 2$ and a 90° curved section of non-dimensional radius $R_c = 6$, shown in figures 2.22(a) and (b). This ensures a curvature of $\kappa = 1/6$ as used in the experiments. The global and local coordinates are also shown in figures 2.22(a) and (b); in the descriptions used henceforth lower-case letters; i.e. x, y, z, refer to quantities in global Cartesian coordinates, while the upper-case counterparts refer to quantities in local, tube coordinates; X, Y, Z. Here the X and Y coordinates define the cross-sectional plane, as shown in figure 2.22(b). Unless stated the X coordinate is aligned with the tube normal vector, $\boldsymbol{N}$, which points toward the centre of curvature. The arclength along the tube is measured by the Z coordinate. In some cases where the coordinate directions align, such as for a straight tube, the descriptions are used interchangeably. Einstein summation notation is also favoured when convenient. The flow is governed by the steady, incompressible Navier-Stokes equations.

Boundary conditions

At the inlet, Γ_1, a Poiseuille velocity profile is prescribed with no-slip, $u_i = 0$, conditions on the wall, Γ_2. The outlet condition, Γ_3, is taken to be traction-free (TF) following from the numerical work of Van de Vosse et al. (1989). The weak form of the Navier-Stokes equations splits the expression for the k-th residual for the i-th component given in equation (A.15) into a volume and surface integral,

$$r_{k,i} = \int_{\partial\Omega} \left(Re \left(St \frac{\partial u_i}{\partial t} + u_j \frac{\partial u_i}{\partial x_j} \right) \psi_k + \sigma_{i,j} \frac{\partial \psi_k}{\partial x_j} \right) \mathrm{d}\Omega + \int_{\partial D} \sigma_{i,j} n_j \psi_k \mathrm{d}S = 0, \tag{2.30}$$

where $\sigma_{i,j}$ is the stress tensor, n_j is the normal to the surface ∂D which encloses a volume $\partial\Omega$. In `oomph-lib`'s representation of the weak form the volume integral in equation (2.30) is handled by the Navier-Stokes elements, with the surface integral assumed zero. The latter condition is based on the fact that this integral evaluates to zero on a boundary for which Dirichlet conditions are specified. In the event that no condition is specified, the implication of equation (2.30) is,

$$\int_{\partial D} \sigma_{i,j} n_j \psi_k \mathrm{d}S = 0 \implies t_i = \sigma_{i,j} n_j = 0, \tag{2.31}$$

where t is the traction on surface ∂D. The exact physical nature of the condition imposed here is determined via the vector `Gamma` which alters the form of the stress-tensor used within `oomph-lib`,

$$\sigma_{i,j} = -p\delta_{i,j} + \mu\left(\frac{\partial u_i}{\partial x_j} + \texttt{Gamma}[i]\frac{\partial u_j}{\partial x_i}\right). \tag{2.32}$$

For $\texttt{Gamma} = [1,1,1]$ the stress tensor reduces to the standard form and the traction-free condition is imposed. Another option is $\texttt{Gamma} = [0,0,0]$ which gives rise the to the so-called "pseudo traction-free" (PTF) condition. This is often favoured for problems with straight-pipe outlets as it weakly enforces a zero axial derivative of the velocity components akin to a fully-developed flow. Both traction-free and pseudo traction-free conditions are enforced in this study to investigate the effects of changing the outlet condition. A summary of the conditions imposed on each of the three boundaries is as follows,

Γ_1: Poiseuille inlet: $W = u_3 = 2 - 2r^2$,

Γ_2: No-slip: $u_i = 0$, and;

Γ_3: Traction-free: $\sigma_{i,j}n_j = 0$;
Or pseudo traction-free: $\left(p\delta_{ij} + \mu\frac{\partial u_i}{\partial x_j}\right)n_j = 0$,

where the boundaries are as marked in figure 2.22(a).

Models

Four base meshes of differing axial mesh refinement, controlled via the parameter `n_layer`, are chosen to study the typical number of elements necessary to achieve convergence of the solvers as well as an appropriate error with respect to the results in the literature. These meshes are detailed in table 2.7. Two uniform refinements of the mesh are performed before solve, increasing the total number of elements by a factor of 64. Each cross-section, which initially comprise four satellite elements arranged around a central core element, now consist of 80 elements, as shown in figure 2.22(b). For each mesh the solution is progressed from an initial solve at $Re = 0$ using numerical continuation to $Re = 150$ with increments of $Re = 10$. Automatic mesh adaptation is employed on Mesh A for comparison, while GMRES is used in one case to compare with the default direct solver, which uses LU decomposition via `SuperLU`.

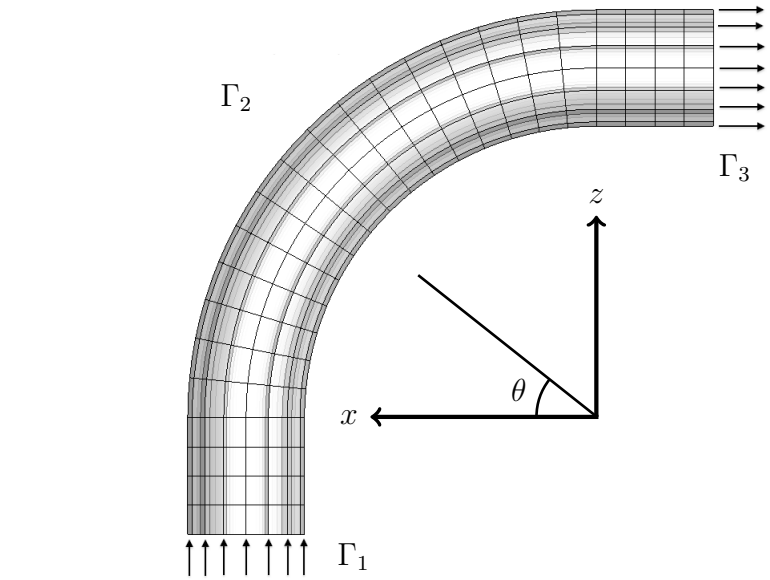

(a)

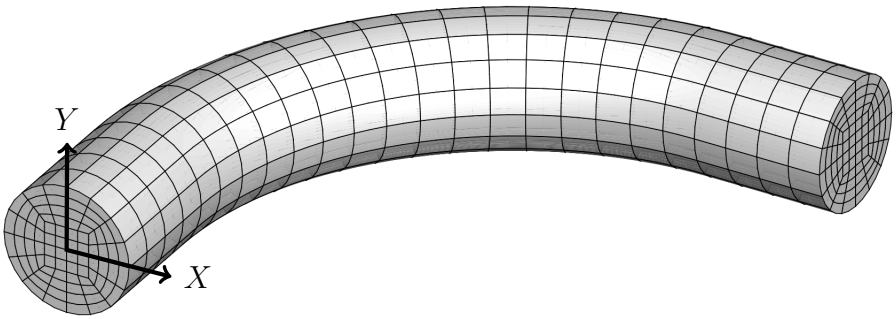

(b)

Figure 2.22: The computational domain for the steady curved pipe entry flow validation. a) The (x, z)-plane with inlet, Γ_1, wall, Γ_2 and outlet, Γ_3 marked, and; b) isometric view showing local coordinates (X, Y) and cross-sectional refinement after two uniform mesh refinements. Shown here is Mesh A.

Mesh	N_E (Base)	N_E (2 UR)
A	30	1920
B	65	4160
C	100	6400
D	130	8320

Table 2.7: The meshes used for the steady curved pipe entry flow validation showing the base mesh number of elements, N_E, as well as the number after two uniform refinements.

2.5.3 Results

Qualitatively, the upstream effect of the curved pipe described in Bovendeerd et al. (1987) is present at the inlet to the bend, $\theta = 0$. Here a net movement of the secondary velocity toward the centre of curvature of the pipe is observed for all models considered and is shown for comparison in figure 2.23. Development of the typical vortical structure occurs downstream, with the axial velocity, W, skewed to the pipe outer, as shown in figure 2.24. The evolution of the axial velocity within the plane of symmetry, $Y = 0$, is plotted in figure 2.25 at five axial stations within the bend. Data from Van de Vosse et al. (1989) is obtained through manual observation of the relevant images in `plotdigitizer`, a process which incurs some small error. In order to compare with the experimental and numerical results from the literature the original `oomph-lib` data is interpolated using piecewise-quadratic interpolation. This procedure can be attempted without further loss of accuracy as Taylor-Hood elements represent the velocity using quadratic basis functions. Good agreement is found for all cases examined, with relatively little difference notable among the models despite the differing mesh refinement, boundary conditions and solvers used. In this case, variation is mostly related to the behaviour of the iterative solver. At the midway point along the curved section, $\theta = \pi/4$, each of the models tend to increase the axial velocity near the pipe outer, replicating the experiments well. This trend continues at $\theta = 3\pi/8$, however the estimates exceed the experimental measurement at this location. The relative errors in the plane of symmetry are plotted in figure 2.26 for the two axial stations which display the highest error; $\theta = 3\pi/8$ and $\pi/2$. For all models the error with respect to the experiments is within 10%, while the numerics are estimated to within 7% with the average cross-sectional error roughly between 1 and 3%. In all cases the error expectedly

exhibits localised peaks near the pipe wall where the gradients are large.

Ultimately the curved pipe flow problem does not provide a reasonable platform on which to test the efficacy of automatic mesh adaptation or the use of iterative linear solvers as the problem is too small in nature. However, is has shown that the steady `oomph-lib` routines perform well and replicate the results from the literature to within an acceptable level of error. The axial refinement level chosen from this study is 0.6 layers per unit arclength which is used throughout the thesis unless otherwise stated. Two uniform refinements of the base mesh cross-section are also automatically progressed before solution in all simulations.

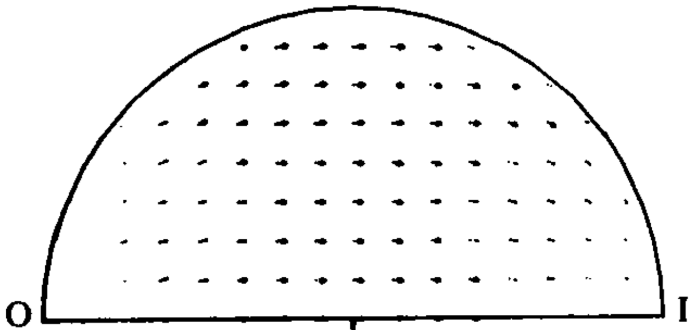

(a)

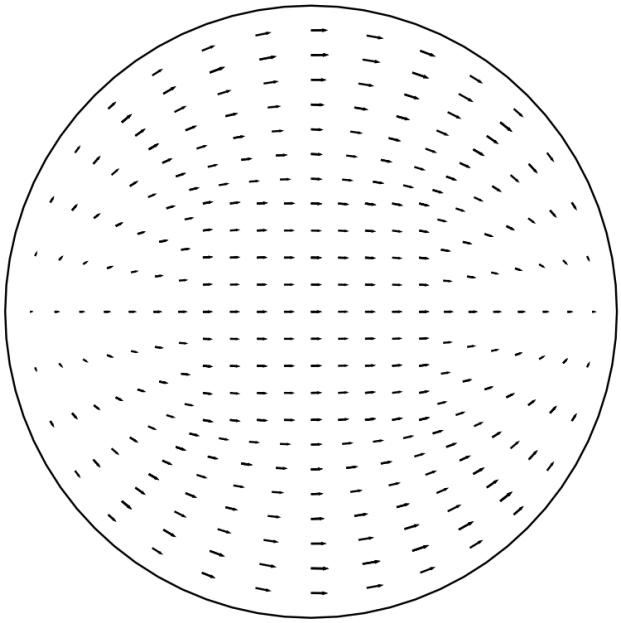

(b)

Figure 2.23: A qualitative comparison of the secondary flow field for $\theta = 0$ at $Re = 350$. Note that vector length scalings are not necessarily equal. Here the flow is directed entirely toward the centre of curvature of the pipe. a) Experimental results used with permission from Bovendeerd et al. (1987); and b) results produced using `oomph-lib` for Mesh A with traction-free outlet boundary conditions and `SuperLU` as the linear solver.

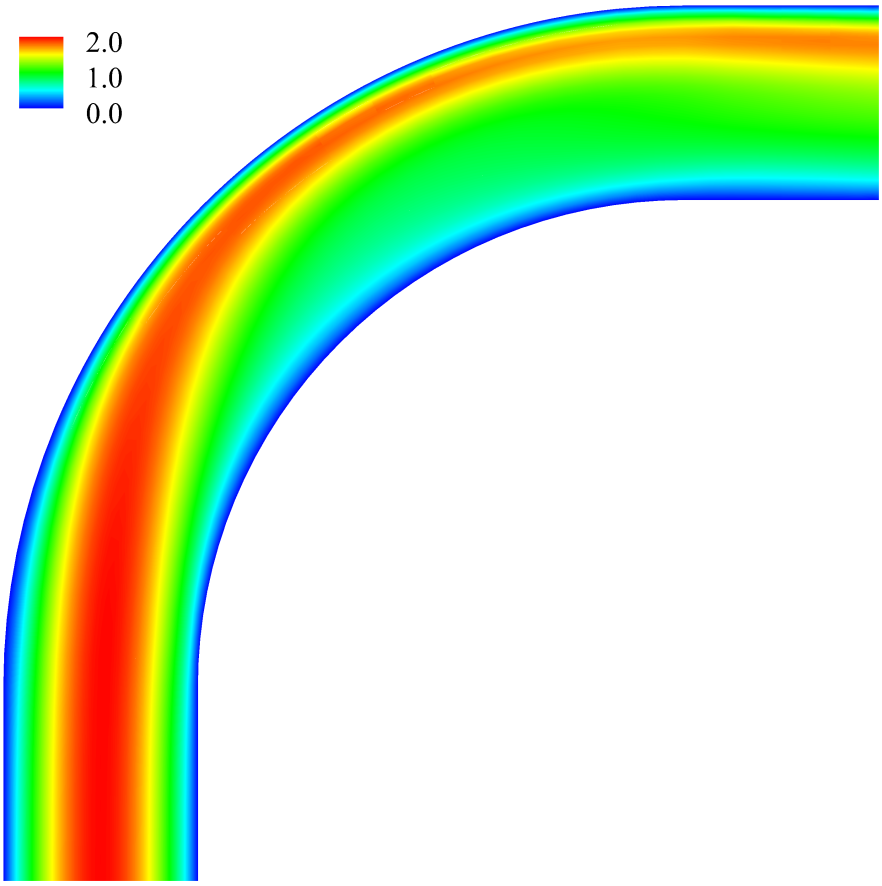

Figure 2.24: Contours of the axial velocity within the plane of symmetry ($Y = 0$) for the steady curved pipe validation.

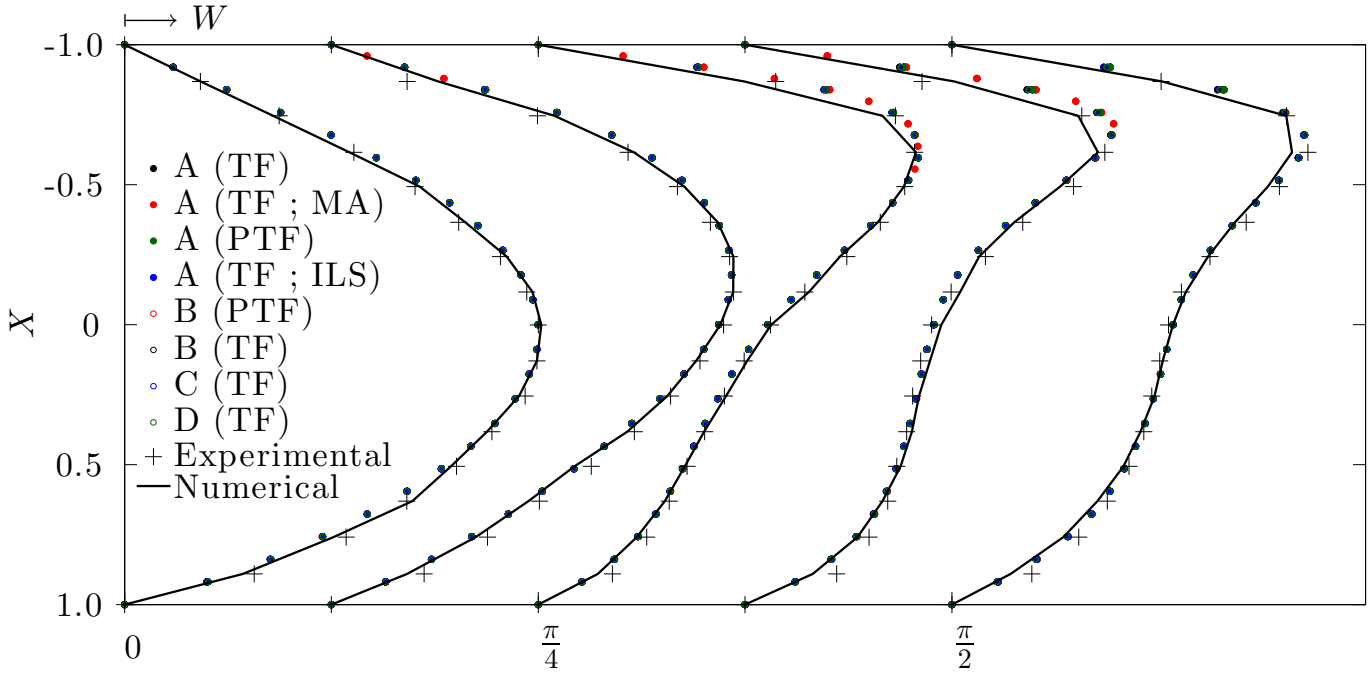

Figure 2.25: Comparison of the axial velocity, W, in the plane of symmetry at five axial stations within the bend; 0, $\pi/8$, $\pi/4$, $3\pi/8$ and $\pi/2$. The numerical results of Van de Vosse et al. (1989) are given by the solid black line, while the experimental results of the same study are shown as (+). The coloured symbols mark the `oomph-lib` results for each of the four meshes; A, B, C and D. The outlet boundary conditions are specified as either traction-free (TF) or pseudo traction-free (PTF) while one model utilised automatic mesh adaptation (MA) and another tested the iterative linear solver (ILS) which here is the generalised minimum residuals method, GMRES, implemented with Trilinos.

2.6 Pulsatile validation

As validation of the unsteady `oomph-lib` solvers, two pulsatile flow problems are considered. The first is a simple straight pipe with a prescribed inlet velocity waveform similar to the physiological forcing of the heart. The second follows from the work of Sherwin and Blackburn (2005) and considers stenotic pipe-flow wherein a constriction is added along the pipe length. This validation has relevance to the study of tight true knots considered in chapter 4.

2.6.1 Boundary conditions

The infinite straight pipe pulsatile solution derived by Womersley (1955) and shown in equation (1.9) is used as the inlet boundary condition throughout the pulsatile work of this thesis. The complex pressure coefficients (P_n) in this expression are difficult to determine from in-vitro measurements and are required to fully determine the velocity waveform. In practice, it is easier to prescribe the velocity variation and determine the requisite P_n. For the straight pipe validation problem the temporal variation of the sectional average, $\overline{w}(t)$, is defined following Sherwin and Blackburn (2005) as the addition of a mean and two harmonic terms,

$$\overline{w}(t) = \overline{w}_m\Big(1 + a_1\sin(\omega_1 t) + a_2\cos(\omega_2 t)\Big), \tag{2.33}$$

where $a_1, a_2 \in \mathbb{R}$ and $\overline{w}_m$ is the temporally and cross-sectionally averaged axial velocity within the cross-section. Two cases of non-reversing sectional flow examined by Sherwin and Blackburn (2005) are chosen which have $(a_1, a_2) = (0.75, 0), (0.75, -0.75)$. Using the solution derived by Womersley (1955), the temporally varying sectional average, $\overline{w}(t)$, may also be written,

$$\overline{w}(t) = \frac{2}{R^2}\int_0^R w(r,t) r \mathrm{d}r, \tag{2.34}$$

$$= \frac{2}{R^2}\int_0^R \left\{ w_0(r) + \sum_{n=1}^{N} \Re\left[\frac{P_n i}{\rho\omega_n}\left(\frac{J_0(i^{3/2}\alpha_n r/R)}{J_0(i^{3/2}\alpha_n)} - 1\right) e^{i\omega_n t}\right]\right\} r\mathrm{d}r, \tag{2.35}$$

where the relevant parameters are as listed in section 1.3.3 and $N = 2$. Following Mazumdar (1992) the real part of the integral is taken for each of the harmonics and the relation,

$$\int_0^\beta \theta J_0(\theta)\mathrm{d}\theta = \beta J_1(\beta), \tag{2.36}$$

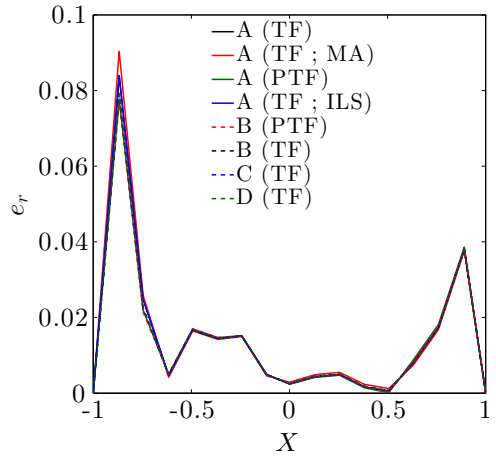

(a) Error with respect to experiments of Van de Vosse et al. (1989) at $\theta = 3\pi/8$.

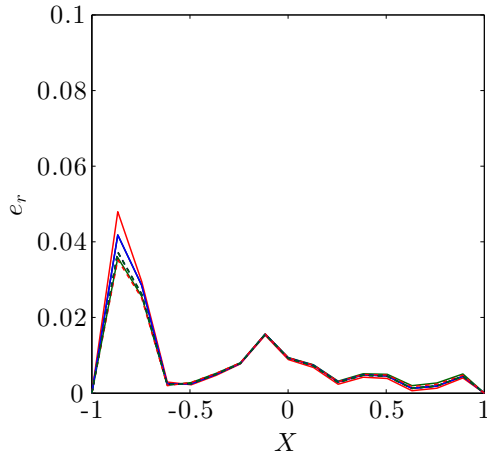

(b) Error with respect to numerics of Van de Vosse et al. (1989) at $\theta = 3\pi/8$.

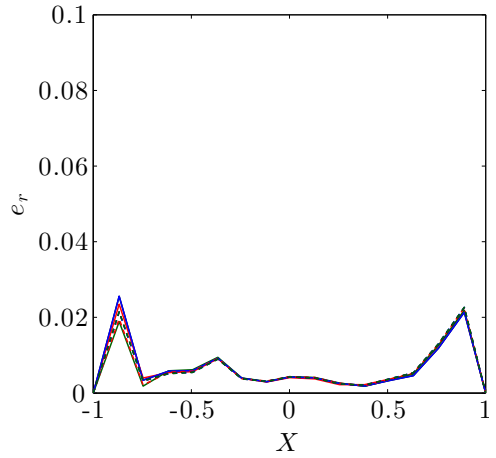

(c) Error with respect to experiments of Van de Vosse et al. (1989) at $\theta = 2\pi$.

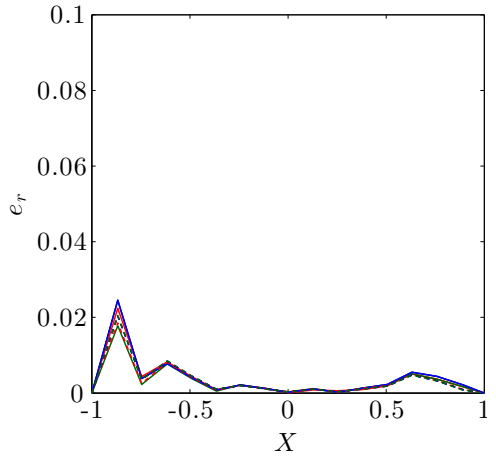

(d) Error with respect to numerics of Van de Vosse et al. (1989) at $\theta = 2\pi$.

Figure 2.26: Relative error, e_r, in the `oomph-lib` numerics for the steady curved pipe validation. Top; $\theta = 3\pi/8$ and bottom; $\theta = \pi/2$, with relation to the results of Van de Vosse et al. (1989). Here the boundary conditions were set as either traction-free (TF) or pseudo traction-free. One model utilised automatic mesh adaptation (MA) and another tested the iterative linear solver (ILS) which here is the generalised minimum residuals method, GMRES, implemented with Trilinos.

is used to simplify the expression in equation (2.35). The temporal variation of the sectional average is then,

$$\overline{w}(t) = w_{mean} + \sum_{n=1}^{N} \Re\left(\frac{P_n i}{\rho\omega_n} \left(\frac{2J_1(\beta_n)}{\beta_n J_0(\beta_n)} - 1 \right) e^{i\omega_n t} \right), \tag{2.37}$$

where $\beta_n = i^{3/2}\alpha_n$ and w_{mean} is the mean of the steady flow (nominally unity). The pressure coefficients, $P_n = C_n + iD_n$ with $n = 1, 2$, can now be determined by equating (2.33) and (2.37). For the waveform given by Sherwin and Blackburn (2005) these are,

$$C_n = -\frac{a_n \rho\omega_n w_{mean} \Re\left[\dfrac{2J_1(\beta_n)}{\beta_n J_0(\beta_n)} \right]}{\left\| \dfrac{2J_1(\beta_n)}{\beta_n J_0(\beta_n)} \right\|^2}, \tag{2.38}$$

$$D_n = -\frac{a_n \rho\omega_n w_{mean} \Im\left[\dfrac{2J_1(\beta_n)}{\beta_1 J_0(\beta_n)} \right]}{\left\| \dfrac{2J_1(\beta_n)}{\beta_n J_0(\beta_n)} \right\|^2} \tag{2.39}$$

where $\Im[x]$ denotes the imaginary component of $x \in \mathbb{C}$. The pressure drop along a pipe of length L is then found from,

$$\Delta P = \Re\left(\sum_{n=0}^{N} P_n e^{i\omega_n t} \right) ReL, \tag{2.40}$$

$$= \left(\frac{8}{Re} + \frac{1}{U_{red}} \sum_{n=1}^{N} C_n \cos(\omega_n t) - D_n \sin(\omega_n t) \right) ReL. \tag{2.41}$$

The temporal variation of the sectional average is plotted with the pressure drop for both waveform one, $(a_1, a_2) = (0.75, 0)$, and waveform two, (0.75, -0.75), in figure 2.27. The full inlet velocity profile for waveform two is plotted with components in figures 2.28(a)-(d).

2.6.2 Straight pipe flow

For straight pipe flow the analytic solution prescribed as the inlet boundary condition is independent of arclength coordinate, Z, for an infinite pipe. However, for validation purposes the domain must be truncated and the non-dimensional length is here arbitrarily set as $L = 10$. A Reynolds number of

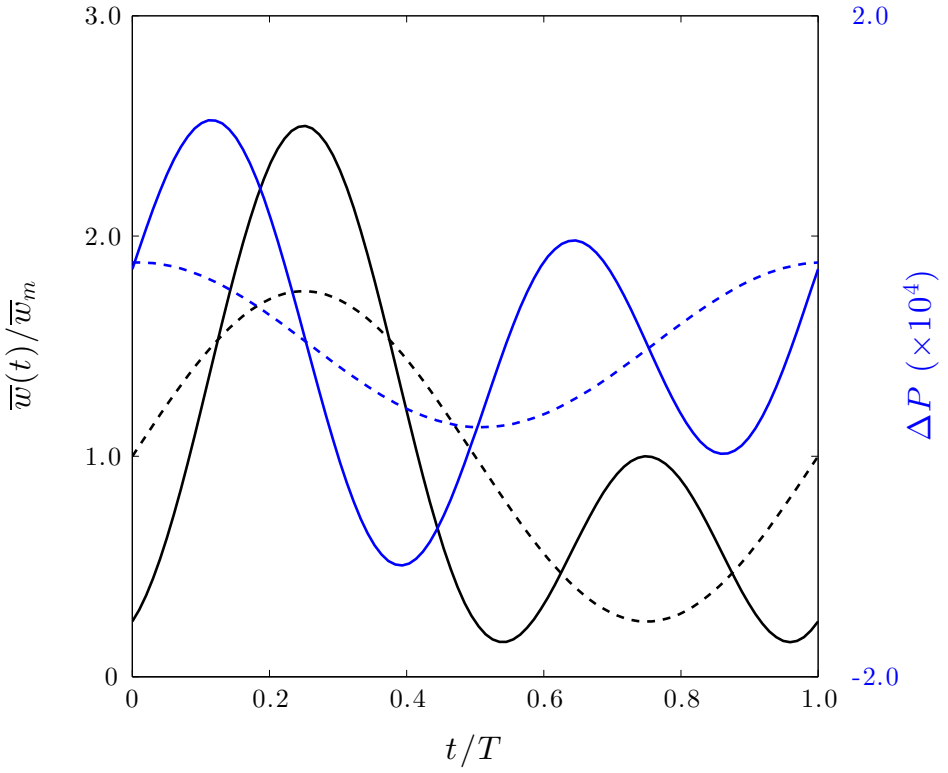

Figure 2.27: Temporal variation of the average sectional velocity (black) and pressure drop (blue) for a straight pipe of length $L = 10$ for the pulsatile validation. Shown with the dashed lines is waveform one with $(a_1, a_2) = (0.75, 0)$, while the solid lines correspond to waveform two, $(a_1, a_2) = (0.75, -0.75)$.

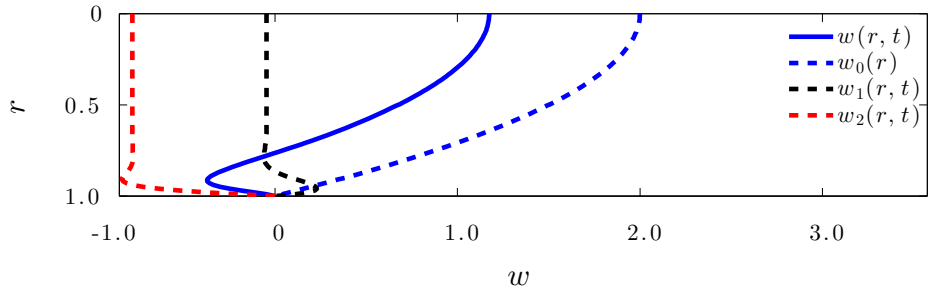

(a) $t/T = 0$

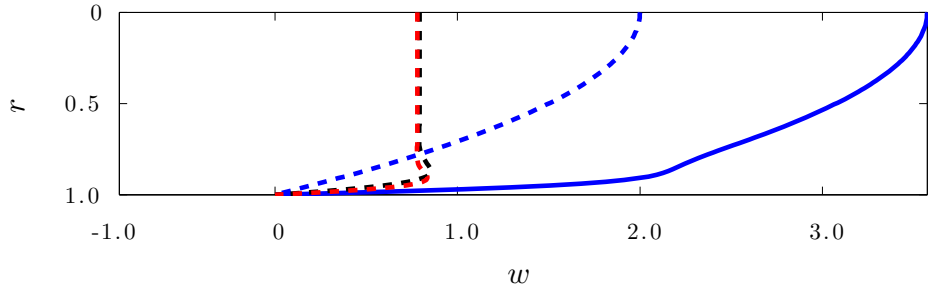

(b) $t/T = 0.25$

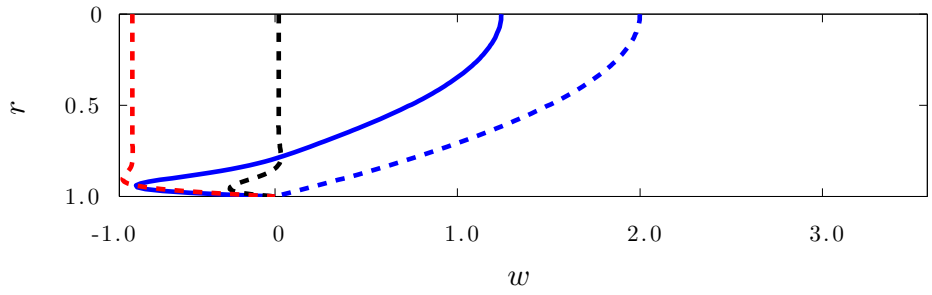

(c) $t/T = 0.5$

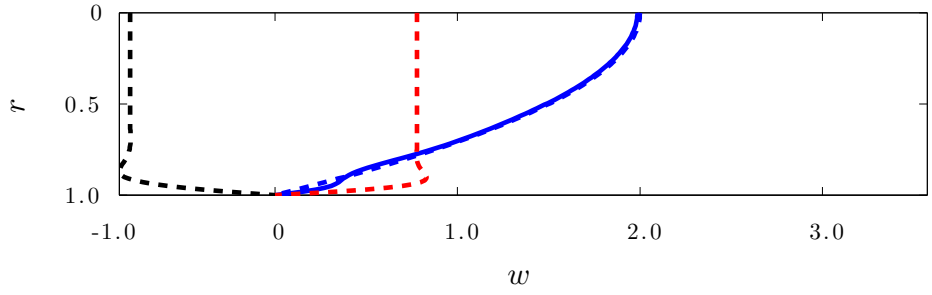

(d) $t/T = 0.75$

Figure 2.28: Temporal variation of the inlet velocity profile for the pulsatile validation, $w(r,t) = w_0(r) + \sum_{n=1}^{2} w_n(r,t)$, at four points within the period for waveform two with $(a_1, a_2) = (0.75, -0.75)$.

$Re = 100$ and reduced velocity of $U_{red} = 1$ reults in a Womersley parameter of $\alpha \approx 25.1$. While this is larger than typically found in the umbilical arteries, flow reversal for this waveform, illustrated in figure 2.28, is quite severe and provides an adequate test of the temporal solvers. The velocity throughout the remainder of the domain is initially set as stagnant ($u_i = 0$) introducing a transient start-up time over which the sectional velocity profile at each location acquires the prescribed inlet profile. The boundary conditions are pseudo-traction free at the outlet and no-slip on the wall as described in section 2.5.2. The number of elements is constant with `n_layer` $= 6$, two uniform refinements and a resultant mesh of 1920 elements. In order to analyse the effect of changing the timestep (Δt) three runs with $\Delta t = T/20$, $T/50$ and $T/100$ are examined with spatial mesh adaptation disabled. For comparison an additional run with adaptation at $\Delta t = T/100$ is computed. The error associated with each run is quantified using the planar error, ϵ_p, defined as,

$$\epsilon_p = \sqrt{\frac{\sum_{i=1}^{N_n} e_i}{N_n}}, \tag{2.42}$$

where N_n is the number of nodes within the plane and $e_i = e_{u,i}^2 + e_{v,i}^2 + e_{w,i}^2$, is the sum of the squares of the errors in the individual velocity components. This error is computed at two locations along the pipe length; the mid-plane (M) at $Z = 5$ and the outlet (O) at $Z = 10$, with the variation shown in figure 2.29(a). From this plot it can be seen that the planar error is not significantly affected by the choice of timestep or location along the pipe. In all cases the error is less than 4% which is considered reasonable. With mesh adaptation the run with $\Delta t = T/100$ produces an outlet planar error of less than 0.5% of the mean velocity suggesting that spatial mesh discretisation bears the most significant influence on error. The pressure drop, shown in figure 2.29(b), reproduces the analytic solution well within a start-up time of approximately $t = T/5$ for all cases, with a further reduction to approximately $T/10$ for $\Delta t = T/100$.

2.6.3 Straight pipe stenotic flow

As further validation of the temporal solvers, pulsatile flow into a stenosed pipe previously investigated by Sherwin and Blackburn (2005) is considered. In order to lower computational cost, waveform one with $(a_1, a_2) = (0.75, 0)$, is used as the inlet condition. Spatial adaptation is allowed, however, with a smaller error target of $e_{max} = 1.5 \times 10^{-2}$. The geometry consists of a straight inlet of length $L_{in} = 8$, a stenosis length of $L_{con} = 4$ and an outlet length of

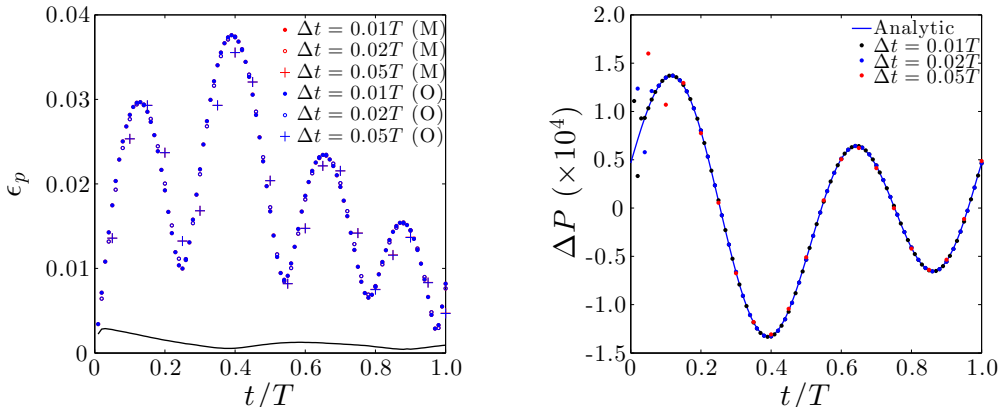

Figure 2.29: Straight pipe pulsatile validation for three timesteps; $\Delta t = T/100$, $T/50$ and $T/20$. a) Variation of the planar error, ϵ_p, over one period. The solid black line indicates the run with $\Delta t = T/100$ and spatial mesh adaptation with the mid-plane designated 'M', and the outlet 'O'; b) variation of the pipe pressure drop, ΔP, over one period compared with the analytic solution.

$L_{out} = 90$, as shown in figure 2.30. The stenosis is prescribed as,

$$R(Z') = R_{min} + (1 - R_{min}) \sin^2 \left(\frac{\pi Z'}{L_s} \right) \qquad -1/2 \leq \frac{Z'}{L_{con}} \leq 1/2, \quad (2.43)$$

where R_{min} is the minimum radius of the constriction, set here as half the nominal radius $R = 1$, Z' is the arclength measured from the centre of the constriction and L_{con} is the total length of the constriction. The base mesh has 61 axial layers distributed with 5 layers in the inlet, 2 layers through the constriction and 54 in the outlet. After two uniform refinements the final mesh has 19520 elements. For the single-harmonic waveform and a reduced velocity of $U_{red} = 5$ a critical Reynolds number, Re_c, of 194.5 is quoted in Sherwin and Blackburn (2005) above which turbulent structures are present. It should be noted that the reference length scale used in this paper is the pipe diameter and hence the quantities are modified appropriately by a factor of two. Two tests are therefore conducted for $Re = 100$ ($\alpha = 11.21$) and $Re = 200$ ($\alpha = 15.85$). This allows a qualitative comparison with and without the onset of turbulent structures.

Case 1: $Re = 100$

This regime corresponds to the approximate Re of umbilical arterial flow and should not exhibit turbulence. It therefore provides a suitable platform to

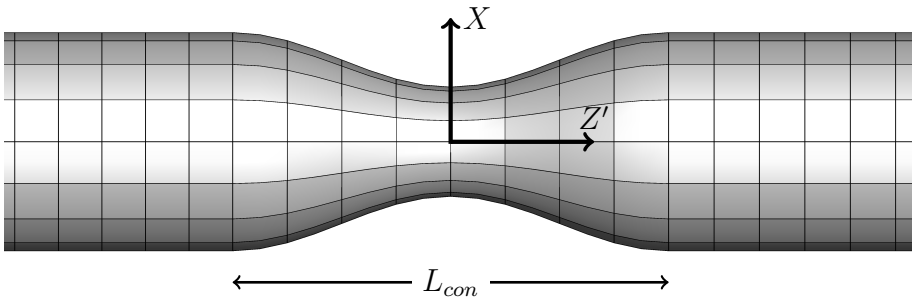

(a)

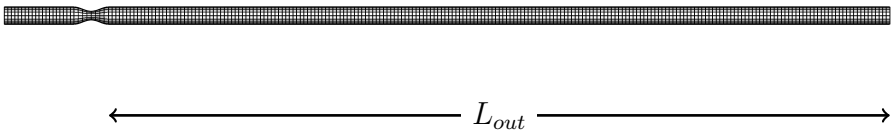

(b)

Figure 2.30: The straight pipe stenosis geometry; a) magnified view of the constriction with lengths annotated, and; b) the full geometry showing the length of the outlet.

compare the effects of a successively reduced timestep on the solution. The solution within the timeframe $t/T = 1 : 2$ is considered as this allows the domain to complete one period with any transients produced by the initial, stagnant condition effectively removed. The cross-sectional axial velocity profile computed with timesteps of $\Delta t = T/25$, $T/50$, $T/100$ and $T/200$ is shown at four stations throughout the period in figures 2.31 and 2.32. The formation of a blunt, plug-flow profile at the location of the constriction as well as the resultant flow-reversal further aft is consistent with the results of Sherwin and Blackburn (2005). The sharp profile evident at the stenosis becomes less severe toward the outlet. The solutions computed with intervals of $T/50$ and $T/100$ are roughly equivalent, however, show small discrepancies downstream of the constriction, as depicted in figure 2.32(a) at $Z' = 22$. Further reduction in timestep to $T/200$ typically produces negligible difference and hence a timestep of $T/100$ is suitable for computations at this Re.

Case 2: $Re = 200$

Flow at $Re = 200$ and $\alpha = 15.85$ becomes fully three-dimensional in the computations run by Sherwin and Blackburn (2005). This is reproduced qualitatively in the current study with the axisymmetric base flow seen to break-down roughly half-way through the period. A plug flow, shown in figure 2.33(b), initially develops as in the stable flow at $Re = 100$. As the jet traverses the pipe length vortical structures develop and the flow becomes full three-dimensional, shown in figures 2.33(c) and (d). Some slight artefacts of the coarse mesh are still present here; further mesh refinement resulted in significantly increased computation time and so was abandoned due to restrictive computational resources.

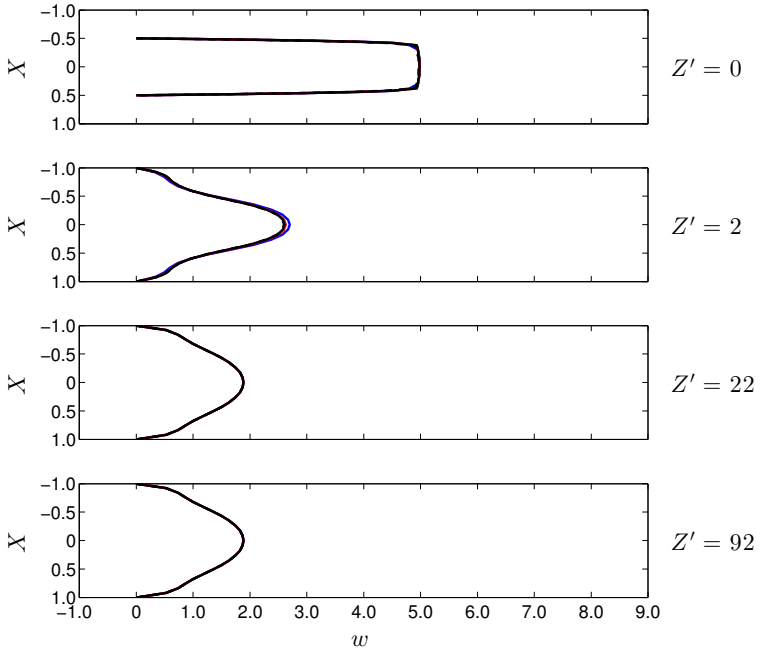

(a) $t/T = 1.0$

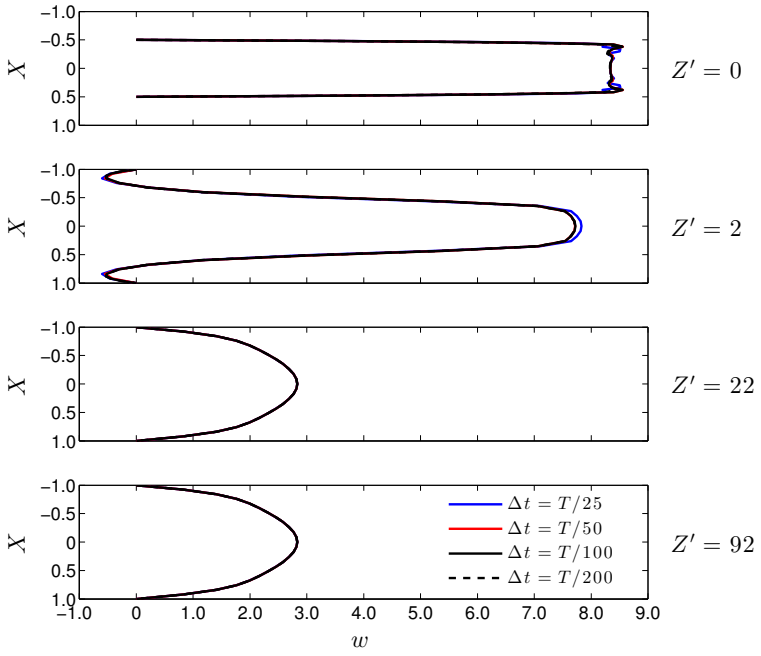

(b) $t/T = 1.24$

Figure 2.31: Stenotic flow at $Re = 100$ showing the cross-sectional axial velocity profile variation with Δt at four stations. The distance along the pipe (Z') is measured from the midpoint of the stenosis, with $Z' = 92$ the outlet. The coordinate (X) is defined as in the steady validation.

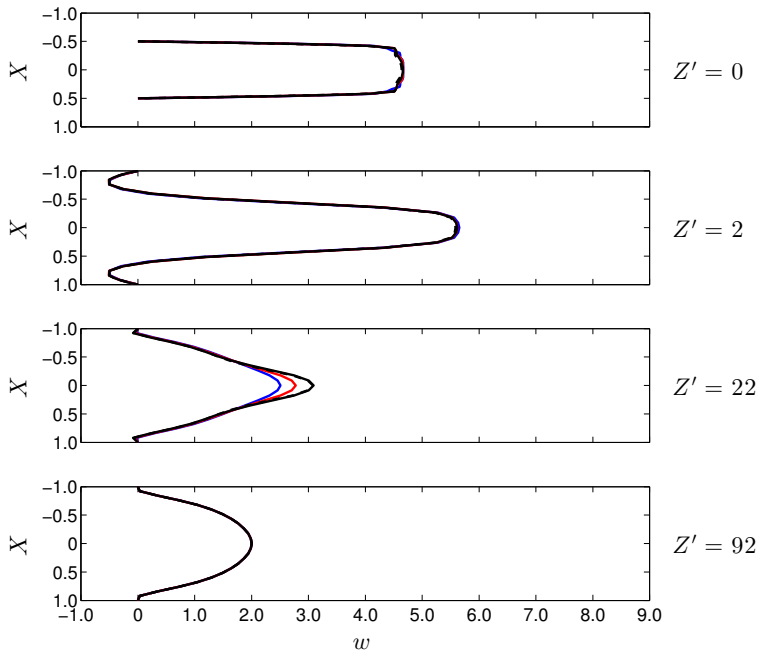

(a) $t/T = 1.52$

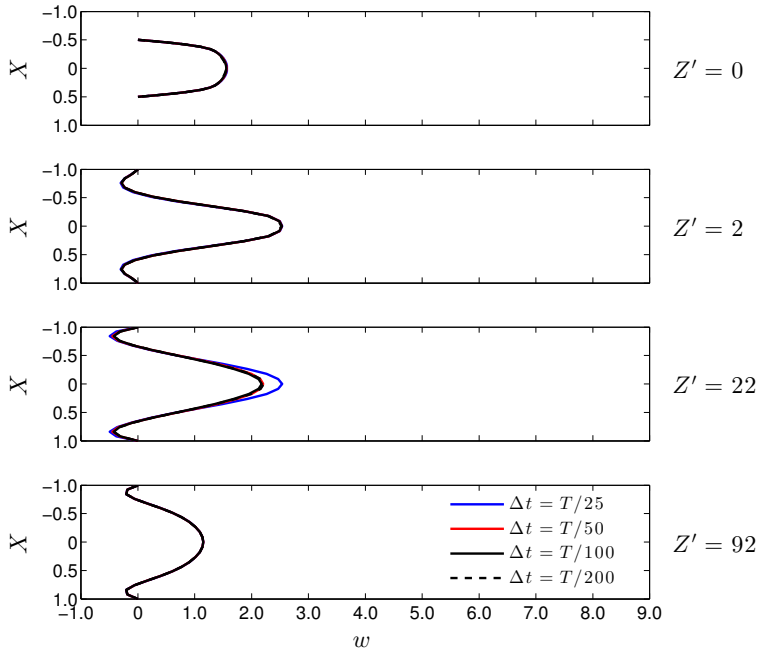

(b) $t/T = 1.76$

Figure 2.32: Stenotic flow at $Re = 100$ showing the cross-sectional axial velocity profile variation with Δt at four stations. The distance along the pipe (Z') is measured from the midpoint of the stenosis, with $Z' = 92$ the outlet. The coordinate (X) is defined as in the steady validation.

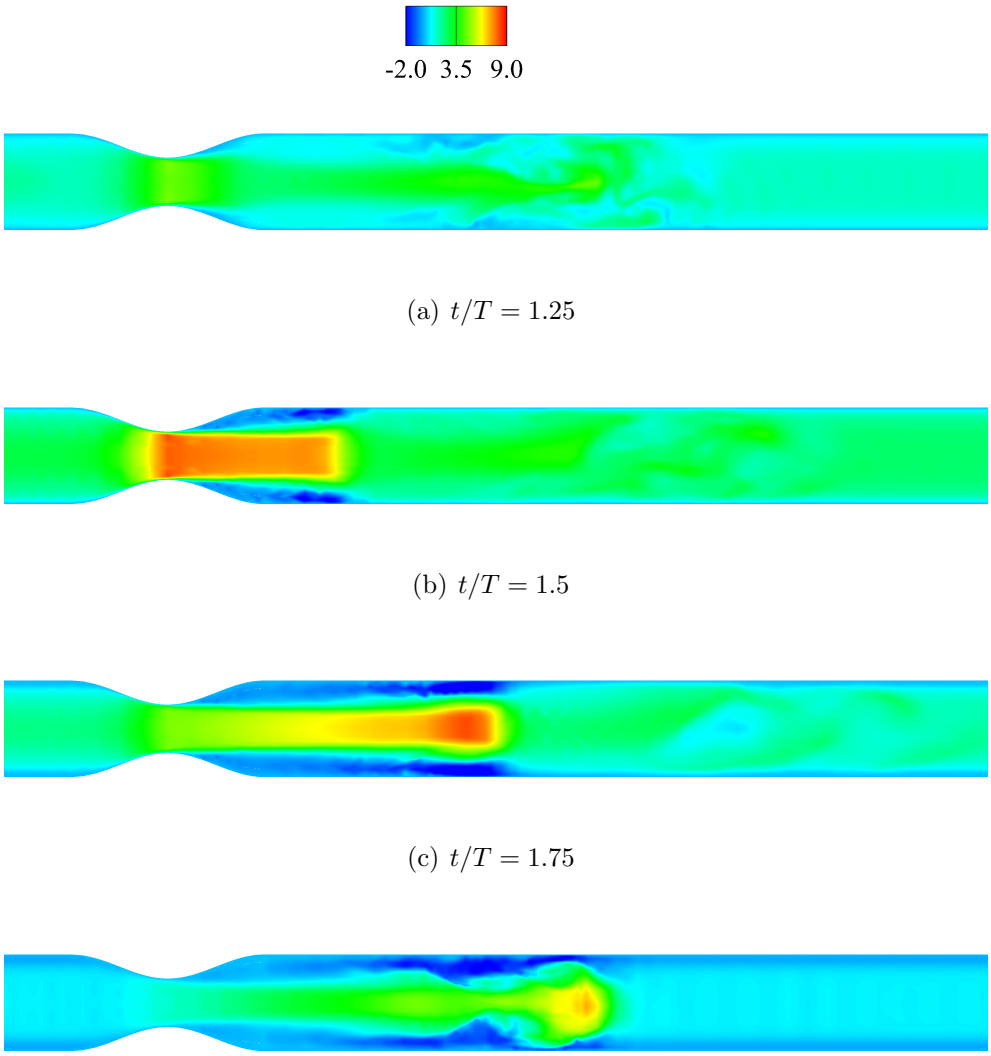

(a) $t/T = 1.25$

(b) $t/T = 1.5$

(c) $t/T = 1.75$

(d) $t/T = 2.0$

Figure 2.33: Contours of the axial velocity within the plane of symmetry ($Y = 0$) for $Re = 200$, $U_{red} = 5$ at four points within the period.

Chapter 3

Steady flow through the umbilical vessels

The purpose of this chapter is to present a steady analysis of flow within geometries representative of the umbilical arteries and vein. The aim is to examine the diagnostic effectiveness of the umbilical coiling index (UCI) as well as to estimate the effects of geometric irregularities on the pressure and flow field. In order to achieve this steady numerical computations for a number of distinct umbilical vessel geometries is conducted. Throughout these studies the pressure drop over the length of the vessel (ΔP) is used as the key diagnostic for umbilical flow resistance. The motivation for this is simple; for the umbilical arteries the vessel pressure drop directly represents the loading on the fetal heart while it will instead indicate the pressure required at the placental insertion in the equivalent venous model. The key questions posed within this chapter are therefore;

i) Does the UCI predict the pressure drop and hence provide clinicians with an understanding of the flow resistance created by a given cord? and;

ii) Do geometric irregularities including non-uniform coiling characteristics and the presence of true or false knots appreciably affect the vessel pressure drop?

In order to address these questions, three broad studies are presented. The first examines a number of simple umbilical geometries based on the work of Kaplan et al. (2010). These cords are each comprised of a helical tube with straight inlet and outlet sections adjoined to the umbilicus and placental insertion, respectively. The characteristics of the helical tubes are designed such that a broad range of cords be examined whilst ensuring that each have

identical UCI and therefore remain diagnostically equivalent. Two separate studies are presented in order to account for ambiguity in the literature regarding the measurement of the cord length and number of coils.

The second study examines the effects of varying the pitch and/or helical radius of a typical umbilical cord. In this way the total cord UCI is again held constant, however, the cord coiling is allowed to vary significantly from one end to the other. Cords rarely exhibit constant UCI over their length and the index is therefore calculated in an average sense. This study scrutinises this averaging procedure in an effort to determine it's validity as well as to more generally elucidate the variation of the cord pressure drop with nonuniformity.

The final study discusses the presence of knots within the umbilical cord. These geometries are further classified into three separate models; loose true knots, where constriction is insignificant and the geometric knotting of the vessel is the primary feature, tight true knots where constriction is deemed significant compared to the geometric knotting, and false knots for which the cord structure briefly deviates from the helical description without geometric knotting or constriction. The loose true knot models allow analysis of the flow and pressure field through coiled geometries which also exhibit a larger-scale spatial variation. This is applicable not only to knotted cords, but also to cords with geometric twisting or curving of lower frequency than the underlying vessel coiling. An example would be coiled cords for which the helical axis also curves in-utero.

Through the aforementioned studies it is determined that the UCI is unable to distinguish between cords of varying pressure drop. The index essentially represents the number of coils of a cord per (cm) length, which critically removes any reference to the total length of the vessels. As for straight pipe flow, the total arclength of a helical tube significantly alters the downstream pressure drop and hence the UCI does not in general represent the corresponding flow resistance. In addition to this, one form of the UCI also lacks any reference to the transverse cord measurement, the coil width, while both fail to explicitly account for its variation. This dimension directly relates to the curvature and torsion of the arterial and venous vessels, affecting the pressure gradient and in turn the total pressure drop. Two physiologically realistic models with equal cord length and number of coils were found to differ in total pressure drop by 40% simply by increasing the coil width.

Considering non-uniform cords, variations in the coil spacing, cord width or combinations of the two are shown to have little effect on the total pressure drop. This result suggests that cords of average coiling are indeed representative of those with significantly varying pitch and radius in terms of the

total computed pressure drop alone. However, velocity and axial pressure gradients over the cord length within these geometries can vary significantly.

Finally, knots modelled as simple geometric perturbations to the helical structure without variation to the cross-section have little effect on the total pressure drop. Constricted cords, however, can exhibit drastically different pressure and flow profiles with the vessel pressure drop increasing by 44% with an axisymmetric reduction in radius to half the nominal value. The presence of these so-called 'tight true knots' is therefore of key importance, and currently has no diagnostic representation in the calculation of the UCI.

3.1 Steady boundary conditions

For steady flow, the boundary conditions are applied similarly to the validation study considered in section 2.5. These conditions have been outlined there and so are merely stated here for reference.

Γ_1 **(inlet)**: Poiseuille velocity profile: $W = 2 - 2r^2$.

Γ_2 **(vessel wall)**: No-slip : $u_i = 0$

Γ_3 **(outlet)**: Pseudo traction-free : $\left(-p\delta_{i,j} + \mu\frac{\partial u_i}{\partial x_j}\right) n_j = 0$

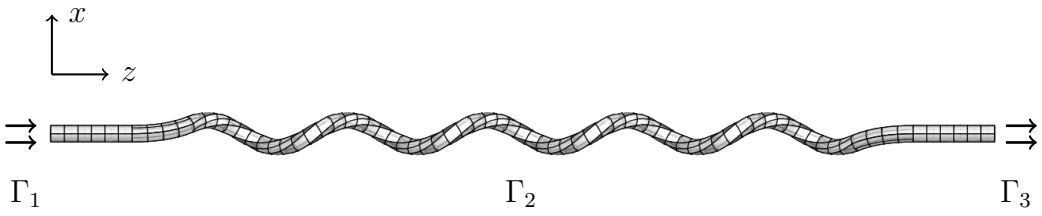

Figure 3.1: Boundary conditions for the steady analysis shown on a regularly coiled vessel.

3.2 Results

In this section the results of the steady numerical computations through the vessel geometries described in section 2.4 are presented. Unless stated, all computations are performed on meshes with 0.6 axial layers per unit arclength, following from the work of chapter 2. Two uniform refinements

are undertaken before an initial solve of the linear Stokes system at $Re = 0$. Numerical continuation with an increment of $Re = 20$ is then undertaken until the desired Re is achieved. For all studies this is the nominal flow Re of 100 except in the U_t analysis, where the flow is computed over $0 \leq Re < 250$. No minimum spatial error bound is set, however, the maximum error bound for spatial adaptation is chosen to be $e_{max} = 1.5 \times 10^{-3}$ with the maximum number of adaptations equal to 10. A cutaway view of the mesh for cord U_{t1} is included in figure 3.2 as it demonstrates the typical refinement pattern present in the regularly coiled vessels. Spatial mesh adaptation results in higher concentrations of elements at regions of high velocity gradient. In the regularly coiled vessels, the joins between the distinct geometries introduce curvature discontinuities and so automatic refinement tends to cluster at these locations. A further discussion of the numerical method as it relates to the steady calculations is included in appendix B with the implementation and convergence of the temporal solvers discussed in appendix B.1. The boundary conditions used are also analysed in appendix B.2.

3.2.1 Constant U_t study

The regularly coiled vessel geometries described in section 2.4.1, and shown on page 45, were chosen with identical U_t but varying R_h, P_h and N_c. Steady results are presented here for each model over a range of Re ($0 < Re < 250$) with the lower Re solutions obtained using `oomphlib`'s steady N-S solvers, and the higher Re solutions facilitated by temporal solves.

This study reveals that vessels of equal U_t can present significantly different flow patterns and pressure profiles over a range of Re, invalidating the theoretical UCI as a diagnostic indicator of umbilical blood vessel pressure. The total pressure drop is strongly affected by arclength, with a four-fold increase in the total pressure drop observed between the shortest and longest vessel geometries. The axial pressure gradient computed over the helical section of the cord is also highly influenced by the helix curvature; an issue investigated in chapter 5.

Pressure and velocity field

As discussed in chapter 1, the flow through a curved tube is complex, being dependent on both the geometry of the centreline curve as well as the flow Re. As the constant U_t cords comprise several distinct geometric sections, the flow varies significantly along the axial direction of the vessel. To illustrate this the streamwise development of the flow for case U_{t6} is summarised in figure 3.3. The development for the remaining cases is qualitatively similar and so is

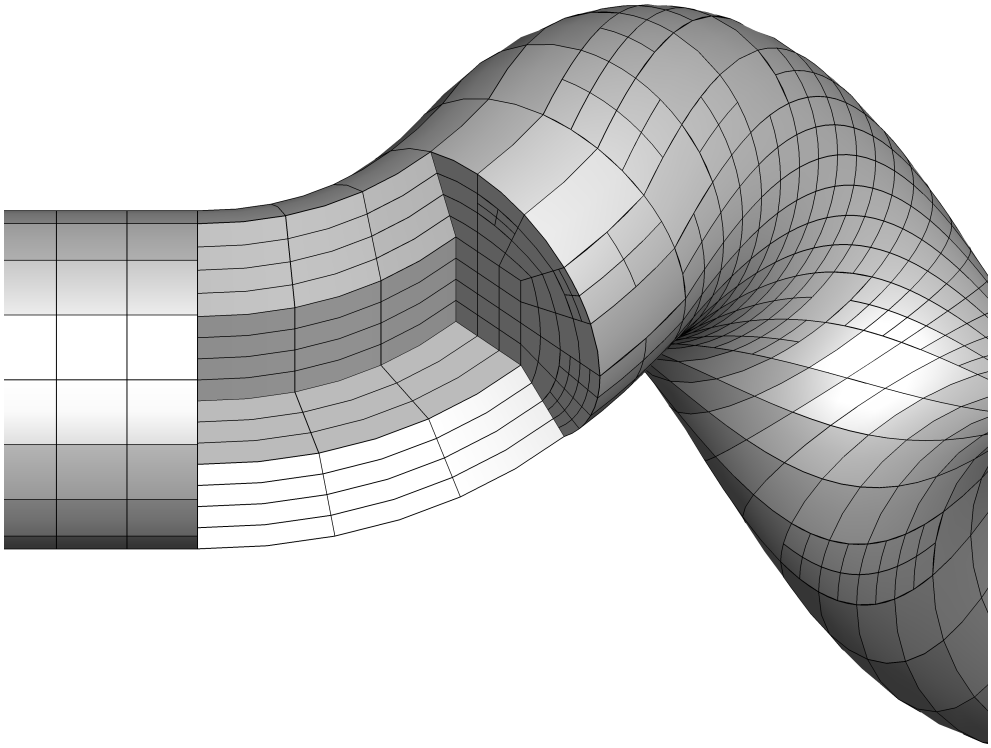

Figure 3.2: A cutaway view of the mesh refinement for cord U_{t1}. Spatial mesh adaptation results in a higher concentration of elements at the joins between distinct sections where the curvature is discontinuous and the velocity gradient is high.

not included here. For all cross-sectional contour plots shown henceforth, the helical axis is located to the right of the cross-section, unless otherwise specified. Poiseuille flow into the straight inlet remains un-perturbed until the join to the planar curved section (S-C) where there is a slight upstream effect, previously noted in the steady validation of chapter 2. Dean-type vortices characterised by two recirculating regions form over the length of the curved section, figure 3.3(a), however fully-developed curved pipe flow does not develop before the join to the helical section (C-H) due to the short length and varying vessel curvature. An entrance distance which depends on the curvature, torsion and flow Re precedes the onset of fully-developed helical flow and is typically several coils for the vessels considered in this study. This development is shown in figures 3.3(b) and (c). With the exception of U_{t1}, each geometry achieves a fully-developed flow in the helical section for the range of Re studied. For case U_{t1}, the entrance effect does not fully diminish at completion of the full 2.75 coils for $Re > 100$.

Figure 3.4 shows a comparison between the fully-developed flow in the helix for each of the six cases at the the nominal flow Re of 100. The secondary flow profile within a helical pipe is known to depend on the curvature and torsion of the centreline (Yamamoto et al., 2002). Kao (1987) performed numerical simulations of the full Navier-Stokes system on a number helical geometries for varying torsion, curvature and flow Dean number. It was observed that for small torsion two near-symmetric recirculating regions similar to the typical Dean flow solution within a curved pipe exist for helical flow. However, as the ratio of the torsion to curvature increases one of these recirculating regions becomes predominant so as to force the other into a small area within the cross-section. This effect is also present in the current work with case U_{t5}, figure 3.4(e), exhibiting a highly symmetric profile ($\tau/\kappa = 0.4$) while case U_{t4}, figure 3.4(d), has one dominant vortex ($\tau/\kappa = 2$). The effect of Re on the flow profile is also demonstrated for case U_{t6} in figure 3.5. For low Re the flow is asymmetric, with a slightly dominant vortex present. This asymmetry increases with Re and at $Re = 240$ the dominant vortex occupies a much larger fraction of the cross-section, with the core of the less-dominant circulation ill-defined.

The key diagnostic parameter, the vessel pressure drop, is determined using an area-weighted averaging through each cross-section. The average vessel pressure at a given arclength, $P(Z)$, is measured relative to the zero-pressure outlet with $P(L_Z) = 0$. The total vessel pressure drop (ΔP) is then simply the cross-sectional average at the inlet, $P(0)$. Figure 3.6(a) catalogues ΔP for each of the vessels. Crucially, a high spread is apparent amongst the cords which each have identical U_t. One might expect the total pressure drop to increase with total vessel length, however, there are exceptions. The

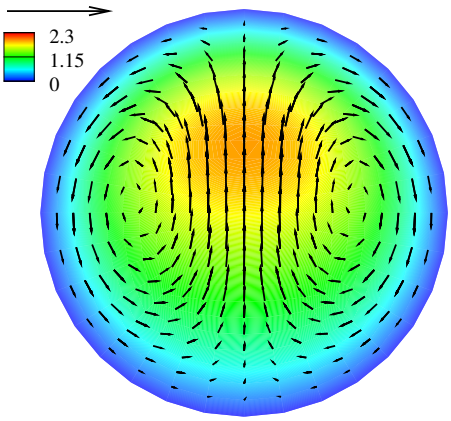

(a) $Z = 15.5$ ($5.5R$ downstream of S-C)

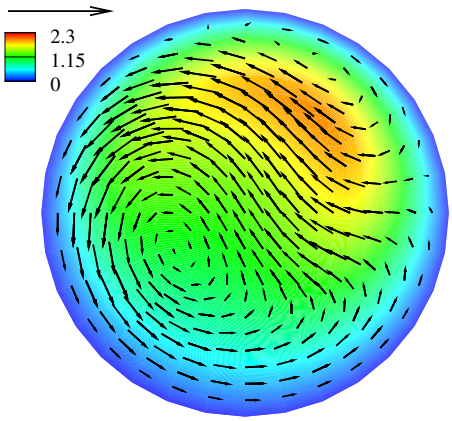

(b) $Z = 19.36$ ($2R$ downstream of C-H)

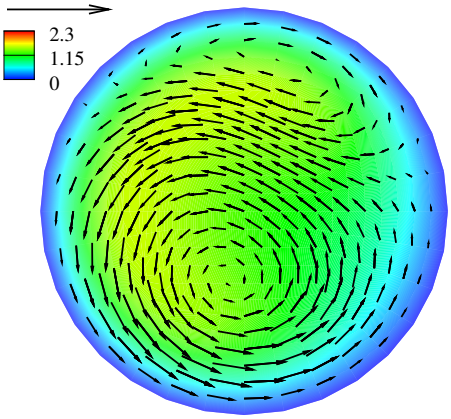

(c) $Z = 170$ (Fully developed helical flow)

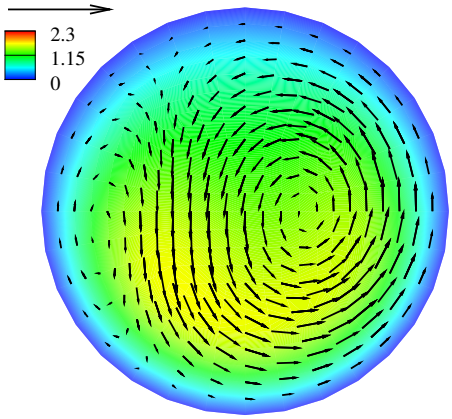

(d) $Z = 239$ ($6.3R$ downstream of H-C)

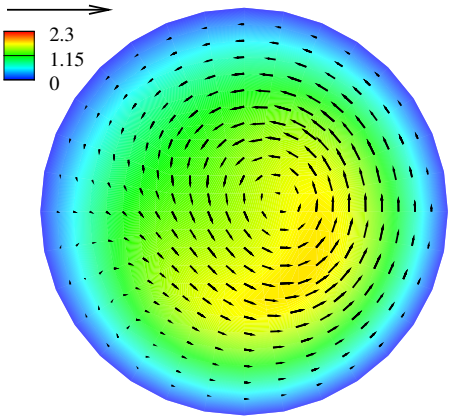

(e) $Z = 245$ ($5R$ downstream of C-S)

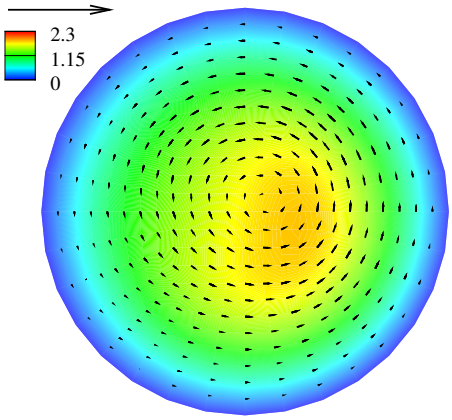

(f) $Z = 250$ (Outlet)

Figure 3.3: Evolution of the steady velocity field with arclength for vessel U_{t6}. The contours are of velocity magnitude with overlayed vector-field representative of the in-plane secondary flow at $Re = 100$. The reference vector is of unit magnitude. S-C: straight to curved join; C-H: curved to helical; H-C: helical to curved; and C-S: curved to straight. The helical axis is located to the right of the cross-section.

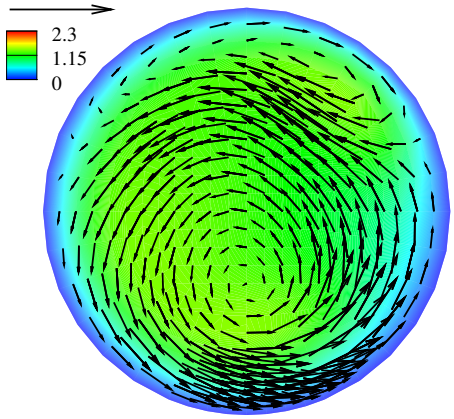

(a) U_{t1}

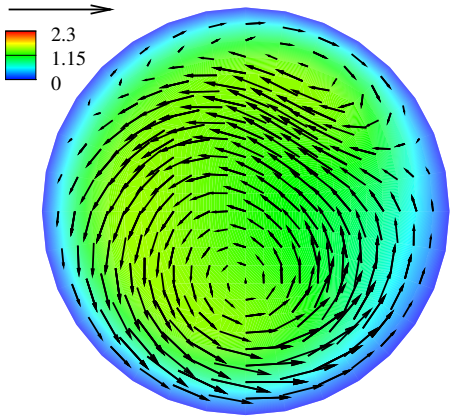

(b) U_{t2}

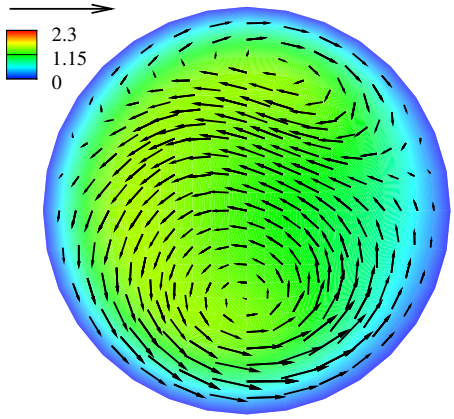

(c) U_{t3}

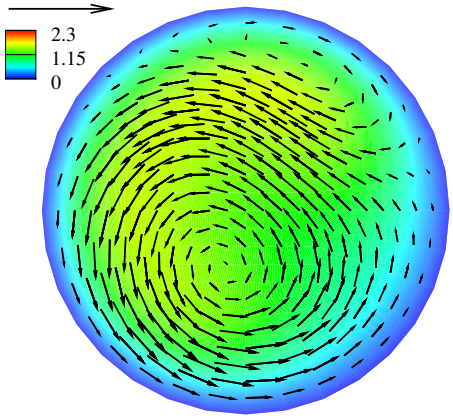

(d) U_{t4}

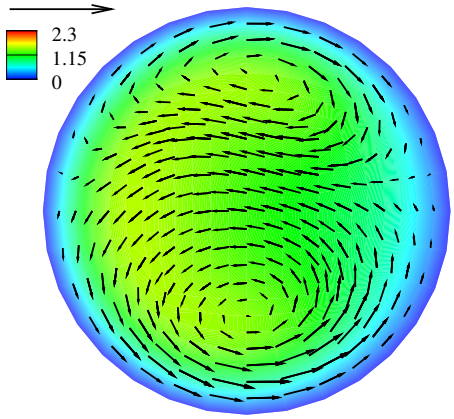

(e) U_{t5}

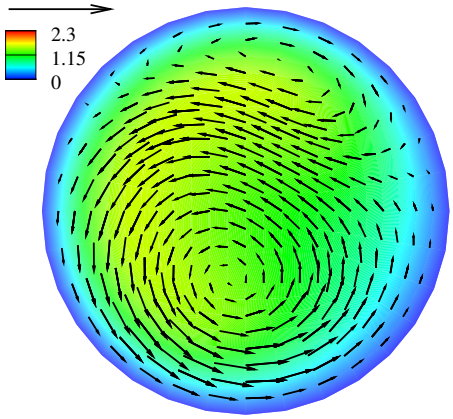

(f) U_{t6}

Figure 3.4: Fully developed helical flow at $Re = 100$ for each of the U_t vessels.

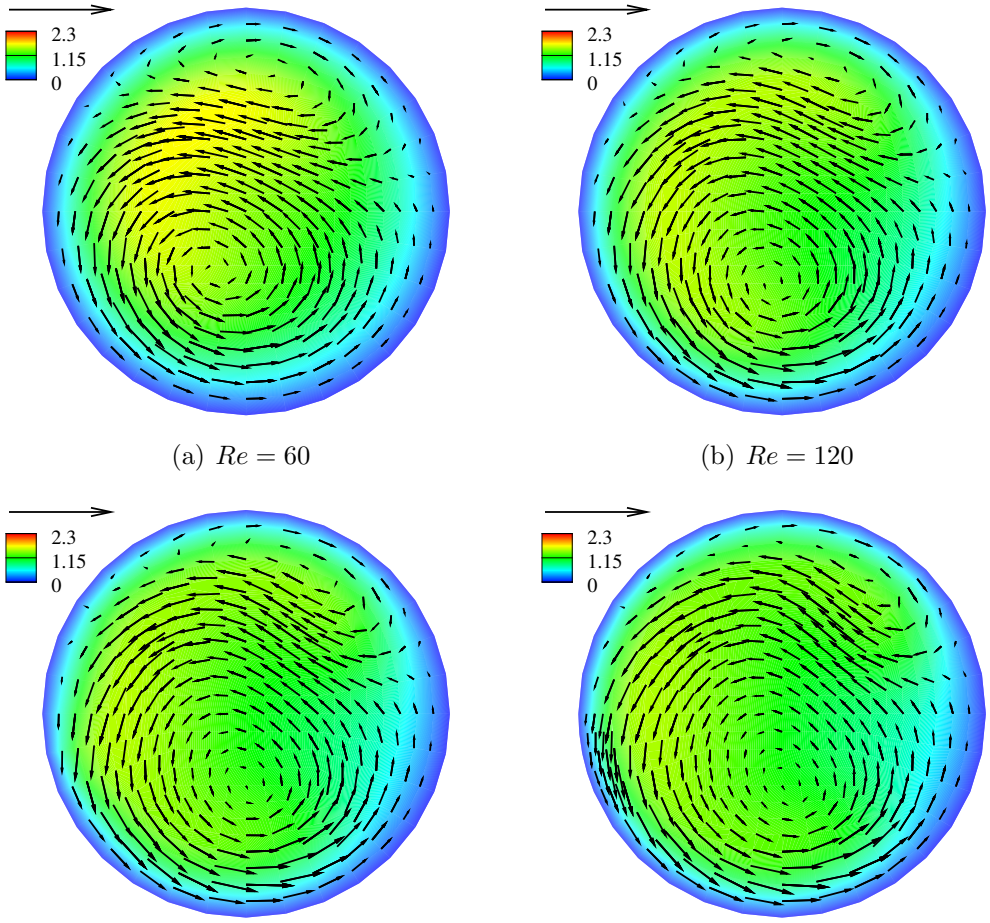

(a) $Re = 60$ (b) $Re = 120$

(c) $Re = 180$ (d) $Re = 240$

Figure 3.5: Fully developed helical flow for vessel U_{t6} for a range of Re.

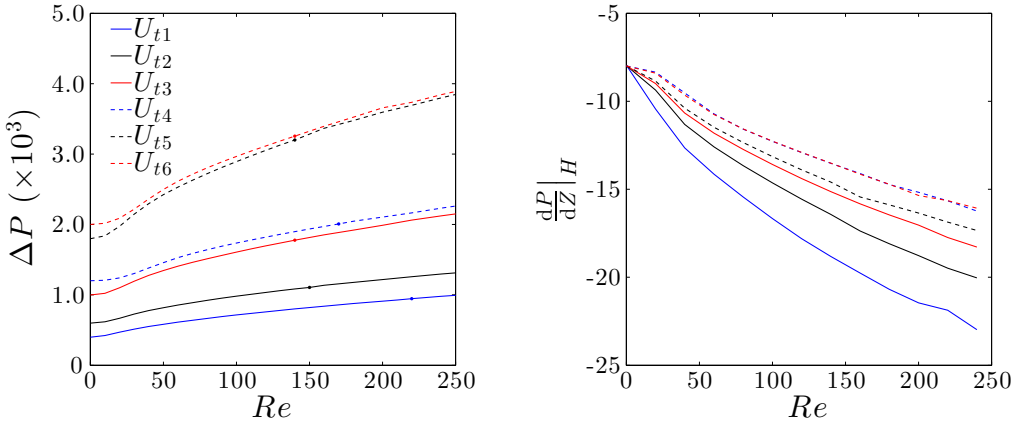

Figure 3.6: Pressure variation with Re for the U_t geometries. a) The total vessel pressure drop with Re for each of the U_t geometries. The solid dots indicate the Re at which the steady solvers failed; b) The helical pressure gradient for each vessel as a function of Re.

pressure drop in cases U_{t5} and U_{t6} are quite similar despite the greater length of U_{t6} (table 2.2, page 45). The curvature, which greatly affects the flow resistance of a curved pipe, is larger in case U_{t5}, accounting for the length discrepancy. This aspect is further discussed in chapter 5.

Removing length effects the steady helical pressure gradient is plotted against Re in figure 3.6(b). This gradient is computed at roughly two-thirds of the length of the helical section of each vessel, where entrance effects have reduced. The $Re = 0$ gradient matches in all cases with the straight pipe solution ($dP/dZ = -8$), with a decreasing gradient due to increased Re. This mechanism of course leads to a larger pressure drop with increasing Re, a fact expressed in figure 3.6(a). The geometries are now ordered in terms of curvature, with vessels of low κ exhibiting less severe pressure gradients. Cases U_{t4} and U_{t6} have almost identical trajectories which, again, is discussed in chapter 5.

Figures 3.7(a)-(f) show the dimensional pressure variation within either the artery or vein with blood viscosity ($\hat{\mu}$) blood flow-rate ($\hat{Q}$) and vessel radius ($\hat{R}$). The pressure drop is seen to increase in each geometry with an increase in either viscosity or flow-rate, with marked differences between the vessels at the nominal parameter value indicated by the dashed black lines. Case U_{t1} produces roughly one quarter of the pressure drop of vessel U_{t6} at $Re = 100$, which equates to a 6.5 mmHg difference in the arteries and 2.4 mmHg in the vein. For reference, Gordon et al. (2007) quote the mean arterial

pressure as between 20 and 80 mmHg so this discrepancy can be on the order of 25% of the total pressure drop. The trend widens with increasing flow-rate and a doubling of $\hat{Q}$ produces differences of 23.8 mmHg in the arteries and 7.8 mmHg in the vein. The trend is reversed for the vessel radius where increasing vein or artery area at constant flow-rate and viscosity reduces the pressure drop. For example, a 50% reduction in the nominal artery cross-sectional area causes the pressure to increase by a factor of 3.15 from 8.56 mmHg, while a 50% increase in area reduces the necessary pressure drop to 33% of the nominal value.

The results depicted in figure 3.6(a) and re-iterated in figure 3.7 quite clearly indicate the large pressure variation that is possible among cords which have nominally identical U_t. There is also significant variability in the flow patterns present and hence it is obvious that the theoretical UCI, U_t, does not provide insight into the pressure or dynamics of umbilical flow. The clinical UCI, U_c, is also unable to predict the pressure variation among these models, with no discernible relation between the computed ΔP and U_c (listed in table 2.2). This study only considers a small selection of geometries and a more general discussion based on empirical pressure estimates is contained within chapter 5.

3.2.2 Constant U_c study

The regularly coiled vessel geometries described in section 2.4.1, and shown on page 47, have identical P_h, N_h and hence U_c but varying R_h. Steady solutions are computed for each model for $0 \leq \mathrm{Re} \leq 100$, with the pressure profile shown in figure 3.8(a). As in the constant U_t study, increases in total pressure drop are predominantly due to increases in the total vessel arclength; at $Re = 100$, case U_{c7} requires roughly 5.5 times the pressure drop present in U_{c1} at the same blood viscosity and flow-rate. The helical pressure gradient at $Re = 100$ also varies significantly with R_h. Figure 3.8(b) shows a large drop in pressure gradient accompanying a small increase in helical radius for which additional geometries (shown as open black circles) were computed in order to more clearly elucidate the nature of the curve in this region. For $R_h < 1.512$ the torsion of the helix reduces with R_h while the curvature increases (see figure 2.8(b) on page 49). The most severe pressure gradient, however, occurs for $0.5 < R_h < 1.0$. Examining figures 3.9(a) and (b), the low R_h vessels have high torsion and low curvature resulting in one predominant recirculation zone with high inclination to the pipe normal axis. As R_h increases the second much weaker recirculation zone intensifies toward the top-right of the cross-section. This is first noted in an additional computation at $R_h = 1.0$ (U_{cN4}) shown in figure 3.9(c). The change of the

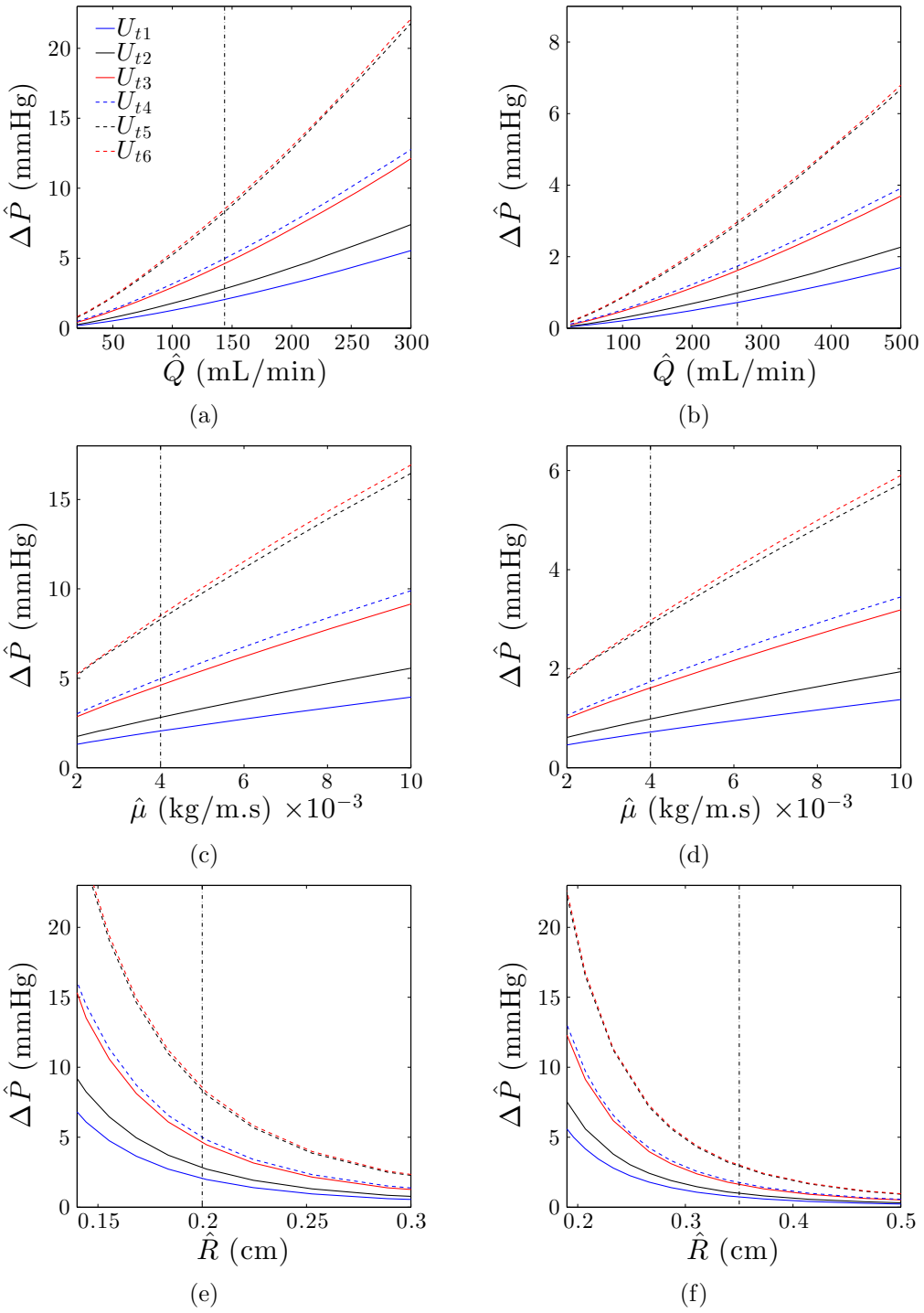

Figure 3.7: Variation of the dimensional pressure drop ($\hat{\Delta}P$) with the blood flow-rate ($\hat{Q}$, top), blood viscosity ($\hat{\mu}$, middle) and vessel radius ($\hat{R}$, bottom) for the arterial (left) and venous flow (right) for the U_t vessels. In each plot the remaining two properties are kept constant as per table 2.1 on page 36 with the blood density set at $\rho = 1060$ kg/m^3. The dashed vertical line indicates the nominal value.

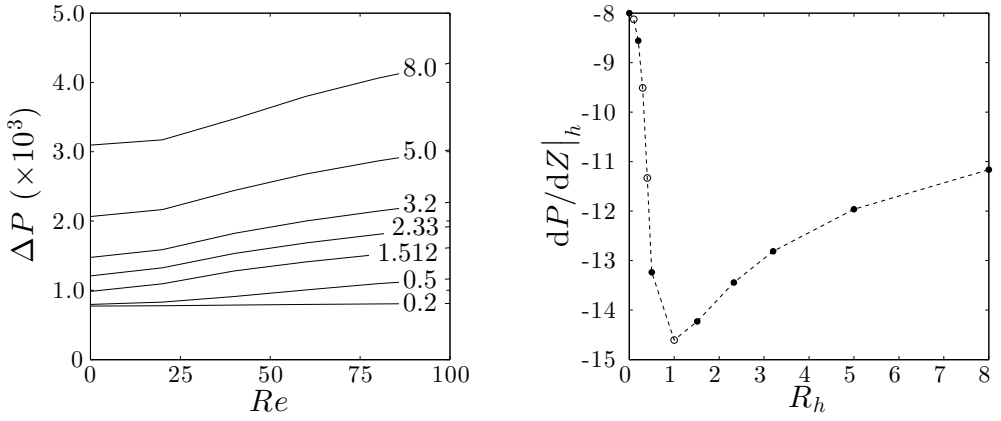

(a) (b)

Figure 3.8: Steady pressure results for the constant U_c study. a) The total vessel pressure drop for each of the cords with helical radius, R_h, annotated; b) The helical pressure gradient for each vessel plotted against R_h at $Re = 100$. The open circles are additional geometries computed over the large gradient as $R_h \to 0$.

flow from a one-vortex type solution to two vortices accompanies a reduced pressure gradient and marks the local minimum in figure 3.8(b). As R_h increases from 1.0 (U_{cN4}) to 1.512 (U_{c3}) the curvature increases however the torsion reduces and the circulation associated with the second upper vortex increases in magnitude. As R_h increases further the second recirculating region occupies a larger area of the upper half of the vessel geometry and the core flow aligns itself with the normal axis of the helical centreline. The flow will approach the asymptotic state of simple curved pipe flow with two symmetric Dean vortices for large R_h. Figure 3.9(f) shows the largest R_h computation considered in this study where the flow has reached a fairly symmetric state.

As for U_t, the clinical UCI is unable to differentiate cords with significantly varied total pressure drop. The simple process of increasing the coil width has a complicated effect on the curvature and torsion of the vessel centreline, however the vessel arclength and total pressure monotonically increase. While cords U_{c6} and U_{c7} represent extreme cases, the pressure drop varies substantially despite restricting the analysis to the physiologically realistic cords. Using equation (2.22) venous geometries U_{c2} and U_{c5} have coil widths of 1.0 and 2.9 cm, respectively, with cord U_{c5} recording a total pressure drop 40% greater. The clinical UCI in this case would report both cords as pathologically equivalent despite the significantly increased flow resistance.

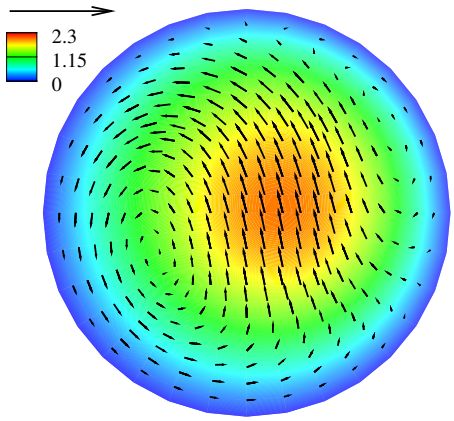

(a) U_{c1} ($R_h = 0.2$)

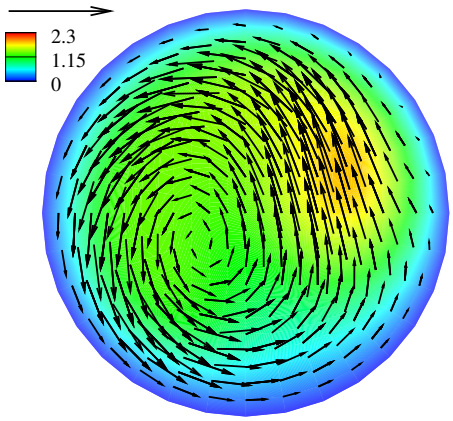

(b) U_{c2} ($R_h = 0.5$)

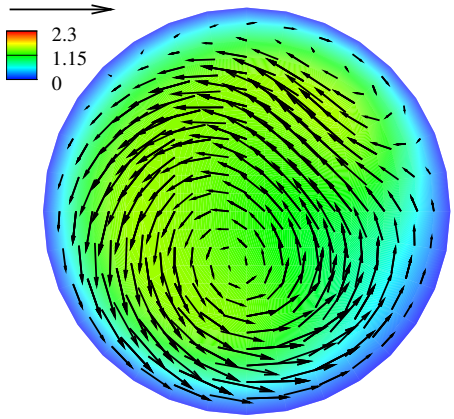

(c) U_{cN4} ($R_h = 1.0$)

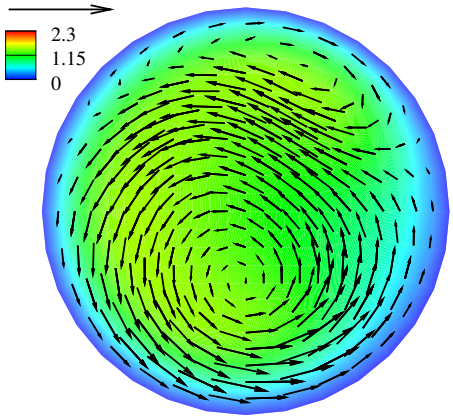

(d) U_{c3} ($R_h = 1.512$)

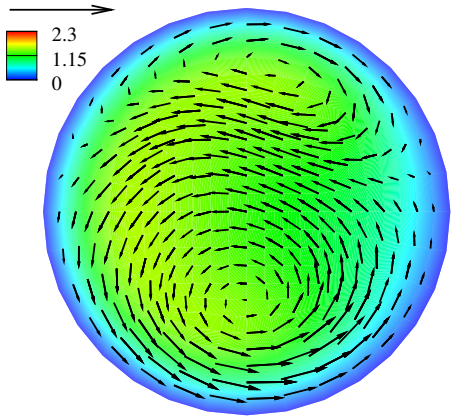

(e) U_{c4} ($R_h = 2.33$)

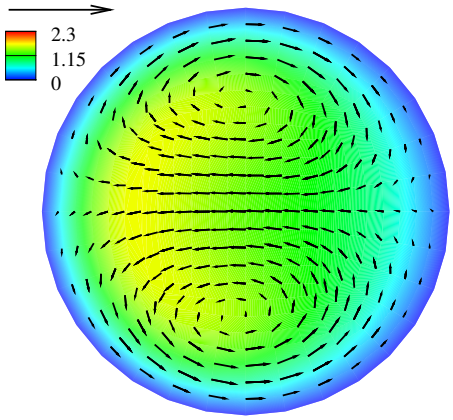

(f) U_{c7} ($R_h = 8.0$)

Figure 3.9: Contour plots of the axial velocity, W, with the secondary velocity field overlayed in helically symmetric flow for vessel geometries with identical clinical UCI, U_c. Vessels U_{c5}, U_{c6} are not included as they have similar form to U_{c7}.

3.2.3 Irregularly coiled cords

Steady solutions computed at $Re = 100$ for the irregularly coiled vessels described in section 2.4.2 are presented here. It is found that variations in the coil spacing, cord width or combinations of the two for the nominally coiled cord ($\hat{U}_c = 0.2$ coils/cm, $\hat{w} = 1.6$ cm) have little effect on the total vessel pressure drop. However, axial pressure gradients and velocity contours over the cord length can vary significantly. Flow through these geometries is subject to the same steady boundary conditions as in the regularly coiled study, however here the pseudo traction-free condition has a slightly less intuitive interpretation as the models lack a straight outlet. The entrance effects are also larger as the straight pipe solution is enforced on a coiled tube. Results with these effects are presented initially. Three of the distinct geometry types; varying coil width, spacing and a combination of the two, are then computed with additional helical sections appended at the inlet and outlet in order to reduce the entrance and exit effects. A discussion of the flow profile is postponed until this study.

Variable coil spacing

The steady results for the vessels shown in figure 2.10 on page 52 are detailed in table 3.1 with plots of the total pressure drop and pressure gradient in figure 3.10. This analysis shows that a 9-fold increase in the local UCI over the cord length at an average cord UCI of 0.2 coils/cm produces only a 2.1% increase in the venous pressure drop. The pressure gradient at the entrance is less severe but compensated by a greater (negative) gradient toward the exit, where the curvature is larger. As the pitch variation increases there is an attendant increase to both the total vessel length and the pressure, however, the relative increase to the length is greatest. For the nominal vein, $\mathcal{N}_v$, which exhibits the largest entrance curvature, the total venous pressure drop based on the downstream fully-developed helical pressure gradient and the vessel length is 0.35% above the value numerically computed with boundary effects. This suggests that the inlet effects are of minimal concern within the context of the broader pressure study, however, may account for a reasonable portion of the discrepancy between vessels in this study, as the total difference is within only 2.1%. A steep negative pressure gradient is also observed at the outlet where the pseudo traction-free condition is imposed. This effect is quite localised and is discussed in the re-computation of the $\mathcal{S}_{v,3}$ geometry with reduced entrance/exit effects.

	χ_S	$\hat{S}_p$ ($\hat{U}_c$)	$\hat{S}_u$ ($\hat{U}_c$)	L	ΔP	δ_P (%)	$\Delta P/L$
$\mathcal{N}_v$	0.0	5.0 (0.20)	5.0 (0.20)	164.12	2074.78	-	12.64
$\mathcal{S}_{v,1}$	0.4	6.0 (0.17)	4.0 (0.25)	164.37	2074.73	-0.002	12.62
$\mathcal{S}_{v,2}$	0.8	7.0 (0.14)	3.0 (0.33)	165.17	2081.39	0.32	12.60
$\mathcal{S}_{v,3}$	1.2	8.0 (0.13)	2.0 (0.50)	166.69	2095.72	1.01	12.57
$\mathcal{S}_{v,4}$	1.6	9.0 (0.11)	1.0 (1.00)	169.24	2117.98	2.08	12.52

Table 3.1: Steady numerical results for the irregularly coiled veins with variable coil spacing. $\hat{S}_p$ is the dimensional coil separation ($1/UCI$) at the placental end, while $\hat{S}_u$ is the equivalent value at the umbilical insertion. δ_P is the relative change in the pressure drop compared with the nominal case, $\mathcal{N}_v$. The vessel identifiers are as listed in figure 2.10.

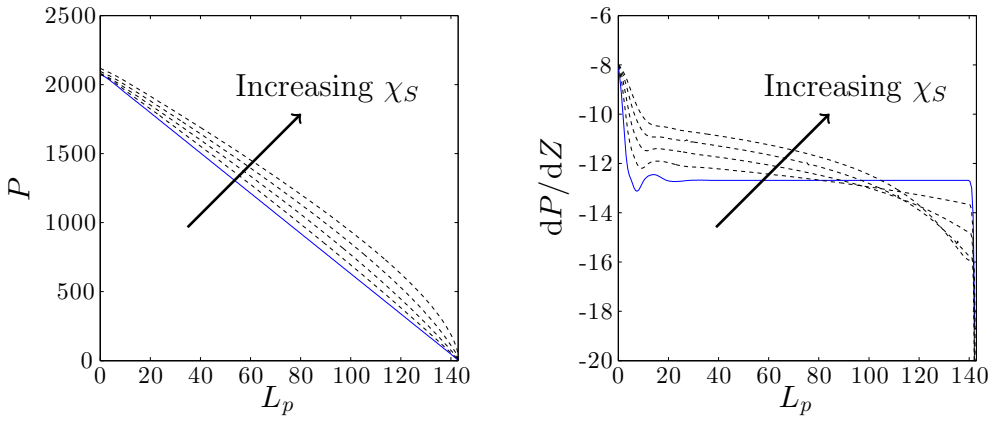

Figure 3.10: Pressure variation for each of the variable pitch veins studied, with boundary effects present. The blue line represents the nominal vein, $\mathcal{N}_v$.

	χ_w	$\hat{w}_p$	$\hat{w}_u$	L	ΔP	δ_P (%)	$\Delta P/L$
$\mathcal{N}_v$	0.0	1.60	1.60	164.12	2074.78	-	12.64
$\mathcal{W}_{v,1}$	0.2	1.44	1.76	164.28	2073.23	-0.07	12.62
$\mathcal{W}_{v,2}$	0.4	1.28	1.92	164.75	2069.89	-0.24	12.56
$\mathcal{W}_{v,3}$	0.6	1.12	2.08	165.55	2062.14	-0.61	12.46
$\mathcal{W}_{v,4}$	1.0	0.80	2.40	168.12	2010.50	-3.10	11.96

Table 3.2: Steady numerical results for the irregularly coiled veins with variable coil width. The dimensional coil width at the placental end is denoted $\hat{w}_p$, while $\hat{w}_u$ is the equivalent value at the umbilical insertion. The relative change in the pressure drop compared with the nominal case, $\mathcal{N}_v$, is δ_P. The vessel identifiers are as listed in figure 2.11.

Variable coil width

Steady results for the vessels shown in figure 2.11 on page 53 are detailed in table 3.2 with plots of the total pressure drop and pressure gradient in figure 3.11. As for the variable coil spacing study, changes to the coil width at constant UCI bare only small influence on the total pressure drop. Increasing width variation causes the pressure drop to decrease, despite an associated increase in vessel length, as there is a lower mean curvature over the length of the cord, see figure 2.13(c). This fact is also true of the variable P_h cords, however here the curvature variation is more severe with a significantly higher value at the outlet tending to increase the magnitude of the pressure gradient there. The results are highly affected by the inlet for $\mathcal{W}_{v,4}$ with the greatest variation occurring here and only moderate variations down-stream. In this case the curvature reaches a peak at approximately $L_p = 133$ and then reduces until the outlet. This effect is seen as a slight increase in the pressure gradient toward the outlet. From table 3.2, a 3.1% reduction in the pressure is observed for a 100% relative variation in the coil width over the length, however, inlet effects appear to dominate the results with little variation in the pressure gradients downstream. Case $\mathcal{W}_{v,4}$ is recomputed with reduced entrance/exit effects.

Variable coil spacing and width

To consider both helical pitch and radius variation, the third geometries of the independent studies ($\mathcal{W}_{v,3}$ and $\mathcal{S}_{v,3}$) were chosen as a basis. The effect

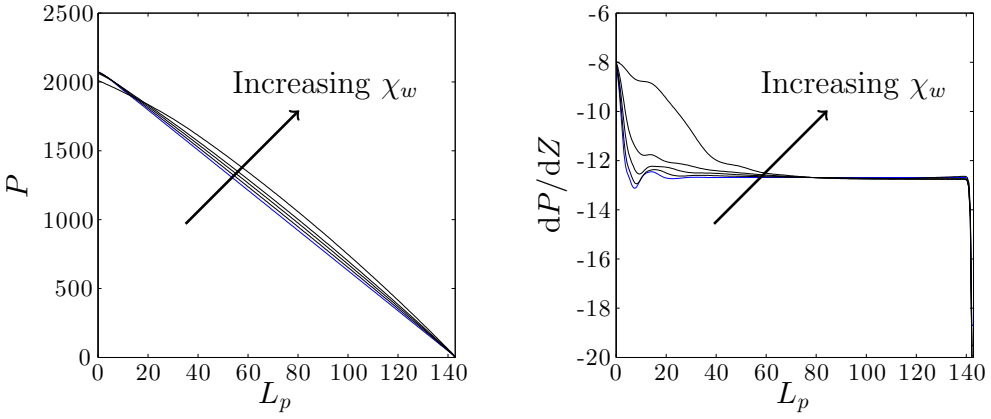

Figure 3.11: Pressure variation for each of the variable width veins studied, with boundary effects present. The blue line represents the nominal vein, $\mathcal{N}_v$.

of compounding these two non-uniformities does not appreciably affect the total pressure drop, though as before, does alter the downstream gradients. Considering firstly $\mathcal{S}_{v,3}$, the addition of 60% width variation tends to reduce the pressure drop regardless of the relative direction of this variation, see table 3.3. This effect, however, is larger in vessel $\mathcal{C}_{v,1}$ for which $\chi_w = +0.6$ (i.e. the width is a *maximum* where the spacing is a *minimum*). From figure 3.12, the reverse case, $\mathcal{C}_{v,2}$, has a lower vessel length but the pressure gradient is more severe at all points along the cord length. The curvature is also larger over most of the cord length for $\mathcal{C}_{v,2}$, except for a small region between $L_p = 98$ and 134. The differences, however, are virtually negligible at approximately 1% from the nominal vessel.

Arterial flow

The effect of varying width and pitch is examined in four arterial geometries for comparison with the pulsatile simulations in chapter 4. The flow direction in this case is in the opposite sense in keeping with the trend that coiling is typically higher at the umbilicus, the arterial inlet. The sensitivity to the flow-direction is assessed by computing flow through the combined arterial geometries in the reverse, or venous, direction. There is less than 0.5% difference in each case, with a higher pressure drop in the arterial direction. The pressure profiles are compared in figure 3.13. The arterial vessel pressure gradients follow roughly the opposite path to those present in the vein, see figure 3.14. From table 3.4 the total variation in pressure drop is within

	χ_S	χ_w	$\hat{S}_p$	$\hat{S}_u$	$\hat{w}_p$	$\hat{w}_u$	L	ΔP	δ_P (%)	$\Delta P/L$
$\mathcal{N}_v$	0.0	0.0	5.0	5.0	1.60	1.60	164.12	2074.78	-	12.64
$\mathcal{W}_{v,3}$	0.0	0.6	5.0	5.0	1.12	2.08	165.55	2062.14	-0.61	12.46
$\mathcal{S}_{v,3}$	1.2	0.0	8.0	2.0	1.60	1.60	166.70	2095.72	1.01	12.57
$\mathcal{C}_{v,1}$	1.2	0.6	8.0	2.0	1.12	2.08	171.60	2079.20	0.21	12.12
$\mathcal{C}_{v,2}$	1.2	-0.6	8.0	2.0	2.08	1.12	164.24	2093.55	0.91	12.75

Table 3.3: Steady numerical results for the irregularly coiled veins with variable coil width and spacing. The subscript p refers to values at the placental end, while u is the equivalent value at the umbilical insertion. The relative change in the pressure drop compared with the nominal case, $\mathcal{N}_v$, is denoted δ_P. The vessel identifiers are as listed in figure 2.12.

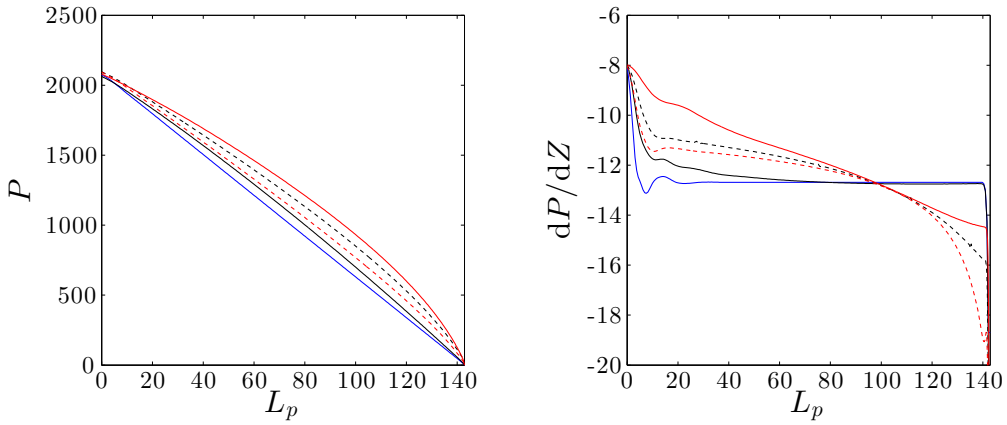

Figure 3.12: Steady pressure variation for each of the combined veins studied. $\mathcal{W}_{v,3}$ (solid black), $\mathcal{S}_{v,3}$ (dashed-black), $\mathcal{C}_{v,1}$ (solid-red), $\mathcal{C}_{v,2}$ (dashed-red) and $\mathcal{N}_v$ (blue).

	χ_S	χ_w	$\hat{S}_p$	$\hat{S}_u$	$\hat{w}_p$	$\hat{w}_u$	L	ΔP	δ_P (%)	$\Delta P/L$
$\mathcal{N}_a$	0.0	0.0	5.0	5.0	1.6	1.6	313.10	3532.47	-	11.28
$\mathcal{W}_{a,3}$	0.0	0.6	5.0	5.0	1.12	2.08	315.05	3541.13	0.245	11.24
$\mathcal{S}_{a,3}$	1.2	0.0	8.0	2.0	1.6	1.6	318.96	3578.30	1.297	11.22
$\mathcal{C}_{a,1}$	1.2	0.6	8.0	2.0	1.12	2.08	326.85	3621.40	2.518	11.08
$\mathcal{C}_{a,2}$	1.2	-0.6	8.0	2.0	2.08	1.12	314.18	3546.53	0.398	11.29

Table 3.4: Steady numerical results for the irregularly coiled arteries. The subscript p refers to values at the placental end, while u is the equivalent value at the umbilical insertion. The relative change in the pressure drop compared with the nominal case, $\mathcal{N}_a$, is denoted δ_P.

2.5% for all arteries, with the highest pressure found in the $\chi_w = +0.6$ ($\mathcal{C}_{a,1}$) vessel. The variable width artery, $\mathcal{W}_{a,3}$, requires a larger pressure drop than the nominal artery, $\mathcal{N}_a$, while it is lower in the vein. This effect is quite low, and is within the uncertainty provided by the entrance/exit effects.

Boundary conditions

Boundary effects associated with enforcing conditions on a coiled section, as opposed to a straight inlet/outlet have a very small effect on the total computed pressure. This, however, is not negligible compared to the variation among the individual models considered. To investigate boundary effects more closely additional helical sections are added at the inlet and outlet of three models, namely $\mathcal{W}_{v,3}$, $\mathcal{S}_{v,3}$ and $\mathcal{C}_{v,1}$. This allows the formation (and resumption) of fully developed helical flow before the variable curvature/torsion section, and hence minimises entrance and exit effects. Despite the added sections there are localised effects due to discontinuities in the derivatives of the curvature and torsion at the joins, though the error is negligible. The pressure profile over the cord length for the three recomputed geometries is shown in figure 3.15(a), while the recomputed pressure gradient is compared with the previous estimates in figure 3.15(b). The entrance effects typically last one third of the vessel length. For $\mathcal{S}_{v,3}$ these effects increase the pressure by 0.56%, while the total pressure drop is reduced by 0.42% for $\mathcal{W}_{v,3}$. $\mathcal{C}_{v,1}$ records a similar sensitivity with a 0.41% increase in pressure drop with entrance effects. This compares with the previous reduction of 0.35% in $\mathcal{N}_v$. These errors however small, do affect the results presented in table 3.3 in section 3.2.3. Without entrance effects $\mathcal{C}_{v,1}$ now records the lowest total

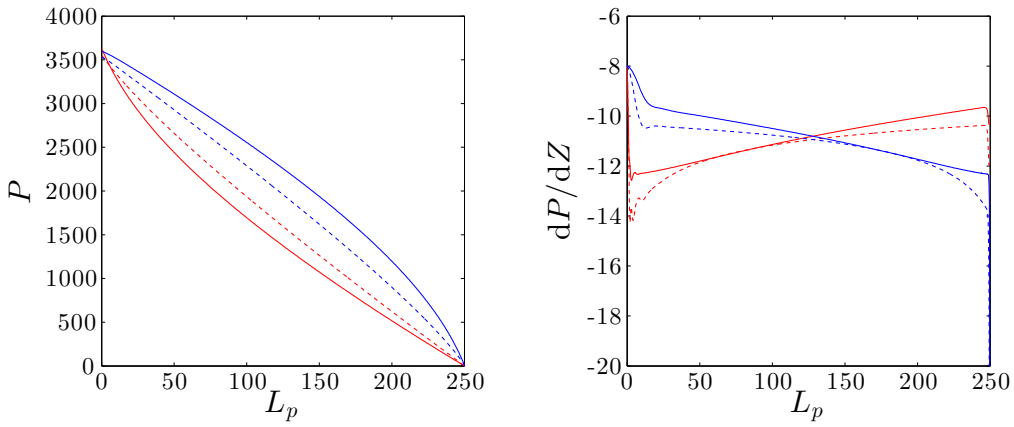

Figure 3.13: Comparison of the flow direction effect on the irregularly coiled arteries. In each case, L_p is the pitch length from the inlet. In the arterial direction; $\mathcal{C}_{a,1}$ (solid-red), $\mathcal{C}_{a,2}$ (dashed-red) and in the venous direction; $\mathcal{C}_{a,1}$ (solid-blue), $\mathcal{C}_{a,2}$ (dashed-blue).

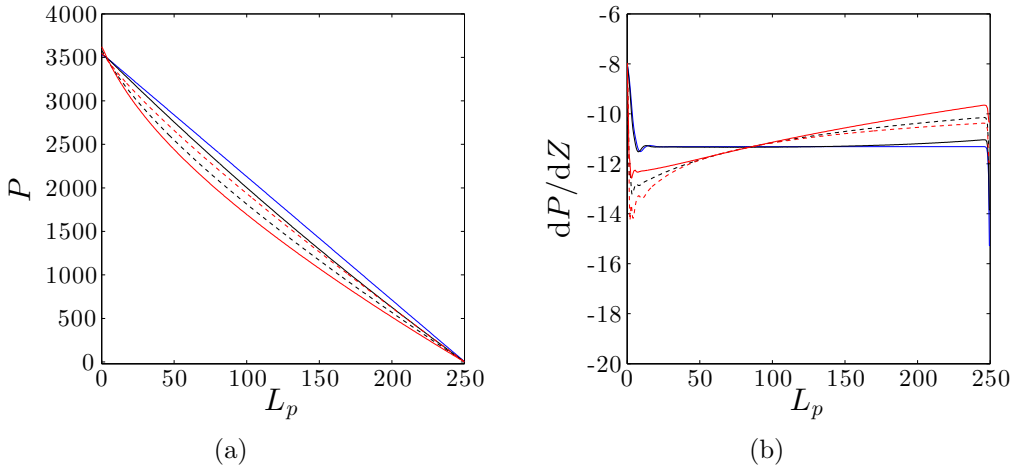

Figure 3.14: Steady pressure variation for each of the irregularly coiled arteries studied. $\mathcal{W}_{a,3}$ (solid black), $\mathcal{S}_{a,3}$ (dashed-black), $\mathcal{C}_{a,1}$ (solid-red), $\mathcal{C}_{a,2}$ (dashed-red) and $\mathcal{N}_a$ (blue).

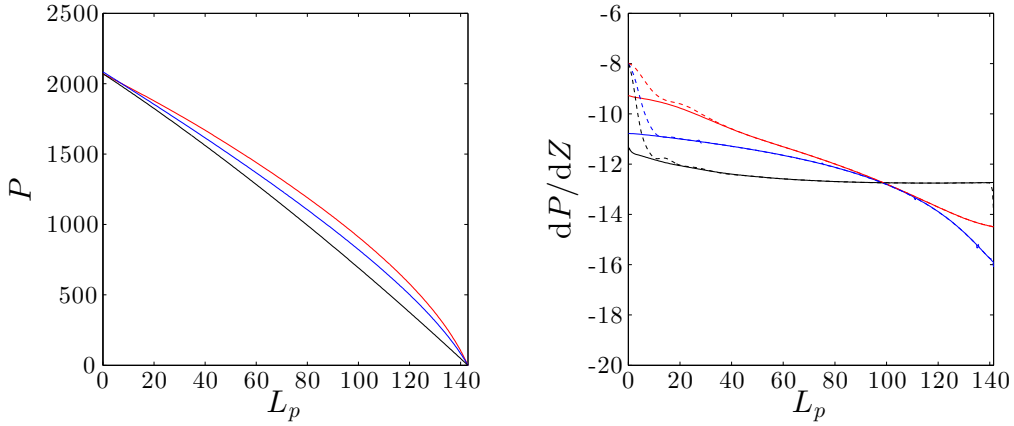

Figure 3.15: Recomputed flow for three irregularly coiled venous geometries with boundary effects minimised; $\mathcal{W}_{v,3}$ (black), $\mathcal{S}_{v,3}$ (blue) and $\mathcal{C}_{v,1}$ (red). The dashed lines indicate the profile with entrance/exit effects from the previous study. a) The pressure variation with arclength, and; b) the pressure gradient variation with arclength.

pressure drop with $\mathcal{S}_{v,3}$ the highest. Previously $\mathcal{W}_{v,3}$ had recorded the lowest pressure. The three recomputed total pressure drops are all within 0.6% of each other, confirming that variation of the width and UCI over the cord length has a very small effect on the pressure drop when the mean values are held constant.

Figures 3.16 to 3.19 show the evolution of the velocity profile over the cord length for the geometries considered. The nominal vein, figure 3.16(a), is composed of a dominant vortex with an axial velocity maxima located around the outside of the vortex centre. The corresponding artery, figure 3.16(b), with its reduced curvature and torsion, displays a secondary flow closer to the symmetric dean vortex solution of a planar curved pipe. The cords with non-uniform coiling exhibit a qualitatively similar flow-profile to each other. In each case the flow at the inlet to the cord has one dominant vortex, becoming more symmetric along the tube length. For the cord exhibiting variable coil spacing, figure 3.17, the secondary flow structure does not vary significantly along the pipe, however, there is an increase in the magnitude observed toward the umbilicus and the axial velocity profile exhibits a corresponding flattening. The dominant vortex at the inlet for the variable coil width cord ($\mathcal{W}_{v,3}$), figure 3.18, is more pronounced, while the combined cord, figure 3.19, has a lower circulation but higher streamwise maximum velocity located closer to the vessel centre.

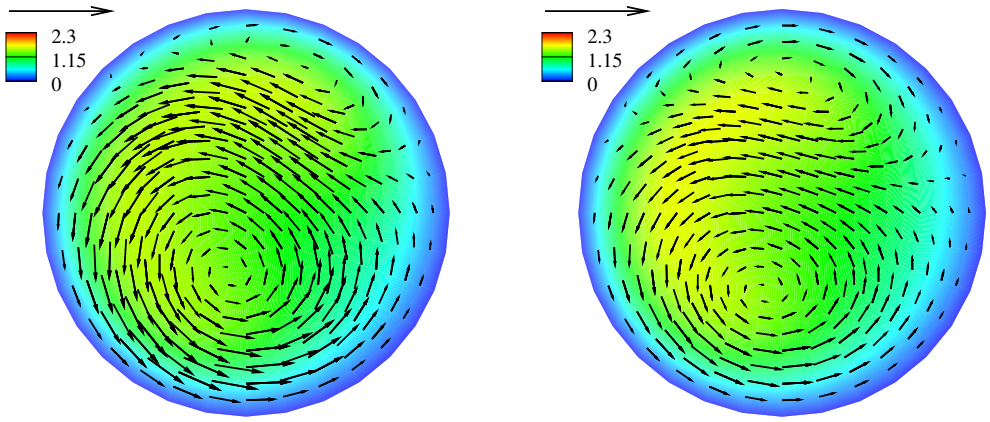

(a) Vein, $\mathcal{N}_v$ ($\kappa = 0.19$, $\tau = 0.33$) (b) Artery, $\mathcal{N}_a$ ($\kappa = 0.12$, $\tau = 0.16$)

Figure 3.16: Fully developed velocity field in the helical geometries ($\chi_S = 0, \chi_w = 0$) within the nominal cord, $\mathcal{N}$, with $N = 10$, $\hat{U}_c = 0.2$ coils/cm and $\hat{w} = 1.6$ cm.

In conclusion, irregularity in the coiling of a cord has little effect on the total pressure drop. Cords of average coiling are typically representative of those with significantly varying pitch and radius in terms of the total computed pressure drop, however, velocity and axial pressure gradients over the cord length within these geometries can vary significantly. For cords with variable coil spacing, a 9-fold increase in the local UCI over the length of the cord produces a 2.1% increase in venous pressure drop. Similarly, a cord with coil width varying by 100% along its length records only a 3% difference in pressure compared with the nominal cord of average coiling. The sensitivity of the pressure drop to both flow-direction and boundary conditions is approximately 0.5%, while combining both coil width and spacing variability produced similar fluctuations as in the individual analyses.

3.2.4 Umbilical knots

Steady solutions computed at $Re = 100$ for the knotted vessels described in section 2.4.3 are presented here. It is found that geometric and false knots as well as twist reversal each provide little effect on the total pressure drop through an affected region compared with a purely helical geometry, however vessel constriction can cause large increases in the flow resistance if the constriction is severe.

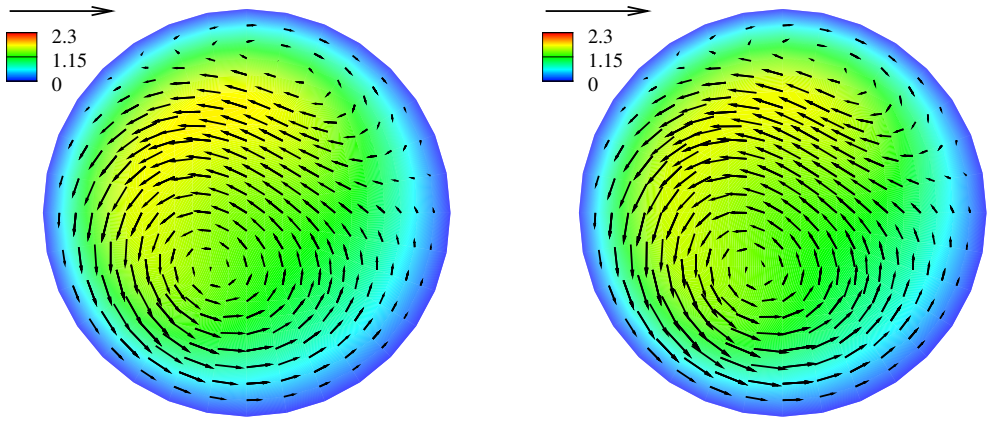

(a) $L_p = 0.0$ (b) $L_p = L/3$

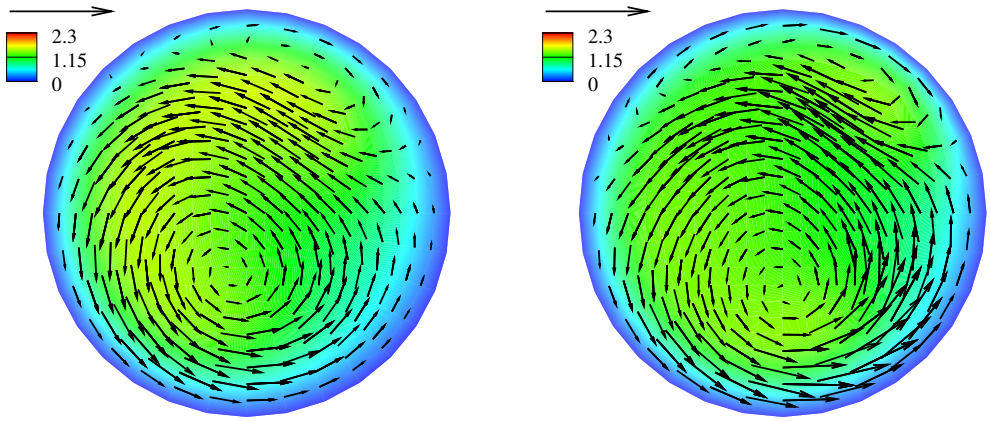

(c) $L_p = 2L/3$ (d) $L_p = L$

Figure 3.17: Velocity field variation with vessel arclength for the venous geometry with reduced boundary effects and coil space variation; $\mathcal{S}_{v,3}$.

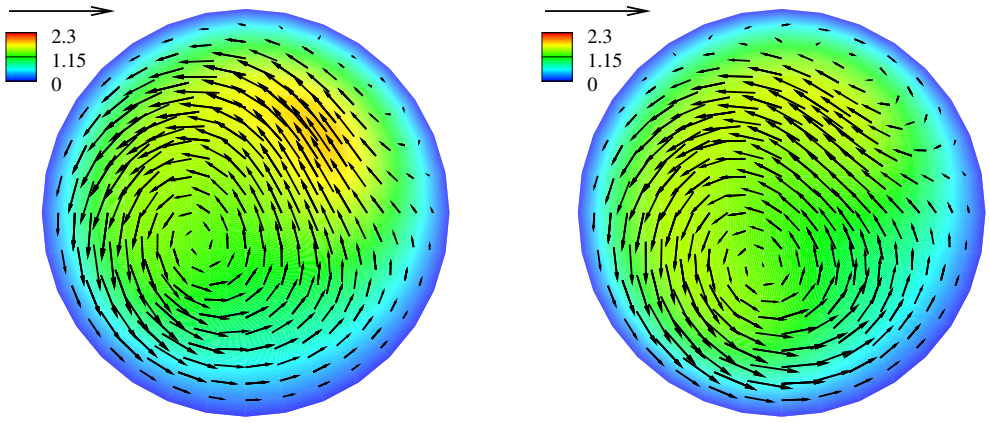

(a) $L_p = 0.0$ (b) $L_p = L/3$

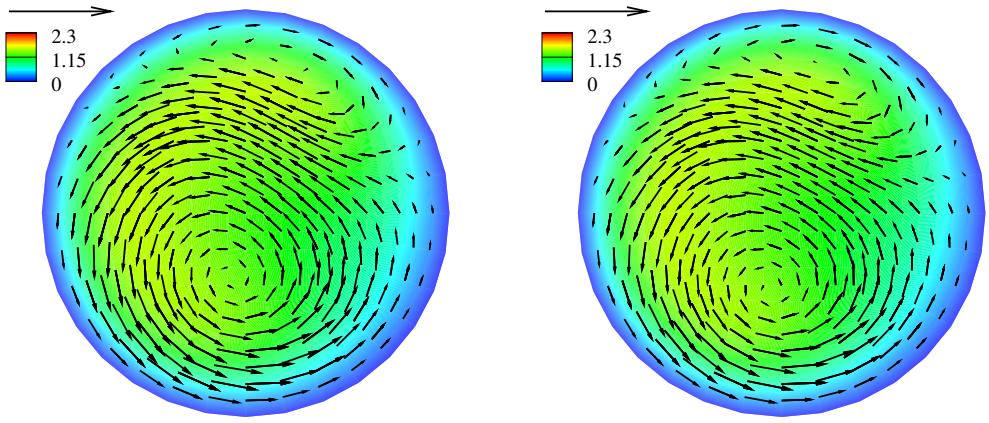

(c) $L_p = 2L/3$ (d) $L_p = L$

Figure 3.18: Velocity field variation with vessel arclength for the venous geometry with reduced boundary effects and width variation; $\mathcal{W}_{v,3}$.

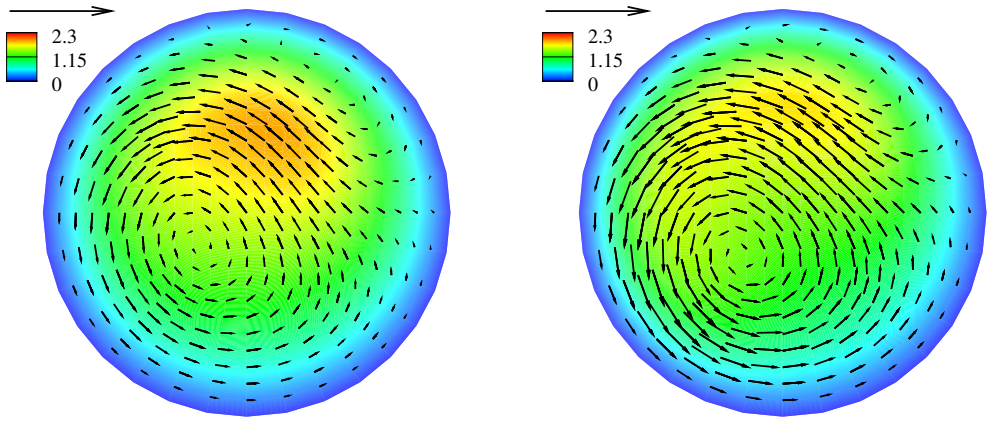

(a) $L_p = 0.0$ (b) $L_p = L/3$

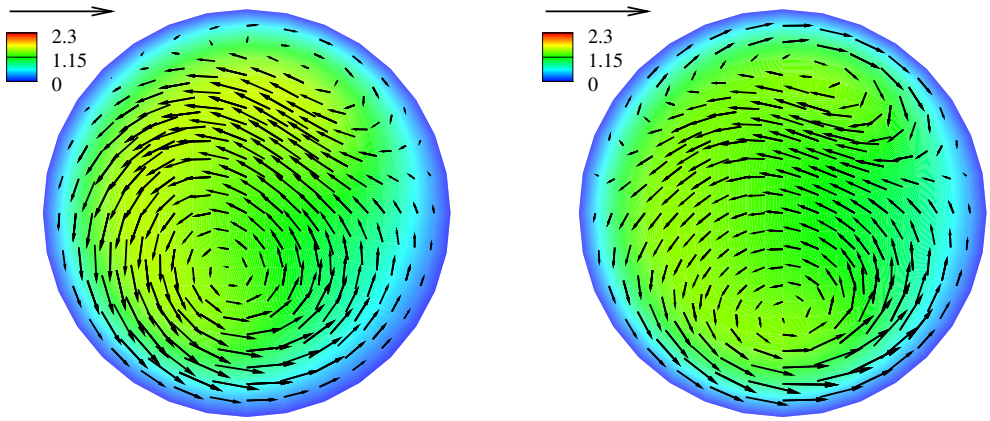

(c) $L_p = 2L/3$ (d) $L_p = L$

Figure 3.19: Velocity field variation with vessel arclength for the venous geometry with reduced boundary effects and width/coil space variation; $\mathcal{C}_{v,1}$.

Loose true knots

Steady flow through the loose true knot, LK, geometries described in section 2.4.3 and shown schematically in figure 2.18 on page 62 are presented here. Steady solvers are used for the undercoiled, UC, and normocoiled, NC, geometries while the overcoiled, OC, geometries require temporal solves for which convergence is assessed as per the details of appendix B.1. The straight inlet sections are chosen such that fully developed helical flow is present at the inlet to the cubic section of the knot. This inlet velocity flow profile is shown in Figure 3.20 for each of the vessels considered, where the arteries tend to reflect a less severe profile to the veins of the corresponding cord. As the coil separation reduces (or equivalently, the UCI increases), the strength of the in-plane secondary flow increases in tandem with the inclination of the core flow to the normal axis.

Figure 3.21 compares the pressure variation for each of the models over the knot length. Intuitively the total pressure and (absolute) mean pressure gradient increase with a reduction in coil spacing in each of the vessels due to the increased curvature and length. The total knot pressure drop increases almost two-fold in each of the vessels between the UC and OC geometries where a four-fold increase in UCI is designated.

The pressure gradient over the knot is shown for each vessel in figures 3.22(a)-(f). The computed value through the knot is found to fluctuate about the value computed through a purely helical vessel of the same coiling, with large gradients around the joins where the curvature and torsion are discontinuous. As the UCI increases the pressure gradients tend to take on a more regular pattern in both vessels. Table 3.5 catalogues the vessel length, knot pressure drop as well as the mean and variance of the pressure gradient in each model. For the arteries the relationship is simple; as the UCI increases the relative difference between the mean pressure gradient and the helical gradient upstream, $\delta_{\mathrm{d}P}$, reduces, as does the variance. The relative error, e_P, in using the helical gradient to estimate the total pressure drop across the knot is also quoted in the table and reduces from 7% in the UC model to 1% in the OC model. For the venous geometries however, the relation is less straightforward and the minimum error is instead observed for the NC vessel. This is a result of the curvature variation over the knot length which is shown in figure 2.19 on page 63, and documented in table 2.6 on page 64. While the mean arterial curvature approaches the helical value with increasing UCI, for the veins the NC cord exhibits the lowest δ_κ. This pattern is reflected in the relative difference in the pressure gradient ($\delta_{\mathrm{d}P}$) and hence the error in using the helical pressure (e_P) is lowest for the NC vein. The variance in κ reduces with UCI in both vessels, whereas the variance

	$L_{V,k}$	ΔP_k	$\overline{\frac{\mathrm{d}P}{\mathrm{d}Z}}$	$\frac{\mathrm{d}P}{\mathrm{d}Z}\|_h$	$\delta_{\mathrm{d}P}$	var $\left(\frac{\mathrm{d}P}{\mathrm{d}Z}\right)$	e_P
UCV	102.23	1138.16	-11.25	-9.97	0.13	1.45	0.10
NCV	113.03	1474.45	-13.22	-12.85	0.03	2.75	0.01
OCV	140.15	2217.72	-16.05	-15.31	0.05	5.85	0.03
UCA	183.78	1875.76	-10.27	-9.50	0.08	0.68	0.07
NCA	216.46	2514.97	-11.69	-11.41	0.02	0.35	0.02
OCA	290.53	3679.16	-12.71	-12.53	0.01	0.21	0.01

Table 3.5: Results of the steady loose knot (LK) study. $L_{V,k}$ refers to the vessel length along the knot and ΔP_k is the knot pressure drop. The error (e) refers to the relative difference between the numerically computed pressure drop (ΔP_k) and the estimate computed using the corresponding helical pressure gradient ($\frac{\mathrm{d}P}{\mathrm{d}Z}|_h$) and the vessel length ($L_{V,k}$).

in τ is largest in the NC cord, and smallest in UC. The magnitude of the variance is also much larger in the veins for both the curvature and torsion. Ultimately these effects are quite small and the total pressure drop through a knot is approximated to within 10% by the helical pressure gradient in all geometries considered. As the mean vessel curvature approaches the helical value, this estimate becomes more accurate. In the umbilical artery models this is equivalent to an increase in UCI, however the relationship is more complicated in the vein models considered as the curvature and torsion vary more significantly and do not observe a linear trend with the coiling index. For both the NC and OC veins and arteries, however, the total pressure drop is within 3% of the helical value.

Tight true knots, false knots and twist reversal

The pressure profile through the geometries detailed in section 2.4.3 and shown in figure 2.20 on page 65 is included in figure 3.23(a). The vessels corresponding to the tight true knot (TK), false knot (FK) and twist reversal (TR) models intuitively exhibit the same pressure profile downstream of the knot section. However, upstream and in the vicinity of the knot the pressure varies significantly depending on the knot type. The TK and FK models, for which constriction is not present, are almost identical with only minor discrepancies in the axial pressure gradient in the vicinity of the knot, shown in figure 3.23(b). The total pressure increases by less than 0.1% when the

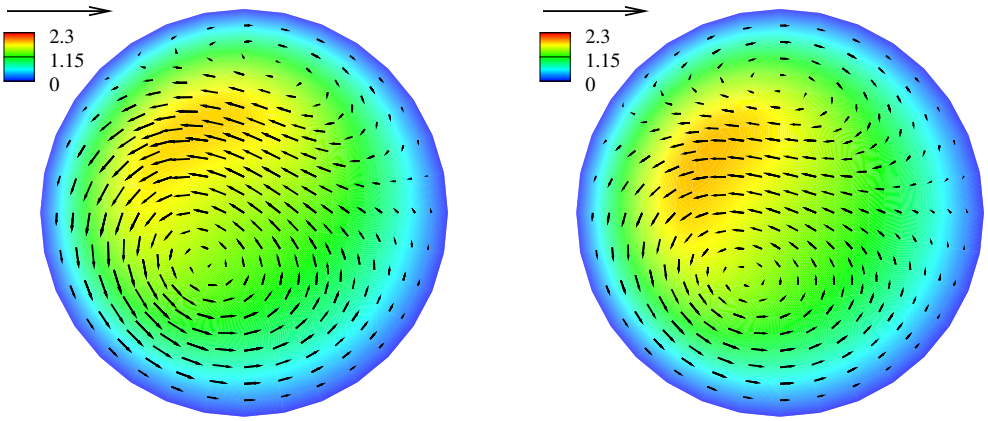

(a) UCV

(b) UCA

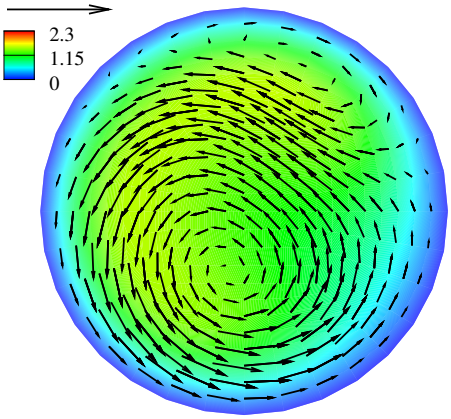

(c) NCV

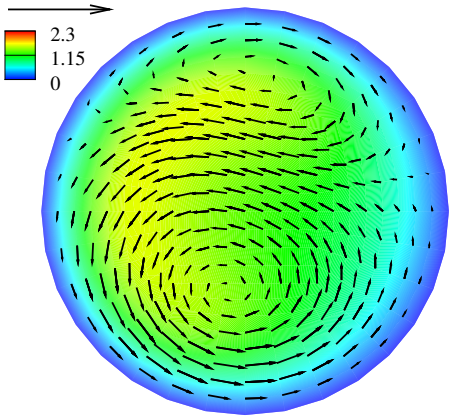

(d) NCA

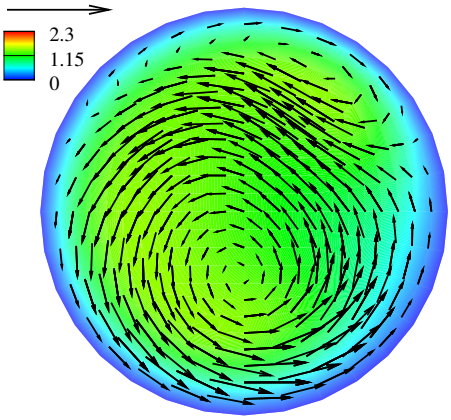

(e) OCV

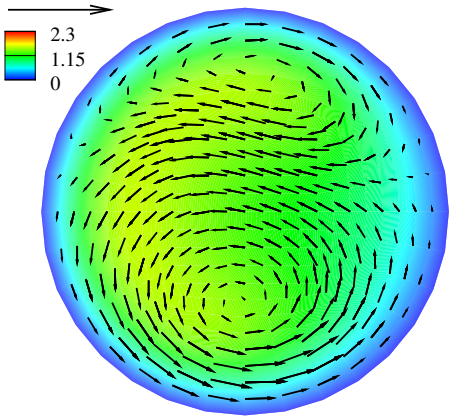

(f) OCA

Figure 3.20: Fully-developed helical flow at the entrance to the knot for the loose knot, LK, geometries with $\hat{w} = 1.6$ cm at $Re = 100$.

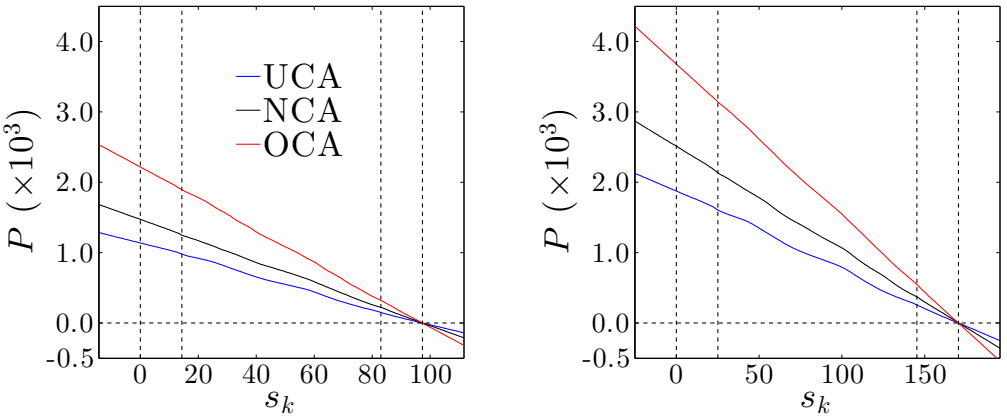

(a) Vein (b) Artery

Figure 3.21: Average axial pressure measured from the end of the cubic outlet for the loose knot geometries; UC (blue), NC (black) and OC (red). The black-dashed lines indicate the knot centreline section boundaries as in figure 2.19 on page 63.

direction of twist is changed in the TR model, validating the clinical practice of ignoring this feature. The pressure variation for the TK models is strongly related to the constriction size. In the vicinity of the knot, large fluctuations in the pressure gradient are observed however the same helical gradient is present on either side of the constriction. For the $R_{min} = 0.5R$ case the total pressure drop is 44% larger than the FK model without constriction. The remaining three constriction sizes, however, increase pressure by less than 15%. For a reduction in area of 23, 44 and 61% the pressure increases by 1.4, 5.1 and 15%, respectively. Case U_{t4} from the U_t study is also included in figure 3.23 for comparison as it has the same vessel length, number of complete coils and hence identical U_t. This vessel measured 85% of the total pressure of the FK model.

In order to reduce computational workload for the pulsatile simulations of chapter 4, shorter cords with one coil either side of the knot are considered. Convergence issues associated with pulsatile runs of the $R_{min} = 0.5R$ geometry necessitated a slightly less strenuous constriction of $0.55R$. Flow reversal, a serious occurrence wherein large regions of the flow oppose the primary direction, is observed for constriction sizes of $R_{min} = 0.55R, 0.625R$ and $0.75R$, however, the $0.875R$ knot and unconstricted vessels do not exhibit separation. Isosurfaces of the axial velocity in figure 3.24 show the size of the flow reversal region for the three vessels affected. The reversed flow volume increases with constriction size aft of the knot, creating a jet of

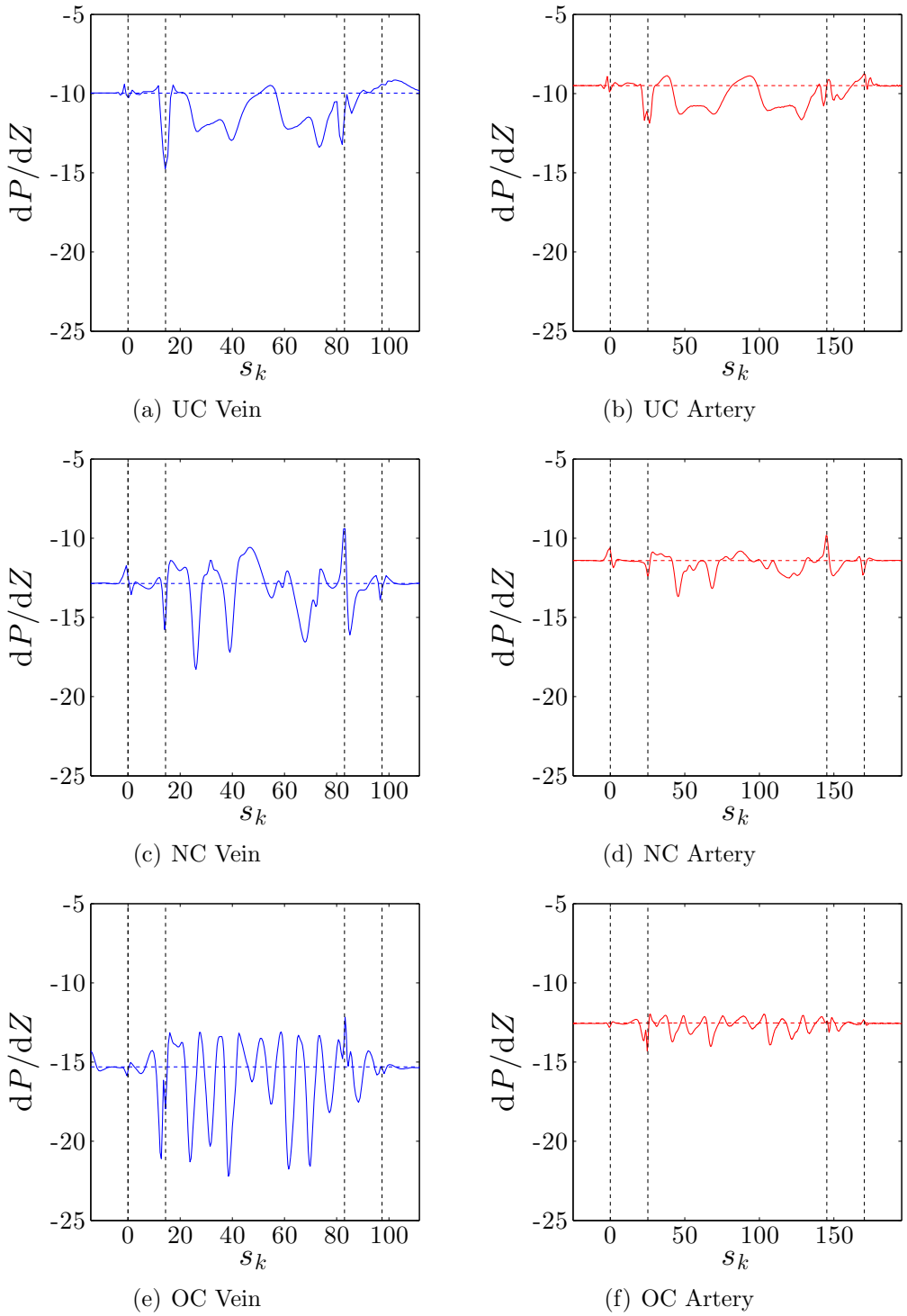

(a) UC Vein (b) UC Artery

(c) NC Vein (d) NC Artery

(e) OC Vein (f) OC Artery

Figure 3.22: Axial pressure gradient measured along the knot length for the loose knot vessels. The regularly coiled value shown as a dashed line.

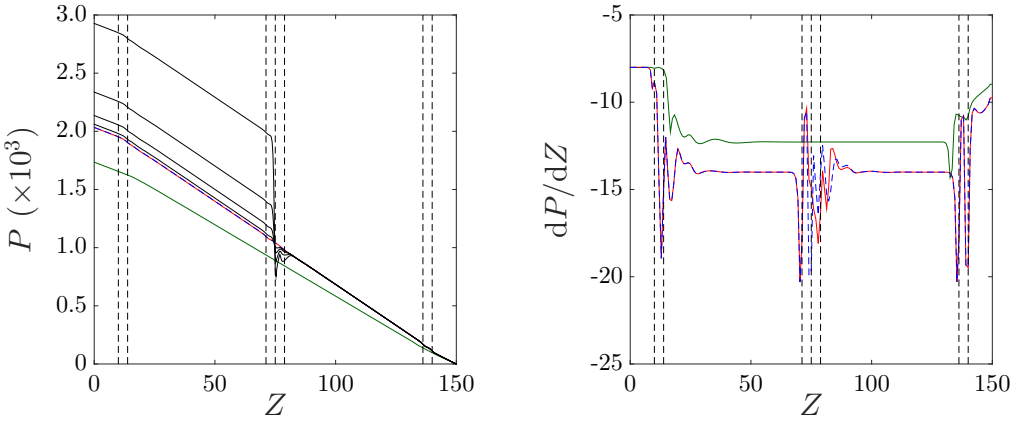

Figure 3.23: Pressure variation with vessel arclength, Z, for the TK (black), TR (blue-dashed) and FK (red) models with the U_{t4} profile shown in green. The TK constriction size is ordered in terms of pressure with higher pressure corresponding to larger constriction area; 0.875, 0.75, 0.625 and 0.5. The vertical black-dashed lines indicate the location of the centreline joins for the knot models.

high velocity fluid near the centre of the constriction which displaces toward the pipe outer further downstream. This reversed region amplifies the effects of the constriction by increasing the reduced flow area and is associated with the drastic increase in the total pressure drop shown in figure 3.23(a). The resumption of helical flow downstream of the constriction typically takes around one coil, and is dependent on the size of the constriction.

In conclusion, knots modelled as simple geometric perturbations to the helical structure without variation to the cross-section have little effect on the total pressure drop. For undercoiled cords, the pressure can be approximated by the purely helical value with an error of approximately 10% reducing to within 3% with increasing UCI for the cords studied. The addition of a false knot or a change to the direction of twist also has negligible effect on the pressure drop, validating the clinical practice of ignoring their presence. Constricted cords, however, can exhibit drastically altered pressure and flow profiles with the vessel pressure drop increasing by 44% with an axisymmetric reduction in radius to half the nominal value. Severe flow reversal, a critical feature related to pathology, is also apparent immediately downstream of constrictions narrower than 87.5% of the nominal vessel radius.

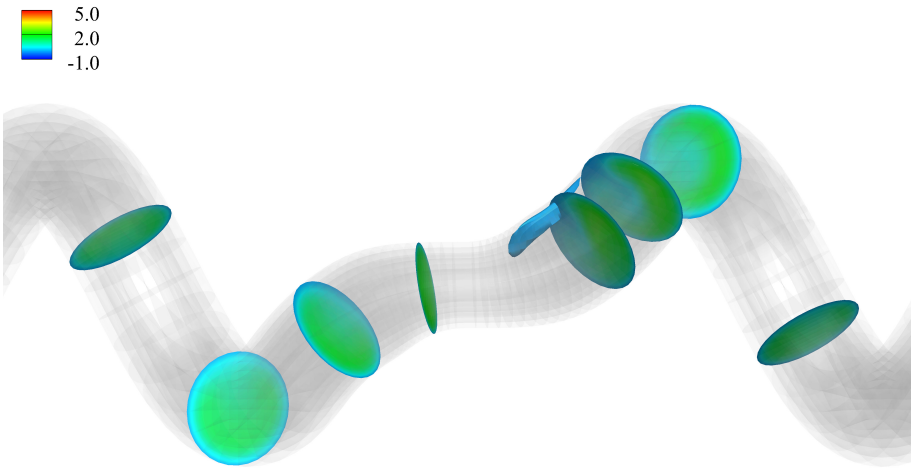

(a) $R_{min} = 0.75R$

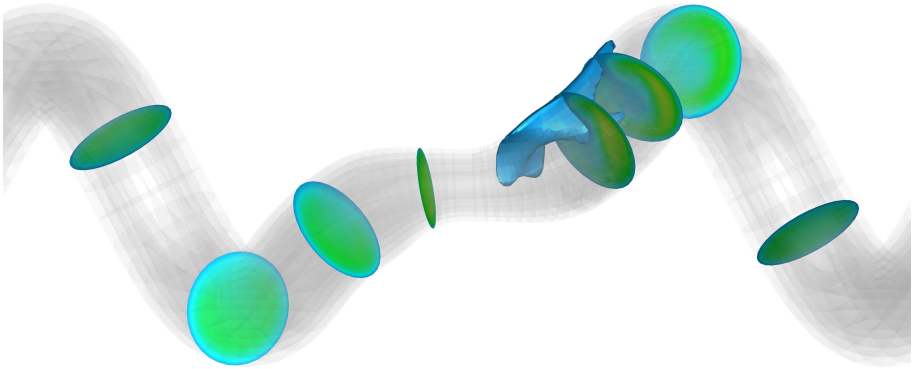

(b) $R_{min} = 0.625R$

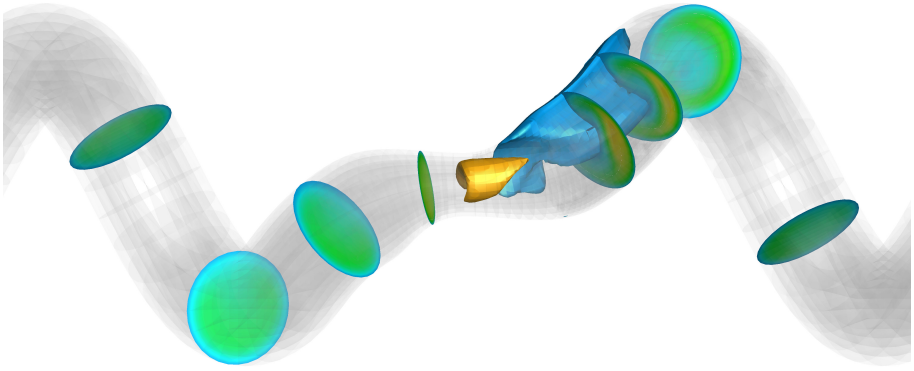

(c) $R_{min} = 0.55R$

Figure 3.24: The region of flow-reversal in the steady calculations for the tight true knots. The contours are drawn for constant surfaces of axial velocity, W. Two iso-surfaces at $W = -0.02$ (showing flow reversal) and 4.0 are included.

3.3 Conclusion

Throughout this chapter a steady analysis of flow within geometries representative of the umbilical arteries and vein was presented. The aim was to examine the diagnostic effectiveness of the umbilical coiling index (UCI), as well as to estimate the effects of geometric irregularities on the pressure and flow field. Firstly a geometric discussion based on the definition of the UCI was presented followed by steady numerical computations for a number of distinct umbilical vessel geometries. Throughout these studies the pressure drop over the length of the vessel (ΔP) was used as the key diagnostic for umbilical pathology. The key questions were therefore; does the UCI predict the pressure drop and hence provide clinicians with an understanding of the flow resistance created by a given cord? Additionally, do geometric irregularities including non-uniform coiling characteristics and the presence of true or false knots appreciably affect the vessel pressure drop?

In order to address these questions, three broad studies were presented. The first examined a number of simple umbilical geometries based on the work of Kaplan et al. (2010). These cords each comprise a helical tube with straight inlet and outlet sections adjoined to the umbilicus and placental insertion, respectively. The characteristics of the helical tubes were designed such that a broad range of cords be examined whilst ensuring that each have identical UCI and therefore remain diagnostically equivalent. Two separate studies were presented in order to account for ambiguity in the literature regarding the measurement of the cord length and number of coils.

The second study examined the effects of varying the pitch and/or helical radius of a typical umbilical cord. In this way the total cord UCI was again held constant, however, the cord coiling was allowed to vary significantly from one end to the other in order to examine cords with nonuniformity.

The final study discussed the presence of knots within the umbilical cord. These geometries were further classified into three separate models; loose true knots, where constriction is insignificant and the geometric knotting of the vessel is the primary feature; tight true knots where constriction is deemed significant compared to the geometric knotting, and false knots for which the cord structure briefly deviates from the helical description without geometric knotting or constriction.

Through the aforementioned studies it was determined that the UCI is unable to distinguish between cords of varying pressure drop. The index essentially represents the number of coils of a cord per (cm) length, which critically removes any reference to the total length of the vessels. As for straight pipe flow, the total arclength of a helical tube significantly alters the downstream pressure drop and hence the UCI does not in general repre-

sent the corresponding flow resistance. In addition to this, one form of the UCI also lacks any reference to the transverse cord measurement, the coil width, while both fail to explicitly account for its variation. This dimension directly relates to the curvature and torsion of the arterial and venous vessels, affecting the pressure gradient and in turn the total pressure drop. Two physiologically realistic models with equal cord length and number of coils were found to differ in total pressure drop by 40% simply by increasing the coil width.

Considering non-uniform cords, variations in the coil spacing, cord width or combinations of the two were shown to have little effect on the total pressure drop. This result suggests that a vessel with the mean coiling of a more complex geometry of significantly varying pitch and radius can be used for the purpose of calculating the total computed pressure drop. However, velocity and axial pressure gradients over the cord length within these geometries can vary significantly. For cords with variable coil spacing, a 9-fold increase in the local UCI over the length of the cord was determined to produce a 2.1% increase in venous pressure drop. Similarly, a cord with coil width varying by 100% along its length recorded only a 3% difference in pressure compared with the nominal cord of average coiling. The sensitivity of the pressure drop to both flow-direction and boundary conditions was found to be approximately 0.5%, while combining both coil width and spacing variability produced similar fluctuations as in the individual analyses.

Finally, knots modelled as simple geometric perturbations to the helical structure without variation to the cross-section have little effect on the total pressure drop. For undercoiled cords, this pressure can be approximated by the purely helical value with an error of approximately 10% reducing to within 3% with increasing UCI for the cords studied. The addition of a false knot, where the geometry deviates slightly from the helical description without constriction, as well as a change to the direction of twist, each have negligible effect on the pressure drop, validating the clinical practice of ignoring their presence. Constricted cords, however, can exhibit drastically altered pressure and flow profiles with the vessel pressure drop increasing by 44% with an axisymmetric reduction in radius to half the nominal value. Severe flow reversal, a critical feature related to pathology, is also apparent immediately downstream of constrictions narrower than 87.5% of the nominal vessel radius. The presence of these so-called 'tight true knots' is therefore of key importance and currently has no diagnostic representation in the calculation of the UCI.

In conclusion, the steady analyses show that the UCI does not correlate with the cord vessel pressure drop. Taking the latter as a diagnostic of pathology, it follows that the UCI is generally unable to distinguish between

cords which are normal in pregnancy and those for which adverse outcomes are possible. The steady pressure drop through purely helical tubes, however, can be used as a reasonable approximation to the flow through more complex geometries. For the non-uniformly coiled vessels considered, the helical result can predict the true pressure drop to within roughly 5% accuracy, while geometric knots are estimated to within 10%, significantly improving with increased coiling. The latter study illustrates the broader point that a larger scale curvature superposed over the inherent coiling does not have a significant bearing on the steady pressure drop through a coiled vein or artery, and hence that an average, helical result may be used in lieu of this information. Importantly, as this result holds for a complex three dimensional knot exhibiting localised regions of high curvature, more slowly varying curves such as the simple bending of the cord in-utero can be expected to have minimal impact on the blood flow.

Chapter 4

Pulsatile flow through the umbilical arteries

The purpose of this chapter is to examine pulsatile flow through the umbilical arteries discussed in chapter 3. Unlike blood flow in the umbilical vein, which is approximately steady, the forcing of the fetal heart induces unsteady flow characteristics within the umbilical arteries. The key questions considered within this chapter are therefore; to what extent does the inherent unsteadiness of the arterial flow affect the average total pressure drop through the arteries? Additionally, can knowledge of the steady flow be used to infer information about the unsteady system?

For the unsteady analysis a time-varying umbilical velocity profile representative of blood flow within the arteries is developed. This profile is modelled on a simple 'saw-tooth' profile approximated by a finite Fourier series expansion which describes the variation of the maximum (centreline) velocity; a quantity typically measured in-utero. To ensure convergence of the temporal solvers and the selection of an appropriate time-step, a numerical validation study is completed on the U_{t1} arterial geometry. The regularly coiled geometries are then examined with nominal blood flow characteristics of $Re = 100$ and a reduced velocity, U_{red}, of 41, before an analysis for the U_{t1} geometry over a range of U_{red} to investigate the variation of the fetal heart-rate, f. Finally, pulsatile flow through irregularly coiled arteries, loose true knots, tight true knots and false knots is examined in order to assess the effect of pulsatile flow within non-standard geometries.

It is found that the temporal average of the unsteady pressure drop (ΔP_{TA}), is predicted to within 5% by the steady results for all of the regularly and irregularly coiled geometries considered. The total pressure profile throughout the period is also remarkably similar among the geometries when normalised by ΔP_{TA}, with systolic and diastolic pressures typically 2.4 and

-0.2 times the temporal average, respectively. The equivalent values for a straight artery are 3.2 and -0.6, respectively, which interestingly suggests that the presence of coiling in the umbilical arteries acts to smooth out extreme pressures at a given Re. This fact may offer another possible explanation for the typically coiled nature of the umbilical geometry.

Reductions in the reduced velocity, U_{red}, were found to increase the ratio of the systolic pressure drop to the temporal average, all else being equal. Changes to the reduced velocity, however, were not observed to appreciably affect the temporal average for the U_{t1} artery, or the tight true knot with a minimum radius of $0.5R$. A fetus with a higher heart-rate may therefore experience larger pressure fluctuations throughout the period, whilst maintaining an otherwise normal, temporally averaged pressure drop.

As in the steady simulations, irregularly coiled cords typically present the same pressure profile as for the nominally coiled cord of equivalent average coil spacing and width. Despite relative variations of up to 120% in coil spacing and 60% in width, the temporally averaged pressure drop varies by less than 2%. The systolic pressure ratio is also similar to the regularly coiled cords; remaining constant at approximately 2.5.

Finally, knotted arteries typically exhibit a temporally averaged total arterial pressure drop consistent with the steady value, however, the discrepancy increases to approximately 10% for the tight true knot of constriction radius $0.55R$. Flow reversal, which is dependent on the base flow, is present in all tight true knot arteries aft of the constriction, with reversal noted on the inside tube wall for $U_{red} = 30$.

In summary, this study shows that the steady pressure drop is suitable as a proxy for the temporally averaged pressure throughout a typical arterial cycle for a wide range of cord geometries. Additionally, knowledge of the temporally averaged pressure can readily be used to infer the systolic and diastolic pressure, elucidating the full pressure range experienced within an artery.

4.1 Pulsatile boundary conditions

In order to model blood flow within the umbilical arteries a velocity waveform representative of the pulsatility of the fetal heart is required. Figure 4.1(a) shows the typical maximum cross-sectional velocity waveform variation in a normal pregnancy. This profile exhibits a pronounced velocity gradient with a single peak (systole) at the start of the cycle followed by a reducing flow-rate throughout the remainder of the period in a typical 'saw-tooth' pattern. This waveform is known to vary both throughout and between pregnancies.

Figure 4.1(b) shows the waveform corresponding to low end-diastolic flow in an abnormal pregnancy wherein the flow-rate reduces to near-zero at the end of the cycle. This outcome is quite rare and according to Geipel and Gembruch (2009) end-diastolic blood-flow is seen in almost all fetuses from 14 weeks of gestation.

There are many methods available to approximate the arterial waveform. For example, Sherwin and Blackburn (2005) employ a single and two-harmonic solution in their analysis of stenotic blood flow, used for validation purposes in section 2.6. Kleiner-assaf et al. (1999) use fluid structure interaction effects in a straight tube to model the time-varying velocity waveform based on pressure measurements taken from the pulmonary artery of a dog. Tejada-Martínez et al. (2011) employ a simple parabolic cross-sectional velocity profile modulated by a cosine wave in time. In this work, a saw-tooth profile that approximately matches measurements taken in-utero and the ultrasound shown in figure 4.1(a) is used to describe the variation of the centreline velocity, with the solution developed by Womersley (1955) employed to determine the full cross-sectional profile.

4.1.1 Saw-tooth approximation

The temporal variation of the centreline velocity in a normal umbilical artery, $w(0,t)$, has a saw-tooth like profile as shown in figure 4.1(a). This can be approximated by the Fourier series of the odd periodic extension of,

$$w(0,t) - w_0 = \begin{cases} \dfrac{(w_{peak} - w_0)t}{t_1} & 0 < t \leq t_1, \\ \dfrac{(w_{peak} - w_0)(T/2 - t)}{T/2 - t_1} & t_1 < t \leq T/2, \end{cases} \tag{4.1}$$

where w_{peak} is the maximum centreline velocity measured over the period, t_1 is the time at which this maximum is achieved and w_0 is the time-averaged centreline velocity. The Fourier sine series is,

$$w^*(0,t) - w_0 = \sum_{n=1}^{\infty} b_n \sin\left(\frac{2n\pi t}{T}\right), \tag{4.2}$$

with,

$$b_n = \frac{4}{T}\int_0^{T/2} \Big(w(0,t) - w_0\Big) \sin\left(\frac{2n\pi t}{T}\right). \tag{4.3}$$

Without truncation the centreline velocity is,

$$w^*(0,t) = \frac{w_{peak}T^2}{2\pi^2 t_1(T/2 - t_1)} \sum_{n=1}^{\infty} \frac{1}{n^2} \sin\left(\frac{2n\pi t_1}{T}\right) \sin\left(\frac{2n\pi t}{T}\right) + w_0. \tag{4.4}$$

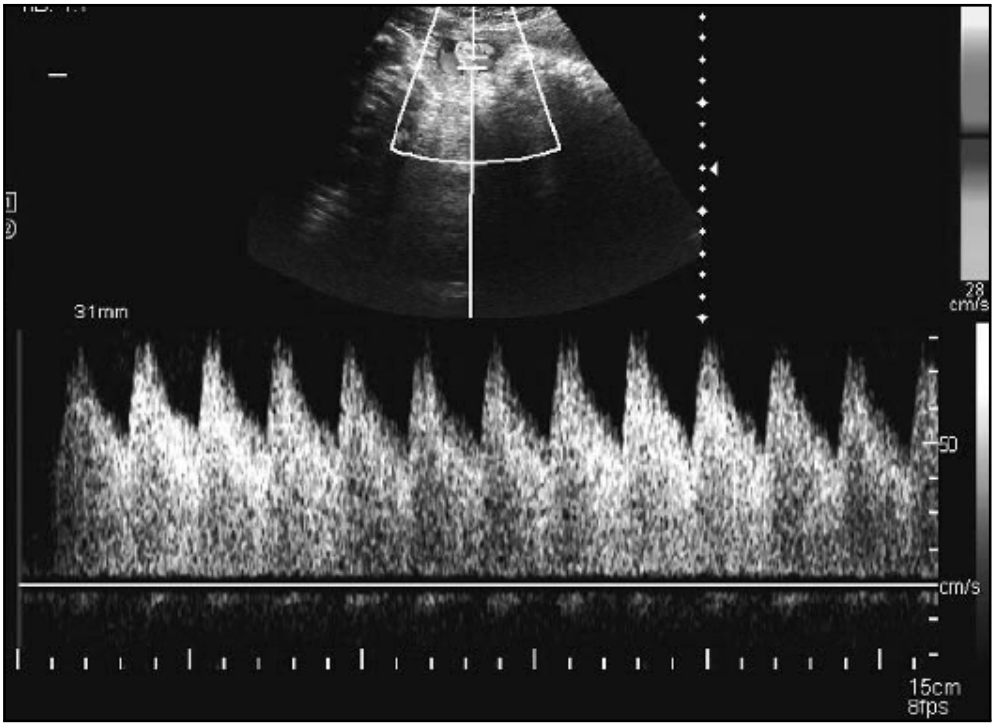

(a)

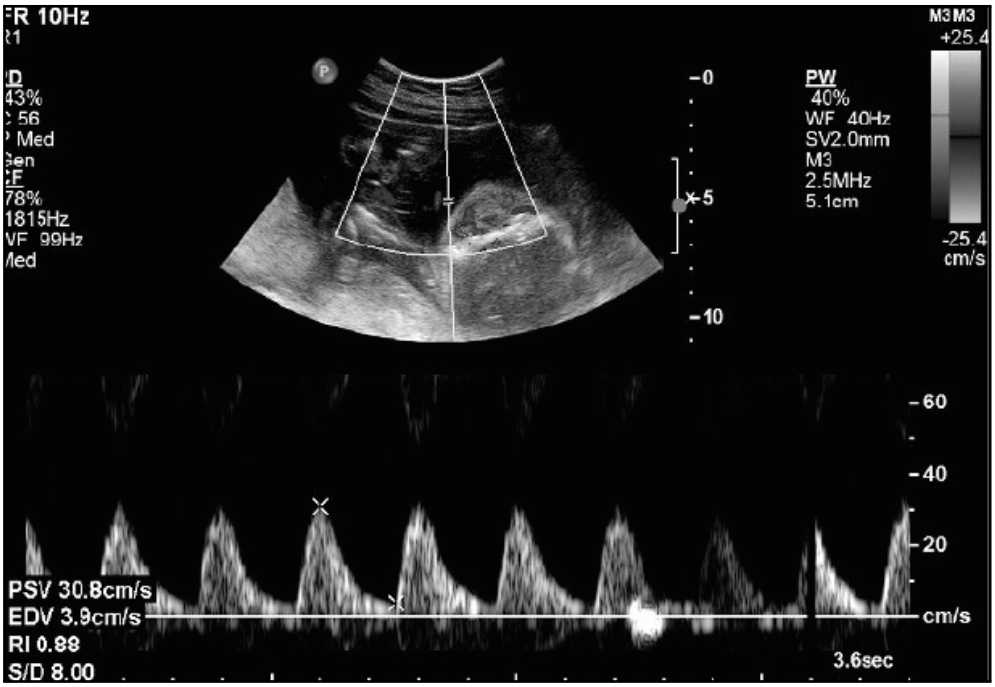

(b)

Figure 4.1: Maximum umbilical arterial velocity waveforms measured using ultrasound; a) normal and; b) low end-diastolic flow used with permission from Hobbins (2008).

As for the pulsatile validation, the velocity variation can also be written using Womersley's solution from equation (1.9), evaluated at the centreline,

$$w(0,t) = w_{max} + \Re\left[\sum_{n=0}^{N} -\frac{iP_n}{\omega_n \rho} e^{i\omega_n t}\right], \tag{4.5}$$

where w_{max} is the maximum of the *steady* parabolic cross-sectional velocity profile. By equating (4.4) and (4.5), an expression for the complex pressure coefficients, $P_n = C_n + iD_n$, can be found in terms of the natural flow parameters and the complex numbers $A_n + iB_n = \frac{1}{J_0(i^{3/2}\alpha_n)} - 1$, with $A_n, B_n \in \mathbb{R}$,

$$C_n = -\frac{A_n D_n}{B_n}, \tag{4.6}$$

$$D_n = \frac{\rho \omega_n w_{peak} T^2}{2\pi^2 t_1 B_n n^2 (T/2 - t_1)(1 + A_n^2/B_n^2)} \sin\left(\frac{2n\pi t_1}{T}\right). \tag{4.7}$$

The full cross-sectional solution is then given by equation (1.9).

The constants in the above expressions are chosen to match data from the literature. As the truncated series underestimates the true peak velocity of the saw-tooth, w_{peak} is chosen to ensure the final velocity profile has a non-dimensional peak systolic velocity, PSV, of 3.1 to match the work of Acharya et al. (2005*a*), listed in table 1.1. The non-dimensional peak and mean velocity are therefore $w_{peak} = 3.24$, $w_0 = 2$, with the number of harmonics of the truncated series chosen as $N = 4$. With a fetal heart-rate of 140 bpm (Kaplan et al., 2010) the typical period of an arterial pulsation is approximately $T \approx 0.43$ s. Using an arterial radius of 0.2 cm and a mean flow-rate of $\bar{Q}_A = 2.4 \times 10^{-6}$ m^3/s, the reduced velocity within the umbilical arteries is therefore, $U_{red} = Q_m T/(\pi R^3) \approx 41$, which corresponds to a Womersley parameter of $\alpha = 3.92$. The timing of the peak velocity within the period is chosen as $t_1 = 0.15T$, with $Re = 100$ as in the steady calculations. Figure 4.2 shows both the saw-tooth profile and the prescribed centreline variation as well as the corresponding pressure pulse in a straight pipe.

With the peak and mean velocity matched to observations, the end-diastolic centreline velocity (EDV) is set at 0.87. This is within the typical bounds quoted by Acharya et al. (2005*a*), but less than the mean of 1.29. The lower EDV has implications for flow-reversal; for a lower end-diastolic velocity the flow is more susceptible to reversal, particularly at diastole, than higher end-diastolic velocity flows. The base flow profile, however, does not exhibit flow-reversal at any point in the period. The pulsatility index (PI) for this waveform is 1.13 which compares with a mean of 0.8 at birth, and a max of 1.46 at 19 wks gestation (Acharya et al., 2005*a*). The full cross-sectional profile with harmonics is shown in figure 4.3 at four points within the period.

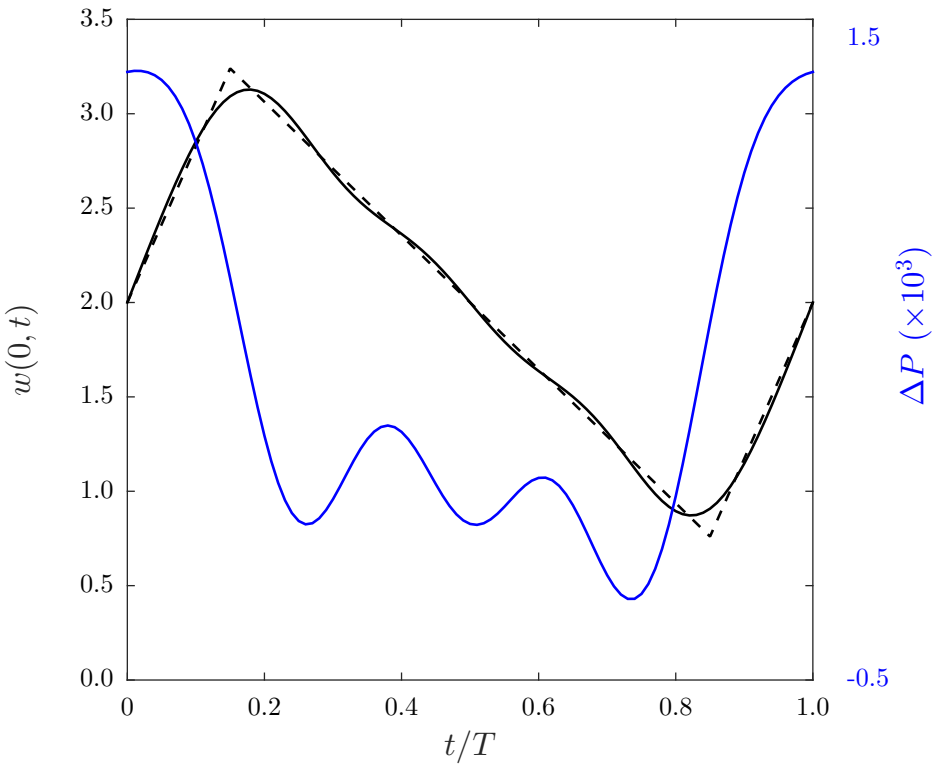

Figure 4.2: The umbilical centreline velocity (black) and arterial pressure drop (blue) for a straight pipe of non-dimensional length 50 over a single period. The dashed line shows the saw-tooth velocity profile approximated by the Fourier series expansion (solid), which here is shown for $N = 4$. The time of systolic velocity is set as $t_1 = 0.15T$, with a value of $w_{peak} = 3.24$ and a time-averaged centreline velocity of $w_0 = 2$.

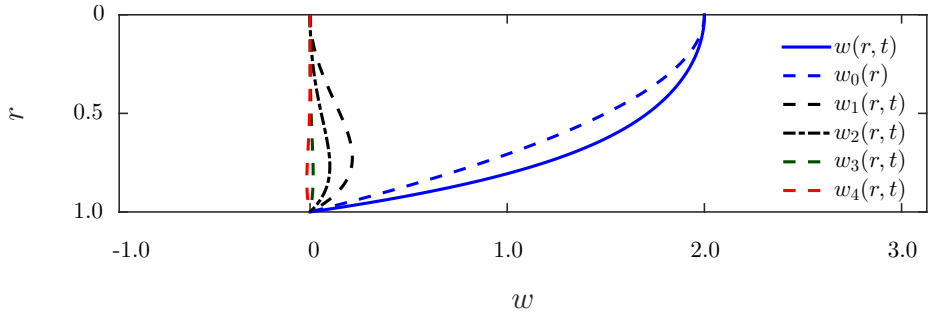

(a) $t/T = 0$

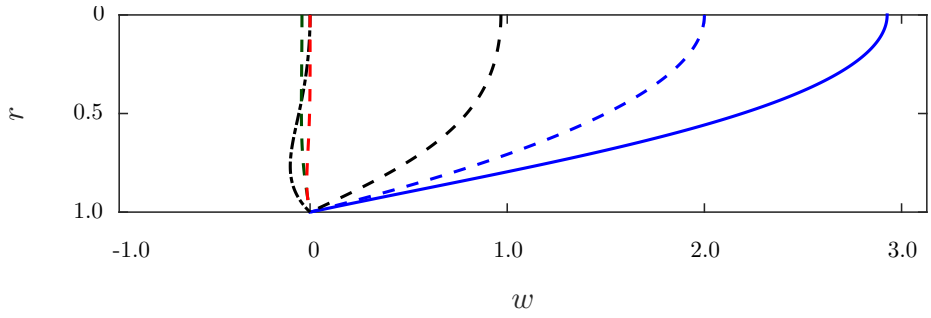

(b) $t/T = 0.25$

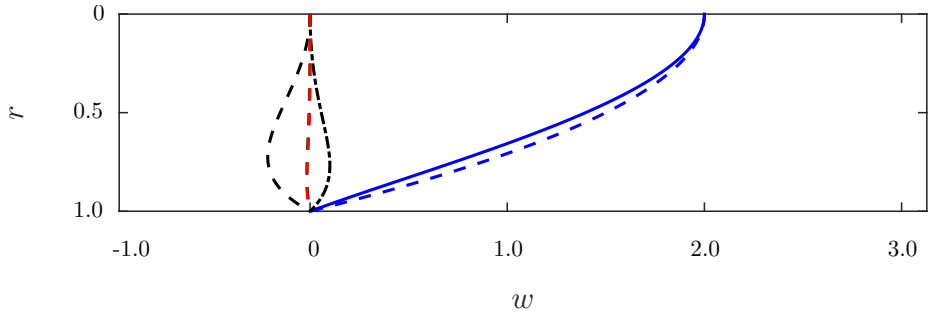

(c) $t/T = 0.5$

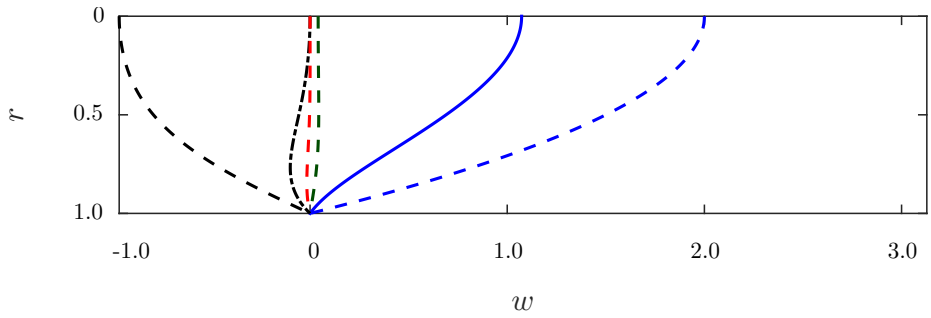

(d) $t/T = 0.75$

Figure 4.3: Variation of the full cross-sectional inlet velocity profile, $w(r,t) = w_0(r) + \sum_2^{n=4} w_n(r,t)$, at four points within the period for the umbilical waveform.

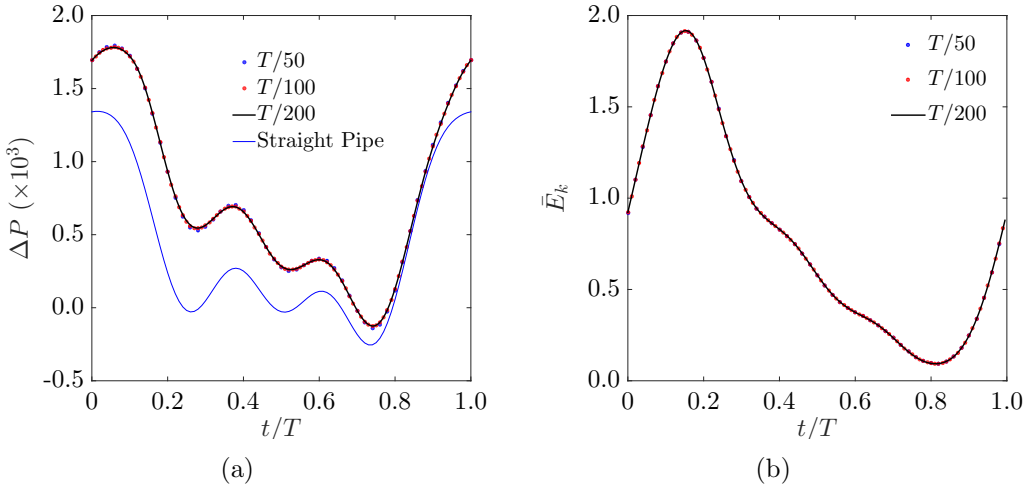

Figure 4.4: Pulsatile validation for artery U_{t1} at $Re = 100$, $U_{red} = 41$, showing a) the total pressure drop (ΔP) compared with the analytic solution for a straight pipe of the same length and; b) the total average kinetic energy ($\hat{E}_k$) throughout the domain.

4.1.2 Numerical validation

The pulsatile validation study of section 2.6 has previously shown that a timestep of $\Delta t = T/100$ is suitable for the straight pipe stenosis calculations at $Re = 100$. As an additional test, pulsatile flow with the umbilical waveform is computed for the U_{t1} artery with $\Delta t = T/50$, $T/100$ and $T/200$. Figure 4.4(a) shows the inlet pressure for the three timesteps, while figure 4.4(b) depicts the total average kinetic energy in the domain, $\bar{E}_k$. There is negligible difference incurred by the choice of timestep between $T/100$ and $T/200$ as previously noted in section 2.6, with spatial resolution dictating the level of convergence within the `oomph-lib` solvers. A timestep of $\Delta t = T/100$ is therefore used henceforth. Figure 4.4(a) also shows a comparison with the pressure drop computed through a straight pipe of equivalent length. The pressure profile for the cord is at all times greater though maintains the same general profile over the period. The systolic pressure, which occurs at $t/T = 0$ in the straight pipe, is now slightly delayed, occurring at approximately $t/T = 0.07$. The diastolic pressure is less affected by the geometry, though still occurs slightly later and with higher minimum.

4.2 Regularly coiled cords

The umbilical waveform described in section 4.1.1 is used as the inlet boundary condition to the six regularly coiled geometries with identical U_t as well as the arterial geometries of constant clinical UCI, U_c, presented in section 2.4.1. A nominal reduced velocity, U_{red}, of 41 coupled with $Re = 100$ is used in sections 4.2.1 and 4.2.2, with a further study of varying U_{red} presented for the U_{t1} artery in section 4.2.4. It is found that the temporal average of the unsteady pressure drop is predicted to within 5% by the steady results for each of the U_t and U_c geometries. As these geometries together cover a wide range of possible theoretical and clinical UCI the results are independent of the index. The pressure profile throughout the period is also remarkably uniform among the geometries when normalised by the average, with systolic and diastolic pressures typically around 2.4 and -0.2 times the temporal average, respectively. This effect is mirrored in the helical pressure gradients ensuring that the result is independent of inlet effects. Interestingly, the reduced relative maximum and minimum pressure suggests that the presence of coiling in the umbilical arteries acts to effectively smooth out extreme pressures at a given Re when compared with an equivalent straight tube. Reductions in the reduced velocity, U_{red}, increase the ratio of the systolic pressure drop to the temporal average, all else being equal. Changes to the reduced velocity, however, are not observed to appreciably affect the temporal average for the U_{t1} artery. A fetus with a higher heart-rate may therefore experience larger pressure fluctuations throughout the period, whilst maintaining an otherwise normal, temporally averaged pressure drop.

4.2.1 Constant U_t study

Pulsatile flow within the geometries of the constant U_t study is considered here. These geometries each have differing centreline arclength and number of coils, however the theoretical UCI, U_t, is preserved. The fully developed helical flow pattern for each of the arteries is shown at systole ($t/T = 0.15$) and diastole ($t/T = 0.76$) in figures 4.5(a)-(f) and 4.6(a)-(f). The pattern is similar to the steady results; two recirculating regions are generated with the relative strength and position dictated by the flow-rate as well as the torsion and curvature of the tube centreline. At systole the flow-rate is larger and the inclination of the two vortices to the pipe normal increases, as noted in the Re variation study for case U_{t6} in figure 3.5. The secondary flow is also stronger at systole, with the axial velocity exhibiting a more pronounced maximum near the tube outer wall than at diastole. The velocity profile oscillates between these two extremes over an average pressure cycle. The

presence of flow reversal within the arteries of the human circulatory system is often a sign of pathogenesis and is of interest here. Case U_{t1} is the only regularly coiled artery to exhibit reversal at the nominal Re and U_{red}. The reversal in this case is very low, with only a small region at the inside wall of the artery inlet and outlet generated at systole. This feature is not shown here. The flow reversal is a result of the larger helical curvature, listed in table 2.2, which results in a more severe inlet/outlet bend present for this geometry. The large flow-rate at systole generates separation at the join which develops regions of backward moving fluid.

The pressure variation over one period is shown for each of the U_t arteries in figure 4.7(a). The peak systolic pressure, ΔP_{sys}, is achieved prior to the peak systolic velocity, PSV, in all arteries consistent with the results of Womersley (1955). The presence of two local maxima between systole and diastole is an artefact of the Fourier series approximation, which is here composed of only four terms. This effect is only slight and could be removed by the choice of larger N.

In general the results, tabulated in table 4.1, mirror those of chapter 3. The highest peak systolic pressure drop (ΔP_{sys}) and temporally averaged pressure drop (ΔP_{TA}) are achieved by the longest artery, U_{t6}, with the remaining cords ordered by decreasing length as in chapter 3. The diastolic pressure drop (ΔP_{dias}) is also lowest in U_{t6}, and increases with cords of decreasing length. This is a result of equation (2.41) wherein a greater arterial length results in a larger variation to the total pressure drop over a cycle. Table 4.1 also shows a comparison between the pressure drop computed via steady simulations (ΔP_{steady}) and the temporally averaged pressure drop. The steady pressure drop estimates the temporally averaged value to within 5% for all U_t geometries.

In order to highlight similarities in the pressure profile, the pressure drop is normalised by the temporal average in figure 4.7(b). Each cord exhibits a peak systolic pressure approximately 2.4 times the temporal average, with a diastolic pressure drop approximately $-$ 0.2 times the average. This relationship is remarkably constant among the geometries. For a straight pipe with the umbilical waveform, shown in green in figure 4.7(b), the pressure drop varies from 3.3 times the temporal average at systole to -0.6 times the average at diastole. The introduction of the coiled geometry here acts to smooth the pressure profile, however further variations to the geometry of the helix do not appreciably change the minimum or maximum pressure.

In order to remove length effects, the inlet pressure is normalised using the instantaneous pressure-drop and the peak-to-mean pressure difference

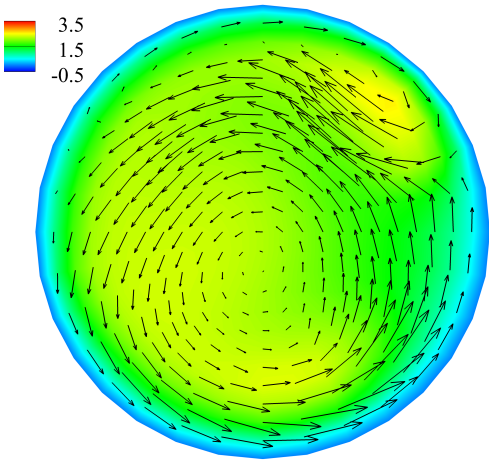

(a) U_{t1}; systole ($t/T = 0.15$)

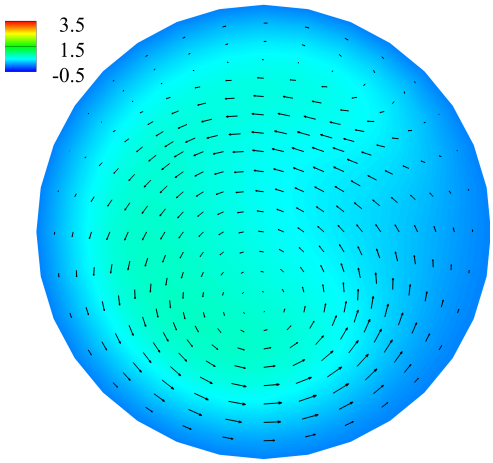

(b) U_{t1}; diastole ($t/T = 0.76$)

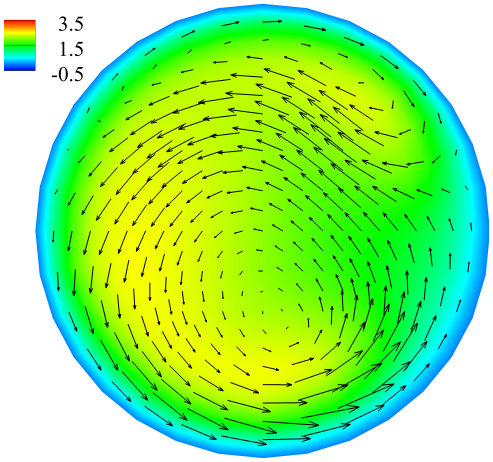

(c) U_{t2}; systole ($t/T = 0.15$)

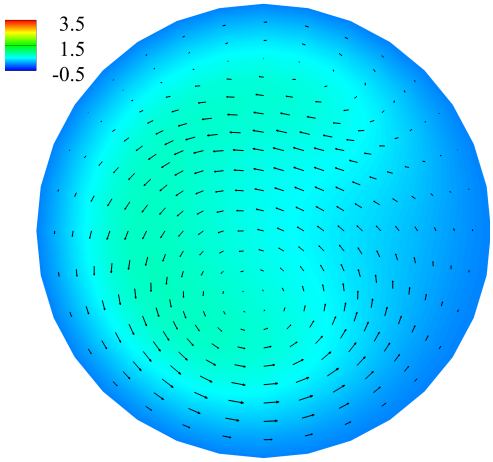

(d) U_{t2}; diastole ($t/T = 0.76$)

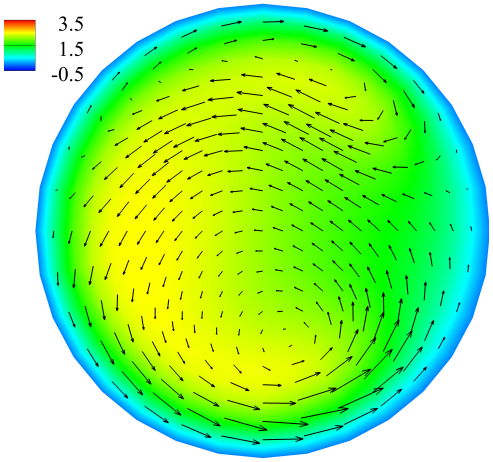

(e) U_{t3}; systole ($t/T = 0.15$)

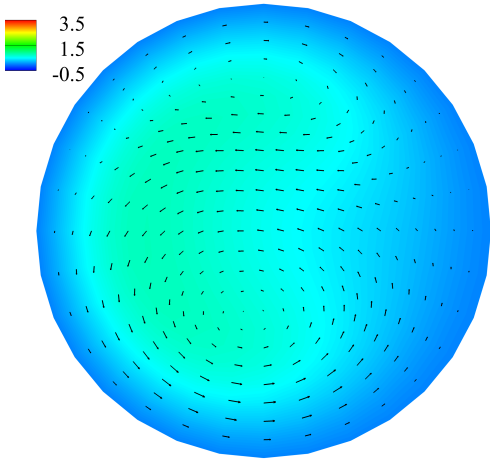

(f) U_{t3}; diastole ($t/T = 0.76$)

Figure 4.5: Helical flow variation for the U_{t1}, U_{t2} and U_{t3} arteries at systole (left) and diastole (right) at $Re = 100$, $U_{red} = 41$.

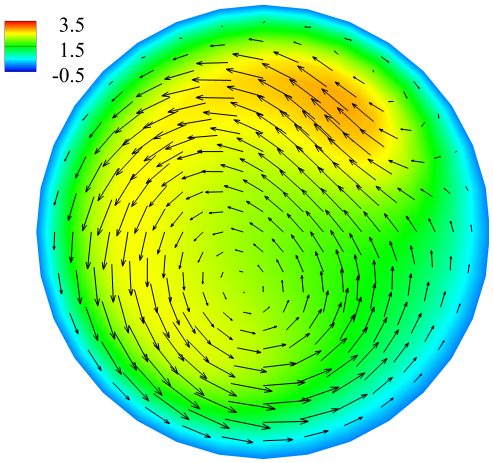

(a) U_{t4}; systole ($t/T = 0.15$)

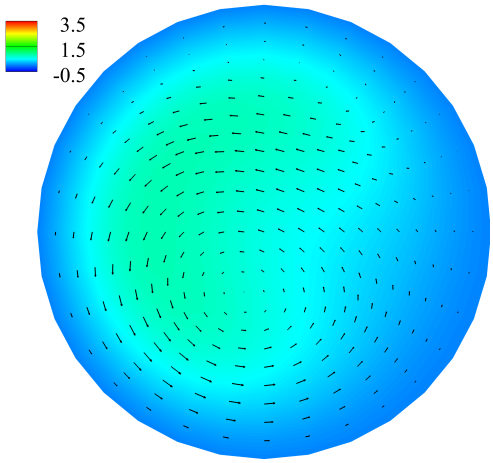

(b) U_{t4}; diastole ($t/T = 0.76$)

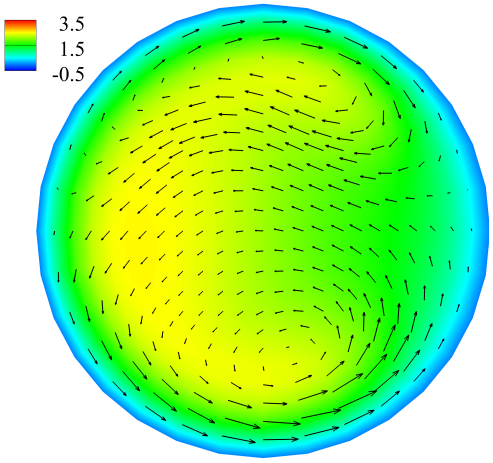

(c) U_{t5}; systole ($t/T = 0.15$)

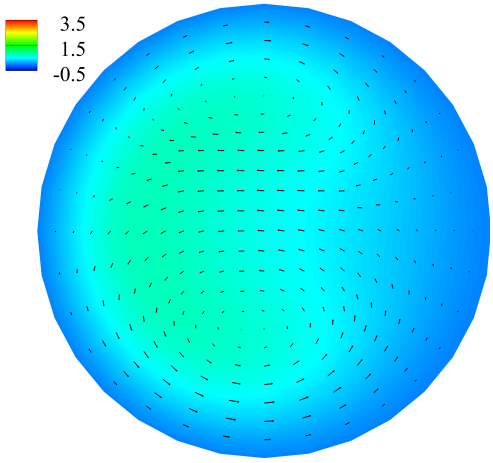

(d) U_{t5}; diastole ($t/T = 0.76$)

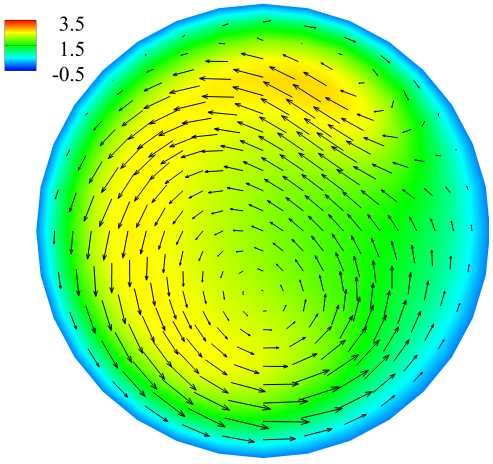

(e) U_{t6}; systole ($t/T = 0.15$)

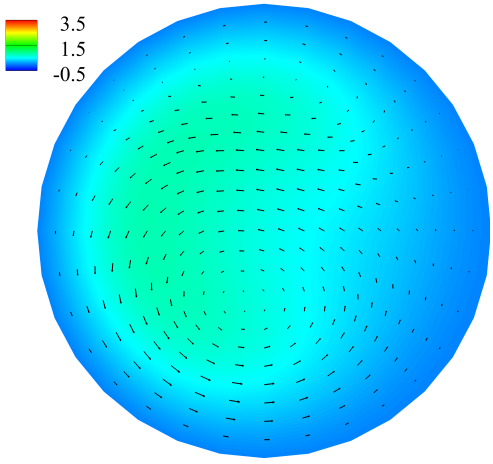

(f) U_{t6}; diastole ($t/T = 0.76$)

Figure 4.6: Helical flow variation for the U_{t4}, U_{t5} and U_{t6} arteries at systole (left) and diastole (right) at $Re = 100$, $U_{red} = 41$.

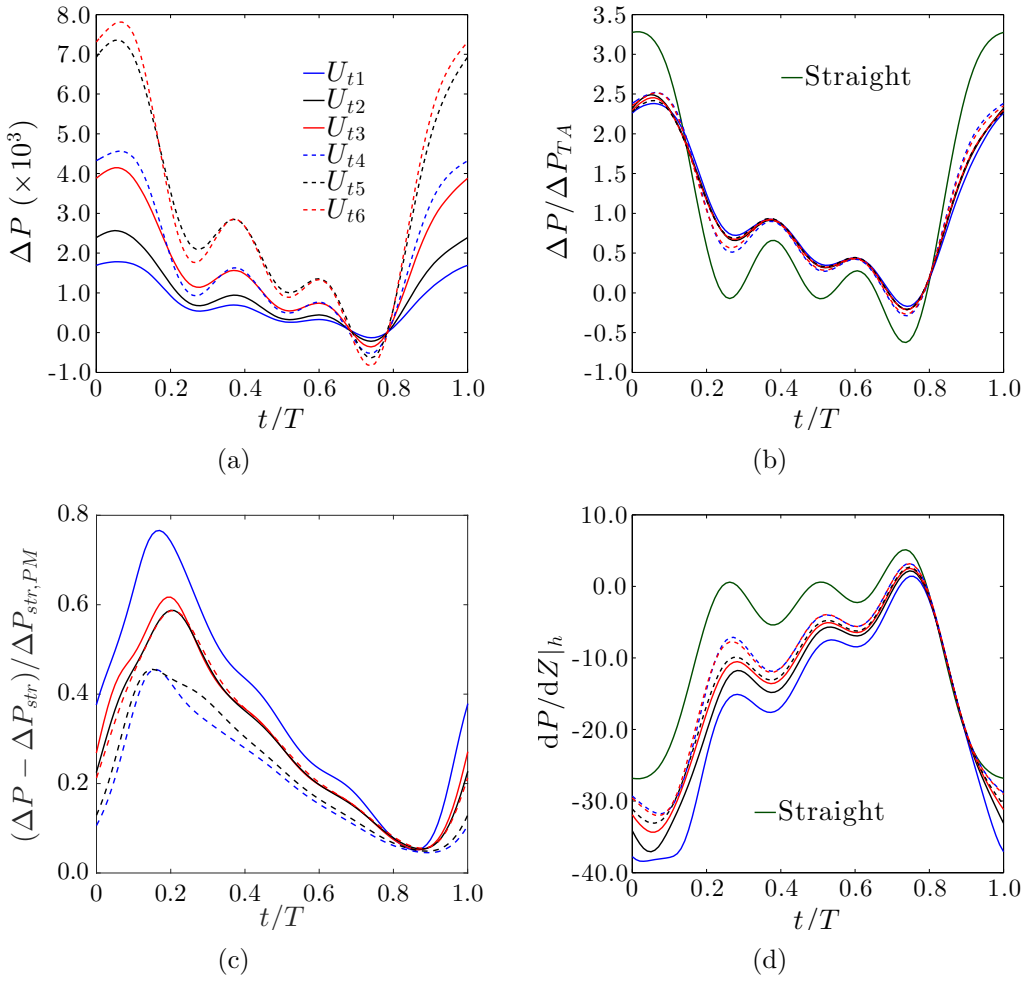

Figure 4.7: Pulsatile pressure results for the constant U_t study at $Re = 100$, $U_{red} = 41$. a) The arterial pressure drop (ΔP) variation over one period; b) normalised by the time averaged pressure drop (ΔP_{TA}); c) normalised by a straight pipe of equivalent length using the straight pipe pressure drop (ΔP_{str}), and the peak-to-mean difference, $\Delta P_{str,PM} = \Delta P_{str,sys} - \Delta P_{str,TA}$ and; c) helical pressure gradient ($\mathrm{d}P/\mathrm{d}Z|_h$).

through a straight pipe of equivalent length with the same forcing;

$$\frac{\Delta P(t) - \Delta P_{str}(t)}{\Delta P_{str,PM}},$$

where ΔP_{str} is the straight pipe pressure drop, and the peak-to-mean difference, $\Delta P_{str,PM} = \Delta P_{str,sys} - \Delta P_{str,TA}$. This quantity therefore represents the change in pressure caused by the addition of the non-straight geometry, relative to the natural pressure fluctuation in a straight pipe. The results are shown in figure 4.7(c). The artery with the highest helical curvature, U_{t1}, exhibits the highest normalised inlet pressure with each cord following in order of reducing curvature. The maximum and minimum approximately co-locate with the systolic and diastolic velocity prescribed in the inlet boundary condition. To remove the effect of the inlet and outlet the pressure gradient through the helical section is included in table 4.2, with a plot of the variation over a period shown in figure 4.7(d). The highest recorded difference between the pulsatile and steady pressure gradient is for case U_{t2} where the steady results are within 5.3% of the time-averaged helical pressure gradient. The most severe gradient is typically 2.4 times the mean, compared with 3.2 for the straight pipe. Similarly, the least severe gradient is approximately -0.2 times the temporal average, compared with -0.6 times the average for the straight pipe. These results mirror the conclusion for the full geometry that the introduction of coiling reduces relatively extreme pressures regardless of the inlet and outlet.

4.2.2 Constant U_c study

Pulsatile flow within the geometries of the constant U_c study is considered here. These geometries each have a constant number of coils (N) pitch length (L_p) and hence identical clinical UCI (U_c). The key geometric difference is derived from the helical radius (R_h) which in-turn affects the torsion and curvature of the centreline. As for the U_t arteries, the systolic and diastolic fully-developed velocity profiles show the same cross-flow and axial velocity pattern as the steady results shown in figure 3.9 and are therefore omitted. Figures 4.8(a) and (b) show the total pressure drop and normalised pressure drop through the artery for one cycle, respectively. As for the U_t study, the highest systolic pressure and lowest diastolic pressure are present in the longest artery, U_{c7}, with the remaining geometries ordered in terms of length. The ratio of the peak systolic and temporally averaged pressure does not vary appreciably between geometries $U_{c2}, ..., U_{c7}$, maintaining a value of approximately 2.4 as in the U_t study, however the U_{c1} geometry, which has the lowest

	ΔP_{TA}	ΔP_{steady} (δ %)	ΔP_{sys} ($/\Delta P_{TA}$)	ΔP_{dias} ($/\Delta P_{TA}$)
U_{t1}	749.1	715 (4.61)	1783 (2.38)	-127.7 (-0.17)
U_{t2}	1030	1009 (2.03)	2566 (2.49)	-216.1 (-0.21)
U_{t3}	1690	1608 (4.88)	4146 (2.45)	-359.2 (-0.21)
U_{t4}	1813	1735 (4.27)	4563 (2.52)	-523.1 (-0.29)
U_{t5}	3044	2893 (4.96)	7357 (2.42)	-636.4 (-0.21)
U_{t6}	3107	2966 (4.55)	7810 (2.51)	-831.8 (-0.27)

Table 4.1: Pulsatile pressure results for each of the U_t arteries at $Re = 100$, $U_{red} = 41$. The temporally averaged inlet pressure (ΔP_{TA}) is compared with the steady results at $Re = 100$, as well as the systolic (ΔP_{sys}) and diastolic pressure (ΔP_{dias}). The relative difference between the steady and temporally averaged results are computed by $\delta = (\Delta P_{TA} - \Delta P_{steady})/\Delta P_{TA}$.

	$\frac{\mathrm{d}P}{\mathrm{d}Z}\|_{TA}$	$\frac{\mathrm{d}P}{\mathrm{d}Z}\|_{steady}$ (δ %)	$\frac{\mathrm{d}P}{\mathrm{d}Z}\|_{\text{max.}}$ (/TA)	$\frac{\mathrm{d}P}{\mathrm{d}Z}\|_{\text{min.}}$ (/TA)
U_{t1}	-17.44	-16.66 (4.43)	1.50 (-0.09)	-38.41 (2.20)
U_{t2}	-15.46	-14.64 (5.29)	2.15 (-0.14)	-37.12 (2.40)
U_{t3}	-14.33	-13.60 (5.17)	2.52 (-0.18)	-34.36 (2.40)
U_{t4}	-12.83	-12.28 (4.33)	3.19 (-0.25)	-31.76 (2.47)
U_{t5}	-13.85	-13.14 (5.08)	2.68 (-0.20)	-33.10 (2.39)
U_{t6}	-12.86	-12.27 (4.66)	3.15 (-0.24)	-32.04 (2.50)

Table 4.2: Pulsatile pressure gradient results for each of the U_t arteries at $Re = 100$, $U_{red} = 41$. The temporally averaged pressure gradient ($\frac{\mathrm{d}P}{\mathrm{d}Z}|_{TA}$) is compared with the steady results at $Re = 100$, as well as the max. and min. pressure gradient throughout the period. The relative difference between the steady and temporally averaged results are computed by $\delta = (\frac{\mathrm{d}P}{\mathrm{d}Z}|_{TA} - \frac{\mathrm{d}P}{\mathrm{d}Z}|_{steady})/\frac{\mathrm{d}P}{\mathrm{d}Z}|_{TA}$.

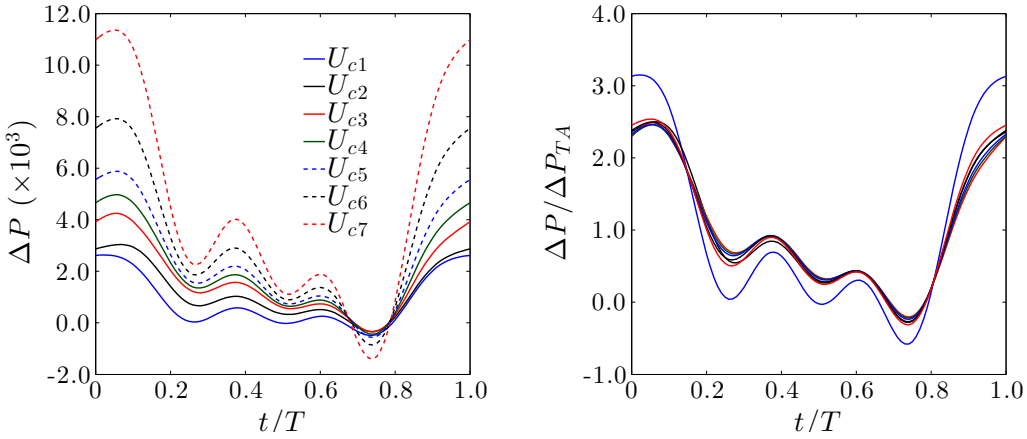

Figure 4.8: Variation of a) total pressure drop, and; b) pressure drop normalised by the temporally averaged pressure over one period for the U_c arteries at $Re = 100$, $U_{red} = 41$.

R_h, κ and largest τ, has a ratio similar to a straight pipe. This geometry, shown in figure 2.6, has very low helical radius and hence low curvature.

4.2.3 Systolic pressure ratio

The fact that the systolic pressure ratio is roughly constant for the regularly coiled arteries considered in the U_c and U_t studies motivates the analysis of a wide range of curved and helical geometries. It is found that the systolic pressure ratio for a broad range of relevant helical vessels is remarkably consistent at approximately 2.3-2.6. To demonstrate, the systolic pressure ratio is calculated for the U_t, U_c and several new geometries chosen to represent a broad class of cords. These include a number of toroidal arteries of varying curvature in addition to a highly coiled artery with $\kappa = 0.86$ and $\tau = 0.28$. This particular artery corresponds to a very high clinical UCI of 2.32 coils/cm and represents the physical limit of a tightly-wound, non-intersecting coiled tube. As these geometries represent a range of non-straight arteries a single geometric identifier is insufficient to describe their variation. The results are therefore plotted in figures 4.9(a)-(d) against several relevant geometric parameters, with the systolic pressure ratio calculated based on the pressure gradient sufficiently removed from the boundaries in order to minimise any inlet/outlet effects. Figure 4.9(a) shows the effect R_h has upon the systolic pressure ratio for the U_c geometries. An initial increase from $R_h = 0$ to 0.5 causes a reduction in the peak systolic ratio of almost 25%. However,

the systolic pressure ratio is roughly constant with further increases to R_h despite the varying curvature and torsion, shown in figure 2.8(b).

Figures 4.9(b)-(d) illustrate the change in systolic pressure ratio with κ, τ and the helical parameter, $\gamma = \mathrm{Gn}/\mathrm{Dn}^{3/2} = \tau/(\sqrt{2Re}\kappa^{3/4})$. The U_{t1} artery, which is the shortest and therefore most susceptible to boundary effects is marked with a cross while the highly coiled artery is shown in green. Figure 4.9(b) also shows the ratio calculated for the toroidal arteries of constant curvature and zero torsion. Length limitations imposed with increasing curvature mean that these toroidal results are only available for $\kappa \leq 0.2$. Broadly speaking, at constant Re the systolic pressure ratio for the arteries considered rapidly decreases with increasing curvature for $\kappa < 0.2$, before remaining relatively constant to further increases. The ratio is also approximately constant for the geometries with $0 < \tau < 0.4$. These parameters are of course not varied independently, and γ, which indicates a measure of their relative strength, provides a more holistic marker. This parameter is discussed shortly. Examination of figure 4.9(b) allows comparison between geometries with and without torsion. The effect of torsion is reasonably small except at low curvature where the pressure ratio increases relative to toroidal pipes of equivalent curvature. The results for the toroidal and helical geometries begin to match around $\kappa = 0.2$ where the curved results start to asymptote to a systolic pressure ratio of approximately 2.3–2.4. Despite a significantly higher curvature the tightly coiled artery shows only a slightly lower systolic pressure ratio of 2.3 when compared with the remaining regularly coiled arteries. This supports the observation that arteries which differ significantly in curvature, provided the curvature is above a threshold of approximately $\kappa = 0.2$, have approximately equal systolic pressure ratio.

To gain a more complete picture of the spread of data, the systolic pressure ratio is plotted against γ in figure 4.9(d). In the context of this constant Re problem, $\gamma = 0$ arteries are those with zero torsion (and non-zero curvature) and include the toroidal sections as well any artery curved in a single plane. The geometries with $0 < \gamma < 0.14$ are helical tubes with moderate relative curvature and torsion and are typical within pregnancy. Conversely, arteries with $\gamma \geq 0.14$ have low curvature relative to torsion and appear as reasonably straight geometries which twist at a high rate. Cord U_{c1}, shown in figure 2.7, has $\gamma \approx 0.3$ and is an example of such an artery. As the torsion and curvature lower further the tube becomes straighter and $\gamma \to \infty$. From figure 4.9(d), the moderate helical arteries with $0 < \gamma < 0.14$ have a roughly equal systolic pressure ratio of 2.3–2.6. The toroidal geometries, which are not shown in figure 4.9(d), contract on this diagram to the point $\gamma = 0$, above which a sharp gradient is evident. For $\gamma \geq 0.14$ the ratio increases with γ to the systolic pressure ratio for a straight pipe. The γ parameter,

here calculated at $Re = 100$, is therefore useful in delineating between three broad geometric categories;

i) Toroidal or planar curved arteries ($\gamma = 0$): The systolic pressure ratio depends on the curvature, κ.

ii) Arteries with moderate curvature and torsion, which comprise the majority of physiologically realistic arteries ($0 < \gamma < 0.14$): The systolic pressure ratio is relatively constant at 2.3–2.6.

iii) Arteries which have relatively high torsion compared with curvature ($\gamma \geq 0.14$), and in the limit become a straight pipe ($\gamma \to \infty$): The systolic pressure ratio increases slowly to the straight pipe value of 3.3 with γ.

A complete study is required with varying Re to determine the full variation of the systolic pressure ratio with γ. However, at the nominal Re of 100, the above bounds on γ provide a reasonable classification of the pressure variation for a range of arteries.

4.2.4 Effect of fetal heart-rate

To consider the effect of varying the fetal heart-rate, three simulations are conducted at $U_{red} = 30$, 50 and 70 for the U_{t1} artery and the tightly coiled geometry discussed in section 4.2.3. These reduced velocities correspond, in a nominal parameter space, to fetal heart rates of 191, 115 and 82 bpm, respectively, which encompass the broad variation observed in-utero. Flow reversal occurs in the straight pipe inlet flow for $U_{red} < 24$ ($\alpha > 5.2$) which corresponds to an extremely high fetal heart-rate of 240 bpm, all else nominal. It is therefore unlikely that flow reversal is present in the inlet flow of an umbilical artery under typical conditions.

For a straight pipe the steady pressure gradient depends only on the length of the pipe, while the components of the unsteady solution depend on the ratio $Re/U_{red} = \alpha^2/2\pi$, from equation (2.41). Figure 4.10(a) shows the variation of the ratio of the systolic and temporally averaged pressure with fetal heart-rate, f, at six values of Re for a straight tube with the umbilical waveform. Increases in both fetal heart-rate and flow Reynolds number result in increases to the systolic pressure ratio, however, Re provides the greatest impact. The variation of the fully developed helical flow profile at systole and diastole over the range of U_{red} is shown for U_{t1} in figure 4.11. As for the $U_{red} = 41$ case, the secondary and axial velocity increase at systole and the inclination of the two vortices to the pipe normal increases for both $U_{red} = 30$

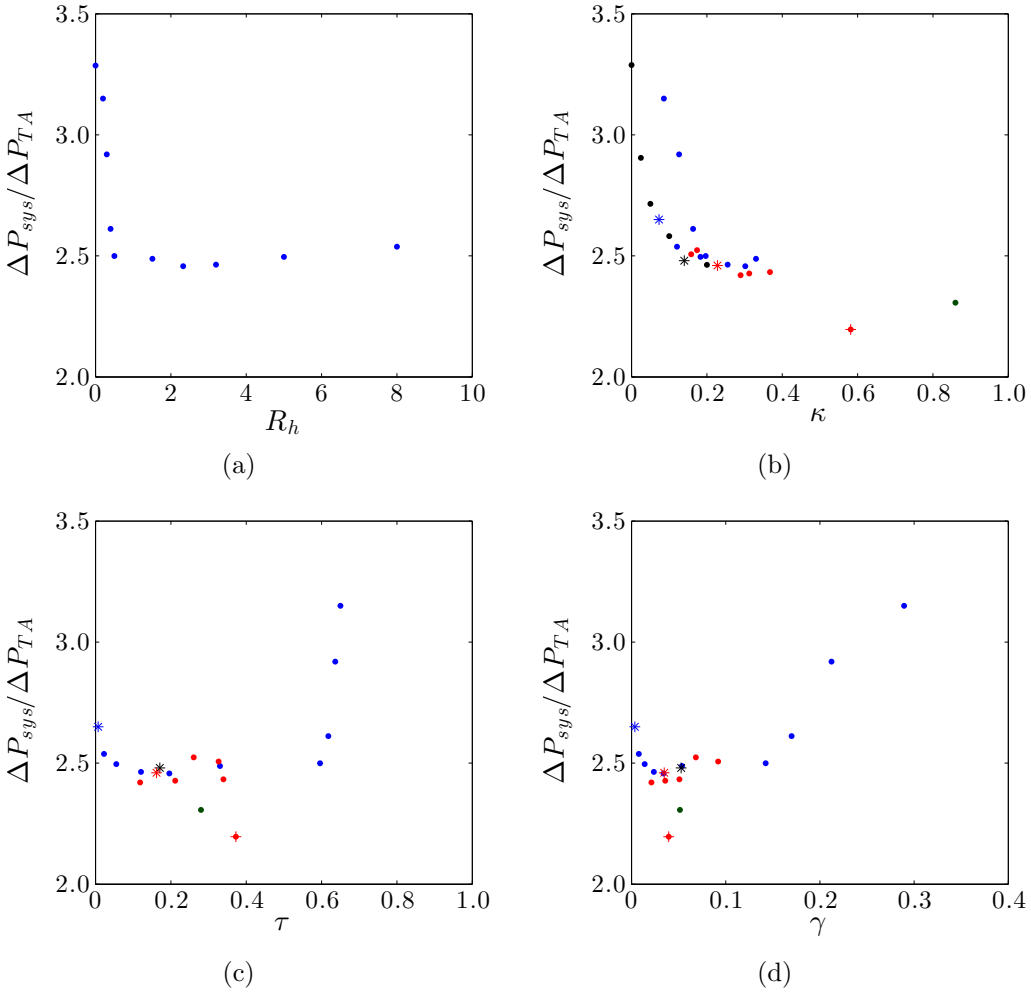

Figure 4.9: The ratio of peak systolic pressure and temporally averaged pressure ($\Delta P_{sys}/\Delta P_{TA}$) at $Re = 100$, $U_{red} = 41$ with; a) R_h for the U_c arteries; b) centreline curvature (κ), for the U_c (blue), U_t (red) and toroidal (black) arteries with U_{t1} denoted ($+$) and an additional highly coiled artery with $\kappa = 0.86$, $\tau = 0.28$ (green); c) centreline torsion (τ) and; d) the helical parameter, $\gamma = \mathrm{Gn}/\mathrm{Dn}^{3/2} = \tau/(\sqrt{2Re}\kappa^{3/4})$. The asterisks in (b)-(d) are points from the LK study with UCA ($*$), NCA ($*$) and OCA ($*$).

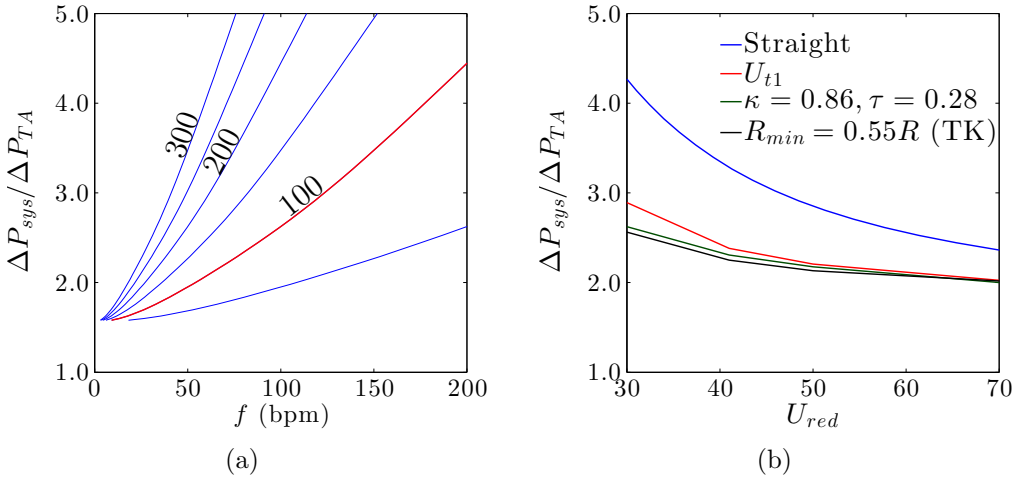

Figure 4.10: Variation of the ratio of peak systolic pressure (ΔP_{sys}) to the temporal average (ΔP_{TA}) for the umbilical waveform. a) Variation with fetal heart-rate (f) for varying Re in a straight tube. The red line indicates the nominal $Re = 100$. b) Variations with reduced velocity (U_{red}) for a straight tube (blue), artery U_{t1} (red), an additional, tightly coiled artery with $\kappa = 0.86$, $\tau = 0.28$, (green) and the tight true knot (TK) with $R_{min} = 0.55R$ (black), assuming all other parameters are nominal.

and 70. The flow profile changes only slightly with U_{red} with an increased secondary and axial velocity accompanying lower U_{red}, though this effect is quite subtle. The severity of flow reversal, which is not shown, also increases slightly for lower U_{red} and is present at both systole and diastole in the same locations as for $U_{red} = 41$. This feature is not present for $U_{red} = 70$. The variation of the pressure drop over a cycle for U_{t1} is shown in figure 4.12(a). The temporal average differs by less than 2% with U_{red}, however the ratio of the peak systolic and temporally averaged pressure ($\Delta P_{sys}/\Delta P_{TA}$) increases with decreasing U_{red}, or with all else constant, increasing heart-rate. The helical pressure gradient, shown in figure 4.12(b), reflects a similar pattern to the total pressure drop with more severe pressure gradients encountered for a reduction in U_{red}. Figure 4.10(b) compares the effect of varying the reduced velocity on the ratio for a straight tube, artery U_{t1} and the tightly coiled artery. As for $U_{red} = 41$, the ratio is significantly lower in the coiled arteries over the range of permissible U_{red}, though it varies little after the addition of coiling. The difference between the computed ratios also reduces with U_{red}, or decreasing heart-rate.

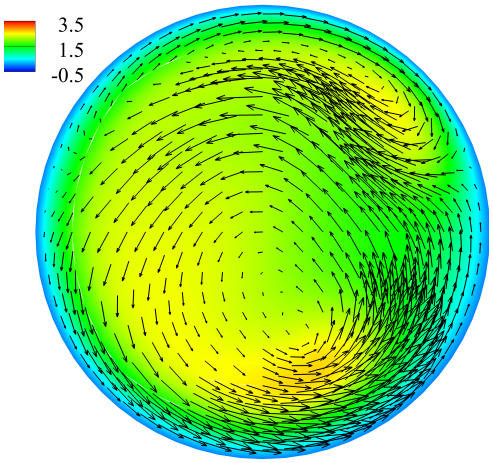

(a) $U_{red} = 30$; systole ($t/T = 0.15$)

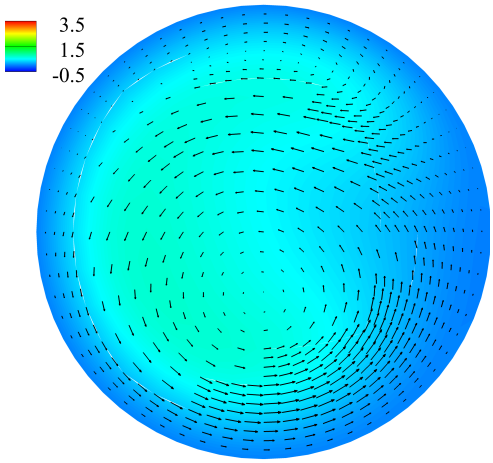

(b) $U_{red} = 30$; diastole ($t/T = 0.76$)

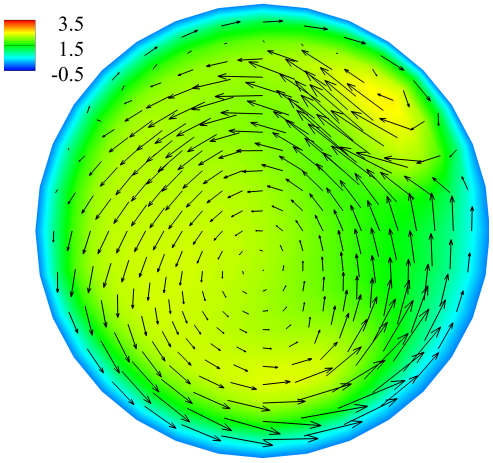

(c) $U_{red} = 41$; systole ($t/T = 0.15$)

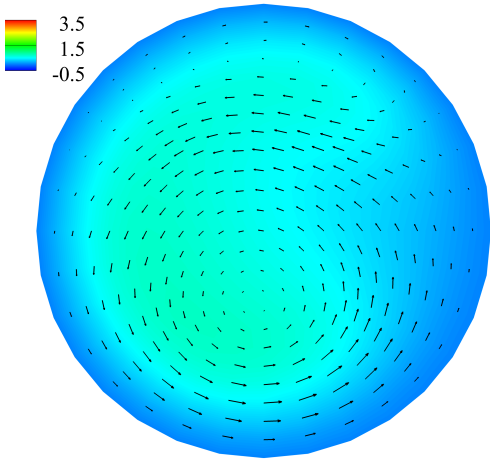

(d) $U_{red} = 41$; diastole ($t/T = 0.76$)

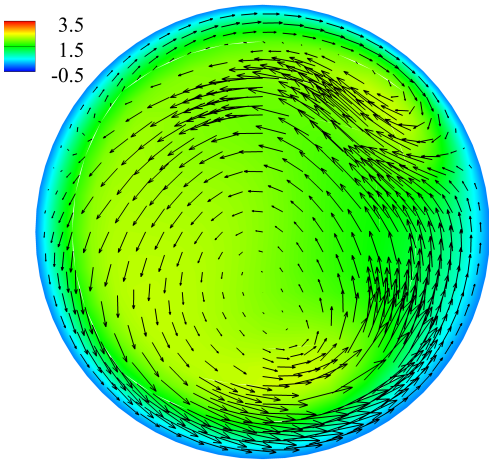

(e) $U_{red} = 70$; systole ($t/T = 0.15$)

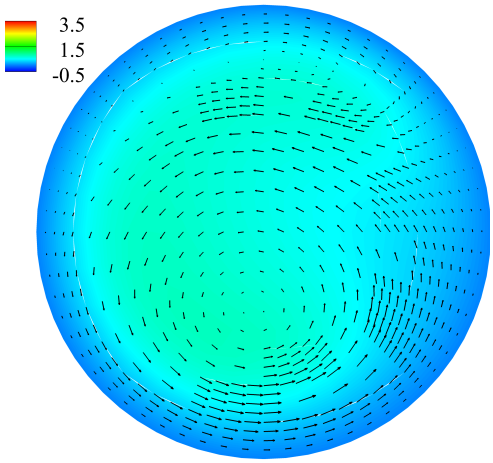

(f) $U_{red} = 70$; diastole ($t/T = 0.76$)

Figure 4.11: Helical flow variation with U_{red} for artery U_{t1} at systole (left) and diastole (right) at $Re = 100$, $U_{red} = 41$.

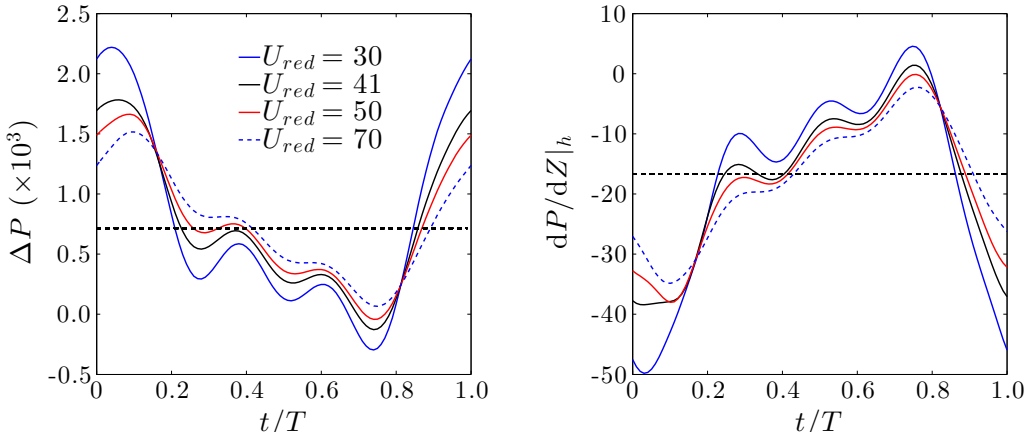

Figure 4.12: Variation of a) total pressure drop (ΔP) and; b) helical pressure gradient ($\mathrm{d}P/\mathrm{d}Z|_h$) with U_{red} for the U_{t1} geometry. The black-dashed line indicates the steady value computed in chapter 3.

4.3 Irregularly coiled cords

Pulsatile flow into three of the irregularly coiled arteries described in section 2.4.2 are considered here. These are $\mathcal{W}_{a,3}$, which has a relative width variance of 60% along the length, $\mathcal{S}_{a,3}$, which has a relative coil space variance of 120% along the length, and $\mathcal{C}_{a,1}$, which has both 60% relative width variance and 120% relative coil space variance. Figure 4.13 shows the variation of the total pressure drop over a fetal heart-beat. As for the steady computations there is little difference between the total pressure drop between the arteries despite the significantly varying curvature. The temporally averaged pressure drop in the nominal artery, $\mathcal{N}_a$, varies from the steady calculation by 5% with each of the irregularly coiled arteries in-turn varying by less than 2% from this value. The systolic pressure ratio computed for each geometry is virtually constant at 2.5, in-line with the results of the regularly coiled study. The variation of curvature and torsion along cord length is therefore of little impact to the pressure profile within the umbilical arteries for both steady and pulsatile flow.

4.4 Umbilical knots

This section presents the results of the pulsatile computations within knotted geometries described in section 2.4.3. In general, the temporally averaged pressure drop is well predicted by the steady pressure drop for both the loose

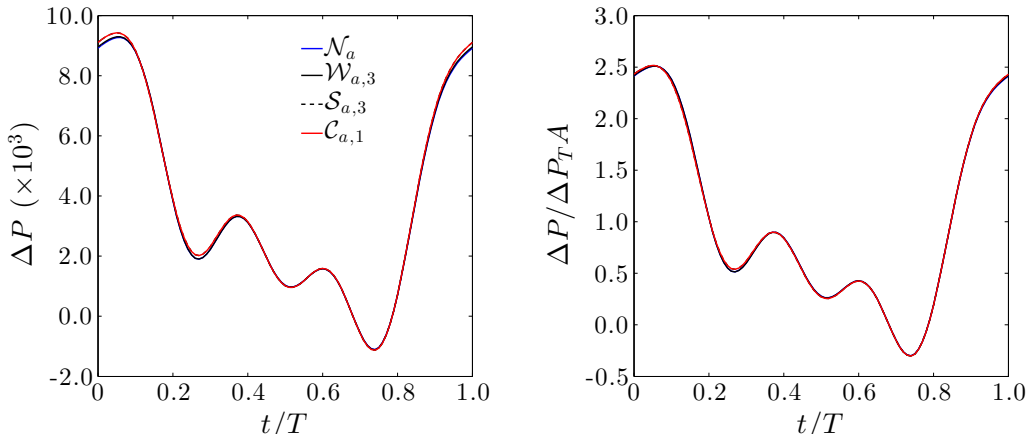

Figure 4.13: Variation of a) total arterial pressure drop and; b) normalised pressure drop, over one period through three of the irregularly coiled geometries considered previously. The regular helical geometry, $\mathcal{N}_a$ is included for comparison.

and tight knot arteries, however, the approximation becomes less accurate as constriction severity increases, reaching an error of approximately 10% for $R_{min} = 0.55R$. The peak systolic pressure ratio computed for the loose knot arteries varies in a manner consistent with the regularly coiled cords, while it reduces with constriction severity and U_{red} for the tight true knots. Flow reversal, previously observed for steady flow through tight true knots of $R_{min} < 0.875R$, is present aft of the constriction in the pulsatile computations for all tight true knots with $R_{min} \leq 0.875R$. The region of reversal becomes more pronounced with constriction severity and for lower U_{red}, where it is observed at the inside of the tube wall for the case with $R_{min} = 0.55R$.

4.4.1 Loose true knots

Variation of the total arterial pressure drop over a single period through the loose knot geometries is shown in figure 4.14(a), with the normalised pressure shown in figure 4.14(b). The pressure drop here is calculated over the entire geometry, purely helical sections included. The same general pattern is observed as for the regularly and irregularly coiled geometries; the longer over-coiled artery records the highest temporally averaged pressure, as well as the lowest diastolic minimum pressure, however, the pressure profile is broadly similar in each case. Normalising by the temporal average the NCA and OCA geometries exhibit a similar profile with roughly equivalent sys-

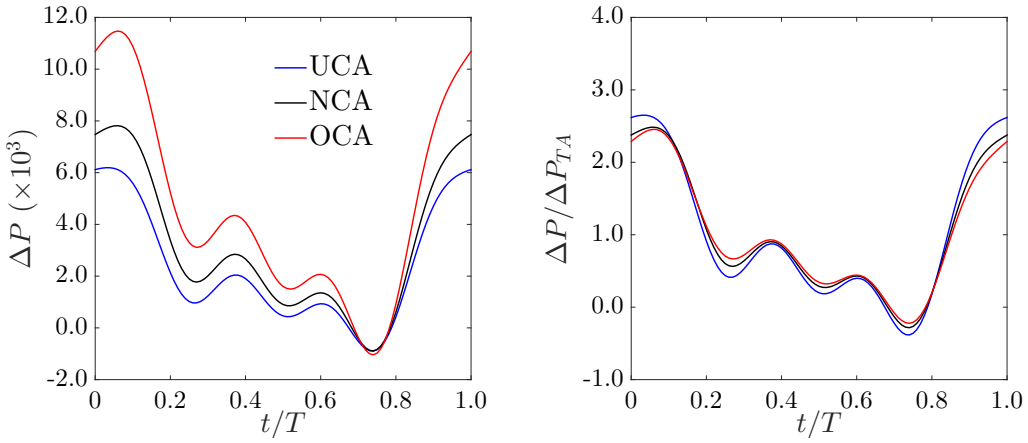

Figure 4.14: Variation of a) total pressure drop, and; b) pressure drop normalised by the temporally averaged pressure over one pulsation for the loose knot arteries of the under-coiled (UCA), normo-coiled (NCA) and over-coiled (OCA) geometries.

tolic pressure ratios. The UCA geometry has a slightly higher ratio, with the three geometries included in figure 4.9 for comparison with the curved and regularly coiled arteries already considered. The similarity between the systolic pressure ratio of helical, curved and the more generally varying knotted arteries further supports the observation that the presence of curvature (and torsion) on the centreline lowers the ratio regardless of whether the curve is a helix. The temporal average is also well approximated by the steady value with a discrepancy of 3% observed for the NCA geometry.

4.4.2 Tight true knots, false knots and twist reversal

The knotted geometries of the steady analysis are shortened to one coil on each side of the constriction in order to reduce computational cost of the unsteady simulations. For comparison, steady solutions are computed for all truncated geometries except the twist-reversal (TR) artery due to its similarity with the false-knot (FK) geometry in previous analyses.

The variation of the total pressure drop and normalised pressure drop over a period is shown in figures 4.15(a) and (b), respectively. As for the steady analyses there is typically less than 0.2% discrepancy between the temporally averaged, systolic and diastolic pressures of the TR and FK arteries, shown in table 4.3. The temporally averaged pressure in the $0.875R$ constriction is within 2% of the (unconstricted) false knot geometry, however, this discrep-

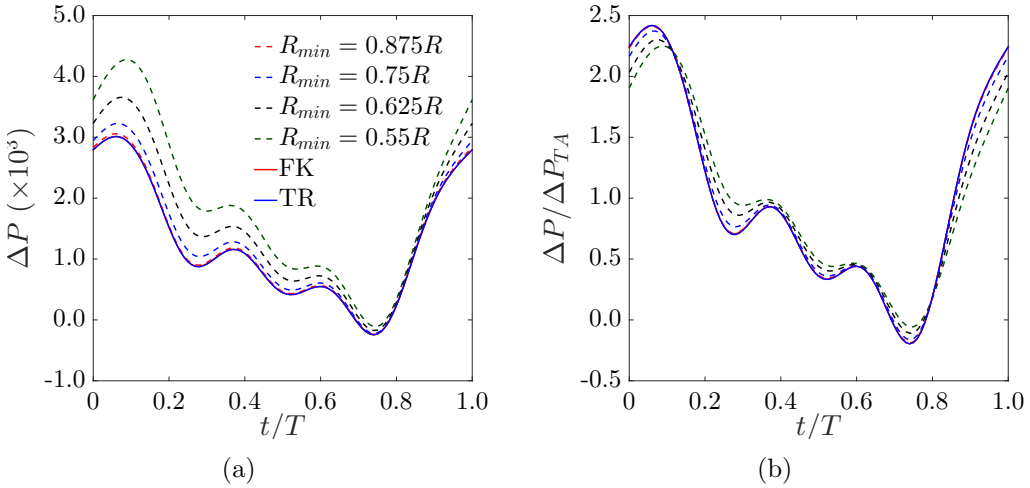

Figure 4.15: Variation of a) total pressure drop, and; b) pressure drop normalised by the temporally averaged pressure over one pulsation for the true knot (TK), false knot (FK) and twist-reversal (TR) geometries. The minimum radius is quoted in the legend for the TK geometries.

ancy grows to 10% for the $0.75R$ constriction and 52% for the $0.55R$ true knot. The addition of a constriction for the pulsatile calculations tends to increase the pressure throughout the cycle, however, the diastolic pressure is left relatively unaffected. This is a result of the severity of flow-reversal.

Flow reversal is observed in the steady computations with a constriction of size $R_{min} = 0.55R, 0.625R$ and $0.75R$, but not the $0.875R$ constriction. Within the pulsatile computations, however, each of the arterial geometries exhibit flow reversal. Contours and isosurfaces showing the flow reversal in the true knot arteries at systole and diastole are included in figures 4.16 and 4.17, respectively. For the $0.875R$ artery, flow reversal aft of the constriction is only present at pressure diastole; $0.7 < t/T < 0.8$, and is reasonably weak, occupying a small volume of the downstream region of the stenosis. Each of the remaining knots exhibit flow reversal behind the constriction throughout most of the period, with only a minor reduction in flow reversal volume near velocity diastole present in the most constricted, $0.55R$, geometry. No reversal is observed for the false knot or twist reversal arteries at any point in the period.

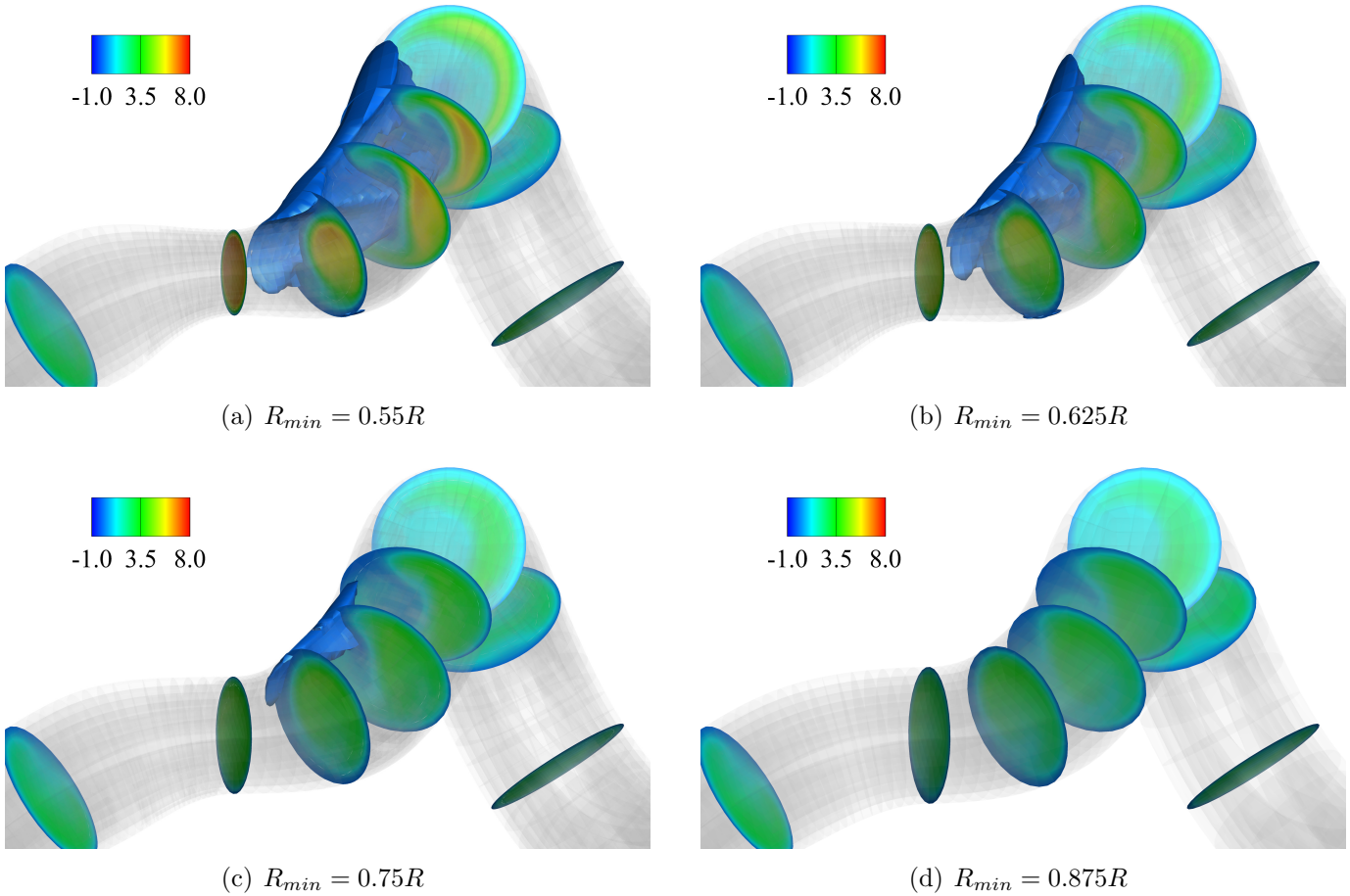

(a) $R_{min} = 0.55R$ (b) $R_{min} = 0.625R$

(c) $R_{min} = 0.75R$ (d) $R_{min} = 0.875R$

Figure 4.16: Contours and isosurfaces of axial velocity, W, at systole ($t/T = 0.15$) for the tight true knots. The blue isosurface is drawn at $W = -0.02$ and demarcates the region of flow-reversal.

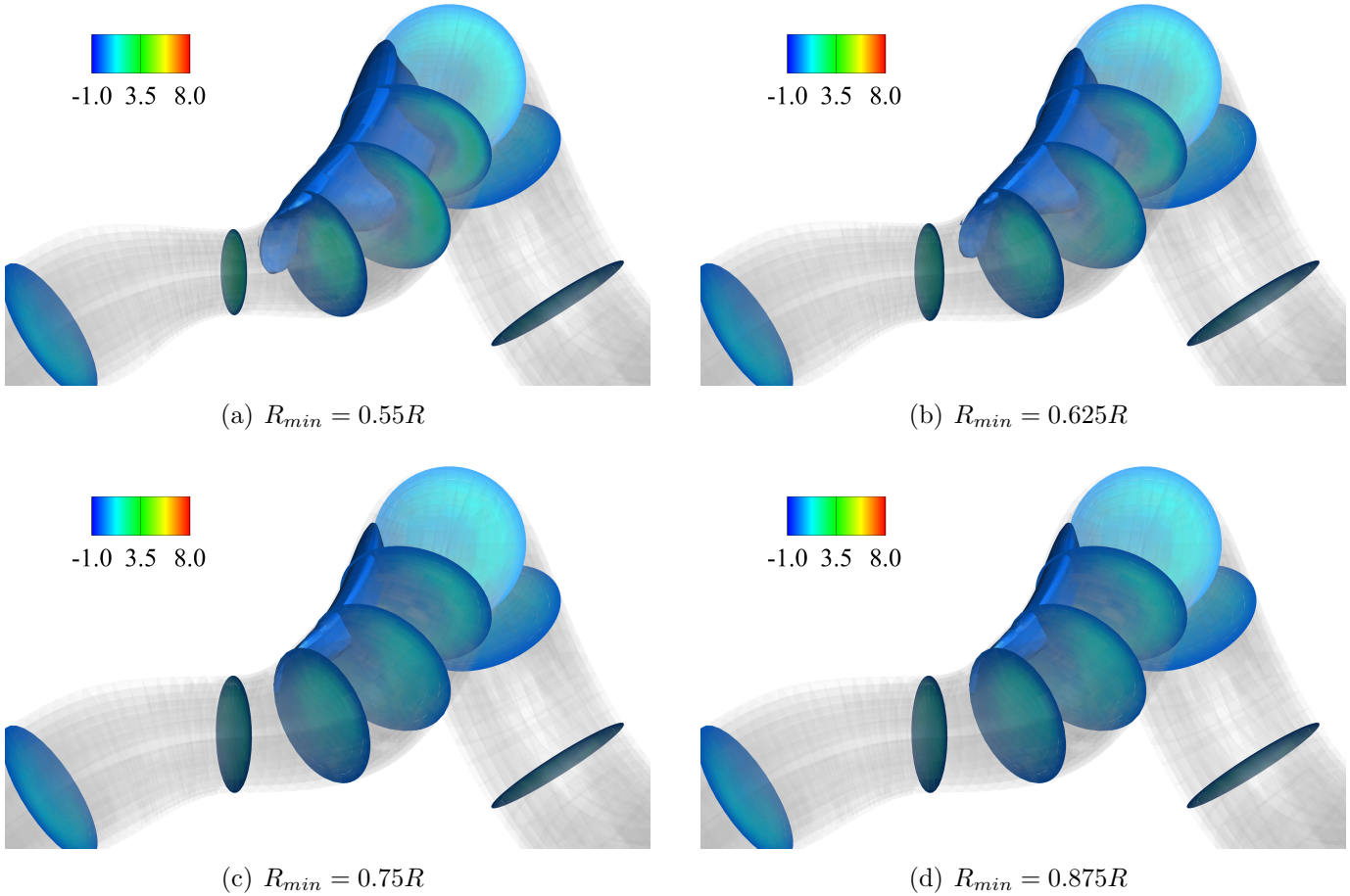

(a) $R_{min} = 0.55R$ (b) $R_{min} = 0.625R$

(c) $R_{min} = 0.75R$ (d) $R_{min} = 0.875R$

Figure 4.17: Contours and isosurfaces of axial velocity, W, at diastole ($t/T = 0.15$) for the tight true knots. The blue isosurface is drawn at $W = -0.02$ and demarcates the region of flow-reversal.

	ΔP_{TA}	ΔP_{steady} (δ %)	ΔP_{sys} /ΔP_{TA}	ΔP_{dias} /ΔP_{TA}
FK	1247	1178 (5.90)	3016 (2.42)	-244.8 (-0.20)
TR	1245	– (–)	3011 (2.42)	-245.0 (-0.20)
TK; 0.875	1268	1204 (5.29)	3059 (2.41)	-240.4 (-0.20)
TK; 0.750	1360	1278 (6.44)	3226 (2.37)	-223.6 (-0.16)
TK; 0.625	1589	1479 (7.43)	3655 (2.30)	-174.6 (-0.11)
TK; 0.550	1900	1750 (8.51)	4277 (2.25)	-108.3 (-0.06)

Table 4.3: Pulsatile pressure results for each of the shortened tight knotted arteries. The temporally averaged inlet pressure, ΔP_{TA}, is compared with the steady results at $Re = 100$, as well as the systolic, ΔP_{sys}, and diastolic pressure, ΔP_{dias}. The relative difference between the steady and temporally averaged results is computed by $\delta = (\Delta P_{TA} - \Delta P_{steady})/\Delta P_{TA}$.

The steady pressure drop predicts the temporally averaged pressure to within 6% for the false knot, twist reversal and $0.875R$ constriction, however, this discrepancy grows with constriction severity to 8.5% for the $0.55R$ artery. There is also a reduction in the peak systolic pressure ratio with constriction radius, shown in figure 4.18(a). The unconstricted case exhibits a ratio of approximately 2.42, typical of the results of the regularly coiled cords. However, the presence of constriction causes a reduction to 2.37 for the $0.75R$ artery and 2.25 for the $0.55R$ geometry.

4.4.3 Effect of fetal heart-rate

Variation of the fetal heart-rate, considered previously for artery U_{t1} in section 4.2.4, is analysed here for the most constricted knot with $R_{min} = 0.55R$. The total pressure drop variation over a period is shown in figure 4.18(b), where the typical trend is as for the U_{t1} artery; the lower reduced velocity computations yield larger total arterial pressure fluctuations, though the temporal average varies by less than 2%. The variation of the peak systolic pressure ratio with U_{red} for the most constricted knot is plotted in figure 4.10(b), with the results for a straight tube and two high curvature, regularly coiled arteries. As shown in section 4.2, regularly coiled vessels have a substantially lower peak systolic pressure ratio compared with straight vessels, however, the variation among cords which may have vastly different torsion and curvature is not significant, provided $0 < \gamma < 0.14$. Despite the presence of a

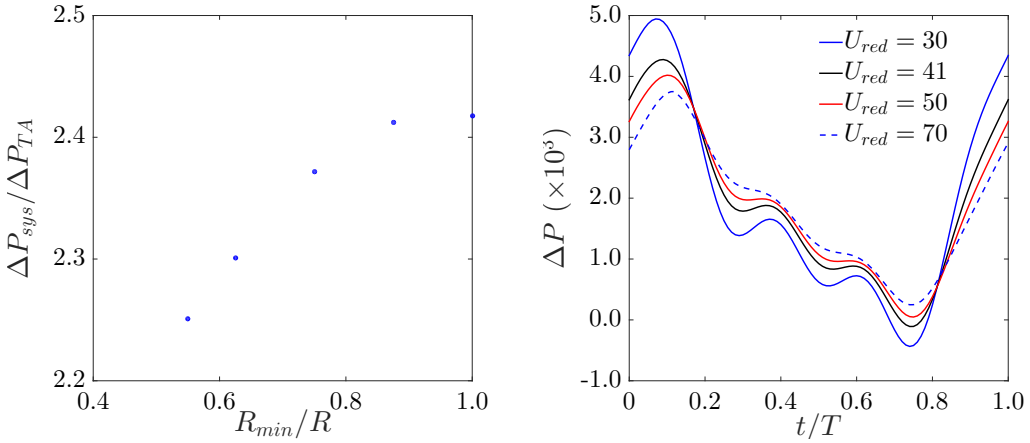

(a) (b)

Figure 4.18: a) Variation of the peak systolic pressure ratio with constriction severity, R_{min}/R, for the tight true knot geometries, and; b) variation of inlet pressure with U_{red} over a period for the $0.55R$ constriction.

constriction to almost half the nominal radius, the tight true knot geometry exhibits a similar normalised pressure profile.

Flow reversal is observed over the range of U_{red} studied, with the streamwise extent increasing slightly as U_{red} reduces. For $U_{red} = 30$, flow reversal is present aft of the constriction for the entire period, with regions around the inside of the artery showing reversed flow at velocity diastole. Figure 4.19 shows the region of reversed flow with $U_{red} = 30$ at systole. The jet maximum is clearly visible on the outside of the tube. The remaining computations at $U_{red} = 50, 70$ have qualitatively similar appearance, though the strength of the jet is less significant.

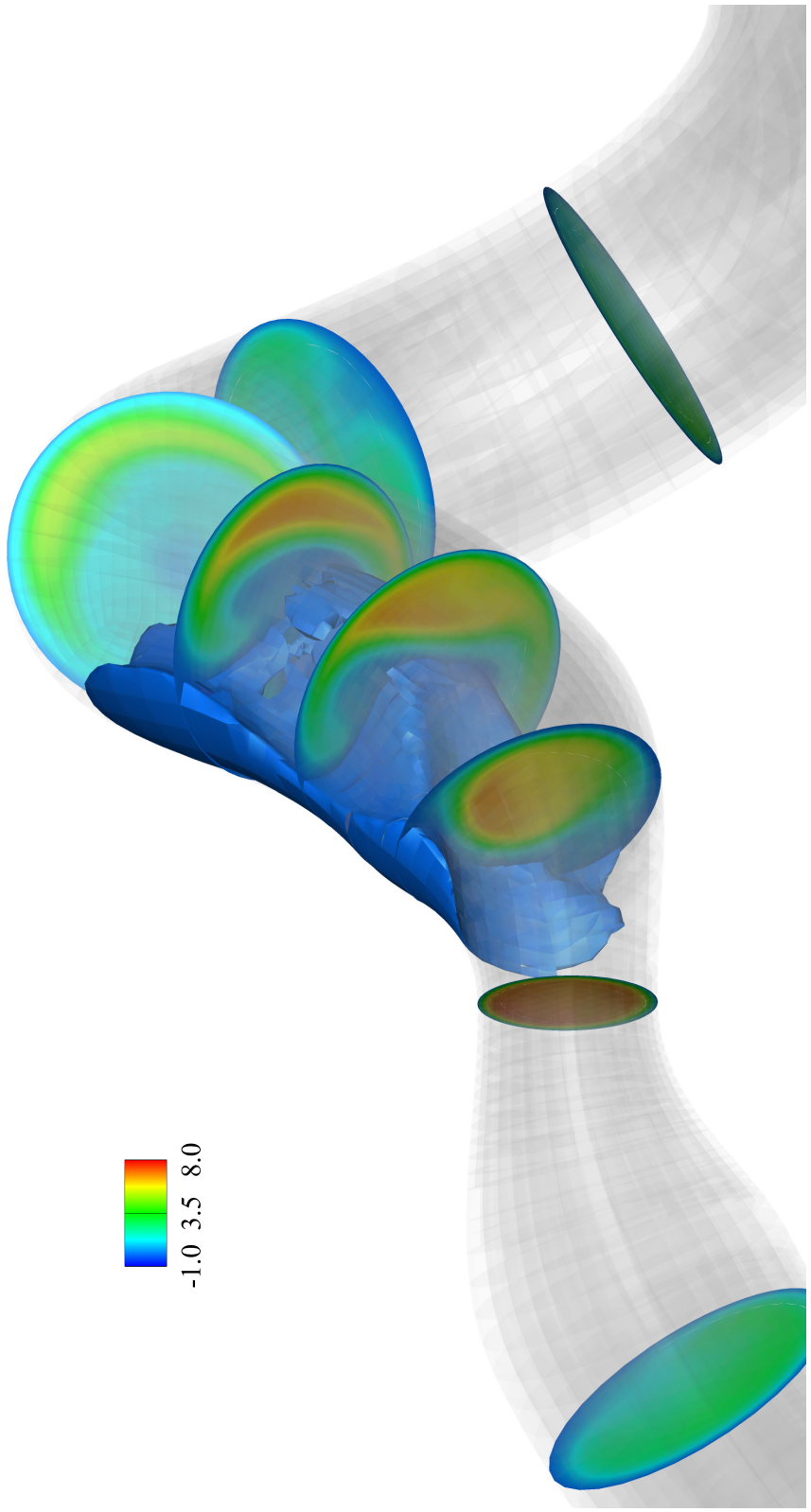

Figure 4.19: Contours and isosurfaces of axial velocity, W, at systole ($t/T = 0.15$) for the tight true knot with $R_{min} = 0.55R$ at $U_{red} = 30$. The blue isosurface is drawn at $W = -0.02$ and demarcates the region of flow-reversal.

4.5 Conclusion

Throughout this chapter an unsteady analysis of blood flow within geometries representative of the umbilical arteries was presented. The aim was to determine the effect of pulsatility on the pressure characteristics of a number of arterial geometries and, specifically, the relevance of a steady computation within a similar parameter space in predicting the average pressure drop. To achieve this an umbilical waveform representative of blood flow within the arteries was constructed based on a simple 'saw-tooth' profile approximated by a finite Fourier series expansion. This waveform describes the variation of the centreline velocity throughout a period of the fetal heart-beat; a quantity typically measured in-utero. To ensure convergence of the temporal solvers and the selection of an appropriate timestep, a numerical validation study was completed on the U_{t1} arterial geometry with the solvers found to be limited by spatial resolution, as was the case in the initial validation study of chapter 2. The regularly coiled geometries were then examined with nominal blood flow characteristics of $Re = 100$ and $U_{red} = 41$, before an analysis of the U_{t1} geometry over a range of U_{red} to investigate the variation of the fetal heart-rate, f. Flow within three irregularly coiled arteries was then analysed to determine the effect of varying coil and width spacing, with a further study of flow through loose true knots, tight true knots and false knots in order to assess the effect of pulsatile flow within non-standard geometries.

Through the aforementioned studies it was determined that the temporal average of the unsteady pressure drop (ΔP_{TA}) is predicted to within 5% by the steady results for each of the regularly and irregularly coiled geometries as well as the loose knots considered, and to within 10% for the tight true knots exhibiting severe constriction. The pressure profile throughout the period is also remarkably uniform among the regularly coiled geometries when normalised by the average, with systolic and diastolic pressures typically around 2.4 and -0.2 times the temporal average, respectively. The systolic pressure ratio is well predicted by the helical parameter, $\gamma = \mathrm{Gn}/\mathrm{Dn}^{3/2}$, which in this constant Re study essentially represents a ratio of torsion and curvature. Low (but non-zero) γ cords were found to have roughly equal systolic pressure ratios approximately 25% below the straight pipe value for $0 < \gamma < 0.14$, while larger γ cords, had larger systolic pressure ratios, similar to the straight pipe case. For the case of $\gamma = 0$, where tubes curve in-plane, the systolic pressure ratio reduces with increasing curvature at a higher rate than geometries exhibiting non-zero torsion. Furthermore, data for the loose knot arteries, which have variable torsion and curvature along the length, fit well amongst the remaining arteries. This suggests that the presence of curvature and torsion substantially lowers the peak systolic pressure ratio compared with a

straight tube of equivalent length, regardless of the geometric description of the curve. The presence of coiling, or any smooth curvature, in the umbilical arteries therefore acts to dampen extreme pressures at a given Re when compared with an equivalent length of straight tube. This fact may offer another possible explanation for the presence of coiling within the typical umbilical geometry.

As in the steady simulations, irregularly coiled cords present the same pressure profile as for the nominally coiled cord of equivalent average coil spacing and width. Despite relative variations of up to 120% in coil spacing, and 60% in width, the temporally averaged pressure drop was determined to vary by less than 2%. Reductions in the reduced velocity, U_{red}, were found to increase the ratio of the systolic pressure drop to the temporal average, all else being equal. Changes to the reduced velocity, however, were not observed to appreciably affect the temporal average for the U_{t1} artery, or the tight true knot with a minimum radius of $0.5R$. A fetus with a higher heart-rate may therefore experience larger pressure fluctuations throughout the period, whilst maintaining an otherwise normal, temporally averaged pressure drop.

Finally, knotted arteries typically exhibit a total arterial pressure drop consistent with the steady value, however, the discrepancy was noted to increase to approximately 10% for the tight true knot of constriction radius $0.55R$. Flow reversal, which is dependent on the inlet flow, was found to present in all tight true knot arteries aft of the constriction, becoming more severe with a reduction in U_{red}, or equivalently, an increase in fetal heart-rate.

In conclusion, the steady flow calculated through geometries representative of the umbilical arteries can be used to estimate the temporally averaged pressure drop to within 5% for arteries without any cross-sectional reduction, with larger errors of up to 10% observed for constrictions to $R_{min} = 0.55R$. The systolic pressure ratio is relatively constant among coiled vessels, meaning that a typical arterial pressure cycle oscillates between a systolic pressure 2.4 times the mean pressure and a diastolic pressure -0.2 times the mean. Knowledge of the steady pressure drop can consequently be used to provide an accurate estimate of the extreme pressures present within a typical artery. This study therefore validates the concept of employing the steady pressure drop as a proxy for the pulsatile pressure variation in the umbilical arteries over a wide range of geometries likely within pregnancy.

Chapter 5

New indices for quantifying umbilical flow resistance

The inability of the UCI to predict the pressure drop through helical geometries representative of the umbilical vessels is demonstrated in chapter 3. Deviations from the regularly coiled geometry, including linearly varying pitch and width, as well as the addition of true and false knots, have little effect on the axial pressure drop provided there is minimal constriction of the vessel. The analysis of unsteady flow in chapter 4 demonstrates that the steady pressure gradient typically represents the time-averaged pulsatile value, and hence can be used as an accurate substitute. As described in chapter 1, current empirical relations for the steady flow friction factor, in particular Liu and Masliyah (1993), cover a large range of τ, κ and Dn. These relations can be used to estimate the steady pressure drop through a range of helical geometries with varying accuracy and applicability. There is, however, no suitable relation for vessels with low Dean number, low κ and non-zero τ.

Here we present a methodology for estimating the flow resistance associated with a given cord based on the calculation of the cord pressure drop. This method is simple and in its most basic form requires only one additional geometric measurement to the calculation of the UCI; namely the cord coiling width, $\hat{w}$. Two related cord indices; the umbilical pressure index, PX, and the umbilical flow index, QX, are defined in order to assess the severity of the cord geometry. PX provides a comparison between the umbilical vessel pressure drop at a standard blood flow-rate to a reference pressure through a defined normo-coiled cord. In this way, cords which develop a larger vessel pressure have $PX > 1$, while cords with lower pressure will yield $PX < 1$. The umbilical flow index, QX, compares the blood flow-rate through a given cord at reference pressure to the reference blood flow-rate. Cords with low flow-rate therefore have $QX < 1$ while those with a higher flow-rate for the

standard pressure have $QX > 1$. The relationship between the two indices is dependent on the length, curvature and torsion of the cord, with cords of high PX exhibiting low QX and vice versa. Both index calculations are based on non-invasive, geometric cord measurements so as to be easily implemented in a clinical setting. These measurements are then used to construct helical vessel geometries representative of the average cord coiling. A combination of empirical and interpolated numerical data is then used to determine the pressure drop through the cord vessels, with the Newton-Raphson method employed for the inverse flow-rate problem.

This chapter begins with a comparison of the steady helical results of chapter 3 to empirical predictions available in the literature. It is shown that the empirical relation of Liu and Masliyah (1993) is a useful and time-efficient alternative to the full numerical solution for a large range of cords. This empirical relation, however, is not applicable for the entire parameter range needed to compute the index for all physically realistic cords. For this set of parameters, additional numerical results are computed at discrete τ, κ and nominal Re. The two solution sets are then combined using radial-basis interpolation in order to provide a complete picture of the flow resistance for a range of cords. The results of the full numerical study of irregularly coiled and geometrically knotted cords are then compared with empirical estimates of the pressure drop for the mean helical vessels. It is found that the empirical estimates provide a reasonably accurate estimate of the actual pressure drop, validating their use in quantifying pathology.

The umbilical flow and pressure indices are defined with respect to a suitable reference cord and it is found that the UCI and these new indices deviate significantly over a range of parameters. To be useful in a clinical setting it is important that a diagnostic index is stable to input error. A sensitivity analysis shows that the pressure and flow indices are robust with respect to slight input perturbations. Finally, several example cords are chosen to illustrate calculation of the indices and the clinical implementation is also discussed.

5.1 Helical pressure gradient estimates

The review of empirical friction factor relations for helical pipes presented in chapter 1 includes a number of possible estimates which may be used in the calculation of the steady pressure gradient along the length of the umbilical vein or arteries. Of these correlations, the one developed by Liu and Masliyah (1993) is the most accurate over a wide-range of helical geometries of finite

pitch at the desired Re. This correlation is restated here for convenience,

$$fRe = \left(16 + \left(\sqrt{2} \times 0.378 Re^{1/2} + 12.1\kappa^{-1/2} Dn^{-1/2}\right)\tau^2\right) \times \left(1 + \frac{\left(0.0908 + 0.0233\kappa^{1/2}\right) Dn^{1/2} - 0.132\kappa^{1/2} + 0.37\kappa - 0.2}{1 + 49/Dn}\right), \tag{5.1}$$

which requires,

$$Dn \leq 5000, \qquad \gamma = \frac{Gn}{Dn^{3/2}} = \frac{\tau}{\sqrt{2Re}\kappa^{3/4}} < 0.1,$$

where Gn is the Germano number ($2\tau Re$) and Dn is the Dean number ($2Re\kappa^{1/2}$). The first constraint is satisfied for blood flow within both umbilical vessels as the Dean number typically lies between 40 and 150. However, the second constraint is not always met. Figure 5.1 shows the torsion and curvature over which the empirical formula in equation (5.1) is inapplicable (shaded) with the relative position of each of the regularly coiled cords previously studied. As Re decreases the envelope in which the empirical formula may be used narrows. At $Re = 100$, most of the previously studied cords fall within the acceptable region except those with low helical radius from the U_c study. Figure 5.1(b) highlights the importance of the curvature compared with the torsion of the cord at the nominal Re; for low τ contours of pressure gradient are approximately lines of constant curvature. As κ increases, however, the torsion typically has a more pronounced effect, increasing the magnitude of the pressure gradient. At low κ the second constraint is not satisfied for relatively low τ. This can lead to large errors in the computed pressure gradient as will be demonstrated in section 5.1.1.

5.1.1 Comparison with numerics

For the regularly coiled vessels with $\gamma < 0.1$, the axial pressure gradient through the helical section is well predicted by equation (5.1). Figures 5.2(a) and (b) compare the helical pressure gradient for the U_t vessels computed using this relation and the numerical results from chapter 3 over a range of Re. For the numerical results the pressure gradient is calculated at a section of the cord sufficiently far removed from the boundaries so as to minimise entrance and exit effects. As the arclength of cord U_{t1} is quite small, this geometry is the most susceptible to this error. Despite this, very good agreement between the empirical and numerical results is present for the U_t geometries in general, particularly at $Re = 100$ where the relative

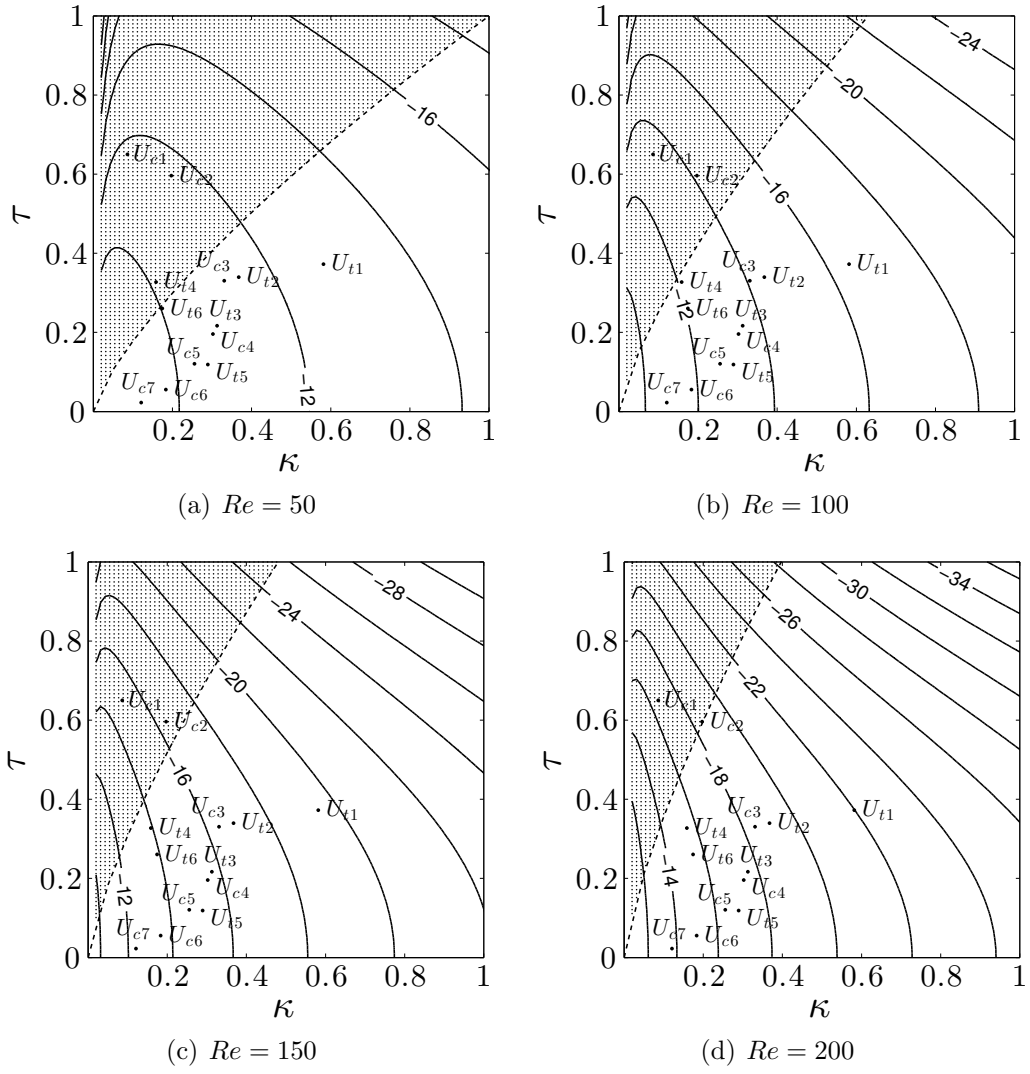

(a) $Re = 50$ (b) $Re = 100$

(c) $Re = 150$ (d) $Re = 200$

Figure 5.1: Contours of constant pressure gradient computed using the correlation of Liu and Masliyah (1993) at four Re. The dashed black line indicates the locus of geometries with $\gamma = 0.1$. The formula is inapplicable to the left of this line (shaded), where $\gamma > 0.1$.

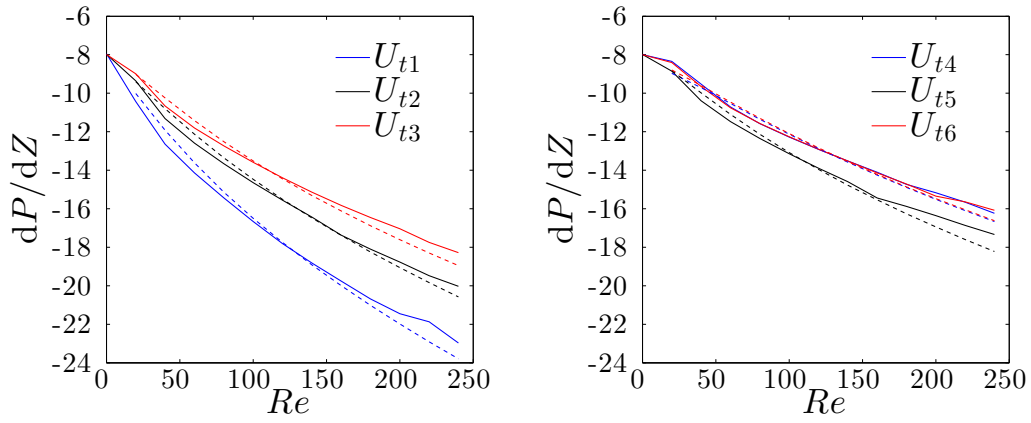

(a) (b)

Figure 5.2: The helical pressure gradient variation with Re for the numerical calculations (solid) compared with the theoretical formula of Liu and Masliyah (1993) (dashed), for the U_t vessels.

difference is typically within 1.5%. Table D.1 in appendix D.1 shows the error in the empirical formula for each of the regularly coiled cords at $Re = 100$. From figure 5.1 the $U_{c,1}$, $U_{c,2}$ and additional small R_h vessels considered in section 3.2.2 lie outside the bounds of Liu and Masliyah (1993). To illustrate the divergence of the empirical estimates for low curvature and moderate torsion a selection of correlations from the literature are plotted against the numerical results of chapter 3 at $Re = 100$ in figure 5.3. Here the red-dashed line indicates the helical radius at which $\gamma = 0.1$, and hence vessels to the left of this are outside of the Liu and Masliyah (1993) correlation. This relation, as noted for the U_t vessels, performs particularly well for $\gamma < 0.1$. For low R_h, however, the pressure gradient is significantly over-estimated with relative errors in excess of 60%. The relations proposed by Van Dyke (1978) and Mishra and Gupta (1979) are also inaccurate for most R_h. This gap in the literature motivates the work of the following section in which additional numerical results are calculated for the region of interest.

5.1.2 Evaluation of ΔP for cords with $\gamma > 0.1$

The empirical relation of Liu and Masliyah (1993) predicts the helical pressure gradient well provided the parameter $\gamma = \tau/(\sqrt{2Re}\kappa^{3/4}) < 0.1$. However, for cord vessels which do not satisfy this constraint there is a significant lack of accurate empirical data available in the literature. The cord vessels with $\gamma > 0.1$ considered previously have very low helical radius and hence

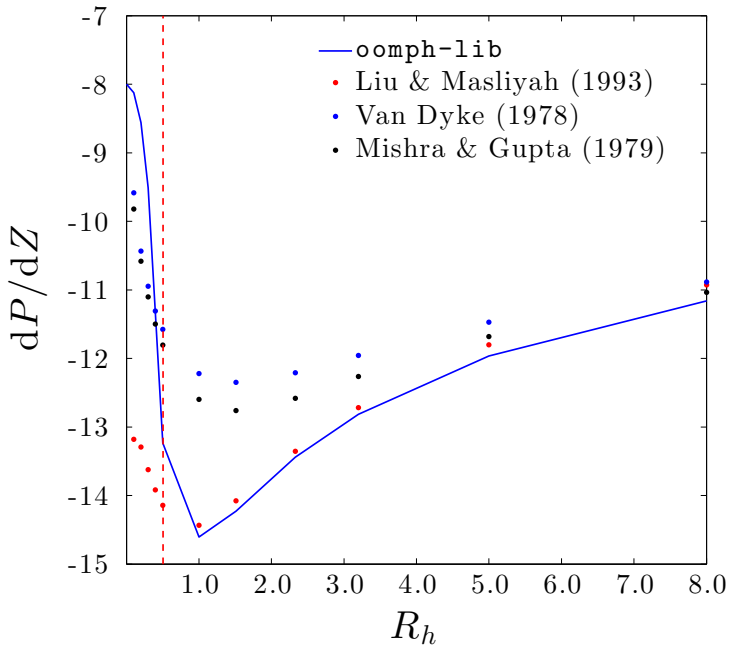

Figure 5.3: The helical pressure gradient versus helical radius for the U_c study showing a comparison of a number of empirical pressure gradient estimates at $Re = 100$. To the left of the red-dashed line vessels have $\gamma > 0.1$.

coiling width; geometries which are not necessarily phyiologically realistic. It is therefore tempting to simply ignore this category of vessels as an irrelevant extreme case. However, it is possible for a cord with normo-coiling and physiological dimensions to have $\gamma > 0.1$. Figure 5.4(a) shows the range of cords which are both physiologically realistic and which lie outside of correlation at $Re = 100$. As an example, using standard values a cord with a coiling width of 1.27 cm and a clinical UCI of 0.2075 coils/cm corresponds to a vein with $\kappa = 0.15$, $\tau = 0.4$ and $\gamma = 0.18$. It is also true that the vessel coiling need not reflect that of the whole cord (see figure 1.6 on page 8) and hence pressure gradient data must be available for a large range of vessels to provide a complete diagnostic picture.

This gap in the literature is bridged by steady numerical computations at $Re = 100$ through a number of helical geometries of discrete τ and κ satisfying $\gamma \geq 0.1$. The results are then concatenated with empirical estimates for $\gamma < 0.1$ to provide a coarse mesh of pressure gradient data for interpolation, (κ_i, τ_i, P'_i). Two-dimensional radial basis functions are used for this task, with the interpolant defined as

$$P'(\kappa, \tau) = a + b_1\kappa + b_2\tau + \sum_{j=1}^{N} c_j \sqrt{(\kappa - \kappa_j)^2 + (\tau - \tau_j)^2}, \qquad (5.2)$$

where $a, b_1, b_2, c_1, ..., c_N$ are constants determined from $N+3$ conditions. The first N conditions arise from simply requiring the interpolant reproduce the pressure gradient at the discrete data points,

$$P'(\kappa_i, \tau_i) = P'_i, \quad i = 1, ..., N.$$

The final three conditions are,

$$\sum_{j=1}^{N} c_j = 0, \quad \sum_{j=1}^{N} c_j\kappa_j = 0, \quad \sum_{j=1}^{N} c_j\tau_j = 0. \qquad (5.3)$$

The pressure gradient interpolant (P') and data mesh are shown in figure 5.4(b). Comparison with the unmodified correlation of figure 5.1(b) shows that the gradient for low curvature is reduced to allow continuity with straight cords for which $\kappa = 0$ and $\mathrm{d}P/\mathrm{d}Z = -8$. Additional smoothing of this data is unnecessary as the slight variations in the gradient do not appreciably affect the total pressure drop.

5.1.3 Non-helical vessels

From chapter 3 the total pressure drop through irregularly coiled or geometrically knotted vessels is closely approximated by the pressure drop through the

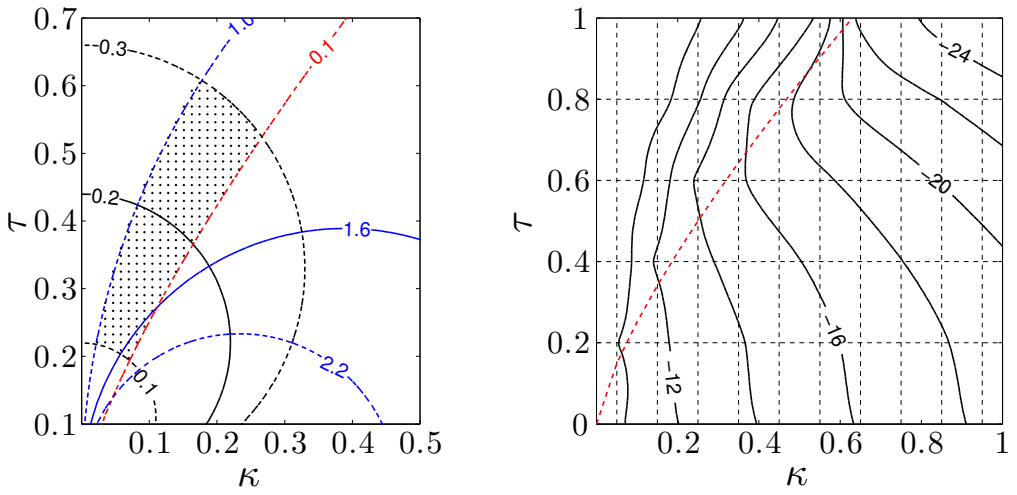

(a) (b)

Figure 5.4: Plots of τ and κ showing; a) the region outside of the correlation of Liu and Masliyah (1993) but within typical geometric bounds for an umbilical vein (shaded). Points to the left of the red-dashed line ($\gamma = 0.1$) are outside correlation. The black lines indicate three contours of UCI ($\hat{U}_c$, in coils/cm) at 0.1, 0.2 and 0.3 coils/cm, while the blue lines show the width in cm at 1.0, 1.6 and 2.2 cm. The shaded area is outside of the empirical correlation but within typical bounds for both UCI and width. The curvature and torsion here are non-dimensionalised by the vein radius (0.35 cm); b) The helical pressure gradient at $Re = 100$ calculated using a radial basis interpolation of numerical and empirical results. The mesh shows the points used for interpolation; `oomph-lib` for $\gamma > 0.1$ and Liu and Masliyah (1993) for $\gamma < 0.1$.

corresponding helical vessel of mean coiling. It therefore follows that an estimate of the latter can be used to determine the pressure drop through complex vessel geometries without requiring full computation. Another method involves determination of the total pressure drop via the continuously varying pressure gradient interpolant, $P'(\kappa, \tau)$, defined in section 5.1.2, where $\kappa = \kappa(Z)$ and $\tau = \tau(Z)$. This method assumes that the pressure gradient at a given point along a continuously varying centreline can be determined from the torsion and curvature at this point alone. This is not necessarily true in general, however, for slowly varying geometries at low Re the approximation performs quite well. The total vessel pressure drop is then found from,

$$\Delta P = \int_0^{L_Z} -P'(Z)\mathrm{d}Z, \tag{5.4}$$

where equation (5.4) is numerically evaluated using the trapezoidal method. To illustrate, figure 5.5 shows the results for three irregularly coiled and two geometrically knotted vessels. The centreline trace for each irregularly coiled cord is shown in figure 5.5(a) while the corresponding trace for the loose knot vessels is much more erratic and hence not included here. This method reproduces the axial pressure gradient along the vessel length for each irregularly coiled cord with reasonable accuracy, shown in figure 5.5(b). The highest error typically occurs at the end of lowest curvature, where the numerical data is used for interpolation. This error, however, is at most 10% of the gradient. For the knotted vessels, the approximation improves with UCI as the helical component of the curvature becomes more significant. The peaks are typically under-estimated though this is within around 0.5% for the OCA vessel.

Despite the promising results, this method is generally impractical as it requires detailed knowledge of the vessel centreline which is not usually available during pregnancy. Three-dimensional imaging, however, could allow the construction of a model of the vessel centreline over which such a procedure may be applied. This method is particularly suited to cords which are difficult to describe in terms of the helical parameters alone. For cords which are very nearly helical, however, the centreline method does not in general improve the total pressure drop estimate compared to the value computed using the mean helical vessel. The biggest improvement is observed for the UCV geometry, where the mean helical gradient is in error by 10.4%, with integration of the interpolated pressure gradient along the centreline reducing this error to 4.2%. In some cases, however, the centreline method actually increases error. This is particularly true if the underlying centreline is very close to helical. This method therefore shows promise for non-uniformly coiled cords where the curvature and torsion vary significantly along the length. As a

simple, discretised approach, the pressure drop for sections of such a vessel can be calculated based on the individual mean helix and then summated to determine the total pressure drop. This is explored further in section 5.3.

5.1.4 The UCI and pressure prediction

The steady analysis of chapter 3 demonstrates the inability of the UCI to predict the pressure drop through the umbilical vessels by comparing the value computed numerically in a small number of cords with equivalent coiling index. Using the composite solution developed in section 5.1.2, this result can be extended more generally through calculation of the pressure in each of the vessels over a range of coil width and UCI. Figures 5.6(a) – (d) show the variation of a number of vessel parameters with N and $\hat{L}_p$ for helical cords of nominal width, $\hat{w} = 1.6$ cm, at $Re = 100$. Radial lines on these figures trace out paths of constant clinical UCI. Intuitively, the helical arclength increases with both the total pitch length of the vessel and the number of coils, shown in figure 5.6(a). At a coil width of 1.6 cm, the downstream pressure gradient is approximately constant with UCI, tracing radial lines in figure 5.6(b). The total vessel pressure drop, however, is found via multiplication of these two parameters and is shown in figure 5.6(c) for the standard vein, and figure 5.6(d) for the corresponding artery. Contours of vessel pressure in each case differ significantly from the radial UCI contours further supporting the result from chapter 3 that the UCI is unable to predict the total cord vessel pressure drop.

While the UCI is fairly constant with pressure gradient at low values of the coiling index, seen in figure 5.6(b), this is not true in general as the UCI is increased. From figure 5.7 width effects become important for UCI > 0.5 coils/cm. For lower coiling, the UCI may be used to estimate the pressure gradient, however the total length (which depends on width), is still necessary to calculate the total vessel pressure drop.

5.2 Toward a new index

It is shown in section 5.1.4 that reduced vessel curvature and length lower the total pressure drop at constant flow-rate. Conversely, increasing these parameters results in an elevated pressure drop through helical vessels. While it is a reasonable first assumption, the flow-rate is not necessarily maintained in a cord with pathology. In reality it is likely that some amount of compromise is achieved between the flow-rate and pressure in order to reach equilibrium in a given vessel. Cords exhibiting pathology may therefore present a combi-

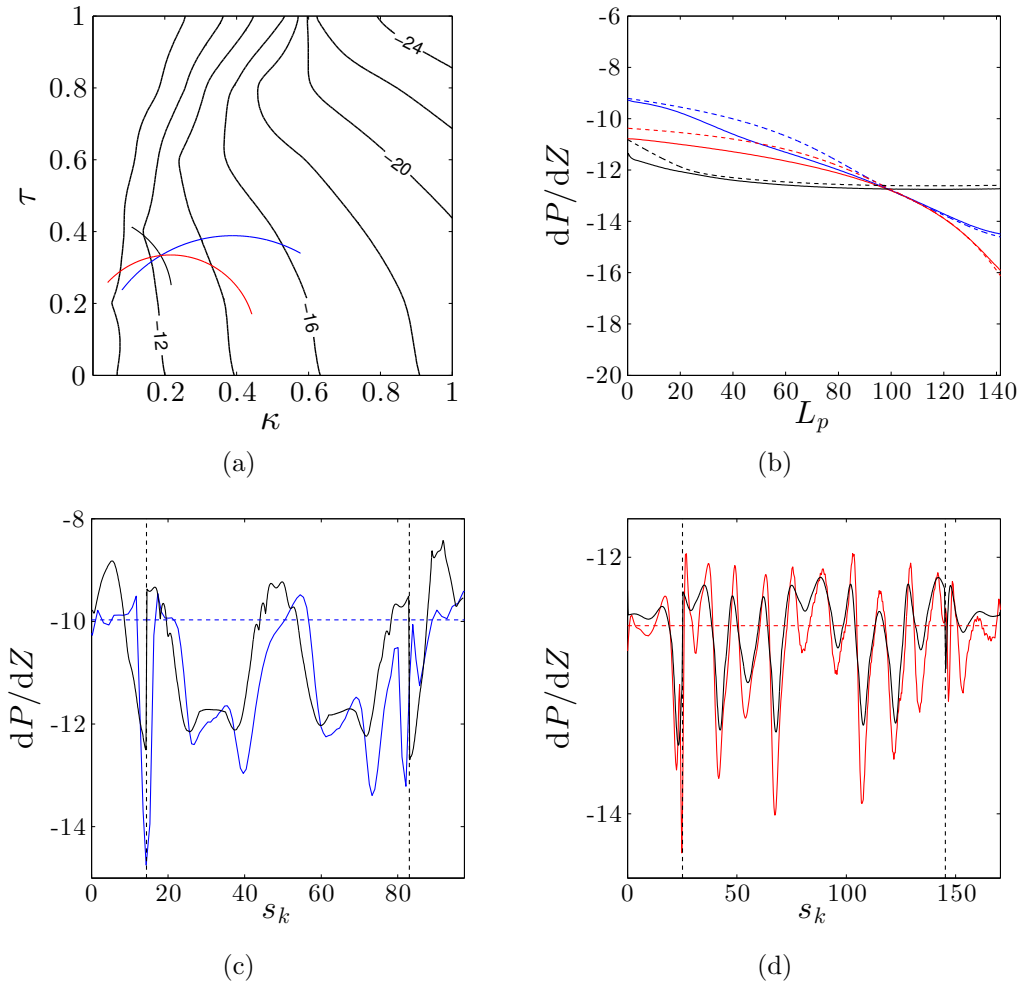

Figure 5.5: A comparison between the helical pressure gradient computed numerically and using the interpolated solution for irregular and loose knotted cords at $Re = 100$. a) A plot of helical pressure gradient versus κ and τ showing the trajectory of the irregular cords considered, $\mathcal{W}_{v,3}$ (black), $\mathcal{P}_{v,3}$ (blue) and $\mathcal{C}_{v,1}$ (red). In all cases the flow-direction is from low to high curvature; b) the pressure gradient versus pitch length computed using radial-basis interpolation (dashed) compared with numerics (solid) for the corresponding irregular geometries; c) the pressure gradient versus knot length for the UCV and d) OCA geometry. The black lines are the radial basis interpolation, the blue (c) and red (d) lines are the numerical gradients with coloured dashed lines showing the regularly coiled value as detailed in chapter 3.

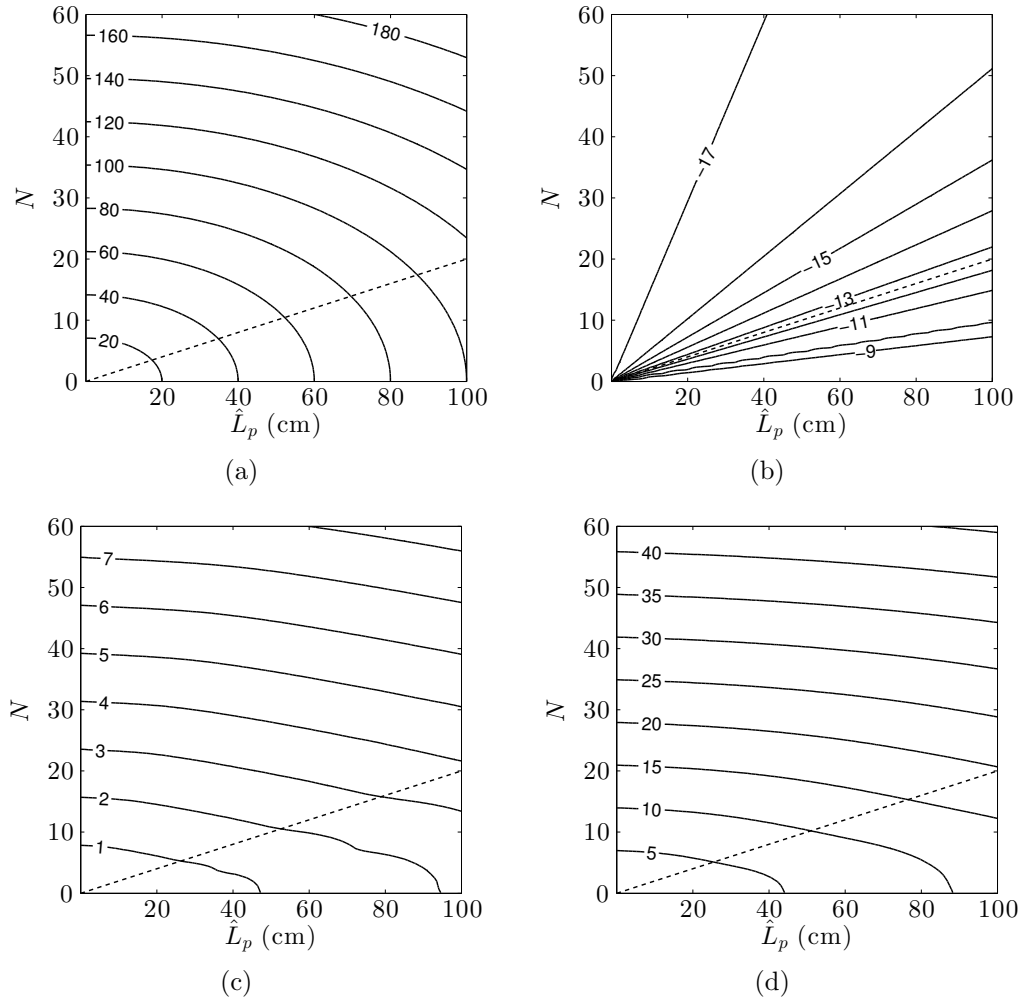

Figure 5.6: Variation of helical vessel parameters over a range of N and $\hat{L}_P$ at $\hat{w} = 1.6$ cm and $Re = 100$. Radial lines trace out contours of U_c; the normo-coiled value of 0.2 coils/cm is here indicated by a black-dashed line. a) Venous arclength, $\hat{L}_h$ in cm; b) non-dimensional venous pressure gradient, $\mathrm{d}P/\mathrm{d}Z$; c) venous pressure drop, $\Delta\hat{P}_V$ in mmHg, and; d) the arterial pressure drop, $\Delta\hat{P}_A$ in mmHg.

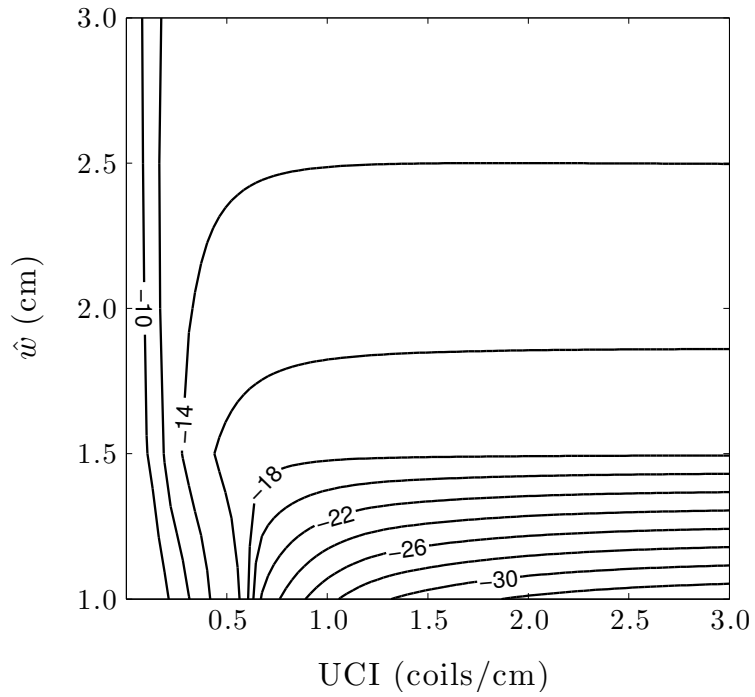

Figure 5.7: Variation of the non-dimensional helical pressure gradient with clinical UCI and coil width for a standard vein. Note that cords of high UCI and low width are not necessarily physiological.

nation of blood pressure and flow-rate outside of the typical range. In order to quantify the potential magnitude of this deviation, the blood pressure at a standard flow-rate can be compared with values computed for vessels with normal outcome. The blood flow-rate at standard pressure can be similarly assessed to develop a level of consensus. These two calculations represent extreme cases from which a compromise is likely found. For example, a long cord may exhibit slightly increased pressure and reduced flow-rate, rather than a significantly increased pressure in isolation.

To perform these assessments both the pressure and flow-rate must be calculated. The composite pressure gradient estimate developed in section 5.1.2 allows calculation of the steady downstream pressure gradient through a helical vessel at $Re = 100$ both quickly and accurately. Given the torsion, curvature and arclength the total pressure drop can be determined at the nominal blood flow-rate. While this method is strictly applicable to helical vessels, the results of chapter 3 show that geometric irregularities such as variable coiling, loose knots and twist-reversal do not appreciably affect the total pressure drop. The results in these cases are therefore well approximated by the helical vessel of mean coiling and the composite method may be used. Determination of the flow-rate at standard pressure, however, cannot be achieved by the composite method of section 5.1.2 as the additional data is restricted to $Re = 100$. The flow-rate is instead available for a range of vessels using Liu and Masliyah (1993), however, the region of applicability narrows for low Re as depicted in figure 5.1.

Within this section two indices formulated by the above approach are outlined. These are the umbilical pressure index, PX, based on the vessel blood pressure drop ($\Delta\hat{P}$) and the umbilical flow index, QX, related to the vessel blood flow-rate ($\hat{Q}$). These indices are computed using geometric measurements of the whole cord as the mean vessel curvature, torsion and arclength are not readily available in a clinical setting. Both indices are designed to quantify the deviation of the blood flow characteristics from the normal state. Normal blood flow in this context is defined with respect to a reference cord; a geometry chosen to reflect normal coiling characteristics from the literature.

In their most basic form PX and QX require only one additional measurement to the UCI; the 'coiling width' of the vessels or, if unavailable, simply the cord width. This measurement facilitates an estimate of the helical radius (R_h) which has been previously shown to significantly affect downstream pressure gradients. The indices have two major advantages over the conventional UCI diagnostic. Firstly, both indices are based on characteristics of the blood flow known to co-present with pathology throughout the human circulatory system. The UCI, conversely, is a simple ratio of measurable geo-

metric parameters with no theoretical motivation. Secondly, the new indices, in particular the pressure index, can account for cord irregularities such as true knots and non-uniform coiling. The UCI is unable to quantify the effect of these features.

5.2.1 The umbilical flow and pressure indices

The pressure drop is non-dimensionalised on the viscous scale so that,

$$\Delta\hat{P} = \frac{\hat{\mu}^2 Re \Delta P}{\hat{\rho}\hat{R}^2}, \tag{5.5}$$

and therefore a ratio of dimensional pressures at the same viscosity, density and vessel radius can be written as

$$\frac{\Delta\hat{P}_1}{\Delta\hat{P}_2} = \frac{Re_1 \Delta P_1}{Re_2 \Delta P_2}. \tag{5.6}$$

Similarly, the flow-rate, $\hat{Q}$, is related to Re by,

$$\hat{Q} = \frac{\pi \hat{R}\hat{\mu} Re}{\hat{\rho}}, \tag{5.7}$$

and hence this ratio (at constant vessel and blood properties) is simply a ratio of the corresponding Re,

$$\frac{\hat{Q}_1}{\hat{Q}_2} = \frac{Re_1}{Re_2}. \tag{5.8}$$

Throughout the following section a description of the pressure and flow indices utilising these ratios is presented.

Definition 1: Umbilical Pressure Index

The umbilical pressure index, PX, measures the relative (dimensional) pressure drop required to facilitate a normal blood flow-rate through a particular cord geometry ($\Delta\hat{P}$) with respect to the pressure drop required in a reference cord geometry ($\Delta\hat{P}_R$) at standard flow-rate ($\hat{Q}_R$).

$$PX = \frac{\Delta\hat{P}}{\Delta\hat{P}_R} \quad \text{when } \hat{Q} = \hat{Q}_R. \tag{5.9}$$

Note that as $\hat{Q} = \hat{Q}_R$, PX can also be computed using the non-dimensional pressure drop from equation (5.6),

$$PX = \frac{\Delta P}{\Delta P_R} \quad \text{when } \hat{Q} = \hat{Q}_R.$$

Normalisation by a reference value allows designation of cords with $PX = 1 \pm \epsilon$ as 'normal pressure', where ϵ is a suitably chosen tolerance. Similarly, vessels with $PX < (1-\epsilon)$ are categorised as low pressure while high pressure cords have $PX > (1+\epsilon)$. A particular advantage of PX is that it is linear. The index may therefore be computed for distinct cord sections with the results added in serial to compute a composite index. This is useful for cord geometries which vary significantly with length or exhibit anomalies such as true and false knots, examined further in section 5.3.

Definition 2: Umbilical Flow Index

The umbilical flow index, QX, measures the relative blood flow-rate maintained in a particular cord geometry ($\hat{Q}$) with respect to the flow in a reference cord geometry ($\hat{Q}_R$) at the reference (dimensional) pressure drop ($\Delta\hat{P}_R$),

$$QX = \frac{Q}{Q_R} \quad \text{when } \Delta\hat{P} = \Delta\hat{P}_R. \tag{5.10}$$

This can be written using equation 5.8 as,

$$QX = \frac{Re}{Re_R}. \tag{5.11}$$

The calculation of the flow index represents the inverse problem to the pressure index. Intuitively a cord with a high pressure index exhibits a low flow index and vice versa. These two indices are intimately related; for the limiting case of a straight cord this relation is linear, however for coiled cords the dependence is complicated and is affected by the length, torsion and curvature of the geometry. Both indices may be calculated for the arteries and the vein.

Assumptions and requisite geometric measurements

In order to estimate the pressure drop from purely geometric observations, it is assumed that;

i) The coiling characteristics (τ, κ) of the arteries and vein are reflected by the whole-cord coiling.

ii) Coiled regions form a perfect, regular helix, which is constant along the coiled length. Any large-scale curving of the whole cord may be ignored.

iii) The outer-most extent of the vessels lie some distance, $\hat{F}$, from the outer-surface of the cord, shown in figure 5.8. This is termed the Wharton's jelly fraction and is nominally assumed zero, i.e. the vessels define the outer extent of the cord. Likewise the vessel wall thickness is assumed negligible.

iv) The blood density and viscosity are 'normal' and are given in table 2.1 on page 36 for each of the vessels.

v) For each of the arteries and the vein, the vessel cross-section is constant, circular and has the nominal radius given in table 2.1.

With these assumptions the pressure drop along the length of a cord vessel can be computed based on three geometric measurements. Namely,

i) The number of coils (fractional turns included), N.

ii) The 'natural' *pitch* length of the coiled section of the cord, $\hat{L}_p$, and the total length of any straight section(s) of the cord, $\hat{L}_s$, if present.

iii) The 'coil width', $\hat{w}$.

These geometric measurements allow an estimate of the vessel curvature, κ, torsion, τ, and arclength, L_Z. The pressure drop along the cord vessel at $Re = 100$ is then found using the composite estimate of section 5.1.2. The flow index calculation is more complicated and is described in section 5.2.1.

Index calculation

A sample cord with relevant dimensions is shown in figure 5.8. Upon obtaining the characteristic (dimensional) measurements, $(N, \hat{L}_{s,1}, \hat{L}_{s,2}, ..., \hat{L}_{s,n}, \hat{L}_p, \hat{w}, \hat{F})$, the following steps are taken to compute the index.

i) Computation of the total length of the straight section(s);

$$\hat{L}_s = \hat{L}_{s,1} + \hat{L}_{s,2} + ... + \hat{L}_{s,n}. \tag{5.12}$$

ii) Length-scales non-dimensionalised by the reference vessel radius, $\hat{R} = 0.2$ cm for the arteries and $\hat{R} = 0.35$ cm for the vein;

$$L_s = \hat{L}_s/\hat{R}, \quad L_p = \hat{L}_p/\hat{R}, \quad w = \hat{w}/\hat{R}, \quad F = \hat{F}/\hat{R}. \tag{5.13}$$

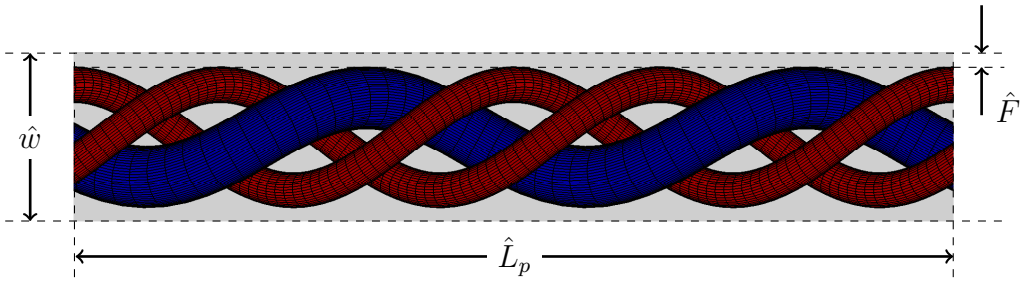

Figure 5.8: A schematic diagram of an umbilical cord showing the length measurements required for calculation of the pressure and flow indices. Note that nominally $\hat{F}$ is set to zero in this work. The grey region represents the Wharton's Jelly fraction.

iii) Computation of the helical radius (R_h) and pitch (P_h);

$$R_h = \frac{w}{2} - 1 - F, \qquad P_h = \frac{L_p}{N}. \tag{5.14}$$

iv) Computation of the non-dimensional arc-length of the coiled section (L_h) as well as the torsion (τ) and curvature (κ);

$$L_h = 2\pi N\sqrt{R_h^2 + (P_h/2\pi)^2}. \tag{5.15}$$

$$\tau = \frac{P_h/2\pi}{R_h^2 + (P_h/2\pi)^2}, \qquad \kappa = \frac{R_h}{R_h^2 + (P_h/2\pi)^2}. \tag{5.16}$$

Iterate (v) - (ix) on Re **with** $Re^{[0]} > 0$.

v) Calculation of the helical parameters;

$$\gamma = \frac{\tau}{\kappa^{3/4}\sqrt{2Re^{[n]}}}, \qquad Dn = 2Re^{[n]}\kappa^{1/2}. \tag{5.17}$$

vi) Computation of the helical pressure drop for the coiled section (ΔP_c);

$$\Delta P_c^{[n]} = -\frac{dP^{[n]}}{dZ} L_h. \tag{5.18}$$

For $Re^{[n]} = 100$ the composite estimate of section 5.1.2 is used, while $Re^{[n]} \neq 100$ requires the result of Liu and Masliyah (1993). In the latter case, cords with $\gamma > 0.1$ or $Dn > 5000$ lie outside of correlation and the index cannot be calculated.

vii) Computation of the total cord pressure drop (ΔP);

$$\Delta P^{[n]} = \Delta P_c^{[n]} + 8L_s. \tag{5.19}$$

viii) Calculation of the flow ratio (QR), a ratio of Re,

$$QR^{[n]} = \frac{Re^{[n]}}{Re_R}. \tag{5.20}$$

ix) Calculation of the pressure ratio (PR). The pressure drop is normalised by the reference pressure (ΔP_R) and multiplied by QR to ensure the pressure ratio is a ratio of *dimensional* pressures from (5.6),

$$PR^{[n]} = \frac{\Delta P^{[n]}}{\Delta P_R} QR^{[n]} = \frac{\Delta P^{[n]}}{\Delta P_R} \frac{Re^{[n]}}{Re_R}. \tag{5.21}$$

The reference pressure (ΔP_R) is the pressure drop computed within a cord exhibiting specified $N, \hat{w}, \hat{L}_p, \hat{L}_s$ and Re, detailed in section 5.2.1. When the flow-ratio is unity (i.e. reference flow-rate, or $QR = 1$) the pressure index is equal to the pressure ratio

$$PX = PR^{[n]} = \frac{\Delta P^{[n]}}{\Delta P_R} \quad \text{at } QR = 1. \tag{5.22}$$

When the pressure ratio is unity (i.e. the cord is at reference pressure) the flow index is equal to the flow ratio,

$$QX = QR^{[n]} = \frac{Re^{[n]}}{Re_R} \quad \text{at } PR = 1. \tag{5.23}$$

In order to be suitable for clinical use, the above iteration is scripted in `matlab` (see appendix C.1) and `python`. An initial condition of $Re^{[0]} = Re_R$ ensures that the first pressure ratio calculated is the pressure index. Newton's method is then used to calculate the Re at which $\Delta P = \Delta P_R$. This is equivalent to finding Re such that

$$g(Re) = \frac{8L_s + \frac{fRe}{2} L_h}{\Delta P_R Re_R} Re - 1 = 0, \tag{5.24}$$

where $g = g(Re)$, fRe is determined using (5.1) and an update to $Re^{[n]}$ is found from,

$$Re^{[n+1]} = Re^{[n]} - \frac{g(Re^{[n]})}{g'(Re^{[n]})}. \tag{5.25}$$

	A	**V**
Number of Coils, N	10	10
Coil width, $\hat{w}$ (cm)	1.6	1.6
Pitch length, $\hat{L}_p$ (cm)	50	50
Straight length, $\hat{L}_s$ (cm)	0	0
Vessel radius, $\hat{R}$ (cm)	0.2	0.35
Blood flow-rate, $\hat{Q}$ (m^3/s)	2.40 $\times 10^-6$	4.42 $\times 10^-6$
Flow Reynolds number, Re_R	100	100

Table 5.1: The reference cord parameters for the artery (A) and vein (V), chosen based on the literature review in chapter 1.

Reference cord

The reference cord chosen from the literature has the parameters given in table 5.1. The corresponding artery and vein have a non-dimensional curvature of 0.12 and 0.19, respectively, with a non-dimensional torsion of 0.16 for the artery and 0.33 for the vein. A schematic diagram of the whole cord is shown in figure 5.9(a) with a close-up of a single coil in figure 5.9(b). By definition, the flow and pressure indices for each vessel of this cord are unity, depicted in figure 5.9(c). This plot also illustrates the boundaries of the correlation; solutions are not available for $Re < 31$ ($QR < 0.31$) in the arteries and $Re < 68$ ($QR < 0.68$) in the vein as $\gamma > 0.1$.

5.2.2 Variation with N and $\hat{L}_p$ at constant $\hat{w}$

For a helical cord the pressure and flow indices are fully determined by $N, \hat{L}_p$ and $\hat{w}$ alone. To provide a comparison with the UCI, the variation of these indices with N and $\hat{L}_p$ at constant $\hat{w}$ is shown in figures 5.10 and 5.11. Radial lines on these plots therefore trace out paths of constant U_c, with increasing slope corresponding to larger UCI. It is apparent from figures 5.10 and 5.11 that the new indices vary significantly with UCI. For example, in figure 5.10(c) at $\hat{w} = 1.6$, PX_V varies between 0.5 and 2 for a normally coiled cord with U_c constant at 0.2 coils/cm. Similar variation exists in the corresponding flow index shown in figure 5.11(c). Considering width changes, at a constant length of 20 cm with 20 coils ($U_c = 1$ coil/cm) the

(a)

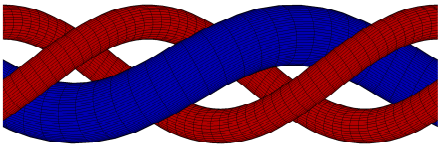

(b)

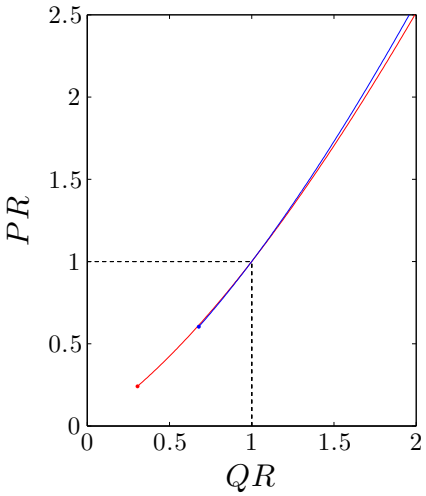

(c)

Figure 5.9: Characteristics of the reference cord used for the index calculation. a) The whole cord showing the arteries (red) and vein (blue); b) a close-up of one full coil and c) the relationship between the pressure and flow ratios determined using the process outlined in section 5.2.1. The blue and red lines indicate characteristics of the venous and arterial flow, respectively. The lower-limit for each of the plots is given by the solid circle, where $\gamma = 0.1$.

venous pressure index is approximately unity for $\hat{w} = 1.2$ cm in figure 5.10(a), almost doubling for $\hat{w} = 2.6$ cm in figure 5.10(e).

The broadscale variation of PX with N and L_p at constant width is quite simple; the number of coils typically dominates the result, particularly at larger width, and when N is low. This is because at low N and constant L, the addition of another coil significantly increases both the helical arclength as well as the severity of the downstream pressure gradient (through an increase to curvature), introducing a two-fold increase to PX. This effect is most pronounced as width increases. In general, an increase in width at constant N and $\hat{L}_p$ will also result in a larger PX.

The flow index has an approximately inverse relation to the pressure index described previously. Figures 5.11(a)-(f) show the variation for the arteries and vein for three widths. The key difference between the indices is that as $N, L_p \to 0$, $QX \to \infty$. There are also large regions which are currently outside of correlation, shaded in figure 5.11. This region is particularly large for low width and larger vessel radius, and hence the vein is more significantly affected.

5.2.3 Index sensitivity

In order to assess the robustness of the pressure and flow indices it is important to have an idea of their sensitivity to the calculation inputs. For the UCI, relative errors in the measurement of the length and number of coils (e_L, e_N) will affect the index accuracy. For a cord with UCI (U) determined from N and $\hat{L}$, the index calculated with error is,

$$U_e = U(1 \pm \delta),$$

where δ is the relative uncertainty,

$$\delta = \frac{1}{2}\left[\frac{N(1+e_N)}{\hat{L}(1-e_L)} - \frac{N(1-e_N)}{\hat{L}(1+e_L)}\right]\frac{\hat{L}}{N} = \frac{e_L + e_N}{1-e_L^2}.$$

This uncertainty is independent of errors in the width (e_w) and will attain only four distinct values; 0 (at no error), $\pm$ 0.10 (at $\pm$ 10% error in N), $\pm$ 0.101 (at $\pm$ 10% error in $\hat{L}$) or $\pm$ 0.202 (at $\pm$ 10% error in both variables). This uncertainty is irrespective of the cord index, and shows that typically changes in the measured values translate to comparable changes in the index.

While relative measurement errors in the UCI are independent of the true value, this does not hold for the pressure or flow indices. Variation of the cord indices is dependent on the particular cord structure, and hence

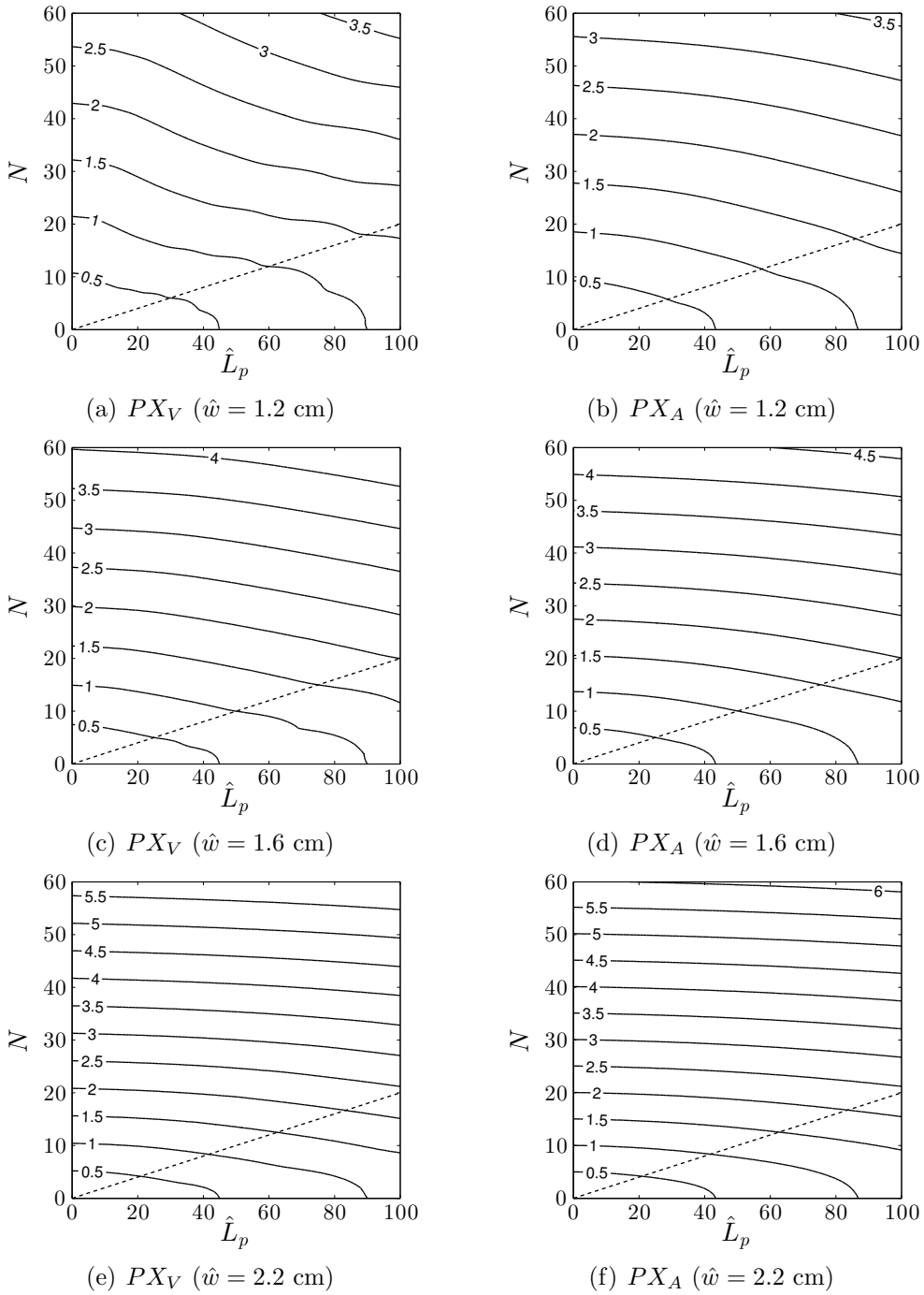

(a) PX_V ($\hat{w} = 1.2$ cm)

(b) PX_A ($\hat{w} = 1.2$ cm)

(c) PX_V ($\hat{w} = 1.6$ cm)

(d) PX_A ($\hat{w} = 1.6$ cm)

(e) PX_V ($\hat{w} = 2.2$ cm)

(f) PX_A ($\hat{w} = 2.2$ cm)

Figure 5.10: Contours of constant pressure index (PX) for each vessel at three coil widths. Data for the vein is shown on the left, with the arteries on the right. The dashed line shows the nominal UCI of 0.2 coils/cm. Cords above this are therefore hypercoiled, while those below are hypocoiled.

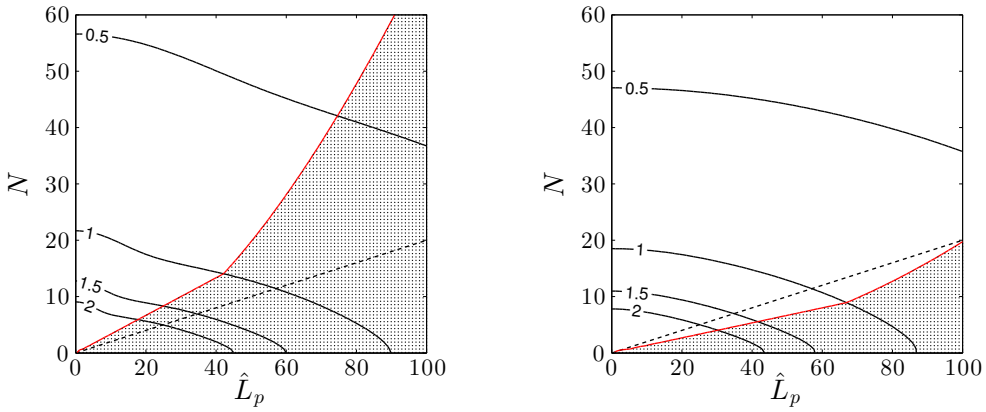

(a) QX_V ($\hat{w} = 1.2$ cm) (b) QX_A ($\hat{w} = 1.2$ cm)

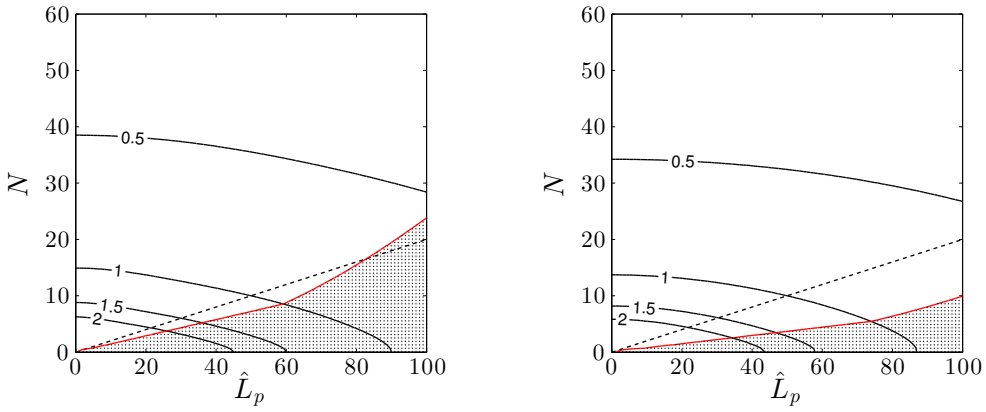

(c) QX_V ($\hat{w} = 1.6$ cm) (d) QX_A ($\hat{w} = 1.6$ cm)

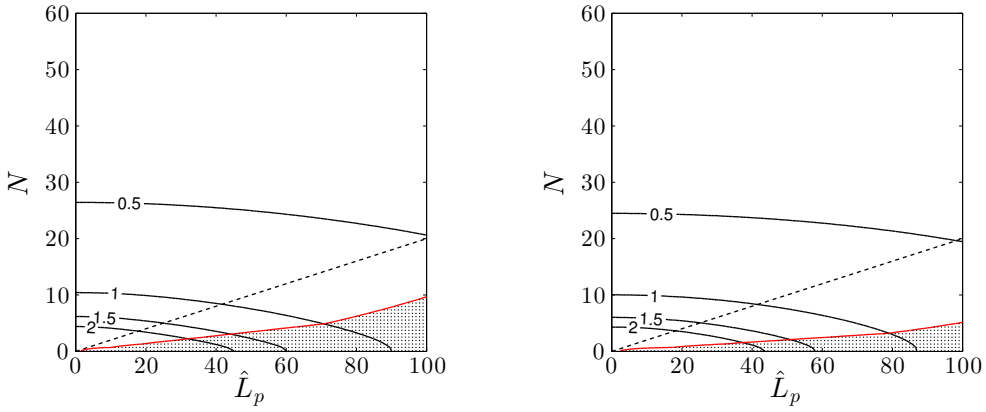

(e) QX_V ($\hat{w} = 2.2$ cm) (f) QX_A ($\hat{w} = 2.2$ cm)

Figure 5.11: Contours of constant flow index (QX) for each vessel at three coil widths. Data for the vein is shown on the left, with the arteries on the right. The red line indicates cords for which $\gamma = 0.1$ with the shaded region marking those vessels outside correlation. Note that contours above $QX = 2$ have not been drawn to clarify the figure as vessels approaching the origin have flow index approaching infinity. The dashed line shows the nominal UCI of 0.2 coils/cm. Cords above this are therefore hypercoiled, while those below are hypocoiled.

some cords will be more sensitive to error. The parameters $\hat{L}_p, N$ and $\hat{w}$ are varied independently to compute the resultant change in PX and QX using a centered finite difference approximation for the derivative, shown here for PX,

$$\frac{\partial(PX)}{\partial M} \approx \frac{PX(M+\delta M) - PX(M-\delta M)}{2\delta M}.$$

Here M is the measured independent variable under consideration and $\delta M = 10^{-6}$ is chosen after ensuring the result is not affected by further reductions. The approximate relative change in the index in response to a relative error, e_M in M, is the sensitivity, S_M, shown again for PX,

$$S_M = \Delta PX_M = \frac{\partial(PX)}{\partial M}\frac{e_M M}{PX},$$

which assumes that the derivative is locally linear. The sensitivity of both PX and QX to each of the measurements is complex, however, is included for $\hat{w} = 1.6$ cm in appendix D.3 in figures D.1 and D.2. For cords within the 'normal' range, a 10% error in a particular measurement will typically result in 3-8% variation in both PX and QX, with the variation roughly determined by the UCI. Errors in N and L are the most important, with width errors typically important for large N and low L. In all realistic cases considered the variation is bounded by 10%, ensuring measurement errors do not amplify in the index calculation.

In order to visualise the collective sensitivity of a given cord, the sensitivity norm is defined as,

$$|S| = \sqrt{S_w^2 + S_N^2 + S_L^2},$$

which provides a combined measure of the (independent) variability of the indices with respect to each of the measurements at a given point. Figure 5.12 shows the variation of the arterial pressure and flow sensitivity norms with cord width for a relative uncertainty of $e_M = 0.1$. If the sensitivity of the index to each measurement is equal (i.e. $S_w = S_N = S_L$), a sensitivity norm of 0.1 corresponds to individual measurement sensitivities of $S_M = \sqrt{|S|^2/3} = 0.058$. This is not true in general, but aids in interpreting the plots. Within the normal physiological range, cords typically show an increase in PX sensitivity with increasing width (except for very high UCI cords where the trend is reversed), and at all widths will have larger sensitivity at higher UCI. The QX sensitivity is more complicated but typically increases with UCI and $\hat{w}$. For both indices the norm is less than approximately 0.15 for the range of vessels and does not exhibit any isolated regions of significant value. The indices are therefore robust to input error and are suitable for diagnostic purposes.

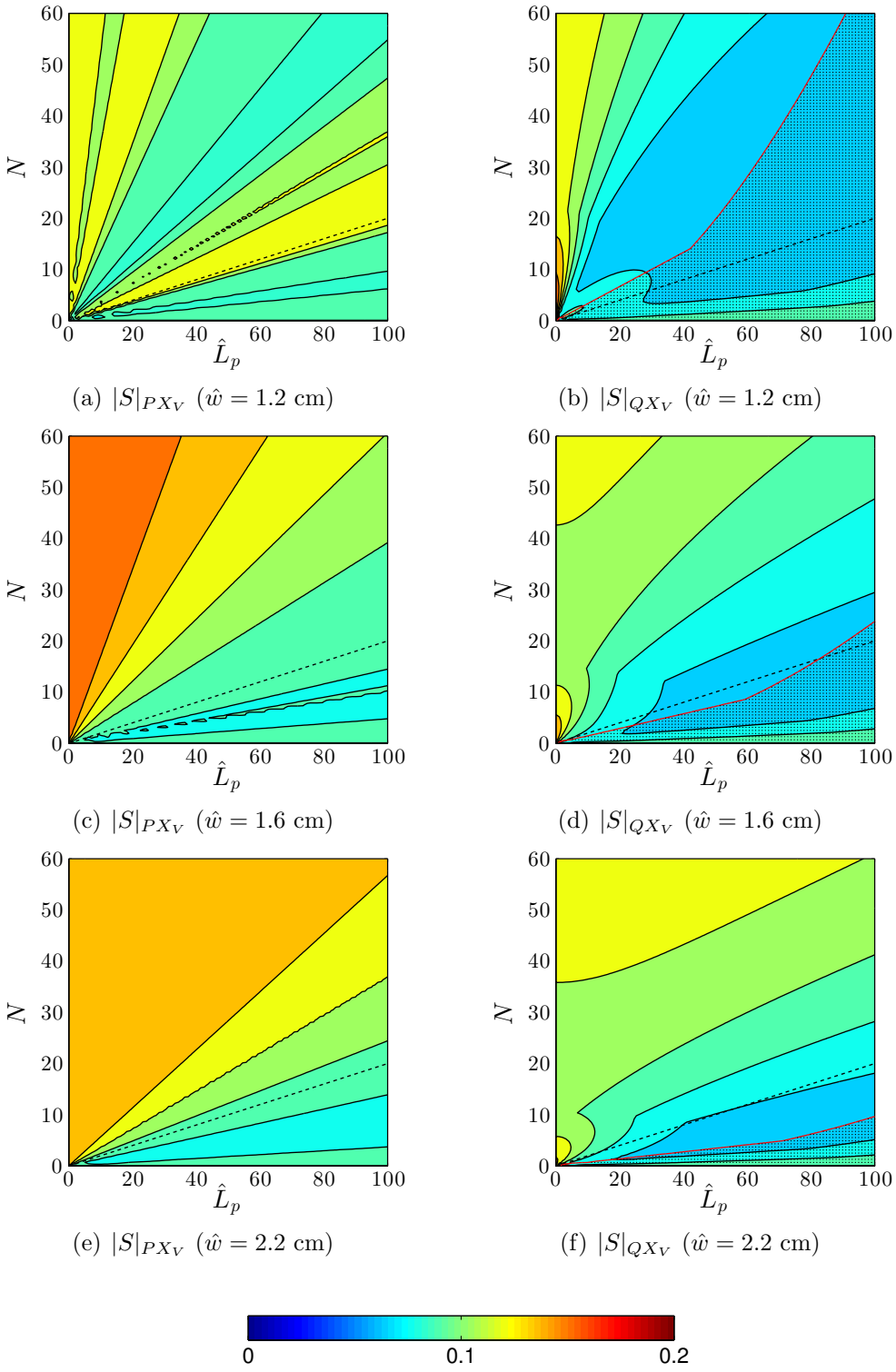

(a) $|S|_{PX_V}$ ($\hat{w} = 1.2$ cm)

(b) $|S|_{QX_V}$ ($\hat{w} = 1.2$ cm)

(c) $|S|_{PX_V}$ ($\hat{w} = 1.6$ cm)

(d) $|S|_{QX_V}$ ($\hat{w} = 1.6$ cm)

(e) $|S|_{PX_V}$ ($\hat{w} = 2.2$ cm)

(f) $|S|_{QX_V}$ ($\hat{w} = 2.2$ cm)

Figure 5.12: Contours of the venous pressure and flow sensitivity norms ($|S|$) over a range of $N, \hat{L}_p$ for three cord widths. The dashed line shows the nominal UCI of 0.2 coils/cm. Cords above this are therefore hypercoiled, while those below are hypocoiled.

5.3 Cord anomalies

Cord anomalies present deviations from the idealised helical structure assumed in the definition of the umbilical pressure and flow indices. The results of chapter 3 show that many anomalies do not appreciably affect the mean helical pressure gradient. Tight true knots, however, can significantly increase local pressure gradients, though methods for identifying and measuring the level of constriction are currently unavailable. This section therefore concentrates on two anomalies that can be readily considered. The first is the added length effect associated with a loose true knot, discussed in section 5.3.1. The second concerns irregularly coiled cords in a manner following from the work of section 5.1.3 where the total pressure drop is computed in discrete sections in order to account for the variability. This method is presented in section 5.3.2.

5.3.1 Loose true knots

From section 3.2.4, the pressure gradient through a tight true knot is significantly affected by large reductions in vessel radius. However, for less severe constrictions where the radius shrinks to at most 87.5% of the nominal radius, the mean pressure gradient through the constriction does not vary appreciably from the helical gradient. With only post-partum images of the cord available it is impossible to measure constriction severity and the resultant pressure increase. The aim of this section is therefore to assess the effect of knots when the constriction is assumed negligible, and to provide an estimate of the pressure drop through a loose knot based purely on the added length effect.

As shown in section 3.2.4, the pressure gradient through a loose knot typically oscillates about the mean helical pressure gradient if the nominal coiling is maintained within the knot structure. The variance of this oscillation reduces as the nominal vessel curvature increases. It is therefore possible to estimate the total pressure drop through the knot using knowledge of the pressure gradient through the rest of the cord, coupled with an estimate of the length of cord in the knot. For an unconstricted cord, the cord knot length will depend only on the width of the cord,

$$\hat{L}_k = \hat{w}K, \tag{5.26}$$

where K is a constant (termed the *ropelength* in knot-theory) that depends on the tightness of the knot. Several studies have attempted to numerically determine the lower-limit on K, with Denne et al. (2006) citing 16.372 for a tight trefoil knot. This value is of course for a *closed* knot, and hence a

shorter overhand knot will typically have a smaller ropelength. The loose knots described in section 3.2.4 are based on a standard trefoil and have $K = 21.3$ when the cubic sections at the inlet and outlet are included, and $K = 15.01$ when the calculation is restricted to the truncated trefoil alone. The number of coils through the knot, N_k, is then,

$$N_k = \frac{\hat{L}_k}{\hat{P}_h} = \hat{w}K \times \text{UCI}. \tag{5.27}$$

To determine the pressure drop through the knot, this estimate of the number of coils is coupled with the helical radius, pitch and pressure gradient through the rest of the geometry for the particular vessel,

$$\Delta P_{knot} \approx -2\pi N_k \frac{dP}{dZ}\sqrt{R_h^2 + \frac{P_h}{(2\pi)^2}}. \tag{5.28}$$

This estimate assumes that the vessel arclength through the knot is equivalent to the arclength of a regularly coiled vessel through the same straight length. In reality there is a small discrepancy though this has negligible bearing on the computed pressure over these length scales. For a normo-coiled cord of nominal width and a moderate ropelength of $K = 15$, the addition of a single knot increases the pressure in both vessels by 49% (an increase to PX of 0.49) corresponding to 0.92 mmHg in the vein and 4.81 mmHg in the arteries. It is therefore impossible to ignore the effect of a loose knot on the total pressure drop.

5.3.2 Irregularly coiled cords

The calculation of the pressure and flow indices assume the umbilical vessels form a perfect helix which can be ascertained by direct examination of the whole-cord. In reality it is unlikely that the cord vessels will form a regular helix, but rather that the torsion and curvature will vary over the cord length. The calculation of the indices is therefore performed on an effectively smoothed, homogenous cord, with an 'average' coiling assumed representative of the actual coiling. In section 3.2.3 it is shown that relative linear variations in the pitch (and hence UCI) of up to 120% along the cord length, as well as cord width variations of up to 100% have a negligible effect of less than 3% on the computed pressure and hence pressure index. This discrepancy is within the bounds of uncertainty of the composite pressure gradient estimate of section 5.1.2 and hence the pressure index computed for an equivalent regular cord will likely predict the pressure adequately. For

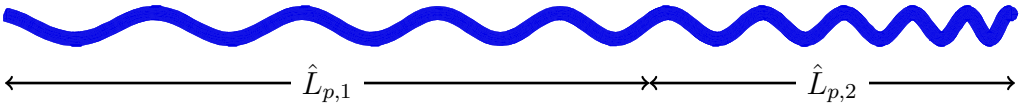

Figure 5.13: Schematic diagram showing an irregularly coiled vein deconstructed into two sections for index calculation. The vein has 120% variation in coil spacing along the length, $\chi_S = 1.2$, with the pitch lengths corresponding to two measurements of 5 coils each.

cords which vary in a less continuous manner, however, it is possible to gain a better estimate by computing the index for distinct cord sections using a discrete method analogous to the work of section 5.1.3. As the pressure index is linear, the results may be added in serial. This procedure is conducted here for the irregularly coiled vessels previously defined in section 3.2.3. Figure 5.13 shows the partitioning of a geometry with $\chi_S = 1.2$ into two separate sections; one with $\hat{L}_{p,1}$, N and $\hat{w}$, the other with identical N and $\hat{w}$ but with a reduced pitch length of $L_{p,2}$ due to the irregular coiling. The pressure indices calculated for these sections are added together in order to determine the total pressure index. This procedure can be followed for any number of subdivisions, n, with the continuous method of section 5.1.3 arising as $n \to \infty$. This procedure is catalogued for several cords and a number of discrete partitions in table 5.2. While the nominal error inherent in using only one section for the index calculation of these cords is within 3%, the relative effect of this procedure on the error demonstrates its efficacy for less smoothly varying geometries. A 50% reduction in error for the cord with $\chi_S = 1.6$ is observed when the pressure index is calculated for each of the 10 coils separately. For a cord with many localised regions of hypercoiling over which the helix centreline varies significantly, this method may provide a useful reduction in error.

5.4 Example index calculations

In this section three example index calculations for cords obtained from SA Pathology are presented. The first cord (I) exhibits normal coiling with respect to the UCI bounds developed by Strong et al. (1994). The second (II) and third (III) cords are classified as hypercoiled using this system, however, exhibit additional features which require specific attention. In the case of the second cord, postpartum shrinkage due to fixation in formalin has occurred while the third cord exhibits possible shrinkage as well as two true knots. This section serves only as an illustration of the procedure underlying

χ_S	e_1	e_2	e_5	e_{10}	e_{10}/e_1
0.0	0.66	0.66	0.66	0.66	1.00
0.1	0.63	0.62	0.62	0.62	0.99
0.2	0.62	0.60	0.59	0.59	0.96
0.5	0.70	0.59	0.56	0.56	0.80
1.0	1.26	0.84	0.73	0.72	0.57
1.6	2.67	1.64	1.40	1.34	0.50

Table 5.2: The error (e %) in the pressure index for each of the cords with variable coil spacing (χ_S) at a given sub-division level of either 1, 2, 5 or 10 subsections. The final column shows the effect this has on the error. Note that there is a 0.66% error inherent in the underlying interpolant for the regularly coiled cord.

index calculation, and no conclusions regarding the efficacy of the indices is intended from this study.

5.4.1 Cord measurements

A graphical software package called `ImajeJ` is used to measure the cord width, $\hat{w}$, natural pitch length, $\hat{L}_p$, and number of coils, N, for each of the cords. This package allows tracing of the helical centreline along the cord length as well as measurement with reference to a known scale within the image. The coil width is computed as the numerical mean of a series of measurements taken at a number of locations along the cord length. The number of coils (N) is taken as the number of full turns of the whole cord along the length. This is because the coiling is often difficult to discern from the image and accuracy is only available to the nearest integer value. In practice the sensitivity to rounding N is quite low and this is not of major concern here.

Cord I is shown in figure 5.14(a) with the helical centreline traced along the length and shown in figure 5.14(b). This cord was associated with a stillbirth at 40 weeks gestation with entanglement of the cord around the neck, arm and leg at delivery. The cord was longer at birth at approximately 97 cm, though some of this length was excised. For the purpose of this study, only the length shown in the image is used. The length of the helical centre-

	Ref.	**I**	**II**	**III**
N	10	22	21	36
$\hat{L}_p$ (cm)	50	75.72	35.5	33.47
$\hat{L}_s$ (cm)	0.0	0.0	0.0	0.0
$\hat{w}$ (cm)	1.60	1.52	1.25	1.16
UCI (coils/cm)	0.20	0.29	0.59	1.08
Classification	Normo-	Normo-	Hyper-	Hyper-

Table 5.3: The reference and example cord measurements.

line, or the cord pitch length ($\hat{L}_p$) is determined using the measurement scale to be approximately 75.7 cm with no straight sections recorded. The cord has approximately 22 coils, with the cord width varying, depending on location, between 1.33 cm, and 1.72 cm. A mean value of 1.52 cm is determined using the 8 sample points shown in figure 5.14(b). The same procedure was followed for Cords II and III, shown in figures 5.15 and 5.16, respectively and recorded in table 5.3. Cord II was associated with an emergency caesarean section for fetal distress however no other details were recorded of the birth. Cord III was associated with a 37 week old IUGR fetus. The full cord was longer than shown, however, this length was not recorded. Two true knots are present for Cord III which are annotated in figure 5.16(b).

5.4.2 Index calculation

A `matlab` script performing the iteration of section 5.2.1 is used to determine PX and QX for both vessels. An example of this code is included in appendix D.2. These indices are included with the helical radius, pitch, torsion and curvature in table 5.4. The pressure index is found to be greatest in Cord III, and lowest in Cord II in both vessels, with the flow index lowest in Cord III, and greatest in Cord II. The model geometries used for index calculation are shown in full in figure 5.17 and magnified in figure 5.18. Figure 5.19 shows a plot of the pressure and flow ratio for each example cord vessel while appendix D.3 documents the index sensitivity for each cord to the three input measurements. Each cord is found to lie within acceptable bounds.

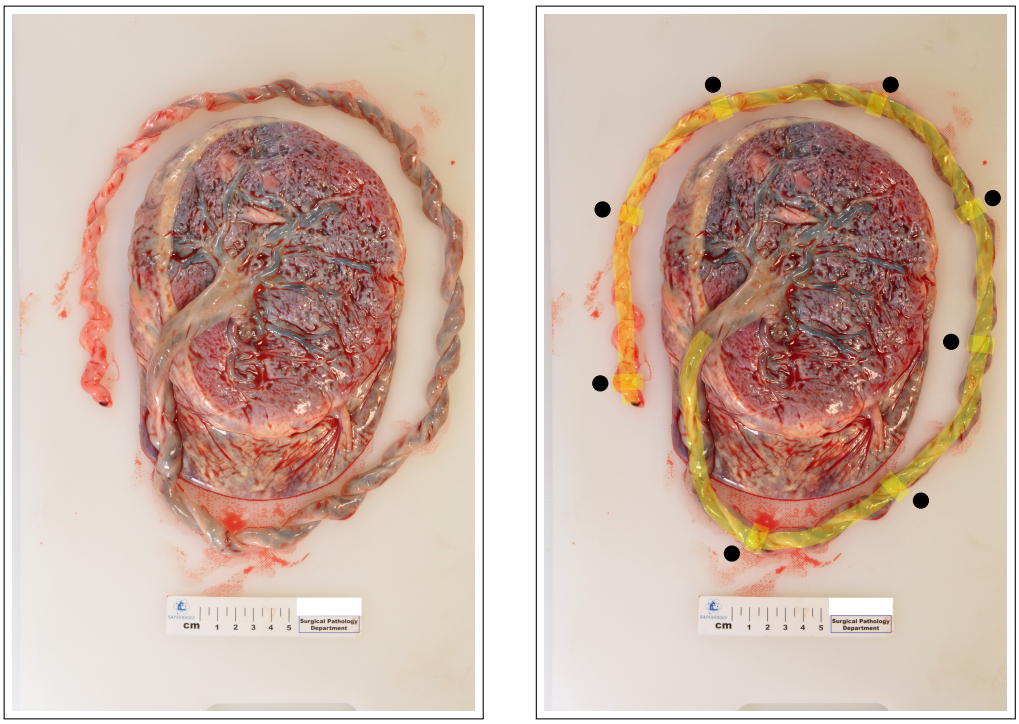

(a) (b)

Figure 5.14: a) Example Cord I; and b) with helical centreline and each of the width measurement locations overlayed.

	Ref.		**I**		**II**		**III**	
	V	A	V	A	V	A	V	A
R_h	1.29	3.00	1.18	2.81	0.78	2.12	0.65	1.90
P_h	14.29	25.00	9.83	17.21	4.83	8.45	2.66	4.65
τ	0.33	0.16	0.41	0.18	0.64	0.21	0.70	0.18
κ	0.19	0.12	0.31	0.18	0.65	0.34	1.08	0.46
QX	1.00	1.00	0.63	0.62	0.82	0.82	0.63	0.61
PX	1.00	1.00	1.87	1.87	1.32	1.31	1.94	1.96

Table 5.4: Results for the example cord veins and arteries.

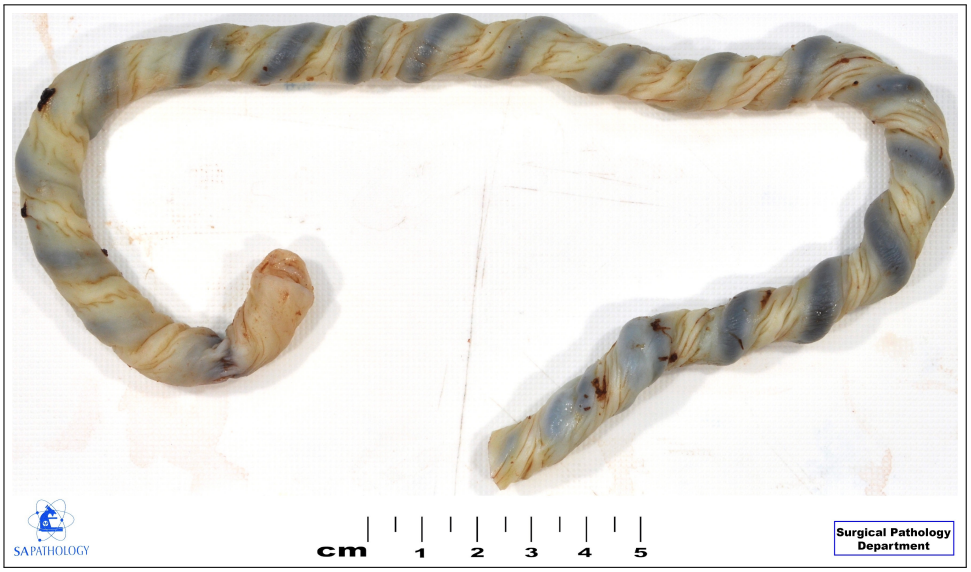

(a)

(b)

Figure 5.15: a) Example Cord II; and b) with helical centreline and each of the width measurement locations overlayed.

(a)

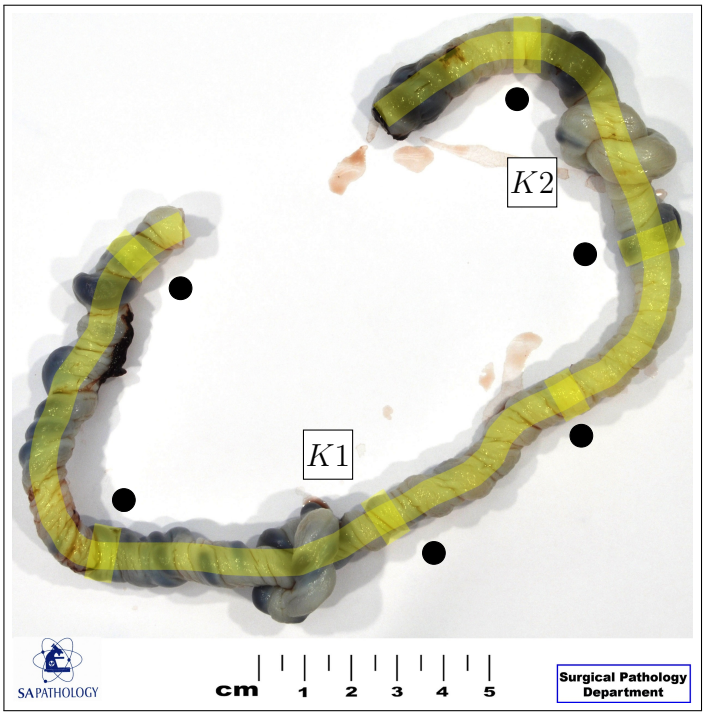

(b)

Figure 5.16: a) Example Cord III; and b) with helical centreline and each of the width measurement locations overlayed. Note the presence of two true knots (annotated $K1, K2$) which have been ignored in the initial index calculation.

(a) Ref Cord ($\hat{w} = 1.6$ cm, $\hat{L}_p = 50$ cm, $N = 10$)

(b) Cord I ($\hat{w} = 1.52$ cm, $\hat{L}_p = 75.72$ cm, $N = 22$)

(c) Cord II ($\hat{w} = 1.25$ cm, $\hat{L}_p = 35.5$ cm, $N = 21$)

(d) Cord III ($\hat{w} = 1.16$ cm, $\hat{L}_p = 33.47$ cm, $N = 36$)

Figure 5.17: Theoretical vessel models of the reference and example cords shown to scale.

5.4.3 Anomalies

Cords II and III show signs of shrinkage due to fixation within formalin and hence the length and width measured may not exactly represent the values present in-utero. The assumptions used to calculate the pressure and flow indices rely on a consistency between the geometric measurements recorded and those at approximately 40 wks gestation. To this end, the indices computed may not be truly indicative of the cord's function throughout pregnancy. In addition to this, Cord III also exhibits two true knots along it's length. The procedure of section 5.3.1 can be followed in order to gain a first estimate of the additional pressure drop. As both knots are reasonably tight, a conservative value of $K = 10$ results in an added length of $2 \times 10 \times 1.16$ cm $= 23.2$ cm. While the previously measured width is appropriate for the new calculation, R_h, P_h and dP/dZ were computed using the cord length ignoring the presence of the knots and treating them simply as regularly coiled sections, as depicted in figure 5.16. These lengths (≈ 2.28 cm each) must be subtracted to recompute the helical properties with the knots. On doing so the pressure indices for the artery and vein become 3.49 and 3.39, respectively, with corresponding flow indices of 0.39 and 0.42. The addition of two negligible-constriction true knots therefore increases the pressure index in the arteries and vein by roughly 75%, while reducing the flow index by approximately 33%. This is quite a severe deviation and further demonstrates that even the added length associated with a knot will affect pressure estimates and should be included, despite the absence of constriction data.

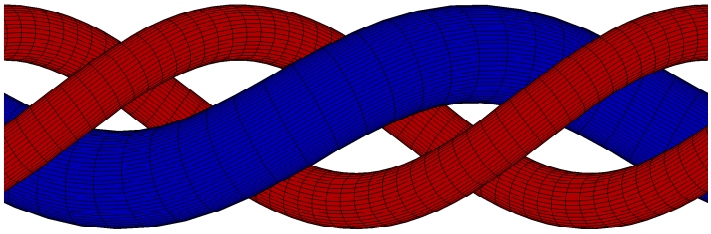

(a) Ref Cord ($\hat{w} = 1.6$ cm, $\hat{L}_p = 50$ cm, $N = 10$)

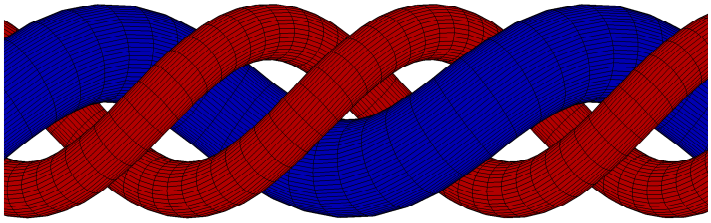

(b) Cord I ($\hat{w} = 1.52$ cm, $\hat{L}_p = 75.72$ cm, $N = 22$)

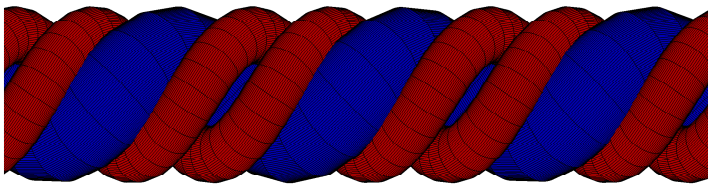

(c) Cord II ($\hat{w} = 1.25$ cm, $\hat{L}_p = 35.5$ cm, $N = 21$)

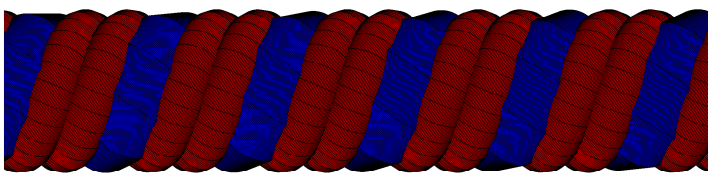

(d) Cord III ($\hat{w} = 1.16$ cm, $\hat{L}_p = 33.47$ cm, $N = 36$)

Figure 5.18: The reference and example cord models shown to scale over one pitch-length of the reference cord (5 cm).

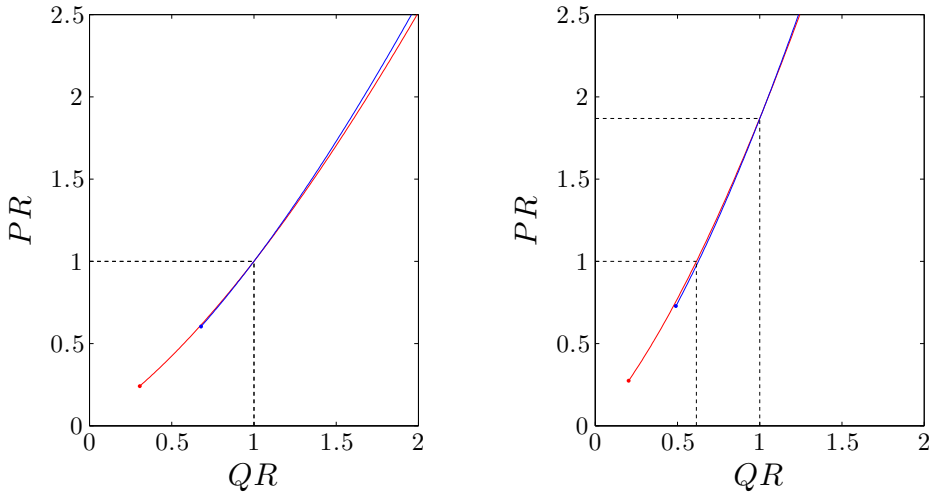

(a) Reference Cord (b) Cord I

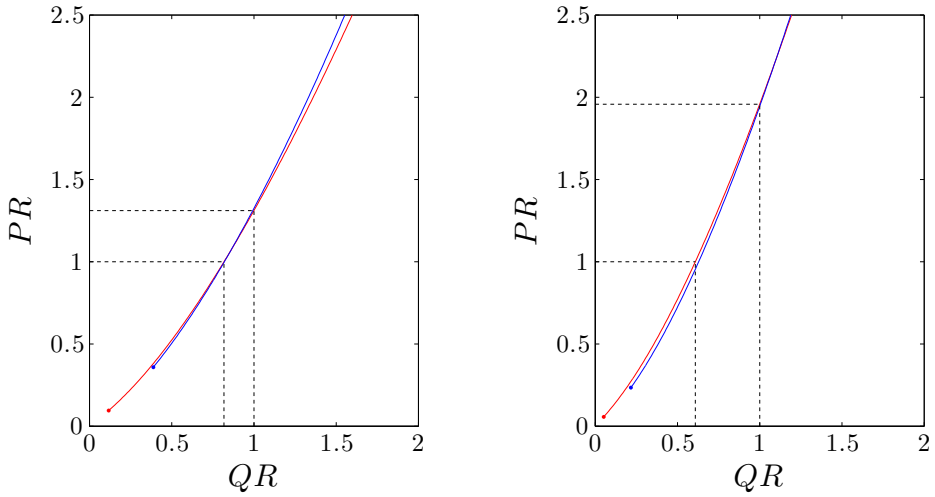

(c) Cord II (d) Cord III

Figure 5.19: Pressure and flow ratios for the reference and example arteries (red) and vein (blue). The lower-limit for each plot is given by the solid circle, where $\gamma = 0.1$. The dashed black lines show the arterial pressure and flow indices.

5.5 Clinical efficacy and implementation

In order to be useful within a clinical setting the indices must be shown to correlate with pathology. A clinical test examining a diverse sample of cords is currently underway for this purpose. Pending a positive outcome, the index calculation currently handled by a `matlab` script could be written into a standalone executable file. This has the added benefit of flexibility regarding cord parameters such as the vessel radius and blood flow-rate. For clinical purposes, a tabular or graphical format could also be constructed to show index values for a discrete set of cords. An approximation to the index for a particular cord could then be determined via simple interpolation.

5.6 Conclusion

Throughout this chapter a method for quantifying the umbilical flow resistance was presented. This chapter initially provided a comparison of the steady helical results of chapter 3 to empirical predictions available in the literature. This process verified the empirical relation of Liu and Masliyah (1993) as a useful and time-efficient alternative to the full numerical solution for a large range of cords. For the cord vessels outside of correlation, additional numerical results were computed at discrete torsion, curvature and nominal Reynolds number. The two solution sets were then combined using radial-basis interpolation in order to provide a complete picture of the flow resistance for a range of cords. The results of the full numerical study of irregularly coiled and geometrically knotted cords were then compared with empirical estimates for the mean helical vessels. Little error is incurred using the estimates, validating their use in quantifying pathology.

The method for quantifying umbilical flow resistance was then presented. This method requires only one additional geometric measurement to the calculation of the UCI; namely the cord coiling width, $\hat{w}$. Two related cord indices; the umbilical pressure index, PX, and the umbilical flow index, QX, were defined in order to assess the severity of the cord geometry. PX provides a comparison between the umbilical vessel pressure drop at a standard blood flow-rate to a reference pressure through a defined normo-coiled cord. The umbilical flow index, QX, instead compares the blood flow-rate through a given cord at reference pressure to the reference blood flow-rate. The relationship between the two indices is dependent on the length, curvature and torsion of the cord, with cords of high PX exhibiting low QX and vice versa. Both index calculations are based on non-invasive, geometric cord measurements so as to be easily implemented in a clinical setting. These

measurements are then used to construct helical vessel geometries representative of the average cord coiling. A combination of empirical and interpolated numerical data is then used to determine the pressure drop through the cord vessels, with the Newton-Raphson method employed for the inverse flow-rate problem.

The UCI was measured against the empirical cord pressure drop in order to examine their relation over a larger cross-section of geometries than previously studied in the discrete work of chapter 3. The UCI was found to be fairly constant with pressure gradient for low UCI cords, however, for UCI $>$ 0.5 coils/cm width effects become significant. Importantly, as the total vessel length is crucial in determining the pressure drop, the UCI was found to have little relation to the total pressure drop and hence pressure index. At a width of 1.6 cm and constant UCI of 0.2 coils/cm, the pressure index was found to vary between 0.5 and 2 by simply varying the number of coils and cord pitch length proportionately. The flow index showed similar independence from the UCI, however given the gap in the literature for lower Re, this index is less appropriate for clinical usage.

The indices were subject to a sensitivity analysis in which measurement uncertainties were included to estimate the variation of the index. Both indices were determined robust, with output variation on the order of the input error. The indices also exhibit reasonably homogenous error variation ensuring that no one cord is particularly susceptible.

Cord anomalies, specifically unconstricted loose true knots and variable pitch helices were also considered in the index calculation. Using an estimate of the length of the knot, or knot ropelength, a first guess at the additional pressure drop incurred from a knot can be determined when used in addition to the calculated pressure gradient through the remainder of the cord. For a normally coiled cord with one loose true knot of moderate ropelength the pressure index increases by 49% corresponding to an additional 0.92mmHg in the vein and 4.81 mmHg in the arteries. The variable coil spacing case was previously determined in chapter 3 to have little effect on the total pressure drop, with errors of less than 0.7%. This however, can be further reduced by a factor of two by considering distinct sections of the cord in serial. The continuous analog of this approach, wherein helical pressure gradient estimates are computed continuously over the length of a varying centreline, reproduces the pressure gradient favourably. However, this method does not appreciably improve the total pressure estimate and requires geometric information not readily available in a clinical setting at this point in time.

Finally, several example cords were considered to demonstrate calculation of the indices. The process used to measure the width, length and number of coils was described, as were the issues with such an approach. Particularly,

the indices rely on the cord measurements representing the geometry at 40 weeks gestation. In some cases fixation within formalin has resulted in cord shrinkage post-pregnancy. Measurements taken on these cords are therefore not wholly representative of the geometry in-utero.

In conclusion, the pressure and flow indices provide a new measure of flow resistance within the umbilical vessels. These indices are based on flow characteristics thought to describe pathology and provide a measure of the deviation of a particular geometry from normal conditions. This is distinct from the current diagnostic, the cord UCI, which is simply a ratio of two measurable cord parameters. The pressure and flow indices require only one additional measurement to the UCI; the cord coiling width, in addition to the pitch length and number of coils, though information regarding vessel size, blood flow-rate and viscosity will improve the estimate. Both new indices have been shown robust to input measurement error and have a fairly homogenous error distribution over cords of interest. The pressure index in particular shows promise as it can be calculated for a large range of cords and has the ability to describe cord irregularities such as knots and non-uniform coiling. The UCI, conversely, can only describe the number of coils per unit length on average and hence is unable to account for such features. Both indices are suited to quick computation via a short executable script, or alternatively a graphical or tabular format for clinical use. The final stage in their assessment as diagnostic indices is a rigorous clinical analysis in order to determine their efficacy. This study is underway.

Chapter 6

Conclusions and further work

This thesis has considered blood flow within the umbilical vessels of the human maternal-fetal circulatory system. Despite the integral role played by the umbilical cord in the development of the fetus, relatively little is known of the effect variations to the cord geometry have on the blood flow. There is currently only a single geometrically derived diagnostic measure used to quantify coiling and attempt to identify adverse outcome. The umbilical coiling index (UCI) is a ratio of the number of coils of the cord to its length (in cm), and aims to describe the level of coiling of a particular cord. This index, however, is not grounded in any theoretical understanding of cord processes and has been noted by several authors to lack proper correlation with adverse outcome. It also fails to account for geometric non-uniformities such as any variation to the nature of the coiling along the cord length as well as to the presence of umbilical knots, which are known to adversely affect fetal development.

The blood vessel pressure drop, which is an important diagnostic parameter in the systemic circulation of the human body, was assumed indicative of pathology within the umbilical vessels for this study. The key questions posed were therefore; does the UCI predict pressure variations among cords of varying geometry? Do geometric irregularities play a significant role in blood flow processes? Finally, if the UCI cannot predict blood vessel pressure, is there another, clinically suitable method for estimating the flow resistance? To answer these questions, a fluid dynamic study of blood flow within the umbilical vessels was developed. The key aims were,

i) To determine the efficacy of the UCI for predicting the mean cord vessel pressure drop and variations to the flow field;

ii) To quantify the effect of geometric irregularities including variable coiling, twist reversal and knots;

iii) To determine the effect of pulsatility within the umbilical arteries, and;

iv) To develop new indices for the prediction of mean umbilical vessel blood pressure and flow-rate based on simple, non-invasive geometric cord measurements.

The primary method of analysis was numerical, employing the finite element method through the open source `c++` library `oomph-lib`. This was used to investigate steady and unsteady incompressible Newtonian fluid flow in rigid three-dimensional tubes. Chapter 2 presented a discussion of this method, in addition to steady and pulsatile validations which facilitate the selection of parameters for the numerical scheme. The finite element method is particularly suited to flow within complex geometries such as those representative of typical and atypical umbilical vessels. The cord geometries used to model the umbilical vessels each exhibit some amount of coiling which is approximated by a helix of specified curvature and torsion. The effects of cord non-uniformities such as knotting, width and coil space variation were also considered through careful geometric prescriptions.

The main structure of the thesis composed three results chapters which link together to demonstrate that a new diagnostic method is necessary, and that it can be derived using steady results through idealised helical tubes. Chapter 3 addressed (i) and (ii), above, by considering steady flow through a selection of geometric models representative of a variety of different cord types. This study shows that the UCI does not correlate with the cord vessel pressure drop. Taking the latter as a diagnostic of pathology, it follows that the UCI is generally unable to distinguish between cords which are normal in pregnancy and those for which adverse outcomes are possible. Geometric cord irregularities, however, do not significantly affect the flow providing the vessel is unconstricted. The steady pressure drop through purely helical tubes can therefore be used as a reasonable approximation to the flow through more complex geometries. For non-uniformly coiled vessels where the spacing of the coils or the width of the cord vary along the length, the mean helical result predicts the true pressure drop to within roughly 5% accuracy. The steady pressure drop through loose knots of the cord are estimated to within 10% by the same method, significantly improving with increased UCI. However, the addition of a constriction such as may be present when a knot is sufficiently tight can have significant impacts on the flow resistance. In one case, the vessel pressure drop increases by 44% due to the addition of an axisymmetric reduction in radius to half the nominal value. Severe flow reversal is also apparent immediately downstream of constrictions narrower than 87.5% of the nominal vessel radius. Conversely, false knots and

twist reversal, which are typically ignored in a clinical setting, have negligible impact on the pressure and flow within the cord.

While the flow is reasonably steady in the umbilical vein, unsteadiness is present within the arteries due to the forcing of the fetal heart. Chapter 4 addressed (ii) and (iii) through consideration of pulsatile flow within the geometries of the steady analysis. This study shows that the steady flow calculated through geometries representative of the umbilical arteries can be used to estimate the temporally averaged pressure drop to within 5% for arteries without any cross-sectional reduction. Larger errors of up to 10% are observed when the constriction shrinks to 55% of the nominal arterial radius. This study therefore validates the concept of employing the steady pressure drop as a proxy for the temporal average for the umbilical arteries over a wide range of geometries likely within pregnancy. Remarkably, the ratio between the peak (systolic) and mean pressure throughout the cycle is relatively constant among coiled vessels, and is not significantly affected by the addition of geometric irregularities such as loose knotting or coil variation. A typical arterial pressure cycle oscillates between systolic and diastolic pressures 2.4 and -0.2 times the mean pressure, respectively. Comparatively, this peak-to-mean pressure ratio is roughly 25% lower than in a straight pipe of equivalent length. This suggests that the presence of coiling in the umbilical arteries acts to effectively smooth out extreme pressures at a given Re when compared with an equivalent straight tube. This fact may offer another possible explanation for the presence of coiling within the typical umbilical geometry.

Having shown that the UCI is unable to describe pressure variations due to the geometry, an alternative method for the description of the flow resistance inherent to a particular cord is necessary. Chapter 3 shows that unconstricted cords can be approximated by a helical tube with the mean curvature and torsion of the geometry. Additionally, chapter 4 shows that pulsatile fluctuations within the arteries result in a fairly uniform pressure profile which oscillates about the steady pressure drop. Chapter 5 therefore addressed (iv) to develop a new methodology for describing the flow resistance within a cord. Using a combination of empirical helical pressure gradient estimates available in the literature and additional numerical data computed using `oomph-lib`, a quick method for determining the pressure drop through umbilical geometries was developed. This was then used as the basis for the development of a new method for describing umbilical flow resistance. This method requires only one additional geometric measurement to the calculation of the UCI; namely the cord coiling width, $\hat{w}$. Two related cord indices; the umbilical pressure index, PX, and the umbilical flow index, QX, were defined in order to assess the severity of the cord geometry. PX

provides a comparison between the umbilical vessel pressure drop at a standard blood flow-rate to a reference pressure through a defined normo-coiled cord. The umbilical flow index, QX, instead compares the blood flow-rate through a given cord at reference pressure to the reference blood flow-rate. The relationship between the two indices is dependent on the length, curvature and torsion of the cord, with cords of high PX exhibiting low QX and vice versa. Both index calculations are based on non-invasive, geometric cord measurements so as to be easily implemented in a clinical setting. These measurements are then used to construct helical vessel geometries representative of the average cord coiling. The combination of empirical and interpolated numerical data is then used to determine the pressure drop through the cord vessels, with the Newton-Raphson method employed for the inverse flow-rate problem. Both indices have been shown robust to input measurement error and have a fairly homogenous error distribution over cords of interest. The pressure index in particular shows promise as it can be calculated for a large range of cords and has the ability to describe cord irregularities such as knots and non-uniform coiling. The UCI, conversely, can only describe the number of coils per unit length on average and hence is unable to account for such features. Both indices are suited to quick computation via a short executable script, or alternatively a graphical or tabular format for clinical use. The final stage in their assessment as diagnostic indices is a rigorous clinical analysis in order to determine their efficacy.

In conclusion, the UCI does not predict pressure variations among cords of varying geometry. The pressure drop over the length of an umbilical vessel depends on many factors including the torsion, curvature, flow Reynolds number and crucially, the length of the cord. The UCI is a ratio of the number of coils of the cord to its length and therefore represents the length of a single coil only. It also lacks a reference to the transverse cord measurement, the cord width, which is important in determining the total vessel arclength as well as the curvature and torsion. Geometric irregularities typically play an insignificant role in blood flow processes at the Reynolds numbers present within the umbilical cord. However, vessel constrictions, such as may occur as a result of a tight true knot, can significantly affect flow and pressure characteristics. Finally, the pressure and flow indices developed represent a clinically suitable method for estimating flow resistance. This method was designed to be simple, however, is malleable to additional information regarding the dynamic or geometric parameters of the flow, such as variable vessel radius or Reynolds number. Additionally there is room for further research regarding the effect of vessel distensibility, non-Newtonian blood flow and non circular cross-sections in the description of umbilical flow resistance.

Appendix A

Numerical method

The following appendix presents an outline of the numerical method used as well at its implementation within `oomph-lib`. This discussion is included as a reference and the reader is directed to Fletcher (1991) and Reddy and Gartling (1994) for a more complete description of the finite element method, as well as to the `oomph-lib` documentation available online for a more comprehensive discussion of the numerics used.

A.1 The finite element method

The finite element method is based on the concept of differential equations expressed in a 'weak form'. A classical (or strong) solution, $\overline{u}$, to a governing equation represented by a differential operator, L, is said to be a function which satisfies the partial differential equation(s) and boundary conditions at every point within the domain, Ω. That is,

$$L\Big(\overline{u}(x_i)\Big) = 0 \quad \forall x_i \in \Omega \quad \text{and} \quad u|_{\partial\Omega} = g, \tag{A.1}$$

where g is some function defined on $\partial\Omega$. For an approximation to this solution, u, the differential operator will yield a non-zero value, termed the residual, R.

$$L(u) = R \neq 0. \tag{A.2}$$

u is termed a weak solution to the governing equation, L, if it satisfies the boundary condition,

$$u(x_i)|_{\partial\Omega} = g, \tag{A.3}$$

and if the "weighted residual", defined as,

$$r = \int_{\Omega} R\phi^{test}(x_i)\mathrm{d}x_1\mathrm{d}x_2\mathrm{d}x_3, \tag{A.4}$$

vanishes for *any* test function, $\phi^{test}(x_i)$ which satisfy the homogeneous boundary conditions,

$$\phi^{test}(x_i)|_{\partial\Omega} = 0. \tag{A.5}$$

The critical point here is that the weak solution requires the integral to vanish for any test function, which can be shown equivalent to requiring that $R \equiv 0$ (the definition of a strong solution). Hence it is true that "weak solutions are strong solutions", and it is sufficient to show that a function, u, is a solution to equation (A.1), provided it satisfies equations (A.3) and (A.4). The weak solution can be written as the sum of two functions,

$$u(x_i) = u_h(x_i) + u_p(x_i), \tag{A.6}$$

where $u_p(x_i)$ is an arbitrary function which satisfies the Dirichlet boundary conditions,

$$u_p(x_i)|_{\partial\Omega} = g, \tag{A.7}$$

and $u_h(x_i)$ is an unknown function which satisfies the homogeneous boundary conditions,

$$u_h(x_i)|_{\partial\Omega} = 0. \tag{A.8}$$

This unknown function, $u_h(x_i)$, is then expanded in terms of a known, complete, infinite set of basis functions which must span the function space $H_0(\Omega)$. This function space is problem-dependent, and is determined based on the (minimal) constraints imposed on both $u(x_i)$ and $\phi^{test}(x_i)$ in order for the integral in the weak form to 'make sense', that is, to exist. All functions which satisfy these constraints form the function space $H(D)$, with those in $H_0(\Omega)$ also satisfying the additional constraint that they vanish on the domain boundary, $\partial\Omega$. That is

$$u(x_i) \in H_0(\Omega) \quad \Longleftrightarrow \quad u(x_i) \in H_0(\Omega) \quad \text{and} \quad u|_{\partial\Omega} = 0. \tag{A.9}$$

Now, suppose that $\psi_j(x_i) \in H_0(\Omega)$ form this basis, for $j = 1, ..., \infty$, so that,

$$u(x_i) = u_p(x_i) + \sum_{j=1}^{\infty} U_j \psi_j(x_i), \tag{A.10}$$

where the U_j are coefficients yet to be determined. The test functions are contained within the aforementioned function space as well, i.e. $\phi^{test}(x_i) \in H_0(\Omega)$, and hence can be similarly expanded in terms of the basis functions, $\psi_j(x_i)$,

$$\phi^{test}(x_i) = \sum_{k=1}^{\infty} \Phi_k \psi_k(x_i). \tag{A.11}$$

The weak form given in equation (A.4) now becomes,

$$r = \int_{\Omega} L\left(u_p(x_i) + \sum_{j=1}^{\infty} U_j \psi_j(x_i)\right) \sum_{k=1}^{\infty} \Big(\Phi_k \psi_k(x_i)\Big) \mathrm{d}x_1 \mathrm{d}x_2 \mathrm{d}x_3 = 0 \quad \text{(A.12)}$$

which can be re-written as,

$$r = \sum_{k=1}^{\infty} \Phi_k r_k(U_1, U_2, ...) = 0, \quad \text{(A.13)}$$

where,

$$r_k(U_1, U_2, ...) = \int_{\Omega} L\left(u_p(x_i) + \sum_{j=1}^{\infty} U_j \psi_j(x_i)\right) \psi_k(x_i) \mathrm{d}x_1 \mathrm{d}x_2 \mathrm{d}x_3. \quad \text{(A.14)}$$

Equation (A.13) must hold $\forall\ \Phi_k$, hence it must be true that

$$r_k(U_1, U_2, ...) = 0 \quad \text{for} \quad k = 1, 2, ... \quad . \quad \text{(A.15)}$$

In practice the expansions given in equations (A.10) and (A.11) must be truncated after a finite number of terms, M, and the resulting M unknown coefficients are determined from the M equations,

$$r_k(U_1, U_2, ..., U_M) = 0 \quad \text{for} \quad k = 1, 2, ..., M. \quad \text{(A.16)}$$

In `oomph-lib`, this is achieved firstly by use of a Gaussian quadrature to calculate the integral for each r_k, and then by Newton's method to solve the resulting system of M non-linear equations (Heil et al., 2008). The basis functions are chosen to have the same functional form, which for Navier-Stokes elements used in the interpolation of the velocity field are quadratic polynomials. The true advantage of the finite element method, however, is that the basis functions, $\psi_j(x_i)$, can be chosen to have finite support, i.e. to be non-zero in only a small region of the domain, termed an element. This leads to a computationally efficient sparse Jacobian matrix arising in Newton's method.

A.2 `oomph-lib`

Implementation of the finite element method is via `oomph-lib`, the **o**bject-**o**riented **m**ulti-**ph**ysics **lib**rary, developed at the University of Manchester.

`oomph-lib` is an open-source library of finite elements written in c++ specifically designed for the solution of physiological fluid dynamics problems. This library consists of a number of high-level classes, namespaces and functions which facilitate the solution of multi-physics problems. Throughout this section the elements, mesh and general functionality offered by `oomph-lib` is detailed.

A.2.1 Elements

Two three-dimensional, LBB-stable isoparametric Navier-Stokes elements are available for use in `oomph-lib`. These are the Taylor-Hood and Crouziex-Raviart elements; both 27-node brick elements which store the three velocity values, u_i, at each node. The two elements map between local and global coordinates using the same quadratic basis functions as for velocity interpolation, however, differ in their representation of the pressure field. Taylor-Hood elements store pressure values at the 8 vertex nodes with a tri-linear interpolation employed to determine the pressure within each element. Crouzeix-Raviart elements, however, store 4 pressure degrees of freedom within each element, with the pressure at any point within the element given by,

$$P = P_0^{(E)} + P_1^{(E)} s_1 + P_2^{(E)} s_2 + P_3^{(E)} s_3, \tag{A.17}$$

where s_i are the elements local coordinates and $P_i^{(E)}$ is the i-th pressure degree of freedom in element E. Taylor-Hood elements do not conserve mass locally, however, ensure that the pressure field is continuous inter-element. This is particularly advantageous for flow problems in which explicit representation of the pressure field is necessary. A mesh constructed from Taylor-Hood elements will also have fewer pressure degrees of freedom as the vertex nodes are coupled to neighbouring elements. In a sufficiently fine mesh this factor ensures that Taylor-Hood elements generate significantly fewer pressure degrees of freedom than Crouzeix-Raviart elements. Taylor-Hood elements are chosen for this study accordingly.

A.2.2 Mesh

Numerous problem-dependent base meshes are available within `oomph-lib`. The most suitable option for umbilical arterial or venous flow is the `TubeMesh`, which maps a vector of local coordinates to the corresponding Cartesian coordinates of a simple tube. The mesh consists of repeating 'macro elements', or axial layers, which each comprise 5 base elements; one central element surrounded by 4 satellite elements as shown in figure A.1(a). The relative

size and position of these elements are controlled via two input parameters; `theta_positions` and `radial_frac` which control the angular location and radial position of the vertices of the central element, respectively. The number of these macro elements are controlled by the parameter `n_layer`, which is passed to the mesh constructor during problem formulation. The axial structure of the mesh is shown in figure A.1(b). The tube can then be deformed into an arbitrary three-dimensional shape by specifying a `geometric_object` which maps the local tube coordinates (r, θ, Z) to the global Cartesian coordinates (x, y, z).

Routines for spatial mesh adaptation allow the mesh to be refined in regions exhibiting particularly high solution gradients. In order to quantify the error associated with the finite element solution, `oomph-lib` uses Z2-error estimation. This estimate is calculated for each element based on the flux of the solution, $f_i = \partial u/\partial x_i$. This error estimate hinges on the premise that the velocity field calculated using the finite element method is piecewise continuous between elements. Hence, a measure of the magnitude of the discontinuity in the flux between elements provides an indication of the smoothness of the solution. To implement this, a quantity termed the recovered flux, f_i^{rec}, is calculated by matching the discontinuous flux field found using finite element data, f_i^{FE}, to a globally smooth polynomial solution constructed using appropriate recovery basis functions. To lessen the computational power required, this projection is performed using low-order polynomials over small patches of elements with the error for each element calculated based on a norm of the difference in calculated fluxes. Spatial mesh adaptation can be conducted after each solve of the system, with tolerances set for the minimum, e_{min}, and maximum, e_{max}, error desired throughout the domain.

A.2.3 Procedure

For the solution of any problem within `oomph-lib`, a problem class, for example `SimpleTubeFlowProblem`, must be constructed in order to define problem specific functions and store relevant pointers. Functions are defined for the specification of the geometry, initial and boundary conditions as well as procedures for setting iterative solvers, mesh refinement and documentation. The main driver code then simply consists of the creation of a `problem` object of class `SimpleTubeFlowProblem`, with the element type passed as an argument. Procedures for defining the geometry are included in the function `build_mesh`, which maps the mesh to the desired geometry defined in an object, for example, `simple_tube`, of class `GeomObject`. If desired, parallel mesh distribution can then be undergone with iterative solvers specified for larger problems. These solvers are discussed in section A.3. For steady prob-

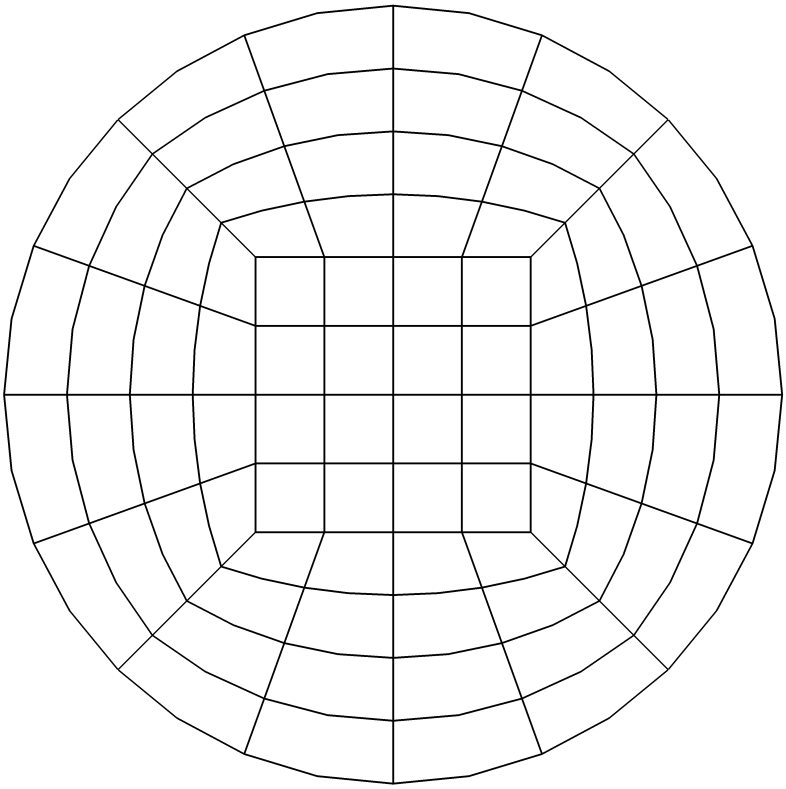

(a)

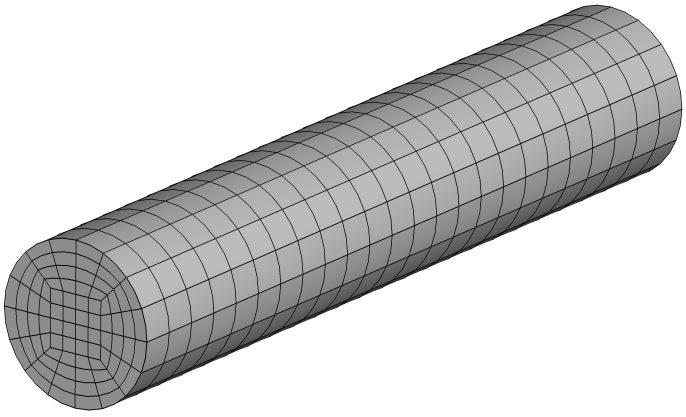

(b)

Figure A.1: The `TubeMesh` used in `oomph-lib` with two uniform refinements; a) cross-sectional view and; b) the full tube showing axial layers.

lems a Gaussian quadrature is used to calculate the integral for each r_k in equation (A.16), with Newton's method employed to solve the resultant system of M non-linear equations via the function `newton_solve` (Heil et al., 2008). For time-dependent problems, the linear system of algebraic equations is instead replaced with a system of ordinary differential equations. The `oomph-lib` library provides a number of explicit and implicit timesteppers for use with the Navier–Stokes equations which must be defined in the problem constructor. These timesteppers allow both spatial and temporal adaptivity, with the final solve facilitated by the function `unsteady_newton_solve` which accepts arguments defining the timestep interval and adaptivity criteria. An example driver code for a loose knot artery with a pulsatile inlet boundary condition is included in appendix C.1.

A.3 Iterative linear solvers

GMRES is implemented in `oomph-lib` via the third-party Trilinos library. A pointer to a `TrilinosAztecOOSolver` object is created in problem construction, with solve parameters such as the size of the Krylov subspace and error tolerance set. Nominally these are chosen as 1000 and 10×10^{-10}, respectively.

As the physical problem incorporates several coupled partial differential equations it is possible to split the original system into 'blocks' in a natural way for preconditioning. `oomph-lib` uses the least-squares commutator (LSC) Navier-Stokes preconditioner which allows the pressure and momentum equations to be handled separately. The linear system analysed has the block structure,

$$\begin{bmatrix} F & G \\ D & \mathbf{0} \end{bmatrix} \begin{bmatrix} \mathbf{z_u} \\ \mathbf{z_p} \end{bmatrix} = \begin{bmatrix} \mathbf{r_u} \\ \mathbf{r_p} \end{bmatrix},$$

where F is the momentum block, G is the discrete gradient operator and D is the discrete divergence operator. In `oomph-lib` this exact Jacobian may be replaced by a block-triangular approximation via a Navier Stokes Schur complement preconditioner,

$$\begin{bmatrix} F & G \\ \mathbf{0} & -M_s \end{bmatrix} \begin{bmatrix} \mathbf{z_u} \\ \mathbf{z_p} \end{bmatrix} = \begin{bmatrix} \mathbf{r_u} \\ \mathbf{r_p} \end{bmatrix},$$

where M_s is an approximation to the Schur-complement ($S = DF^{-1}G$). This

system may then be solved in two steps,

$$\mathbf{z_p} = -{M_s}^{-1}\mathbf{r_p}, \tag{A.18}$$

$$\mathbf{z_u} = -F^{-1}(\mathbf{r_u} - G\mathbf{z_p}). \tag{A.19}$$

The Navier Stokes Schur complement preconditioner replaces ${M_s}^{-1}$ in the first step by,

$${M_s}^{-1} = -P^{-1}EP^{-1}, \tag{A.20}$$

where $P = DQ^{-1}G$ and $E = DQ^{-1}FQ^{-1}G$ and Q is the diagonal of the velocity mass matrix. Each of equations (A.18) and (A.19) may be separately preconditioned in order to optimise speed and memory usage. The Navier-Stokes pressure and momentum blocks are solved using one AMG cycle of the Hypre `BoomerAMG` preconditioner. One damped Jacobi smoothing step is performed with the AMG strength ($0 < \theta \leq 1$) and damping ($0 < \omega \leq 2$) parameters determined via trial and error on a helical pipe flow problem. The optimal strength and damping were determined as 0.7 and 1.0 for the pressure block, respectively, with 0.9 and 0.0 for the corresponding parameters of the momentum block.

Appendix B

Steady flow

The technical details of the numerical continuation scheme are similar for each geometry and so only the specifics for the U_t study are included here. First a discussion of the temporal solvers and the method for assessing convergence is presented, followed by an analysis of the outlet boundary conditions.

In general there was significant difficulty encountered performing numerical calculations of, admittedly, moderate size. A number of issues arose in the implementation of `oomph-lib` which may have occurred due, in part, to problems with the local installation. This typically meant that larger problems of a higher level of refinement failed to solve within a reasonable time-frame, as evidenced by the large walltime of over 90hrs for a problem of under half a million degrees of freedom on 48 processors, table B.1. In some cases, segmentation faults occurred which could not be reliably diagnosed. For this reason a lower level of refinement was often favoured, provided the results could be deemed accurate to within an acceptable error tolerance. Access to computational resources was another restrictive factor which encouraged the use of mesh systems of fewer degrees of freedom.

B.1 Temporal calculations within `oomph-lib`

Steady solvers are incremented from an initial solve at $Re = 0$ until failure of convergence at Re_F, which is geometry dependent. Case U_{t1} failed after a successful solve at $Re = 220$, while U_{t3}, U_{t5} and U_{t6} failed at $Re = 140$. A summary of the run data is displayed in table B.1. Temporal solvers specified with steady boundary conditions are then used in order to find solutions at Re beyond those attainable through the use of the steady solvers alone. This method requires,

i) Initialisation of the domain to stagnant, $u_i = 0$, flow throughout the

Cord	Re_F	$n_{dof,F}$	n_{proc}	Walltime
U_{t1}	220	483,481	48	90:18:25
U_{t2}	150	376,865	48	34:30:05
U_{t3}	140	575,992	48	31:56:24
U_{t4}	170	692,828	48	50:31:32
U_{t5}	140	1,036,260	96	63:17:29
U_{t6}	140	1,143,724	96	77:37:38

Table B.1: Steady solve statistics for the U_t study.

domain, with a Poiseuille inlet velocity and pseudo traction-free outlet condition as prescribed in the steady calculations.

ii) Solution of the flow at $t = 0$ for $Re = 0$.

iii) Marching of the Re with timestep in increments of $Re = 10$ until the first Re at which failure had previously occurred in the steady calculations (Re_F). At this point the Re dependence is removed and the temporal simulation is conducted until a steady solution (if present) is found.

In order to perform temporal calculations a timestepper object must be specified. Within `oomph-lib`, the standard timestepper is of the BDF (Backward-Difference Formula) family for which a second-order solver is selected. The Courant-Friedrichs-Lewy condition states that for stability of an explicit scheme the timestep, Δt, should be related to the spatial discretisation, Δx, according to,

$$C = \frac{u\Delta t}{\Delta x} < C_{max}$$

where C is termed the *Courant number* and C_{max} is typically taken as unity for an explicit scheme. In practice $C_{max} > 1$ for implicit schemes. Using this relation, an expression for the suitable timestep can be obtained. Δx is taken to be the smallest of the mesh distances; in this case the cross-sectional distance within the central box,

$$\Delta x = \frac{R}{2\sqrt{2}}.$$

The maximum velocity for a parabolic velocity flow profile is,

$$u = 2\mathcal{U},$$

where $\mathcal{U}$ is the average cross-sectional velocity. The requisite timestep is then found from,

$$\Delta t < \frac{\Delta x}{u} = \frac{R}{2\sqrt{2}}\frac{1}{2\mathcal{U}} \approx 0.1768,$$

where $R = 1 = \mathcal{U}$. The timestep is therefore $\Delta t = 0.17$. For temporal problems, `oomph-lib` requires the specification of a Reynolds number multiplied by the Strouhal number ($ReSt$). This is defined as,

$$ReSt = \frac{\mathcal{U}R}{\nu}\frac{R}{\mathcal{U}\mathcal{T}} = \frac{R^2}{\nu\mathcal{T}}.$$

Lacking any physical motivation for the time–scale it is taken as $\mathcal{T} = \mathcal{L}/\mathcal{U}$ (i.e. the natural timescale associated with the flow). Hence, $St = 1$ and $ReSt = Re$.

In order to assess the convergence of the temporal simulations, case U_{t1} is investigated due to it's high curvature and smaller mesh. For this cord, the steady solutions fail at $Re = 230$. As such a temporal solution is sought at the previous successful solve of $Re = 220$ with the initial condition formed from an approximate solution at $Re = 200$. Figure B.1 shows the evolution of the time-derivative of the vessel pressure drop and total average kinetic energy, $\bar{E}_k$, at $Re = 220$. After roughly 250 timesteps there is little change in the computed ΔP and $\bar{E}_k$ with each having converged to within 0.0116% and 0.0106% of the values at the 500^{th} time-step, respectively. The relative difference between the temporal solution at $t_s = 200$ and the pressure computed for the steady simulation is 0.63% while the discrepancy in the total average kinetic energy is 0.23%. This can be attributed in part to the mesh; the steady solve has 22993 elements while the temporal mesh has 33851 elements. Figure B.2 shows the secondary velocity field computed using steady and temporal solvers at two locations along the domain length. The different mesh refinement is visible however the underlying flow is almost identical. For the remainder of the temporal calculations a larger timestep of $\Delta t = 0.5$ was chosen to speedup convergence.

B.2 Outlet boundary conditions

To assess the impact of the straight outlet length the flow at $Re = 300$ was computed through vessel U_{t1} with $L_s = 100$. The average axial pressure

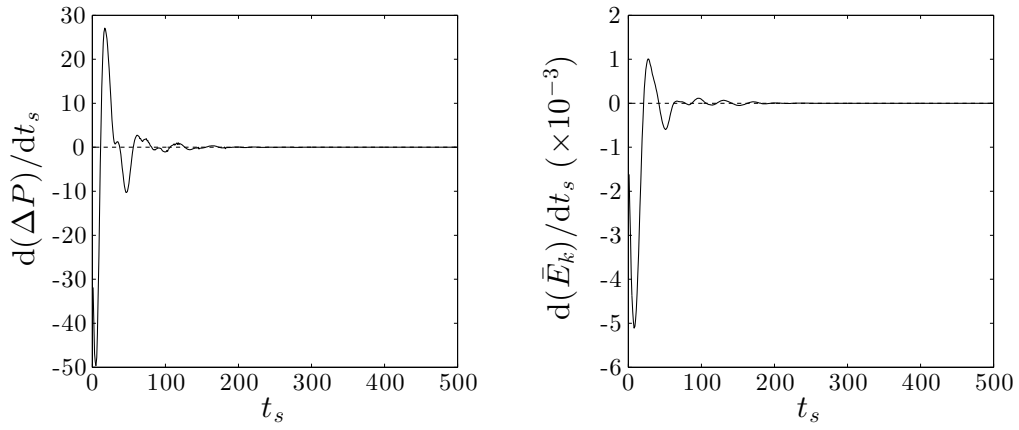

Figure B.1: Convergence of the temporal solvers showing the evolution of a) the time derivative of the pressure drop, ΔP, and; b) the average Kinetic Energy, $\bar{E}_k$, for Case U_{t1} at $Re = 220$.

gradient computed at each mesh cross-section within the shorter domain was found to differ by at most 9.93% to the extended domain run, the largest discrepancy at the curvature discontinuities where the helix joins the planar bend. At the outlet the pressure gradient was within 0.83% of the extended value. The total pressure drop along the vessel length was within 0.078% of the corresponding extended section, which was deemed sufficiently low to justify the shorter outlet length. A comparison of the flow profiles at the original domain outlet location is provided in figures B.3(a) and (b) with very little difference to the secondary flow profile evident between geometries. The flow at the outlet of the extended domain is shown in figure B.3(c), where it can be seen that the velocity profile has still yet to resume the straight pipe solution.

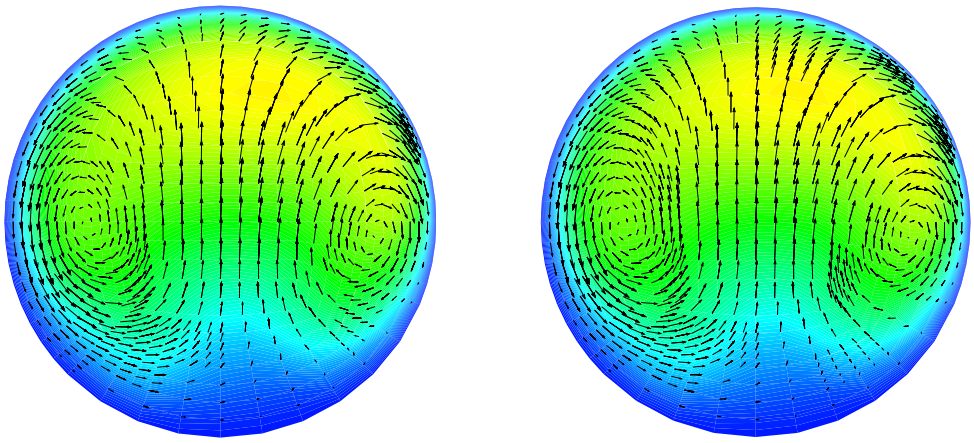

(a) (b)

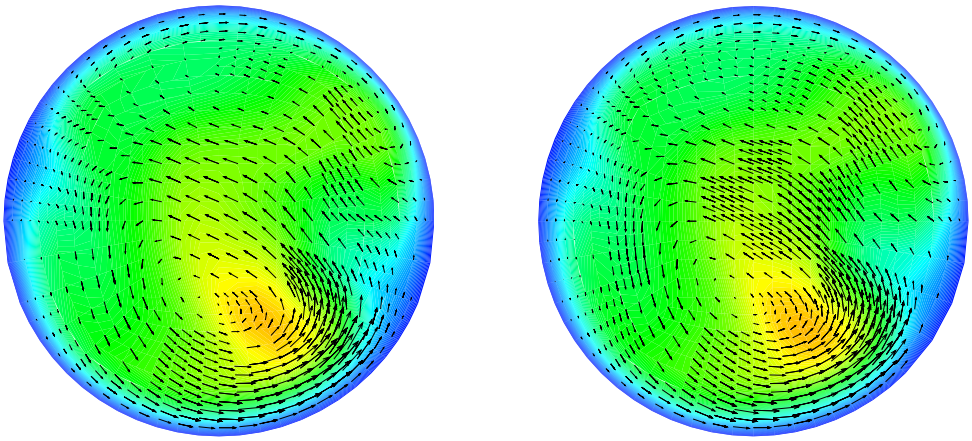

(c) (d)

Figure B.2: Convergence of the temporal solvers showing contours of the axial velocity, W, with the secondary velocity field overlayed at two locations within the tube for the steady simulation (left) and temporal simulation (right). Top: entrance to the helical section; Bottom: fully developed flow.

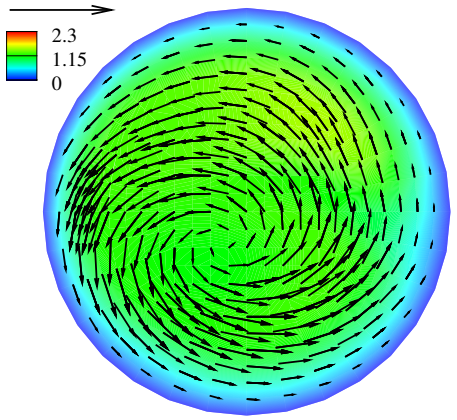

(a) Z = 50.0 ($L_s = 10$)

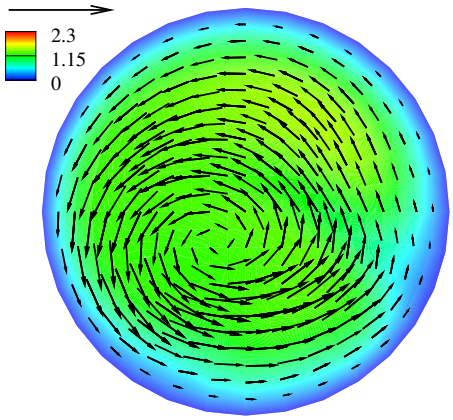

(b) Z = 50.0 ($L_s = 100$)

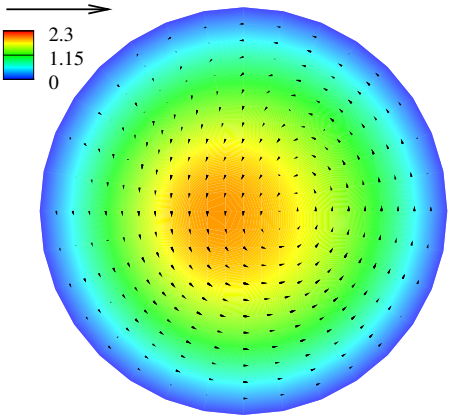

(c) Z = 140.0 ($L_s = 100$)

Figure B.3: Contours of the axial velocity, W, with the secondary velocity field overlayed at $Re = 300$. a) the outlet to the standard U_{t1} vessel with $L_s = 10$, b) the same distance from the inlet, computed on a vessel with $L_s = 100$ at the outlet, and; c) the outlet of the $L_s = 100$ vessel.

Appendix C

Pulsatile flow

C.1 Pulsatile `oomph-lib` code

This section contains an example driver for pulsatile flow through a loose-knot geometry. The geometric description is aided by the use of splines.

```
//LIC// ====================================================================
//LIC// This file forms part of oomph-lib, the object-oriented,
//LIC// multi-physics finite-element library, available
//LIC// at http://www.oomph-lib.org.
//LIC//
//LIC//           Version 0.90. August 3, 2009.
//LIC//
//LIC// Copyright (C) 2006-2009 Matthias Heil and Andrew Hazel
//LIC//
//LIC// This library is free software; you can redistribute it
//LIC// and/or modify it under the terms of the GNU Lesser
//LIC// General Public License as published by the Free
//LIC// Software Foundation; either version 2.1 of the
//LIC// License, or (at your option) any later version.
//LIC//
//LIC// This library is distributed in the hope that it
//LIC// will be useful, but WITHOUT ANY WARRANTY;
//LIC// without even the implied warranty of MERCHANTABILITY
//LIC// or FITNESS FOR A PARTICULAR PURPOSE.
//LIC// See the GNU Lesser General Public
//LIC// License for more details.
//LIC//
```

```
//LIC// You should have received a copy of the GNU
//LIC// LesserGeneral Public License along with this
//LIC// library; if not, write to theFree Software
//LIC// Foundation, Inc., 51 Franklin Street,
//LIC// Fifth Floor,Boston, MA
//LIC// 02110-1301  USA.
//LIC//
//LIC// The authors may be contacted
//LIC//  atoomph-lib@maths.man.ac.uk.
//LIC//
//LIC//====================================================

// D. Wilke 2014

/// Driver for 3D pulsatile, Navier-Stokes flow through a loose
// knot artery using splines.

//Generic routines
#include "generic.h"
#include "navier_stokes.h"

// The mesh
#include "meshes/tube_mesh.h"

// Complex bessel functions
#include "libAmosBessel.h"

// Splines
#include <stdlib.h>
#include <stdio.h>
#include <iostream>
#include <fstream>
#include <math.h>
#include <gsl/gsl_errno.h>
#include <gsl/gsl_spline.h>

using namespace std;

using namespace oomph;

#ifdef OOMPH_HAS_HYPRE
```

```
//========================================================
/// Helper method to set AMG settings for tube flow
//========================================================

namespace Hypre_Solver_Settings
{
// Define AMG solve parameters:

//      // Default AMG control parameters -- these seem OK;
//      // see hypre documenation for details.
//      AMG_using_simple_smoothing=true;
//      AMG_simple_smoother = 1; i.e. GS
//      AMG_complex_smoother = 6; i.e.
//      AMG_smoother_iterations = 2;
//      AMG_damping = 1.0;
//      AMG_strength = 0.25;
//      AMG_truncation = 0.0;
//      AMG_coarsening = 0;
//      AMG_max_levels = 100;
//      AMG_max_row_sum = 1.0;
//      AMG_print_level = 0;


// Pressure
unsigned pressure_iterations = 1;
double pressure_stength = 0.7;
unsigned pressure_simple_smoother = 1;
unsigned pressure_smoother_iterations = 2;
double pressure_damping = 1.0;
unsigned pressure_coarsening = 0; // Def(0)


// Momentum
unsigned momentum_iterations = 1;
double momentum_stength = 0.9;
unsigned momentum_simple_smoother = 0;
unsigned momentum_smoother_iterations = 2;
double momentum_damping = 0.0;
unsigned momentum_coarsening = 0; // Def(0)
```

```
void
set_pressure_defaults_for_3DTube_problem(HyprePreconditioner*
hypre_preconditioner_pt){

// Pressure Block:

hypre_preconditioner_pt->hypre_method() =
HyprePreconditioner::BoomerAMG;
hypre_preconditioner_pt->set_amg_iterations(
pressure_iterations);
hypre_preconditioner_pt->amg_using_simple_smoothing();
hypre_preconditioner_pt->amg_simple_smoother() =
pressure_simple_smoother;
hypre_preconditioner_pt->amg_smoother_iterations() =
pressure_smoother_iterations;
hypre_preconditioner_pt->amg_strength() =
pressure_stength;
hypre_preconditioner_pt->amg_coarsening() =
pressure_coarsening;
hypre_preconditioner_pt->amg_damping() =
pressure_damping;

hypre_preconditioner_pt->enable_hypre_error_messages();
hypre_preconditioner_pt->amg_print_level() = 0;

}

void
set_momentum_defaults_for_3DTube_problem(HyprePreconditioner*
hypre_preconditioner_pt){

// Momentum Block:

hypre_preconditioner_pt->hypre_method() =
HyprePreconditioner::BoomerAMG;
hypre_preconditioner_pt->set_amg_iterations(
momentum_iterations);
hypre_preconditioner_pt->amg_using_simple_smoothing();
hypre_preconditioner_pt->amg_simple_smoother() =
```

```
momentum_simple_smoother;
hypre_preconditioner_pt->amg_smoother_iterations() =
momentum_smoother_iterations;
hypre_preconditioner_pt->amg_strength() =
momentum_stength;
hypre_preconditioner_pt->amg_coarsening() =
momentum_coarsening;
hypre_preconditioner_pt->amg_damping() =
momentum_damping;

hypre_preconditioner_pt->enable_hypre_error_messages();
hypre_preconditioner_pt->amg_print_level() = 0;

}
}

//============================================================
/// Helper method for the block diagonal F block preconditioner
to use hypre as a subsidiary block preconditioner
//============================================================
namespace Hypre_Subsidiary_Preconditioner_Helper
{
Preconditioner* set_hypre_preconditioner()
{

HyprePreconditioner* HypPt = new HyprePreconditioner;

// Set default settings as for 2D Poisson
Hypre_Solver_Settings::
set_momentum_defaults_for_3DTube_problem(HypPt);

return HypPt;
}
}

#endif


//=start_of_namespace========================================
/// Namespace for physical parameters
//============================================================
```

```
namespace Global_Physical_Variables
{
/// Pi
const double pi = 4.0*atan(1.0);

/// Reynolds number
double Re= 100.0;
double Re_Initial = 100.0;
double Re_Final = 100.0;
double Re_increment = 10.0;

/// Unsteady parameters
double Ured = 41.0; // Reduced velocity

double ReSt = Re/Ured;
double T = 1.0; // Period
double t_max = 10.0*T;

double omega = 2.0*pi/T;
double alpha = sqrt((2.0*pi*Re)/(Ured));

double umax_s = 2.0;
double Rho = 1.0;

/// Pulsatile Waveform:
double t1 = 0.15*T;
double umax_t_desired = 3.24; // Desired "Peak" velocity
double umax_t = umax_t_desired-umax_s;


double dt = T/100.0; // Initial timestep

// Dimensional input quantities:
double Radius_dimensional = 0.35; // Vessel radius
double P_dimensional = 2.6691;  // Cord pitch
double w_dimensional = 1.6; // Cord width
double offset = 0.0*(2.0*pi)/3.0; //
double scale_original = 1.25; //  Scale of the knot
double width_original = 2.5;
double length_original = 2.4;
double straight_z_end_dim = 5.0;
```

```
// Non-dimensional quantities:
double Radius = 1.0;
double P = P_dimensional/Radius_dimensional;
double Rh = 0.5*(w_dimensional/Radius_dimensional)-1.0;
double scale = scale_original/Radius_dimensional;
double width = width_original/Radius_dimensional;
double length = length_original/Radius_dimensional;
double straight_z_end =
straight_z_end_dim/Radius_dimensional;

/// Storage for total Length:
double Length = 0.0;

// Spline data:
unsigned Npoints_spline_in_straight = 11;
unsigned Npoints_spline_in_curve = 8;
unsigned Npoints_spline_knot = 50;
unsigned Npoints_spline_out_curve = 8;
unsigned Npoints_spline_out_straight = 11;
// Total number of spline points:
unsigned Npoints_spline = Npoints_spline_in_straight +
Npoints_spline_in_curve + Npoints_spline_knot +
Npoints_spline_out_curve + Npoints_spline_out_straight - 4;

// No. of points in arclength calc. over distinct sections
unsigned Npoints_knot = 5.0e4;
unsigned Npoints_curve = 5.0e4;
unsigned Npoints_arclength = 5.0e4;

// For spline:
double epsilon = 1.0e-13;
double t0 = 0.0 + epsilon;
double tf = (Npoints_spline-1.0) - epsilon;


} // end_of_namespace


/// Namespace for mesh parameters
//=============================================================
```

```
namespace Mesh_Parameters
{
unsigned nlayer = 0;
double alpha = 0.6;
double radial_frac_box = 0.5;
unsigned adapt_no = 0;
double emax = 1.5e-3;
double emin = 0.0;
unsigned nelement = nlayer*5;
unsigned max_adapt = 10;
unsigned n_uniform = 2;
unsigned n_wall_refinements = 0;

} // end_of_namespace//

/// Namespace for solve parameters
//============================================================
namespace Solve_Parameters
{

const char directory[] =
"/data/maths/data/dwilke/DATA/TrefKnot/";
const char file_title[] = "OCV_temporal"; //

bool checkRestart = false;
const char restart_file_title[] ="UCI_alpha";
double restart_Re = 40.0;

bool check_inlet = false;

bool temporal_steady_inlet = true;

bool startup = false; // flag to use steady inlet for
startup
bool steady_startup = false;

unsigned ts = 0; // total solves

bool temporal_adaptivity = true;
double Epsilon_t=1.0e-2; // Set target error for adaptive
timestepping
```

```
bool use_iterative_solver=true;
bool use_trilinos_solver = true;
bool use_lsc = true;
bool use_hypre_for_pressure=true;
bool use_block_diagonal_for_momentum=true;
bool use_hypre_for_momentum=true;

bool use_load_balance = true;
int load_balance_freq = 10;

int dump_it_freq = 100;

} // end_of_namespace//

/// Namespace for geometry
//=============================================================
namespace Geometry
{

// Spline functions:
// x-spline:
gsl_interp_accel *acc_x ;
gsl_spline *spline_x;

// y-spline:
gsl_interp_accel *acc_y;
gsl_spline *spline_y;

// z-spline:
gsl_interp_accel *acc_z;
gsl_spline *spline_z;

void init_spline()
{

unsigned i, k;
const double pi = 4.0*atan(1.0);

// Physical constants:
```

```
double P = Global_Physical_Variables::P;
double Rh = Global_Physical_Variables::Rh;
double scale = Global_Physical_Variables::scale;
double offset = Global_Physical_Variables::offset;
double Radius_dimensional =
Global_Physical_Variables::Radius_dimensional; // Dimensional
radius of the tube:

// The 'lengths' of each of the sections:
double straight_z_end =
Global_Physical_Variables::straight_z_end;
double knot_t_end = 4.0*pi/3.0;

// For the cubic curve:
double width = Global_Physical_Variables::width;
double length = Global_Physical_Variables::length;


// Initialise variables used to find centreline:
double t, zp, xh, yh, xc, yc, zc, dsdt, Tx, Ty, Tz,
ModB, Bx, By, Bz, ModN, Nx, Ny, Nz;

// Pre-define the normal/binormal and tangent to the
knot inlet, and outlet:
t = 0.0;
dsdt = sqrt(0.144e3 * pow(cos(t), 0.6e1) - 0.216e3 *
pow(cos(t), 0.4e1) + 0.32e2 * pow(cos(t), 0.3e1) + 0.81e2 *
pow(cos(t), 0.2e1) - 0.24e2 * cos(t) + 0.17e2);
ModB = sqrt(-(0.9216e4 * pow(cos(t), 0.9e1) - 0.20736e5
* pow(cos(t), 0.7e1) + 0.12416e5 * pow(cos(t), 0.6e1) +
0.15552e5 * pow(cos(t), 0.5e1) - 0.18624e5 * pow(cos(t), 0.4e1)
- 0.4880e4 * pow(cos(t), 0.3e1) + 0.6984e4 * pow(cos(t), 0.2e1)
+ 0.744e3 * cos(t) - 0.2338e4) * pow(0.144e3 * pow(cos(t),
0.6e1) - 0.216e3 * pow(cos(t), 0.4e1) + 0.32e2 * pow(cos(t),
0.3e1) + 0.81e2 * pow(cos(t), 0.2e1) - 0.24e2 * cos(t) +
0.17e2, -0.2e1)) * pow(0.144e3 * pow(cos(t), 0.6e1) - 0.216e3 *
pow(cos(t), 0.4e1) + 0.32e2 * pow(cos(t), 0.3e1) + 0.81e2 *
pow(cos(t), 0.2e1) - 0.24e2 * cos(t) + 0.17e2, 0.3e1 / 0.2e1);
ModN = (0.144e3 * pow(cos(t), 0.6e1) - 0.216e3 *
pow(cos(t), 0.4e1) + 0.32e2 * pow(cos(t), 0.3e1) + 0.81e2 *
pow(cos(t), 0.2e1) - 0.24e2 * cos(t) + 0.17e2) *
```

```
sqrt(-(0.9216e4 * pow(cos(t), 0.9e1) - 0.20736e5 * pow(cos(t),
0.7e1) + 0.12416e5 * pow(cos(t), 0.6e1) + 0.15552e5 *
pow(cos(t), 0.5e1) - 0.18624e5 * pow(cos(t), 0.4e1) - 0.4880e4
* pow(cos(t), 0.3e1) + 0.6984e4 * pow(cos(t), 0.2e1) + 0.744e3
* cos(t) - 0.2338e4) * pow(0.144e3 * pow(cos(t), 0.6e1) -
0.216e3 * pow(cos(t), 0.4e1) + 0.32e2 * pow(cos(t), 0.3e1) +
0.81e2 * pow(cos(t), 0.2e1) - 0.24e2 * cos(t) + 0.17e2,
-0.2e1));

double Nx_in = (1.0/ModN)*(0.96e2 * pow(cos(t), 0.5e1)
- 0.24e2 * pow(cos(t), 0.4e1) - 0.120e3 * pow(cos(t), 0.3e1) +
0.36e2 * pow(cos(t), 0.2e1) - 0.9e1);
double Ny_in = (1.0/ModN)*(0.12e2 * sin(t) * (0.8e1 *
pow(cos(t), 0.4e1) + 0.2e1 * pow(cos(t), 0.3e1) - 0.6e1 *
pow(cos(t), 0.2e1) + 0.3e1));
double Nz_in = (1.0/ModN)*(0.16e2 * pow(cos(t), 0.3e1)
- 0.12e2 * cos(t) + 0.31e2);

double Bx_in = (1.0/ModB)*((0.31e2 + 0.1152e4 *
pow(cos(t), 0.7e1) + 0.288e3 * pow(cos(t), 0.6e1) - 0.1728e4 *
pow(cos(t), 0.5e1) - 0.344e3 * pow(cos(t), 0.4e1) + 0.1096e4 *
pow(cos(t), 0.3e1) + 0.96e2 * pow(cos(t), 0.2e1) - 0.584e3 *
cos(t)) * sin(t));
double By_in = (1.0/ModB)*(-0.1152e4 * pow(cos(t),
0.8e1) + 0.288e3 * pow(cos(t), 0.7e1) + 0.2304e4 * pow(cos(t),
0.6e1) - 0.520e3 * pow(cos(t), 0.5e1) - 0.1064e4 * pow(cos(t),
0.4e1) + 0.272e3 * pow(cos(t), 0.3e1) + 0.236e3 * pow(cos(t),
0.2e1) - 0.2e1 * cos(t) - 0.124e3);
double Bz_in = (1.0/ModB)*(-(0.576e3 * pow(cos(t),
0.5e1) - 0.576e3 * pow(cos(t), 0.3e1) + 0.612e3 * pow(cos(t),
0.2e1) + 0.108e3 * cos(t) - 0.153e3) * sin(t));

double Tx_in = (1.0/dsdt)*(cos(t) + 0.4e1 * cos(0.2e1 *
t));
double Ty_in = (1.0/dsdt)*(-sin(t) + 0.4e1 * sin(0.2e1
* t));
double Tz_in = (1.0/dsdt)*(0.3e1 * cos((double) (3 *
t)));


t= knot_t_end;
```

```
dsdt = sqrt(0.144e3 * pow(cos(t), 0.6e1) - 0.216e3 *
pow(cos(t), 0.4e1) + 0.32e2 * pow(cos(t), 0.3e1) + 0.81e2 *
pow(cos(t), 0.2e1) - 0.24e2 * cos(t) + 0.17e2);
ModB = sqrt(-(0.9216e4 * pow(cos(t), 0.9e1) - 0.20736e5
* pow(cos(t), 0.7e1) + 0.12416e5 * pow(cos(t), 0.6e1) +
0.15552e5 * pow(cos(t), 0.5e1) - 0.18624e5 * pow(cos(t), 0.4e1)
- 0.4880e4 * pow(cos(t), 0.3e1) + 0.6984e4 * pow(cos(t), 0.2e1)
+ 0.744e3 * cos(t) - 0.2338e4) * pow(0.144e3 * pow(cos(t),
0.6e1) - 0.216e3 * pow(cos(t), 0.4e1) + 0.32e2 * pow(cos(t),
0.3e1) + 0.81e2 * pow(cos(t), 0.2e1) - 0.24e2 * cos(t) +
0.17e2, -0.2e1)) * pow(0.144e3 * pow(cos(t), 0.6e1) - 0.216e3 *
pow(cos(t), 0.4e1) + 0.32e2 * pow(cos(t), 0.3e1) + 0.81e2 *
pow(cos(t), 0.2e1) - 0.24e2 * cos(t) + 0.17e2, 0.3e1 / 0.2e1);
ModN = (0.144e3 * pow(cos(t), 0.6e1) - 0.216e3 *
pow(cos(t), 0.4e1) + 0.32e2 * pow(cos(t), 0.3e1) + 0.81e2 *
pow(cos(t), 0.2e1) - 0.24e2 * cos(t) + 0.17e2) *
sqrt(-(0.9216e4 * pow(cos(t), 0.9e1) - 0.20736e5 * pow(cos(t),
0.7e1) + 0.12416e5 * pow(cos(t), 0.6e1) + 0.15552e5 *
pow(cos(t), 0.5e1) - 0.18624e5 * pow(cos(t), 0.4e1) - 0.4880e4
* pow(cos(t), 0.3e1) + 0.6984e4 * pow(cos(t), 0.2e1) + 0.744e3
* cos(t) - 0.2338e4) * pow(0.144e3 * pow(cos(t), 0.6e1) -
0.216e3 * pow(cos(t), 0.4e1) + 0.32e2 * pow(cos(t), 0.3e1) +
0.81e2 * pow(cos(t), 0.2e1) - 0.24e2 * cos(t) + 0.17e2,
-0.2e1));

double Nx_out = (1.0/ModN)*(0.96e2 * pow(cos(t), 0.5e1)
- 0.24e2 * pow(cos(t), 0.4e1) - 0.120e3 * pow(cos(t), 0.3e1) +
0.36e2 * pow(cos(t), 0.2e1) - 0.9e1);
double Ny_out = (1.0/ModN)*(0.12e2 * sin(t) * (0.8e1 *
pow(cos(t), 0.4e1) + 0.2e1 * pow(cos(t), 0.3e1) - 0.6e1 *
pow(cos(t), 0.2e1) + 0.3e1));
double Nz_out = (1.0/ModN)*(0.16e2 * pow(cos(t), 0.3e1)
- 0.12e2 * cos(t) + 0.31e2);

double Bx_out = (1.0/ModB)*((0.31e2 + 0.1152e4 *
pow(cos(t), 0.7e1) + 0.288e3 * pow(cos(t), 0.6e1) - 0.1728e4 *
pow(cos(t), 0.5e1) - 0.344e3 * pow(cos(t), 0.4e1) + 0.1096e4 *
pow(cos(t), 0.3e1) + 0.96e2 * pow(cos(t), 0.2e1) - 0.584e3 *
cos(t)) * sin(t));
double By_out = (1.0/ModB)*(-0.1152e4 * pow(cos(t),
0.8e1) + 0.288e3 * pow(cos(t), 0.7e1) + 0.2304e4 * pow(cos(t),
```

```
0.6e1) - 0.520e3 * pow(cos(t), 0.5e1) - 0.1064e4 * pow(cos(t),
0.4e1) + 0.272e3 * pow(cos(t), 0.3e1) + 0.236e3 * pow(cos(t),
0.2e1) - 0.2e1 * cos(t) - 0.124e3);
double Bz_out = (1.0/ModB)*(-(0.576e3 * pow(cos(t),
0.5e1) - 0.576e3 * pow(cos(t), 0.3e1) + 0.612e3 * pow(cos(t),
0.2e1) + 0.108e3 * cos(t) - 0.153e3) * sin(t));

double Tx_out = (1.0/dsdt)*(cos(t) + 0.4e1 * cos(0.2e1
* t));
double Ty_out = (1.0/dsdt)*(-sin(t) + 0.4e1 * sin(0.2e1
* t));
double Tz_out = (1.0/dsdt)*(0.3e1 * cos((double) (3 *
t)));

// Vector intersecting both curve planes. This vector
must lie in both
// outlet and inlet planes, hence it must be orthogonal
to both normals:
double rx = Ny_in*Nz_out - Nz_in*Ny_out;
double ry = Nz_in*Nx_out - Nx_in*Nz_out;
double rz = Nx_in*Ny_out - Ny_in*Nx_out;

double mod_r = sqrt(rx*rx + ry*ry + rz*rz);

// Normalise this vector as N_in and N_out are not
orthogonal
rx=rx/mod_r;
ry=ry/mod_r;
rz=rz/mod_r;


// Angle which determines the slope:
// In the inlet plane:
double theta = acos(rx*Tx_in + ry*Ty_in + rz*Tz_in);
double slope = tan(theta);

double X0 = width;
double Y0 = -length;
double D0 = -slope;

oomph_info << "X0 = " << X0 << std::endl;
```

```
oomph_info << "Y0 = " << Y0 << std::endl;
oomph_info << "D0 = " << D0 << std::endl;


double curved_X_end = X0;

// For the cubic:
double alpha2 = (3.0*X0*X0*Y0 -
X0*X0*X0*D0)/(X0*X0*X0*X0);
double alpha3 = (-2.0*X0*Y0 + X0*X0*D0)/(X0*X0*X0*X0);


// Put the cubic 'binormal' at the free-end here

double X = X0;
double ModBin = sqrt((double) (pow((double) (3.0 * X *
alpha3 + alpha2), (double) 2.0) * pow((double) (9.0 *
pow((double) X, (double) 4.0) * alpha3 * alpha3 + 12.0 *
pow((double) X, (double) 3.0) * alpha2 * alpha3 + 4.0 * X * X *
alpha2 * alpha2 + 1.0), (double) (-2.0)))) * pow((double) (9.0
* pow((double) X, (double) 4.0) * alpha3 * alpha3 + 12.0 *
pow((double) X, (double) 3.0) * alpha2 * alpha3 + 4.0 * X * X *
alpha2 * alpha2 + 1.0), 0.3e1 / 0.2e1);
double Bcurveinx_1 = (1.0/ModBin)*(-1.0 * X * (9.0 * X
* X * alpha3 * alpha3 + 9.0 * X * alpha2 * alpha3 + 2.0 *
alpha2 * alpha2));
double Bcurveiny_1 = (1.0/ModBin)*(3.0 * X * alpha3 +
alpha2);
double Bcurveoutx_end = Bcurveinx_1;
double Bcurveouty_end = Bcurveiny_1;

double cg1 =  (3.0 * X * alpha3 + alpha2)*(3.0 * X *
alpha3 + alpha2);
double cg2a = (9.0*X*X*X*X*alpha3*alpha3 +
12.0*X*X*X*alpha2*alpha3 + 4.0*X*X*alpha2*alpha2 + 1.0);
double cg2 = cg2a*cg2a;
double cg3 = pow(cg2a,3.0/2.0);
double ModBin2 = sqrt(cg1/cg2)*cg3;

oomph_info << "ModBin = " << ModBin << std::endl;
oomph_info << "cg1 = " << cg1 << std::endl;
```

```
oomph_info << "cg2 = " << cg2 << std::endl;
oomph_info << "cg3 = " << cg3 << std::endl;

oomph_info << "ModBin2 = " << ModBin2 << std::endl;

double B1x_1 = Bcurveinx_1*(-Tx_in) +
Bcurveiny_1*(Bx_in);
double B1y_1 = Bcurveinx_1*(-Ty_in) +
Bcurveiny_1*(By_in);
double B1z_1 = Bcurveinx_1*(-Tz_in) +
Bcurveiny_1*(Bz_in);

double B2x_end = Bcurveoutx_end*(Tx_out) +
Bcurveouty_end*(Bx_out);
double B2y_end = Bcurveoutx_end*(Ty_out) +
Bcurveouty_end*(By_out);
double B2z_end = Bcurveoutx_end*(Tz_out) +
Bcurveouty_end*(Bz_out);


t = 0.0;
// The start of the knot:
double xknot_1 = scale*(sin(t) + 2.0*sin(2.0*t));
double yknot_1 = scale*(cos(t) - 2.0*cos(2.0*t));
double zknot_1 = scale*sin(3.0*t);

t = knot_t_end;
// The end of the knot:
double xknot_end = scale*(sin(t) + 2.0*sin(2.0*t));
double yknot_end = scale*(cos(t) - 2.0*cos(2.0*t));
double zknot_end = scale*sin(3.0*t);

// The curved centreline:
double Lin_x_1 = X0*(-Tx_in) + Y0*(Bx_in) + xknot_1;
double Lin_y_1 = X0*(-Ty_in) + Y0*(By_in) + yknot_1;
double Lin_z_1 = X0*(-Tz_in) + Y0*(Bz_in) + zknot_1;


// The end of the curved outlet:
double Lout_x_end = X0*(Tx_out) + Y0*(Bx_out) +
xknot_end;
```

```
double Lout_y_end = X0*(Ty_out) + Y0*(By_out) +
yknot_end;
double Lout_z_end = X0*(Tz_out) + Y0*(Bz_out) +
zknot_end;


// Check:

oomph_info << "Tx_in = " << Tx_in << ", Ty_in = " <<
Ty_in << ", Tz_in = " << Tz_in << std::endl;
oomph_info << "Nx_in = " << Nx_in << ", Ny_in = " <<
Ny_in << ", Nz_in = " << Nz_in << std::endl;
oomph_info << "Bx_in = " << Bx_in << ", By_in = " <<
By_in << ", Bz_in = " << Bz_in << std::endl;


oomph_info << "Tx_out = " << Tx_out << ", Ty_out = " <<
Ty_out << ", Tz_out = " << Tz_out << std::endl;
oomph_info << "Nx_out = " << Nx_out << ", Ny_out = " <<
Ny_out << ", Nz_out = " << Nz_out << std::endl;
oomph_info << "Bx_out = " << Bx_out << ", By_out = " <<
By_out << ", Bz_out = " << Bz_out << std::endl;

oomph_info << "rx = " << rx << ", ry = " << ry << ", rz
= " << rz << std::endl;

oomph_info << "theta = " << theta << std::endl;
oomph_info << "slope = " << slope << std::endl;
oomph_info << "alpha2 = " << alpha2 << std::endl;
oomph_info << "alpha3 = " << alpha3 << std::endl;

oomph_info << "Lin_x_1 = " << Lin_x_1 << ", Lin_y_1 = "
<< Lin_y_1 << ", Lin_z_1 = " << Lin_z_1 << std::endl;
oomph_info << "Lout_x_end = " << Lout_x_end << ",
Lout_y_end = " << Lout_y_end << ", Lout_z_end = " << Lout_z_end
<< std::endl;

oomph_info << "B1x_1 = " << B1x_1 << ", B1y_1 = " <<
B1y_1 << ", B1z_1 = " << B1z_1 << std::endl;
oomph_info << "B2x_end = " << B2x_end << ", B2y_end = "
<< B2y_end << ", B2z_end = " << B2z_end << std::endl;
```

```
oomph_info << "Bcurveinx_1 = " << Bcurveinx_1 <<
std::endl;
oomph_info << "Bcurveiny_1 = " << Bcurveiny_1 <<
std::endl;

oomph_info << "Bcurveoutx_end = " << Bcurveoutx_end <<
std::endl;
oomph_info << "Bcurveouty_end = " << Bcurveouty_end <<
std::endl;


// Initialise the end of arclength each of each
section:

double curved_in_z_end, knot_z_end, curved_out_z_end;

ofstream cl_file;
char clfilename[100];
sprintf(clfilename,"./%s_BaseCL.dat",Solve_Parameters::
file_title);
cl_file.open(clfilename);


// Number of points in each section:
unsigned Npoints_spline_in_straight =
Global_Physical_Variables::Npoints_spline_in_straight;
unsigned Npoints_spline_in_curve =
Global_Physical_Variables::Npoints_spline_in_curve; // Number
of spline points on inlet
unsigned Npoints_spline_knot =
Global_Physical_Variables::Npoints_spline_knot; // Number of
spline points between t=0, 4*pi/3 on knot
unsigned Npoints_spline_out_curve =
Global_Physical_Variables::Npoints_spline_out_curve; // Number
of spline points on outlet
unsigned Npoints_spline_out_straight =
Global_Physical_Variables::Npoints_spline_out_straight;

// Total number of spline points:
unsigned Npoints_spline =
```

```
Global_Physical_Variables::Npoints_spline;

// Number of points for arclength calcs:
unsigned Npoints_knot =
Global_Physical_Variables::Npoints_knot;
unsigned Npoints_curve =
Global_Physical_Variables::Npoints_curve;

// Initialise the x,y,z points as well as the
'arclength' parameter, t
double x[Npoints_spline-1], y[Npoints_spline-1],
z[Npoints_spline-1], t_arclength[Npoints_spline-1];


for (i=0; i < Npoints_spline_in_straight; i++) {

// A map from i to our arclength:
zp =
((double(i))/(double(Npoints_spline_in_straight)-1.0))*
straight_z_end;


// Straight centreline:
xc = rx*zp+(Lin_x_1-rx*straight_z_end);
yc = ry*zp+(Lin_y_1-ry*straight_z_end);
zc = rz*zp+(Lin_z_1-rz*straight_z_end);


// The helical centreline:
xh = Rh*sin(((2.0*pi*zp)/P)+offset);
yh = Rh*cos(((2.0*pi*zp)/P)+offset);

// Curve normal:
Nx = Nx_in;
Ny = Ny_in;
Nz = Nz_in;

// Curve binormal:
Bx = -B1x_1;
By = -B1y_1;
Bz = -B1z_1;
```

```
k = i;

if (i < Npoints_spline_in_straight-1) {

//oomph_info << "SI: k = " << k << std::endl;

// The final centreline:
x[k] = xc + xh*(Nx) + yh*(Bx);
y[k] = yc + xh*(Ny) + yh*(By);
z[k] = zc + xh*(Nz) + yh*(Bz);

cl_file << k << " " << zp << " " << xc << " "
<< yc << " " << zc << " " << Nx << " " << Ny << " " << Nz << "
" << Bx << " " << By << " " << Bz << " " << x[k] << " " << y[k]
<< " " << z[k] << std::endl;

}

}

// Create inlet curve:

for (i=0; i < Npoints_spline_in_curve; i++) {

// Note that X must not start at X0!
double start =
0.0;//curved_X_end/Npoints_spline_in_curve;

double X = (curved_X_end-start)*(1.0 -
((double(i))/(double(Npoints_spline_in_curve)-1.0))); // Varies
in the opposite direction

// Increment for trap int:
double trapzinc =
curved_X_end/double(Npoints_curve);
zp = 0.0;
double Xj = curved_X_end;
double dsdXj_1, dsdXj_0;

for (unsigned j = 0; Xj>=X; j=j+1) {
```

```
if (j==0) {
dsdXj_1 = sqrt(0.9e1 * pow(Xj, 0.4e1) *
alpha3 * alpha3 + 0.12e2 * pow(Xj, 0.3e1) * alpha2 * alpha3 +
0.4e1 * Xj * Xj * alpha2 * alpha2 + 0.1e1);
zp = 0.0;
}
else {
dsdXj_0 = dsdXj_1;
dsdXj_1 = sqrt(0.9e1 * pow(Xj, 0.4e1) *
alpha3 * alpha3 + 0.12e2 * pow(Xj, 0.3e1) * alpha2 * alpha3 +
0.4e1 * Xj * Xj * alpha2 * alpha2 + 0.1e1);
zp = zp +
abs((trapzinc)*0.5*(dsdXj_1+dsdXj_0)); // Use abs as X is
varying in the other direction
}
Xj=Xj-trapzinc;
}

zp = zp+straight_z_end; // Match to the end of the
straight.


double Y = alpha2*X*X + alpha3*X*X*X;

double ModBin = sqrt((double) (pow((double) (3.0 *
X * alpha3 + alpha2), (double) 2.0) * pow((double) (9.0 *
pow((double) X, (double) 4.0) * alpha3 * alpha3 + 12.0 *
pow((double) X, (double) 3.0) * alpha2 * alpha3 + 4.0 * X * X *
alpha2 * alpha2 + 1.0), (double) (-2.0)))) * pow((double) (9.0
* pow((double) X, (double) 4.0) * alpha3 * alpha3 + 12.0 *
pow((double) X, (double) 3.0) * alpha2 * alpha3 + 4.0 * X * X *
alpha2 * alpha2 + 1.0), 0.3e1 / 0.2e1);
double Bcurveinx = (1.0/ModBin)*(-1.0* X * (9.0 * X
* X * alpha3 * alpha3 + 9.0 * X * alpha2 * alpha3 + 2.0 *
alpha2 * alpha2));
double Bcurveiny = (1.0/ModBin)*(3.0 * X * alpha3 +
alpha2);

// The helical centreline:
xh = Rh*sin(((2.0*pi*zp)/P)+offset);
```

```
yh = Rh*cos(((2.0*pi*zp)/P)+offset);

// The curved centreline:
xc = X*(-Tx_in) + Y*(Bx_in) + xknot_1;
yc = X*(-Ty_in) + Y*(By_in) + yknot_1;
zc = X*(-Tz_in) + Y*(Bz_in) + zknot_1;

// Curve normal:
Nx = Nx_in;
Ny = Ny_in;
Nz = Nz_in;

// Curve binormal:

Bx = -1.0*(Bcurveinx*(-Tx_in) + Bcurveiny*(Bx_in));
By = -1.0*(Bcurveinx*(-Ty_in) + Bcurveiny*(By_in));
Bz = -1.0*(Bcurveinx*(-Tz_in) + Bcurveiny*(Bz_in));

k = i + (Npoints_spline_in_straight-1);

if (i < Npoints_spline_in_curve-1) {

//oomph_info << "CI: k = " << k << std::endl;

// The final centreline:
x[k] = xc + xh*(Nx) + yh*(Bx);
y[k] = yc + xh*(Ny) + yh*(By);
z[k] = zc + xh*(Nz) + yh*(Bz);

cl_file << k << " " << zp << " " << xc << " "
<< yc << " " << zc << " " << Nx << " " << Ny << " " << Nz << "
" << Bx << " " << By << " " << Bz << " " << x[k] << " " << y[k]
<< " " << z[k] << std::endl;


}

// The final point stores the arclength but we do
not include in the spline

curved_in_z_end = zp;
```

```
}

// Create knot:

for (i=0; i < Npoints_spline_knot; i++) {

double start =
0.0;//knot_t_end/Npoints_spline_knot;

// t is the ~KNOT~ curve parameter:
t =
((double(i))/(double(Npoints_spline_knot)-1.0))*(knot_t_end-
start)+start;

// Increment for trap int:
double trapzinc = knot_t_end/double(Npoints_knot);
zp = 0.0;
double tj = 0.0;
double dsdtj_1, dsdtj_0;

for (unsigned j = 0; tj<=t; j=j+1) {

if (j==0) {
dsdtj_1 = sqrt(0.144e3 * pow(cos(tj),
0.6e1) - 0.216e3 * pow(cos(tj), 0.4e1) + 0.32e2 * pow(cos(tj),
0.3e1) + 0.81e2 * pow(cos(tj), 0.2e1) - 0.24e2 * cos(tj) +
0.17e2);
zp = 0.0;
}
else {
dsdtj_0 = dsdtj_1;
dsdtj_1 = sqrt(0.144e3 * pow(cos(tj),
0.6e1) - 0.216e3 * pow(cos(tj), 0.4e1) + 0.32e2 * pow(cos(tj),
0.3e1) + 0.81e2 * pow(cos(tj), 0.2e1) - 0.24e2 * cos(tj) +
0.17e2);
zp = zp +
scale*(trapzinc)*0.5*(dsdtj_1+dsdtj_0);
}
tj=tj+trapzinc;
```

```
}

zp = zp+curved_in_z_end; // Match to the end of the
straight.

// The helical centrelines:
xh = Rh*sin(((2.0*pi*zp)/P)+offset);
yh = Rh*cos(((2.0*pi*zp)/P)+offset);

// The knot centreline:
xc = scale*(sin(t) + 2.0*sin(2.0*t));
yc = scale*(cos(t) - 2.0*cos(2*t));
zc = scale*sin(3.0*t);

// Knot Frenet vectors: (Output from Maple)

dsdt = sqrt(0.144e3 * pow(cos(t), 0.6e1) - 0.216e3
* pow(cos(t), 0.4e1) + 0.32e2 * pow(cos(t), 0.3e1) + 0.81e2 *
pow(cos(t), 0.2e1) - 0.24e2 * cos(t) + 0.17e2);

ModB = sqrt(-(0.9216e4 * pow(cos(t), 0.9e1) -
0.20736e5 * pow(cos(t), 0.7e1) + 0.12416e5 * pow(cos(t), 0.6e1)
+ 0.15552e5 * pow(cos(t), 0.5e1) - 0.18624e5 * pow(cos(t),
0.4e1) - 0.4880e4 * pow(cos(t), 0.3e1) + 0.6984e4 * pow(cos(t),
0.2e1) + 0.744e3 * cos(t) - 0.2338e4) * pow(0.144e3 *
pow(cos(t), 0.6e1) - 0.216e3 * pow(cos(t), 0.4e1) + 0.32e2 *
pow(cos(t), 0.3e1) + 0.81e2 * pow(cos(t), 0.2e1) - 0.24e2 *
cos(t) + 0.17e2, -0.2e1)) * pow(0.144e3 * pow(cos(t), 0.6e1) -
0.216e3 * pow(cos(t), 0.4e1) + 0.32e2 * pow(cos(t), 0.3e1) +
0.81e2 * pow(cos(t), 0.2e1) - 0.24e2 * cos(t) + 0.17e2, 0.3e1 /
0.2e1);

Bx = (1.0/ModB)*((0.31e2 + 0.1152e4 * pow(cos(t),
0.7e1) + 0.288e3 * pow(cos(t), 0.6e1) - 0.1728e4 * pow(cos(t),
0.5e1) - 0.344e3 * pow(cos(t), 0.4e1) + 0.1096e4 * pow(cos(t),
0.3e1) + 0.96e2 * pow(cos(t), 0.2e1) - 0.584e3 * cos(t)) *
sin(t));
By = (1.0/ModB)*(-0.1152e4 * pow(cos(t), 0.8e1) +
0.288e3 * pow(cos(t), 0.7e1) + 0.2304e4 * pow(cos(t), 0.6e1) -
0.520e3 * pow(cos(t), 0.5e1) - 0.1064e4 * pow(cos(t), 0.4e1) +
0.272e3 * pow(cos(t), 0.3e1) + 0.236e3 * pow(cos(t), 0.2e1) -
```

```
0.2e1 * cos(t) - 0.124e3);
Bz = (1.0/ModB)*(-(0.576e3 * pow(cos(t), 0.5e1) -
0.576e3 * pow(cos(t), 0.3e1) + 0.612e3 * pow(cos(t), 0.2e1) +
0.108e3 * cos(t) - 0.153e3) * sin(t));

ModN = (0.144e3 * pow(cos(t), 0.6e1) - 0.216e3 *
pow(cos(t), 0.4e1) + 0.32e2 * pow(cos(t), 0.3e1) + 0.81e2 *
pow(cos(t), 0.2e1) - 0.24e2 * cos(t) + 0.17e2) *
sqrt(-(0.9216e4 * pow(cos(t), 0.9e1) - 0.20736e5 * pow(cos(t),
0.7e1) + 0.12416e5 * pow(cos(t), 0.6e1) + 0.15552e5 *
pow(cos(t), 0.5e1) - 0.18624e5 * pow(cos(t), 0.4e1) - 0.4880e4
* pow(cos(t), 0.3e1) + 0.6984e4 * pow(cos(t), 0.2e1) + 0.744e3
* cos(t) - 0.2338e4) * pow(0.144e3 * pow(cos(t), 0.6e1) -
0.216e3 * pow(cos(t), 0.4e1) + 0.32e2 * pow(cos(t), 0.3e1) +
0.81e2 * pow(cos(t), 0.2e1) - 0.24e2 * cos(t) + 0.17e2,
-0.2e1));

Nx = (1.0/ModN)*(0.96e2 * pow(cos(t), 0.5e1) -
0.24e2 * pow(cos(t), 0.4e1) - 0.120e3 * pow(cos(t), 0.3e1) +
0.36e2 * pow(cos(t), 0.2e1) - 0.9e1);
Ny = (1.0/ModN)*(0.12e2 * sin(t) * (0.8e1 *
pow(cos(t), 0.4e1) + 0.2e1 * pow(cos(t), 0.3e1) - 0.6e1 *
pow(cos(t), 0.2e1) + 0.3e1));
Nz = (1.0/ModN)*(0.16e2 * pow(cos(t), 0.3e1) -
0.12e2 * cos(t) + 0.31e2);

k = i +
(Npoints_spline_in_straight-1+Npoints_spline_in_curve-1);


if (i < Npoints_spline_knot-1) {

//oomph_info << "Knot: k = " << k << std::endl;

// The final centrelines:
x[k] = xc + xh*(Nx) + yh*(Bx);
y[k] = yc + xh*(Ny) + yh*(By);
z[k] = zc + xh*(Nz) + yh*(Bz);

cl_file << k << " " << zp << " " << xc << " "
<< yc << " " << zc << " " << Nx << " " << Ny << " " << Nz << "
```

```
" << Bx << " " << By << " " << Bz << " " << x[k] << " " << y[k]
<< " " << z[k] << std::endl;
}

knot_z_end = zp;


}

// Create curved outlet:

for (i=0; i < Npoints_spline_out_curve; i++) {

// A map from k to our arclength:

double start =
0.0;//curved_X_end/Npoints_spline_out_curve;

double X =
((double(i))/(double(Npoints_spline_out_curve)-1.0))*(
curved_X_end-start)+start;

// Increment for trap int:
double trapzinc =
curved_X_end/double(Npoints_curve);
zp = 0.0;
double Xj = 0.0;
double dsdXj_1, dsdXj_0;

for (unsigned j = 0; Xj<=X; j=j+1) {

if (j==0) {
dsdXj_1 = sqrt(0.9e1 * pow(Xj, 0.4e1) *
alpha3 * alpha3 + 0.12e2 * pow(Xj, 0.3e1) * alpha2 * alpha3 +
0.4e1 * Xj * Xj * alpha2 * alpha2 + 0.1e1);
zp = 0.0;
}
else {
dsdXj_0 = dsdXj_1;
dsdXj_1 = sqrt(0.9e1 * pow(Xj, 0.4e1) *
alpha3 * alpha3 + 0.12e2 * pow(Xj, 0.3e1) * alpha2 * alpha3 +
```

```
0.4e1 * Xj * Xj * alpha2 * alpha2 + 0.1e1);
zp = zp + (trapzinc)*0.5*(dsdXj_1+dsdXj_0);

}
Xj=Xj+trapzinc;
}

zp = zp+knot_z_end; // Match to the end of the
straight.


double Y = alpha2*X*X + alpha3*X*X*X;

double ModBin = sqrt((double) (pow((double) (3.0 *
X * alpha3 + alpha2), (double) 2.0) * pow((double) (9.0 *
pow((double) X, (double) 4.0) * alpha3 * alpha3 + 12.0 *
pow((double) X, (double) 3.0) * alpha2 * alpha3 + 4.0 * X * X *
alpha2 * alpha2 + 1.0), (double) (-2.0)))) * pow((double) (9.0
* pow((double) X, (double) 4.0) * alpha3 * alpha3 + 12.0 *
pow((double) X, (double) 3.0) * alpha2 * alpha3 + 4.0 * X * X *
alpha2 * alpha2 + 1.0), 0.3e1 / 0.2e1);
double Bcurveoutx = (1.0/ModBin)*(-1.0* X * (9.0 *
X * X * alpha3 * alpha3 + 9.0 * X * alpha2 * alpha3 + 2.0 *
alpha2 * alpha2));
double Bcurveouty = (1.0/ModBin)*(3.0 * X * alpha3
+ alpha2);

// The helical centreline:
xh = Rh*sin(((2.0*pi*zp)/P)+offset);
yh = Rh*cos(((2.0*pi*zp)/P)+offset);

// The curved centreline:
xc = X*(Tx_out) + Y*(Bx_out) + xknot_end;
yc = X*(Ty_out) + Y*(By_out) + yknot_end;
zc = X*(Tz_out) + Y*(Bz_out) + zknot_end;

// Curve normal:
Nx = Nx_out;
Ny = Ny_out;
Nz = Nz_out;
```

```
// Curve binormal:
Bx = -1.0*(Bcurveoutx*(Tx_out) +
Bcurveouty*(Bx_out));
By = -1.0*(Bcurveoutx*(Ty_out) +
Bcurveouty*(By_out));
Bz = -1.0*(Bcurveoutx*(Tz_out) +
Bcurveouty*(Bz_out));

k =
i+(Npoints_spline_in_straight-1+Npoints_spline_in_curve-1+
Npoints_spline_knot-1);

if (i < Npoints_spline_out_curve-1) {

// The final centreline:
x[k] = xc + xh*(Nx) + yh*(Bx);
y[k] = yc + xh*(Ny) + yh*(By);
z[k] = zc + xh*(Nz) + yh*(Bz);

cl_file << k << " " << zp << " " << xc << " "
<< yc << " " << zc << " " << Nx << " " << Ny << " " << Nz << "
" << Bx << " " << By << " " << Bz << " " << x[k] << " " << y[k]
<< " " << z[k] << std::endl;

}

curved_out_z_end = zp;


}

// Create straight outlet:

for (i=0; i < Npoints_spline_out_straight; i++) {

// A map from k to our arclength:

double start =
0.0;//straight_z_end/Npoints_spline_in_straight;

double Z =
```

```
((double(i))/(double(Npoints_spline_in_straight)-1.0))*(
straight_z_end-start)+start;

zp = Z+curved_out_z_end;

// Straight centreline:
xc = rx*(Z)+ Lout_x_end;
yc = ry*(Z)+ Lout_y_end;
zc = rz*(Z)+ Lout_z_end;

// The helical centreline:
xh = Rh*sin(((2.0*pi*zp)/P)+offset);
yh = Rh*cos(((2.0*pi*zp)/P)+offset);

// Curve normal:
Nx = Nx_out;
Ny = Ny_out;
Nz = Nz_out;

// Curve binormal:
Bx = -B2x_end;
By = -B2y_end;
Bz = -B2z_end;

k =
i+(Npoints_spline_in_straight-1+Npoints_spline_in_curve-1+
Npoints_spline_knot-1+Npoints_spline_out_curve-1);


// The final centreline:
x[k] = xc + xh*(Nx) + yh*(Bx);
y[k] = yc + xh*(Ny) + yh*(By);
z[k] = zc + xh*(Nz) + yh*(Bz);

cl_file << k << " " << zp << " " << xc << " " << yc
<< " " << zc << " " << Nx << " " << Ny << " " << Nz << " " <<
Bx << " " << By << " " << Bz << " " << x[k] << " " << y[k] << "
" << z[k] << std::endl;

}
```

```
oomph_info << "Npoints_spline = " << Npoints_spline <<
std::endl;


cl_file.close();

for (i = 0; i < Npoints_spline; i++)
{
t_arclength[i] = double(i);
//oomph_info << "t = " << t_arclength[i]
<<std::endl;
}

{
// x-spline:
Geometry::acc_x = gsl_interp_accel_alloc ();
Geometry::spline_x = gsl_spline_alloc
(gsl_interp_cspline, Npoints_spline);
gsl_spline_init (spline_x, t_arclength, x,
Npoints_spline);

// y-spline:
Geometry::acc_y = gsl_interp_accel_alloc ();
Geometry::spline_y = gsl_spline_alloc
(gsl_interp_cspline, Npoints_spline);
gsl_spline_init (Geometry::spline_y, t_arclength,
y, Npoints_spline);

// z-spline:
Geometry::acc_z = gsl_interp_accel_alloc ();
Geometry::spline_z = gsl_spline_alloc
(gsl_interp_cspline, Npoints_spline);
gsl_spline_init (Geometry::spline_z, t_arclength,
z, Npoints_spline);


}

}
```

```
void free_spline()
{

gsl_spline_free (Geometry::spline_x);
gsl_interp_accel_free (Geometry::acc_x);
gsl_spline_free (Geometry::spline_y);
gsl_interp_accel_free (Geometry::acc_y);
gsl_spline_free (Geometry::spline_z);
gsl_interp_accel_free (Geometry::acc_z);

}


void eval_spline(const double& ti, double& xi, double& yi,
double& zi, double& Txi, double& Tyi, double& Tzi, double& Nxi,
double& Nyi, double& Nzi, double& Bxi, double& Byi, double&
Bzi, double& curvature)
{

double dxdti, dydti, dzdti, d2xdt2i, d2ydt2i, d2zdt2i;

{

xi = gsl_spline_eval (Geometry::spline_x, ti,
Geometry::acc_x);
yi = gsl_spline_eval (Geometry::spline_y, ti,
Geometry::acc_y);
zi = gsl_spline_eval (Geometry::spline_z, ti,
Geometry::acc_z);

dxdti = gsl_spline_eval_deriv (Geometry::spline_x,
ti, Geometry::acc_x);
dydti = gsl_spline_eval_deriv (Geometry::spline_y,
ti, Geometry::acc_y);
dzdti = gsl_spline_eval_deriv (Geometry::spline_z,
ti, Geometry::acc_z);

d2xdt2i = gsl_spline_eval_deriv2
(Geometry::spline_x, ti, Geometry::acc_x);
d2ydt2i = gsl_spline_eval_deriv2
(Geometry::spline_y, ti, Geometry::acc_y);
```

```
d2zdt2i = gsl_spline_eval_deriv2
(Geometry::spline_z, ti, Geometry::acc_z);

// Now calculate Frenet triad:

double dsdti = sqrt(dxdti*dxdti + dydti*dydti +
dzdti*dzdti);

// Tangent:
Txi = dxdti/dsdti;
Tyi = dydti/dsdti;
Tzi = dzdti/dsdti;

// Normal:
double dTdtxi = d2xdt2i/(sqrt(dxdti*dxdti +
dydti*dydti + dzdti*dzdti)) - dxdti*(dxdti*d2xdt2i +
dydti*d2ydt2i + dzdti*d2zdt2i)/pow(dxdti*dxdti + dydti*dydti +
dzdti*dzdti,1.5);
double dTdtyi = d2ydt2i/(sqrt(dxdti*dxdti +
dydti*dydti + dzdti*dzdti)) - dydti*(dxdti*d2xdt2i +
dydti*d2ydt2i + dzdti*d2zdt2i)/pow(dxdti*dxdti + dydti*dydti +
dzdti*dzdti,1.5);
double dTdtzi = d2zdt2i/(sqrt(dxdti*dxdti +
dydti*dydti + dzdti*dzdti)) - dzdti*(dxdti*d2xdt2i +
dydti*d2ydt2i + dzdti*d2zdt2i)/pow(dxdti*dxdti + dydti*dydti +
dzdti*dzdti,1.5);

double mag_dTdti = sqrt((dTdtxi)*(dTdtxi) +
(dTdtyi)*(dTdtyi) + (dTdtzi)*(dTdtzi));

curvature = mag_dTdti/dsdti;


Nxi = dTdtxi/mag_dTdti;
Nyi = dTdtyi/mag_dTdti;
Nzi = dTdtzi/mag_dTdti;

// Binormal: (B = T x N)
Bxi = Tyi*Nzi - Tzi*Nyi;
Byi = -Txi*Nzi + Tzi*Nxi;
Bzi = Txi*Nyi - Tyi*Nxi;
```

```
}

}

void return_arclength(const double& ti, double& si)
{

double t0=Global_Physical_Variables::t0;
double tf=Global_Physical_Variables::tf;

double trapzinc = (tf -
t0)/double(Global_Physical_Variables::Npoints_arclength);

si = 0.0;
double t = 0.0;
double dsdti_1, dsdti_0, dxdti, dydti, dzdti;

for (unsigned i = 0; t<ti; i=i+1) {

dxdti = gsl_spline_eval_deriv (Geometry::spline_x,
t, Geometry::acc_x);
dydti = gsl_spline_eval_deriv (Geometry::spline_y,
t, Geometry::acc_y);
dzdti = gsl_spline_eval_deriv (Geometry::spline_z,
t, Geometry::acc_z);

if (i==0) {
dsdti_1 = sqrt(dxdti*dxdti + dydti*dydti +
dzdti*dzdti);
si = 0.0;
}
else {
dsdti_0 = dsdti_1;
dsdti_1 = sqrt(dxdti*dxdti + dydti*dydti +
dzdti*dzdti);
si = si + (trapzinc)*0.5*(dsdti_1+dsdti_0);
}

t=t+trapzinc;
}
```

```
}


}



/// Namespace for steady BCs
//====================================================================
namespace steady_boundary_conditions
{
/// Get inlet boundary comdition at time t, location (X,Y).
void get_inlet_bc(const double& t, const double& X, const
double& Y, double& u_axial)
{

double r = sqrt(X*X + Y*Y);

u_axial = 2.0*(1.0-pow(r,2.0));
}


} // end_of_namespace//


/// Namespace for PulsatileVariables
//====================================================================
namespace PulsatileVariables
{

void get_pressure(cdouble& P_1, cdouble& P_2, cdouble& P_3,
cdouble& P_4)
{

/// Compute pulsatile variables:

double T = Global_Physical_Variables::T;
double umax_t = Global_Physical_Variables::umax_t;
double t1 = Global_Physical_Variables::t1;
```

```
double Rho = Global_Physical_Variables::Rho;
double pi = Global_Physical_Variables::pi;

double omega = Global_Physical_Variables::omega;
double omega_1 = omega;
double omega_2 = omega*2.0;
double omega_3 = omega*3.0;
double omega_4 = omega*4.0;

double alpha = Global_Physical_Variables::alpha;
double alpha_1 = alpha;
double alpha_2 = alpha*sqrt(2.0);
double alpha_3 = alpha*sqrt(3.0);
double alpha_4 = alpha*sqrt(4.0);

cdouble beta_1 = (1.0fi-1.0)*alpha_1/sqrt(2.0); //
Complex Sq Root
cdouble beta_2 = (1.0fi-1.0)*alpha_2/sqrt(2.0); //
Complex Sq Root
cdouble beta_3 = (1.0fi-1.0)*alpha_3/sqrt(2.0); //
Complex Sq Root
cdouble beta_4 = (1.0fi-1.0)*alpha_4/sqrt(2.0); //
Complex Sq Root

cdouble besselJ0_1;
cdouble besselJ0_2;
cdouble besselJ0_3;
cdouble besselJ0_4;

AmosBessel('J', beta_1, 0.0, 1, 0, &besselJ0_1);
AmosBessel('J', beta_2, 0.0, 1, 0, &besselJ0_2);
AmosBessel('J', beta_3, 0.0, 1, 0, &besselJ0_3);
AmosBessel('J', beta_4, 0.0, 1, 0, &besselJ0_4);


cdouble complex_1 = 1.0/(besselJ0_1) - 1.0;
cdouble complex_2 = 1.0/(besselJ0_2) - 1.0;
cdouble complex_3 = 1.0/(besselJ0_3) - 1.0;
cdouble complex_4 = 1.0/(besselJ0_4) - 1.0;

double A_1 = __real__ complex_1;
```

```
double B_1 = __imag__ complex_1;
double A_2 = __real__ complex_2;
double B_2 = __imag__ complex_2;
double A_3 = __real__ complex_3;
double B_3 = __imag__ complex_3;
double A_4 = __real__ complex_4;
double B_4 = __imag__ complex_4;


double D_1 = 1.0/(1.0 +
(A_1*A_1)/(B_1*B_1))*(Rho*omega_1)/(B_1*1.0*1.0)*(umax_t*T*T)/(
2.0*pi*pi*t1*(T/2.0 - t1))*sin((2.0*pi*1.0*t1)/T);
double C_1 = (-A_1*D_1)/B_1;

double D_2 = 1.0/(1.0 +
(A_2*A_2)/(B_2*B_2))*(Rho*omega_2)/(B_2*2.0*2.0)*(umax_t*T*T)/(
2.0*pi*pi*t1*(T/2.0 - t1))*sin((2.0*pi*2.0*t1)/T);
double C_2 = (-A_2*D_2)/B_2;

double D_3 = 1.0/(1.0 +
(A_3*A_3)/(B_3*B_3))*(Rho*omega_3)/(B_3*3.0*3.0)*(umax_t*T*T)/(
2.0*pi*pi*t1*(T/2.0 - t1))*sin((2.0*pi*3.0*t1)/T);
double C_3 = (-A_3*D_3)/B_3;

double D_4 = 1.0/(1.0 +
(A_4*A_4)/(B_4*B_4))*(Rho*omega_4)/(B_4*4.0*4.0)*(umax_t*T*T)/(
2.0*pi*pi*t1*(T/2.0 - t1))*sin((2.0*pi*4.0*t1)/T);
double C_4 = (-A_4*D_4)/B_4;

P_1 = C_1 + 1.0fi*D_1;
P_2 = C_2 + 1.0fi*D_2;
P_3 = C_3 + 1.0fi*D_3;
P_4 = C_4 + 1.0fi*D_4;

}

} // end_of_namespace//


/// Namespace for unsteady BCs
//=============================================================
```

```
namespace unsteady_boundary_conditions
{
/// Get inlet boundary comdition at time t, location (X,Y).
void get_inlet_bc(const double& t, const double& X, const
double& Y, double& u_axial)
{

//double T = Global_Physical_Variables::T;
//double pi = Global_Physical_Variables::pi;

double r = sqrt(X*X + Y*Y);

double umax_s = Global_Physical_Variables::umax_s;
double Rho = Global_Physical_Variables::Rho;

double T = Global_Physical_Variables::T;
double umax_t = Global_Physical_Variables::umax_t;
double t1 = Global_Physical_Variables::t1;

double omega = Global_Physical_Variables::omega;
double omega_1 = omega;
double omega_2 = omega*2.0;
double omega_3 = omega*3.0;
double omega_4 = omega*4.0;

double alpha = Global_Physical_Variables::alpha;
double alpha_1 = alpha;
double alpha_2 = alpha*sqrt(2.0);
double alpha_3 = alpha*sqrt(3.0);
double alpha_4 = alpha*sqrt(4.0);

cdouble beta_1 = (1.0fi-1.0)*alpha_1/sqrt(2.0); //
Complex Sq Root
cdouble beta_2 = (1.0fi-1.0)*alpha_2/sqrt(2.0); //
Complex Sq Root
cdouble beta_3 = (1.0fi-1.0)*alpha_3/sqrt(2.0); //
Complex Sq Root
cdouble beta_4 = (1.0fi-1.0)*alpha_4/sqrt(2.0); //
Complex Sq Root

cdouble P_1;
```

```
cdouble P_2;
cdouble P_3;
cdouble P_4;

PulsatileVariables::get_pressure(P_1,P_2,P_3,P_4);


cdouble besselJ0A_1;
cdouble besselJ0B_1;
cdouble besselJ0A_2;
cdouble besselJ0B_2;
cdouble besselJ0A_3;
cdouble besselJ0B_3;
cdouble besselJ0A_4;
cdouble besselJ0B_4;

AmosBessel('J', beta_1*r, 0.0, 1, 0, &besselJ0A_1);
AmosBessel('J', beta_1, 0.0, 1, 0, &besselJ0B_1);

AmosBessel('J', beta_2*r, 0.0, 1, 0, &besselJ0A_2);
AmosBessel('J', beta_2, 0.0, 1, 0, &besselJ0B_2);


AmosBessel('J', beta_3*r, 0.0, 1, 0, &besselJ0A_3);
AmosBessel('J', beta_3, 0.0, 1, 0, &besselJ0B_3);

AmosBessel('J', beta_4*r, 0.0, 1, 0, &besselJ0A_4);
AmosBessel('J', beta_4, 0.0, 1, 0, &besselJ0B_4);


double U_0 = umax_s*(1.0-pow(r,2.0));

cdouble U_1_c =
((P_1*1.0fi)/(Rho*omega_1))*(besselJ0A_1/besselJ0B_1-1.0)*(cos(
omega_1*t) + 1.0fi*sin(omega_1*t));
cdouble U_2_c =
((P_2*1.0fi)/(Rho*omega_2))*(besselJ0A_2/besselJ0B_2-1.0)*(cos(
omega_2*t) + 1.0fi*sin(omega_2*t));
cdouble U_3_c =
((P_3*1.0fi)/(Rho*omega_3))*(besselJ0A_3/besselJ0B_3-1.0)*(cos(
omega_3*t) + 1.0fi*sin(omega_3*t));
```

```
cdouble U_4_c =
((P_4*1.0fi)/(Rho*omega_4))*(besselJ0A_4/besselJ0B_4-1.0)*(cos(
omega_4*t) + 1.0fi*sin(omega_4*t));

double U_1 = __real__ U_1_c;
double U_2 = __real__ U_2_c;
double U_3 = __real__ U_3_c;
double U_4 = __real__ U_4_c;

/// Full Solution:

u_axial = U_0 + U_1 + U_2 + U_3 + U_4;


}


} // end_of_namespace//

// Customised element
// The wrapper class for the element has to be included into
// the oomph-lib namespace
namespace oomph
{
//======customised_TH element================================
/// Customised TH element -- simply overloads the output
function.
/// All other functionality is retained.
/// This ouputs the 'local' tube coordinates of a regular
cord
//============================================================

//template<unsigned DIM>
class CustomisedRefineableQTaylorHoodElement : public
virtual RefineableQTaylorHoodElement<3>
{

public:

/// Empty constructor
CustomisedRefineableQTaylorHoodElement(){};
```

```
/// Empty virtual constructor
~CustomisedRefineableQTaylorHoodElement(){};

/// Overload output function
void output(std::ostream& outfile,const unsigned
&nplot)
{
//Vector of local coordinates
Vector<double> s(3);

//Require pi
double Pi = 4.0*atan(1.0);


//Storage for number of layers in intial mesh -
adjust as appropriate
// (See call to constructor of RefineableTubeMesh
below)
//unsigned nlayer=Mesh_Parameters::nlayer;

//Storage for centreline limits of initial mesh -
adjust as appropriate
// (See call to constructor of RefineableTubeMesh
below)
//double centreline_start=0.;
//double centreline_end=nlayer;

//Calculate the layer of the initial mesh to which
the macro element belongs
unsigned
macro_number=this->macro_elem_pt()->macro_element_number();
//finds the element of the initial mesh to which the current
element belongs.
unsigned layer=unsigned(macro_number/5); //number
of layers before 'current' layer. integer division gives this
value.

//Calculate the start coordinates and thickness of
that layer
double g_start_macro_el=layer;
```

```
double layer_thickness=1.0;

//Storage for position within macro element
Vector<double> s_macro(3); //store position within
macro element

// Tecplot header info
outfile << this->tecplot_zone_string(nplot);

// Loop over plot points
unsigned num_plot_points=this->nplot_points(nplot);

for (unsigned
iplot=0;iplot<num_plot_points;iplot++) // for every plot point
{

// Get local coordinates of plot point
this->get_s_plot(iplot,nplot,s); //find the
local coords

//Obtain the position within the macro element
of our current local coordinate s
for(unsigned i=0;i<3;i++)
{
s_macro[i]=this->s_macro_ll(i)+0.5*(s[i]+1.
0)*(this->s_macro_ur(i)-this->s_macro_ll(i));
}

//Compute zeta from second coordinate of
position within macro element
//together with macro element's location in
mesh as calculated above
double
g=g_start_macro_el+0.5*(s_macro[2]+1.0)*layer_thickness;

// Initialise local coordinates
double X,Y,Z;

// Initialise local velocities
double U,V,W;
```

```
// Cartesian Coordinates
// Flip x,y for positive Jacobian
double x = interpolated_x(s,0);
double y = interpolated_x(s,1);
double z = interpolated_x(s,2);

// Velocities
// Flip u,v for positive Jacobian
double u = interpolated_u_nst(s,0);
double v = interpolated_u_nst(s,1);
double w = interpolated_u_nst(s,2);

// Must find the local coordinate:

double t0 = Global_Physical_Variables::t0;
double tf = Global_Physical_Variables::tf;

double t =
(tf-t0)*g/double(Mesh_Parameters::nlayer) + t0;
double si, xc, yc, zc, Tx, Ty, Tz, Nx, Ny, Nz,
Bx, By, Bz, curvature;

Geometry::eval_spline(t,xc,yc,zc,Tx,Ty,Tz,Nx,Ny
,Nz,Bx,By,Bz,curvature);

Geometry::return_arclength(t,si);

Y = (Ny*(x-xc)-Nx*(y-yc))/(Bx*Ny-By*Nx);
X = (x-xc - Y*Bx)/Nx;
Z = si;

double r = sqrt(X*X + Y*Y);
double theta = atan2(Y,X);

U =
1.0/(Nx*By*Tz-Nx*Ty*Bz-Bx*Ny*Tz+Bx*Ty*Nz+Tx*Ny*Bz-Tx*By*Nz)*((
By*Tz-Ty*Bz)*u + (Tx*Bz-Bx*Tz)*v + (Bx*Ty-Tx*By)*w);
V =
1.0/(Nx*By*Tz-Nx*Ty*Bz-Bx*Ny*Tz+Bx*Ty*Nz+Tx*Ny*Bz-Tx*By*Nz)*((
Ty*Nz-Ny*Tz)*u + (Nx*Tz-Tx*Nz)*v + (Tx*Ny-Nx*Ty)*w);
W =
```

```
1.0/(Nx*By*Tz-Nx*Ty*Bz-Bx*Ny*Tz+Bx*Ty*Nz+Tx*Ny*Bz-Tx*By*Nz)*((
Ny*Bz-By*Nz)*u + (Bx*Nz-Nx*Bz)*v + (Nx*By-Bx*Ny)*w); // Fixed


// BEGIN: Calculating the WSS:
Vector<double> traction(3);
Vector<double> T(3);
double SS;

if (r>0.98) {

T[0] = Tx;
T[1] = Ty;
T[2] = Tz;

double NSx = xc-x;
double NSy = yc-y;
double NSz = zc-z;

NSx = NSx/sqrt(NSx*NSx + NSy*NSy +
NSz*NSz);
NSy = NSy/sqrt(NSx*NSx + NSy*NSy +
NSz*NSz);
NSz = NSz/sqrt(NSx*NSx + NSy*NSy +
NSz*NSz);

get_traction(s, T, traction);
SS = traction[0]*NSx + traction[1]*NSy +
traction[2]*NSz;
}
else {
SS = 0.0;

}
// END: Calculating the WSS:

// Output the global coordinates:
outfile << x << " " << y << " " << z << " " ;
outfile << u << " " << v << " " << w << " ";
outfile << X << " " << Y << " " << Z << " " ;
outfile << U << " " << V << " " << W << " ";
```

```
// Output the velocity magnitude:
outfile << g << " " ;
outfile << t << " " ;
outfile << sqrt(u*u + v*v + w*w) << " ";
// Pressure
outfile << this->interpolated_p_nst(s)  << " "
;
// Tangent
outfile << r << " " << theta << " ";
outfile << SS << " ";


outfile << std::endl;
}
outfile << std::endl;

// Write tecplot footer (e.g. FE connectivity
lists)
this->write_tecplot_zone_footer(outfile,nplot);

}//end customised output function

};

} //end extension of oomph-lib namespace


//=start_of_LHCord=============================================
//============================================================
class Tube : public GeomObject
{
public:

/// Constructor for the tube (the arguments are the number
of lagrangian variables and dimension)
Tube(const double &radius) :
GeomObject(3,3), Radius(radius) { }


/// Destructor
virtual~Tube(){}
```

```
///Lagrangian coordinate xi
void position (const Vector<double>& xi, Vector<double>& r)
const
{
// Local Tube Coordinates
double X = Radius*xi[2]*cos(xi[1]);
double Y = Radius*xi[2]*sin(xi[1]);
double t = xi[0];

double x, y, z, xc, yc, zc, Tx, Ty, Tz, Nx, Ny, Nz, Bx,
By, Bz, curvature;

Geometry::eval_spline(t,xc,yc,zc,Tx,Ty,Tz,Nx,Ny,Nz,Bx,
By,Bz,curvature);

x = xc + X*Nx + Y*Bx;
y = yc + X*Ny + Y*By;
z = zc + X*Nz + Y*Bz;

// Output global coordinates
// Flip x,y for correct sign of Jacobian
r[0] = x;
r[1] = y;
r[2] = z;

}


/// Return the position of the tube as a function of time
/// (doesn't move as a function of time)
void position(const unsigned& t,
  const Vector<double>& xi, Vector<double>& r)
const
{
position(xi,r);
}

private:
double Radius;
double Pi;
```

```
};


///=start_of_problem_class=====================================
/// Flow in straight pipe
//============================================================
template<class ELEMENT, class TIMESTEPPER>
class UnsteadyTubeProblem : public Problem
{

public:

 /// Constructor: Pass DocInfo object and target errors
 UnsteadyTubeProblem();

 /// Destructor (empty)
 ~UnsteadyTubeProblem() {

 }


/// After adaptation: Pin redudant pressure dofs.
void actions_after_adapt()
{
// Unpin all pdofs. Note that this step is redundant
unless
// some pressure values have been actively set in the
mesh
// (i.e. through boundary conditions or for reference)
RefineableNavierStokesEquations<3>::
unpin_all_pressure_dofs(mesh_pt()->element_pt());

// Pin redudant pressure dofs
RefineableNavierStokesEquations<3>::
pin_redundant_nodal_pressures(mesh_pt()->element_pt());

mesh_pt()->node_update();
Mesh_Parameters::adapt_no++;
oomph_info << "Adaptation number " <<
Mesh_Parameters::adapt_no << std::endl;
```

```
}

 /// After distribution: same as after adapt.
void actions_after_distribute()
{
// Unpin all pdofs. Note that this step is redundant
unless
// some pressure values have been actively set in the
mesh
// (i.e. through boundary conditions or for reference)
RefineableNavierStokesEquations<3>::
unpin_all_pressure_dofs(mesh_pt()->element_pt());

// Pin redudant pressure dofs
RefineableNavierStokesEquations<3>::
pin_redundant_nodal_pressures(mesh_pt()->element_pt());

// Could choose to pin a single pressure value at the
outlet, however, this is most likely handled regardless if
velocity boundary conditions are not specified

mesh_pt()->node_update();

}

// Actions before timestep: Update BCs
void actions_before_implicit_timestep()
{

// Assign velocity profile at inflow values
//-----------------------------------------
unsigned ibound=0;
unsigned num_nod= mesh_pt()->nboundary_node(ibound);
for (unsigned inod=0;inod<num_nod;inod++)
{
// Recover coordinates

double
x=mesh_pt()->boundary_node_pt(ibound,inod)->x(0);
double
```

```
y=mesh_pt()->boundary_node_pt(ibound,inod)->x(1);
double
z=mesh_pt()->boundary_node_pt(ibound,inod)->x(2);

double t0 = Global_Physical_Variables::t0;
double xc, yc, zc, Tx, Ty, Tz, Nx, Ny, Nz, Bx, By,
Bz, curvature;

Geometry::eval_spline(t0,xc,yc,zc,Tx,Ty,Tz,Nx,Ny,Nz
,Bx,By,Bz, curvature);

double Y = (Ny*(x-xc)-Nx*(y-yc))/(Bx*Ny-By*Nx);
double X = (x-xc - Y*Bx)/Nx;

double r = sqrt(X*X + Y*Y);

double time=time_pt()->time();
double u_axial;
if ((Solve_Parameters::startup &&
Solve_Parameters::steady_startup) ||
Solve_Parameters::temporal_steady_inlet) {
steady_boundary_conditions::get_inlet_bc(time,X
,Y,u_axial);
}
else {

unsteady_boundary_conditions::get_inlet_bc(time
,X,Y,u_axial);

}

double u_x = Tx*u_axial;
double u_y = Ty*u_axial;
double u_z = Tz*u_axial;

// Set axial velocity flow profile
mesh_pt()->boundary_node_pt(ibound,inod)->
set_value(0,u_x);
mesh_pt()->boundary_node_pt(ibound,inod)->
set_value(1,u_y);
mesh_pt()->boundary_node_pt(ibound,inod)->
```

```
set_value(2,u_z);
}



// Unpin all pdofs. Note that this step is redundant
unless
// some pressure values have been actively set in the
mesh
// (i.e. through boundary conditions or for reference)
RefineableNavierStokesEquations<3>::
unpin_all_pressure_dofs(mesh_pt()->element_pt());

// Pin redudant pressure dofs
RefineableNavierStokesEquations<3>::
pin_redundant_nodal_pressures(mesh_pt()->element_pt());

// Set no-slip wall
//unsigned num_nod_outlet =
mesh_pt()->nboundary_node(2);
for (unsigned
inod=0;inod<mesh_pt()->nboundary_node(1);inod++)
{
mesh_pt()->boundary_node_pt(1,inod)->set_value(0,0.
0);
mesh_pt()->boundary_node_pt(1,inod)->set_value(1,0.
0);
mesh_pt()->boundary_node_pt(1,inod)->set_value(2,0.
0);
}


}
 // end of actions_before_implicit_timestep

 /// Run an unsteady simulation
 void unsteady_run(DocInfo& doc_info);
 /// Build mesh for problem construction and load_balance:
 void build_mesh();
 /// Set/reset the iterative solver()
 void set_iterative_solver();
```

```
 /// Set the global temporal error norm for temporal
adaptation:
 double global_temporal_error_norm();
 /// Function for restart
 void restartmpi();
 /// Create a function to refine the mesh uniformly:
 void refine_mesh_uniformly(unsigned &n_uniform);
 /// Doc the solution
 void doc_solution(DocInfo& doc_info);
 /// Dump the solution
 void dump_it(DocInfo& doc_info);
 /// Read the solution
 void restart(ifstream& restart_file);

 /// Set initial condition (incl previous timesteps) according
 /// to specified function.
 void set_initial_condition();

 /// \short Overload generic access function by one that
returns
 /// a pointer to the specific  mesh
 RefineableTubeMesh<ELEMENT>* mesh_pt()
  {
   return
dynamic_cast<RefineableTubeMesh<ELEMENT>*>(Problem::mesh_pt());
  }

  /// Suggestion for next timestep (stored to allow it to be
written
/// to (or read from) restart file)
double& next_dt(){return Next_dt;}

/// Target error for adaptive timestepping
double& epsilon_t() {return Epsilon_t;}

private:

 /// Doc info object
 DocInfo Doc_info;
 ///Pointer to GeomObject that specifies the domain boundary
 GeomObject* Wall_pt;
```

```
 /// Trace file
 ofstream Trace_file;

  /// Suggestion for next timestep (stored to allow it to be
written
/// to (or read from) restart file)
double Next_dt;

/// Target error for adaptive timestepping
double Epsilon_t;


/// oomph-lib iterative linear solver
IterativeLinearSolver* Solver_pt;

/// Preconditioner

// In the svn dist:
NavierStokesSchurComplementPreconditioner* Prec_pt;
/// Inexact solver for P block
Preconditioner* P_matrix_preconditioner_pt;
/// Inexact solver for F block
Preconditioner* F_matrix_preconditioner_pt;


// Standard Prec:
Preconditioner* Prec_pt_standard;

}; // end_of_problem_class




//=start_of_constructor=======================================
/// Constructor: Pass DocInfo object and error target
//============================================================
template<class ELEMENT, class TIMESTEPPER>
UnsteadyTubeProblem<ELEMENT,TIMESTEPPER>::UnsteadyTubeProblem()

{
```

```
// Set Newton solve parameters:
Max_residuals = 300;
Max_newton_iterations = 15;

// Set target error for adaptive timestepping
//Epsilon_t=Solve_Parameters::Epsilon_t;

// Setup timestepping
//-------------------

// Allocate the timestepper -- this constructs the time
object as well.
add_time_stepper_pt(new
TIMESTEPPER(Solve_Parameters::temporal_adaptivity));

// Overwrite max_neighbour_finding_tolerance (default
1.0e-14)
// Two uniform refinements exceed the default
Tree::max_neighbour_finding_tolerance() = 1.0e-13;

// Initialise all pointers:
// Initialise pointer to oomph-lib iterative linear solver
Solver_pt=0;
// Initialise pointer to Preconditioner
Prec_pt=0;
Prec_pt_standard=0;
// Create internal preconditioners used on Schur block
P_matrix_preconditioner_pt=0;
// Create block-diagonal preconditioner used on momentum
block
F_matrix_preconditioner_pt=0;

// Build the mesh
build_mesh();

// Setup iterative linear solver if required
if (Solve_Parameters::use_iterative_solver)
{
set_iterative_solver();
}
```

```
 //Output number of equations:
 oomph_info <<"Initial number of equations: " <<
assign_eqn_numbers() << std::endl;

} // end_of_constructor


//=start_of_build_mesh=========================================
/// Setup the mesh
//=============================================================

template<class ELEMENT, class TIMESTEPPER>
void UnsteadyTubeProblem<ELEMENT,TIMESTEPPER>::build_mesh()
{

// Setup mesh:
//------------
//Build geometric object that forms the domain boundary: a
tapered curved tube

double r=Global_Physical_Variables::Radius;

// Create GeomObject that specifies the domain boundary
Wall_pt=new Tube(r);

//Define pi
const double pi = 4.0*atan(1.0);

// Number of layers in the mesh
unsigned nlayer=Mesh_Parameters::nlayer;

//Set the centerline coordinates for the start and end of
the tube
Vector<double> centreline_limits(2);
centreline_limits[0] = Global_Physical_Variables::t0;
centreline_limits[1] = Global_Physical_Variables::tf;

//Set the positions of the angles that divide the outer
ring of elements
Vector<double> theta_positions(4);
theta_positions[0] = -0.75*pi;
```

```
theta_positions[1] = -0.25*pi;
theta_positions[2] = 0.25*pi;
theta_positions[3] = 0.75*pi;

double radial_frac_box =
Mesh_Parameters::radial_frac_box;

//Define the radial fraction for the central box in the
domain
Vector<double> radial_frac(4,radial_frac_box);  // (4,0.5)

// Build and assign mesh
Problem::mesh_pt() =new
RefineableTubeMesh<ELEMENT>(Wall_pt,centreline_limits,
theta_positions,radial_frac,nlayer,time_stepper_pt());

// Refine the mesh uniformly if required
if (Mesh_Parameters::n_uniform>0) {
UnsteadyTubeProblem::refine_mesh_uniformly(
Mesh_Parameters::n_uniform);
}

// Set error estimator
Z2ErrorEstimator* error_estimator_pt=new Z2ErrorEstimator;
mesh_pt()->spatial_error_estimator_pt()=error_estimator_pt;

// Error targets for adaptive refinement
mesh_pt()->max_permitted_error()=Mesh_Parameters::emax;
mesh_pt()->min_permitted_error()=Mesh_Parameters::emin;



// Set the boundary conditions for this problem: All nodal
values are
// free by default -- just pin the ones that have Dirichlet
conditions
// here.
//Choose the conventional form by setting gamma to zero
//The boundary conditions will be pseudo-traction free
(d/dn = 0)
ELEMENT::Gamma[0] = 0.0;
```

```
ELEMENT::Gamma[1] = 0.0;
ELEMENT::Gamma[2] = 0.0;


// Loop over the elements to set up element-specific
// things that cannot be handled by constructor
unsigned n_element = mesh_pt()->nelement();

oomph_info <<"Initial number of elements: " << n_element <<
std::endl;

for(unsigned i=0;i<n_element;i++)
{
// Upcast from GeneralisedElement to the present
element
ELEMENT* el_pt =
dynamic_cast<ELEMENT*>(mesh_pt()->element_pt(i));

//Set the Reynolds number, etc
el_pt->re_pt() = &Global_Physical_Variables::Re;
el_pt->re_st_pt() = &Global_Physical_Variables::ReSt;

//Assign the time pointer
el_pt->time_pt() = time_pt();

}

// Pin redudant pressure dofs
RefineableNavierStokesEquations<3>::
pin_redundant_nodal_pressures(mesh_pt()->element_pt());

unsigned num_bound = mesh_pt()->nboundary();
for(unsigned ibound=0;ibound<num_bound;ibound++)
{
unsigned num_nod= mesh_pt()->nboundary_node(ibound);
for (unsigned inod=0;inod<num_nod;inod++)
{
// Boundary 0 is the inlet boundary:
// Boundary 1 is the tube wall
// Boundary 2 is the outlet
// Pin all values
```

```
if((ibound==0) || (ibound==1))
{
mesh_pt()->boundary_node_pt(ibound,inod)->pin(0
);
mesh_pt()->boundary_node_pt(ibound,inod)->pin(1
);
mesh_pt()->boundary_node_pt(ibound,inod)->pin(2
);
}

}
} // end loop over boundaries

} // End of build_mesh


//============================================================
/// Helper function to switch solver to GMRES, preconditioned
with the LSE preconditioner
//============================================================

template<class ELEMENT,class TIMESTEPPER>
void
UnsteadyTubeProblem<ELEMENT,TIMESTEPPER>::set_iterative_solver(
)
{

// Kill any previous instantiations

if (Solver_pt!=0)
{
delete Solver_pt;
Solver_pt=0;
}

// Setup iterative linear solver if required

if (Solve_Parameters::use_iterative_solver)
{
// Build solver:
if (Solve_Parameters::use_trilinos_solver) {
```

```
#ifdef OOMPH_HAS_TRILINOS

TrilinosAztecOOSolver* iterative_linear_solver_pt =
new TrilinosAztecOOSolver;

// Pass solver type
// 0 - CG
// 1 - GMRES (default)
// 2 - BiCGStab
unsigned solver_type = 1;
iterative_linear_solver_pt->solver_type() =
solver_type;

// Set max number of iterations (default is 1000)
// Note that max_iter() is passed to the solver as
the size of kspace
iterative_linear_solver_pt->max_iter() = 1000;

Solver_pt=iterative_linear_solver_pt;
#endif
}
else {
Solver_pt = new GMRES<CRDoubleMatrix>;
dynamic_cast<GMRES<CRDoubleMatrix>*>(Solver_pt)->
set_preconditioner_RHS();
}

// Set linear solver
linear_solver_pt() = Solver_pt;

// Set preconditioner

// If using the Navier-Stokes Schur Complement
Preconditioner:
if (Solve_Parameters::use_lsc) {

//Delete any previous values

if(Prec_pt!=0)
{
```

```
delete Prec_pt;
Prec_pt=0;
}

Prec_pt=new
NavierStokesSchurComplementPreconditioner();
Prec_pt->set_navier_stokes_mesh(this->mesh_pt());

Solver_pt->preconditioner_pt()=Prec_pt;


// By default, the LSC Preconditioner uses SuperLU
as
// an exact preconditioner (i.e. a solver) for the
// momentum and Schur complement blocks.
// Can overwrite this by passing pointers to
// other preconditioners that perform the
(approximate)
// solves of these blocks.

// Create internal preconditioners used on Schur
block

//------------------------------------------------
----

#ifdef OOMPH_HAS_HYPRE

if (Solve_Parameters::use_hypre_for_pressure)
{
//Delete previous values
if(P_matrix_preconditioner_pt!=0)
{
delete P_matrix_preconditioner_pt;
P_matrix_preconditioner_pt=0;
}

P_matrix_preconditioner_pt = new
HyprePreconditioner;

// Set parameters for use as preconditioner on
```

```
Poisson-type problem
Hypre_Solver_Settings::
set_momentum_defaults_for_3DTube_problem(static_cast<
HyprePreconditioner*>(P_matrix_preconditioner_pt));

// Use Hypre for the Schur complement block
Prec_pt->set_p_preconditioner(
P_matrix_preconditioner_pt);

// Shut up!
static_cast<HyprePreconditioner*>(
P_matrix_preconditioner_pt)->disable_doc_time();
}

#endif
// Create internal preconditioners used on momentum
block
//-------------------------------------------------
-------

if
(Solve_Parameters::use_block_diagonal_for_momentum)
{
//Delete previous values
if(F_matrix_preconditioner_pt!=0)
{
delete F_matrix_preconditioner_pt;
F_matrix_preconditioner_pt = 0;
}

F_matrix_preconditioner_pt = new
BlockDiagonalPreconditioner<CRDoubleMatrix>;

#ifdef OOMPH_HAS_HYPRE

if (Solve_Parameters::use_hypre_for_momentum)
{

dynamic_cast<BlockDiagonalPreconditioner<
CRDoubleMatrix>*
>(F_matrix_preconditioner_pt)->
```

```
set_subsidiary_preconditioner_function(
Hypre_Subsidiary_Preconditioner_Helper::
set_hypre_preconditioner);

}
#endif
// Use Hypre for momentum block
Prec_pt->set_f_preconditioner(
F_matrix_preconditioner_pt);
}
else
{

#ifdef OOMPH_HAS_HYPRE

//Trap because HYPRE can't handle the case when

//OOMPH_HAS_MPI, but we run in serial

if (Solve_Parameters::use_hypre_for_momentum)
{
if(F_matrix_preconditioner_pt!=0)
{
delete F_matrix_preconditioner_pt;
F_matrix_preconditioner_pt = 0;
}

F_matrix_preconditioner_pt = new
HyprePreconditioner;

// Shut up!
static_cast<HyprePreconditioner*>(
F_matrix_preconditioner_pt)->disable_doc_time();

// Set parameters for use as preconditioner
in for momentum
// block in Navier-Stokes problem

Hypre_Solver_Settings::
set_momentum_defaults_for_3DTube_problem(static_cast<
HyprePreconditioner*>(F_matrix_preconditioner_pt));
```

```
// Use Hypre for momentum block
Prec_pt->set_f_preconditioner(
F_matrix_preconditioner_pt);
}
#endif

}
}
else {
if(Prec_pt_standard!=0)
{
delete Prec_pt_standard;
Prec_pt_standard = 0;
}


TrilinosIFPACKPreconditioner* Prec_pt_standard =
new TrilinosIFPACKPreconditioner;

/*
 Prec_pt_standard = new HyprePreconditioner;
 Solver_pt->preconditioner_pt()=Prec_pt_standard;
 static_cast<HyprePreconditioner*>(Prec_pt_standard
)->hypre_method() = HyprePreconditioner::BoomerAMG;
 */

Solver_pt->preconditioner_pt()=Prec_pt_standard;
}

}
}

//======================start_of_set_initial_condition=========
/// \short Set initial condition: Assign previous and current
values
/// from exact solution.
//=============================================================
template<class ELEMENT,class TIMESTEPPER>
void
UnsteadyTubeProblem<ELEMENT,TIMESTEPPER>::set_initial_condition
```

```
()
{

if (Solve_Parameters::checkRestart) {

// Get current processor rank:
int my_rank=this->communicator_pt()->my_rank();
int nproc=this->communicator_pt()->nproc();

char filename[100];
sprintf(filename,"%s/%s_L%g_Re%g_%iproc%i_DUMP.dat",
Solve_Parameters::directory,Solve_Parameters::
restart_file_title,
Global_Physical_Variables::Length,Solve_Parameters:
:restart_Re,nproc,my_rank);

// Pointer to restart file
ifstream* restart_file_pt=0;

// Open restart file from stem
restart_file_pt= new ifstream(filename,ios_base::in);
if (restart_file_pt!=0)
{
oomph_info << "Have opened " << filename <<
" for restart. " << std::endl;
}
else
{
std::ostringstream error_stream;
error_stream
<< "ERROR while trying to open " << filename
<< " for restart." << std::endl;

throw OomphLibError(
error_stream.str(),
"UnsteadyTubeProblem<ELEMENT,
TIMESTEPPER>::restartmpi()",
OOMPH_EXCEPTION_LOCATION);
}

// Read restart data:
```

```
//-------------------
if (restart_file_pt!=0)
{
// Read the data from restart file and find out if the
restart file
// was from an unsteady run
oomph_info << "Restarting..." << std::endl;
UnsteadyTubeProblem::restart(*restart_file_pt);
oomph_info << "Restart file loaded." << std::endl;
}

}
else {
// Initialise domain to stagnant flow:
//-----------------------------------------
unsigned num_nod= mesh_pt()->nnode();
for (unsigned inod=0;inod<num_nod;inod++)
{
// Recover coordinates

double u_x = 0.0;
double u_y = 0.0;
double u_z = 0.0;

// Set axial velocity flow profile
mesh_pt()->node_pt(inod)->set_value(0,u_x);
mesh_pt()->node_pt(inod)->set_value(1,u_y);
mesh_pt()->node_pt(inod)->set_value(2,u_z);
}

}



assign_initial_values_impulsive();

// Choose initial timestep
double dt0=Global_Physical_Variables::dt;

// Initialise timestep -- also sets the weights for all
timesteppers
```

```
// in the problem.
initialise_dt(dt0);

// Use this as the first "suggested" timestep
Next_dt=dt0;

// Set inflow/outflow BC
actions_before_implicit_timestep();


} // end of set_initial_condition


//=========start_of_restart=====================================

/// Read solution from disk
//==============================================================

template<class ELEMENT, class TIMESTEPPER>
void
UnsteadyTubeProblem<ELEMENT,TIMESTEPPER>::restart(ifstream&
restart_file)
{

// Refine the mesh and read in the generic problem data
Problem::read(restart_file);

} // end of restart


//===start_of_unsteady_run======================================
/// Unsteady run...
//==============================================================
template<class ELEMENT, class TIMESTEPPER>
void
UnsteadyTubeProblem<ELEMENT,TIMESTEPPER>::unsteady_run(DocInfo&
doc_info)
{

// Initial timestep: Use the one used when setting up the
initial
```

```
// condition or the "suggested next dt" from the restarted
run
//double dt=next_dt();
double dt=Global_Physical_Variables::dt;

// Initialise all history values for an impulsive start
assign_initial_values_impulsive(dt);
oomph_info << "IC = impulsive start" << std::endl;




if (Solve_Parameters::startup) {

//

//Now do many timesteps

unsigned ntsteps1 =
(Global_Physical_Variables::Re_Final -
Global_Physical_Variables::Re_Initial)/
Global_Physical_Variables::Re_increment;

Global_Physical_Variables::Re =
Global_Physical_Variables::Re_Initial;
Global_Physical_Variables::ReSt =
Global_Physical_Variables::Re/Global_Physical_Variables::Ured;

// Set the initial condition:
set_initial_condition();

// Doc initial condition
doc_solution(doc_info);

// increment counter
doc_info.number()++;
Solve_Parameters::ts++;

time_pt()->time() = time_pt()->time();

//Loop over the inital timesteps to arrive at desired
```

```
Re
for(unsigned t1=1;t1<=ntsteps1;t1++)
{

//Output the time
oomph_info << "TIMESTEP (startup)" << t1 << " (ts =
" << Solve_Parameters::ts << ")" << std::endl;
oomph_info << "TIME (t): " << time_pt()->time() <<
", PERIOD (T): " << Global_Physical_Variables::T << std::endl;
oomph_info << "t/T: " <<
time_pt()->time()/Global_Physical_Variables::T << std::endl;
oomph_info << "Re = " <<
Global_Physical_Variables::Re << std::endl;
oomph_info << "ReSt = " <<
Global_Physical_Variables::ReSt << std::endl;
oomph_info << "dt = " << dt << "\n\n" << std::endl;

bool first;
unsigned max_adapt;

if (t1==1) {
first = true;
max_adapt = Mesh_Parameters::max_adapt;
}
else {
first = false;
if (Mesh_Parameters::max_adapt>0) {
max_adapt = 1;
}
else {
max_adapt = 0;
}
}

//Take one fixed timestep (no temporal adaptation)
unsteady_newton_solve(dt,max_adapt,first);

//Output the time
oomph_info << "Time is now " << time_pt()->time()
<< std::endl;
```

```
// Doc solution
doc_solution(doc_info);
// increment counter
doc_info.number()++;

// Increment Re:
Global_Physical_Variables::Re =
Global_Physical_Variables::Re +
Global_Physical_Variables::Re_increment;
Global_Physical_Variables::ReSt =
Global_Physical_Variables::Re/Global_Physical_Variables::Ured;


#ifdef OOMPH_HAS_MPI
if (Solve_Parameters::use_load_balance) {
if (doc_info.number() < 10) {
oomph_info <<"Performing load balance\n" <<
std::endl;
load_balance();
// Reset the iterative solver because the
meshes have changed
if (Solve_Parameters::use_iterative_solver)
{
oomph_info <<"Reset iterative
solvers\n\n" << std::endl;
set_iterative_solver();}
}
else {
if (doc_info.number() %
Solve_Parameters::load_balance_freq == 0) {
oomph_info <<"Performing load
balance\n" << std::endl;
load_balance();
// Reset the iterative solver because
the meshes have changed
if
(Solve_Parameters::use_iterative_solver) {
oomph_info <<"Reset iterative
solvers\n\n" << std::endl;
set_iterative_solver();}
```

```
}
}



}

#endif

Solve_Parameters::ts++;

}


}
else {
oomph_info << "\n\n " << std::endl;
oomph_info << "No startup \n" << std::endl;

Global_Physical_Variables::Re =
Global_Physical_Variables::Re_Final;
Global_Physical_Variables::ReSt =
Global_Physical_Variables::Re/Global_Physical_Variables::Ured;

// Set the initial condition:
set_initial_condition();

// Doc initial condition
doc_solution(doc_info);

// increment counter
doc_info.number()++;
Solve_Parameters::ts++;

time_pt()->time() = time_pt()->time();

}

Global_Physical_Variables::Re =
Global_Physical_Variables::Re_Final;
Global_Physical_Variables::ReSt =
```

```
Global_Physical_Variables::Re/Global_Physical_Variables::Ured;

oomph_info << "Desired Re reached... iterate... \n\n" <<
std::endl;

Solve_Parameters::startup=false;

// timestep counter
unsigned t2=1;


// Timestepping loop
while (time_pt()->time()<Global_Physical_Variables::t_max)
{

oomph_info << "TIMESTEP " << t2 << " (ts = " <<
Solve_Parameters::ts << ")" << std::endl;
oomph_info << "TIME (t): " << time_pt()->time()+dt <<
", PERIOD (T): " << Global_Physical_Variables::T << std::endl;
oomph_info << "t/T: " <<
(time_pt()->time()+dt)/Global_Physical_Variables::T <<
std::endl;
oomph_info << "Re = " << Global_Physical_Variables::Re
<< std::endl;
oomph_info << "ReSt = " <<
Global_Physical_Variables::ReSt << std::endl;
oomph_info << "dt = " << dt << "\n\n" << std::endl;
oomph_info << "alpha = " <<
Global_Physical_Variables::alpha << std::endl;

bool first;
unsigned max_adapt;

if (Solve_Parameters::ts==1) {
first = true;
max_adapt = Mesh_Parameters::max_adapt;
}
else {
first = false;
if (Mesh_Parameters::max_adapt>0) {
max_adapt = 1;
```

```
}
else {
max_adapt = 0;
}
}


//Take one fixed timestep
unsteady_newton_solve(dt,max_adapt,first);


//double
dt_new=doubly_adaptive_unsteady_newton_solve(dt,epsilon_t(),
max_adapt,first);
//oomph_info << "Suggested new dt: " << dt_new <<
std::endl;
//dt=dt_new;

// Store for restart
//next_dt()=dt_new;


#ifdef OOMPH_HAS_MPI
if (Solve_Parameters::use_load_balance) {
if (doc_info.number() < 10) {
oomph_info <<"Performing load balance\n" <<
std::endl;
load_balance();
// Reset the iterative solver because the
meshes have changed
if (Solve_Parameters::use_iterative_solver) {
oomph_info <<"Reset iterative solvers\n\n"
<< std::endl;
set_iterative_solver();}
}
else {
if (doc_info.number() %
Solve_Parameters::load_balance_freq == 0) {
oomph_info <<"Performing load balance\n" <<
std::endl;
load_balance();
```

```
// Reset the iterative solver because the
meshes have changed
if (Solve_Parameters::use_iterative_solver)
{
oomph_info <<"Reset iterative
solvers\n\n" << std::endl;
set_iterative_solver();}

}
}



}

#endif

// Doc solution
doc_solution(doc_info);
// increment counter
doc_info.number()++;

t2++;
Solve_Parameters::ts++;

}
oomph_info <<"Exceeded t_max\n\n" << std::endl;

} // end of unsteady run


//========start_of_global_temporal_error_norm=================
/// Global error norm for adaptive timestepping: RMS error,
based on
/// difference between predicted and actual value at all nodes.
//============================================================
template<class ELEMENT, class TIMESTEPPER>
double
UnsteadyTubeProblem<ELEMENT,TIMESTEPPER>::
global_temporal_error_norm()
{
```

```
#ifdef OOMPH_HAS_MPI

double global_error = 0.0;

//Find out how many nodes there are in the problem
unsigned n_node = mesh_pt()->nnode();

// Loop over the nodes and calculate the estimated error in
the values
// for non-haloes
int count=0;
for(unsigned i=0;i<n_node;i++)
{
Node* nod_pt=mesh_pt()->node_pt(i);
if (!(nod_pt->is_halo()))
{
// Get error in solution: Difference between
predicted and actual
// value for nodal value 0

double error_u = nod_pt->time_stepper_pt()->
temporal_error_in_value(nod_pt,0);

double error_v = nod_pt->time_stepper_pt()->
temporal_error_in_value(nod_pt,1);

double error_w = nod_pt->time_stepper_pt()->
temporal_error_in_value(nod_pt,2);

double error = error_u*error_u + error_v*error_v +
error_w*error_w;


//Add the square of the individual error to the
global error
global_error += error;
count++;
}
}
```

```
// Accumulate
int n_node_local=count;
int n_node_total=0;
MPI_Allreduce(&n_node_local,&n_node_total,1,MPI_INT,MPI_SUM
,
  communicator_pt()->mpi_comm());

double global_error_total=0.0;
MPI_Allreduce(&global_error,&global_error_total,1,
MPI_DOUBLE,MPI_SUM,
  communicator_pt()->mpi_comm());

// Divide by the number of nodes
global_error_total /= double(n_node_total);

// Return square root...
oomph_info << "Total error " << n_node_total << " "
<<  sqrt(global_error_total) << std::endl;
return sqrt(global_error_total);

#else

double global_error = 0.0;

//Find out how many nodes there are in the problem
unsigned n_node = mesh_pt()->nnode();

//Loop over the nodes and calculate the errors in the
values
for(unsigned i=0;i<n_node;i++)
{
// Get error in solution: Difference between predicted
and actual
// value for nodal values

double error_u =
mesh_pt()->node_pt(i)->time_stepper_pt()->
temporal_error_in_value(mesh_pt()->node_pt(i),0);

double error_v =
mesh_pt()->node_pt(i)->time_stepper_pt()->
```

```
temporal_error_in_value(mesh_pt()->node_pt(i),1);

double error_w =
mesh_pt()->node_pt(i)->time_stepper_pt()->
temporal_error_in_value(mesh_pt()->node_pt(i),2);

double error = error_u*error_u + error_v*error_v +
error_w*error_w;


//Add the square of the individual error to the global
error
global_error += error;
}

//Now the global error must be divided by the number of
nodes
global_error /= double(n_node);

//Return the square root of the error
return sqrt(global_error);

#endif


} // end of global_temporal_error_norm



//=start of
refine_mesh_uniformly=========================================
/// Refine Uniformly
//============================================================

template<class ELEMENT, class TIMESTEPPER>
void
UnsteadyTubeProblem<ELEMENT,TIMESTEPPER>::refine_mesh_uniformly
(unsigned &n_uniform)
{
oomph_info << "\n\n" << std::endl;
oomph_info << "Refining Uniformly:\n" << std::endl;
```

```
for (unsigned i_count=0; i_count<n_uniform; i_count++) {
refine_uniformly();
unsigned n_element1 = mesh_pt()->nelement();
Mesh_Parameters::nelement = n_element1;
oomph_info <<"Number of elements: " << n_element1 <<
std::endl;
oomph_info << "Completed " << i_count+1 << " uniform
refinement(s)\n\n" << std::endl;
}

oomph_info <<"Finished " << n_uniform << " Uniform Mesh
Refinement(s) " << std::endl;


} // end of refine_wall_elements


//=start_of_doc_solution=======================================
/// Doc the solution
//==============================================================

template<class ELEMENT, class TIMESTEPPER>
void
UnsteadyTubeProblem<ELEMENT,TIMESTEPPER>::doc_solution(DocInfo&
doc_info)
{
ofstream some_file;
char filename[200];

// Number of plot points
unsigned npts;
npts=3; /// no. of plot points per element

// Get current processor rank:
int my_rank=this->communicator_pt()->my_rank();
int nproc=this->communicator_pt()->nproc();


oomph_info << std::endl;
oomph_info <<
"================================================" <<
```

```
std::endl;
oomph_info << "Documenting solution at t = " <<
time_pt()->time() << std::endl;
oomph_info <<
"================================================" <<
std::endl;


sprintf(filename,"%s/%s_L%g_Re%g_ReSt%g_%iproc%i_t%iSOLN.
dat",doc_info.directory().c_str(),Solve_Parameters::file_title,
Global_Physical_Variables::Length,
Global_Physical_Variables::Re,Global_Physical_Variables::ReSt,
nproc,my_rank,doc_info.number());

some_file.open(filename);

// Output problem parameters:

mesh_pt()->output(some_file,npts);

/*
// Write file as a tecplot text object
some_file << "TEXT
X=2.5,Y=93.6,F=HELV,HU=POINT,C=BLUE,H=26,T=\"time = "
<< time_pt()->time() << "\"";
// ...and draw a horizontal line whose length is
proportional
// to the elapsed time
some_file << "GEOMETRY X=2.5,Y=98,T=LINE,C=BLUE,LT=0.4" <<
std::endl;
some_file << "1" << std::endl;
some_file << "2" << std::endl;
some_file << " 0 0" << std::endl;
some_file << time_pt()->time()*20.0 << " 0" << std::endl;
*/
    some_file.close();

} // end_of_doc_solution


//=======start_of_dump_it=======================================
```

```
/// Dump the solution to disk
//========================================================

template<class ELEMENT, class TIMESTEPPER>
void UnsteadyTubeProblem<ELEMENT,TIMESTEPPER>::dump_it(DocInfo&
doc_info)
{
// Dump the refinement pattern and the generic problem data

ofstream dump_file;
char filename[200];

// Get current processor rank:
int my_rank=this->communicator_pt()->my_rank();
int nproc=this->communicator_pt()->nproc();

sprintf(filename,"%s/%s_L%g_Re%g_%iproc%i_t%iDUMP.dat",
doc_info.directory().c_str(),Solve_Parameters::file_title,
Global_Physical_Variables::Length,
Global_Physical_Variables::Re,nproc,my_rank,
doc_info.number());
dump_file.open(filename);

Problem::dump(dump_file);
dump_file.close();

} // end of dump_it




//=start_of_main=========================================

/// Driver for 3D entry flow into a tapered tube. If there are
/// any command line arguments, we regard this as a validation
run
/// and perform only a single adaptation
//========================================================

int main(int argc, char **argv)
{
```

```
#ifdef OOMPH_HAS_MPI
// Initialise MPI
MPI_Helpers::init(argc,argv);
oomph_info << "\n" << std::endl;
oomph_info << "We have MPI" << endl;
#else
oomph_info << "Built without MPI" << endl;
#endif
#ifdef OOMPH_HAS_HYPRE
oomph_info << "We have Hypre" << endl;
#else
oomph_info << "Built without Hypre" << endl;
#endif
#ifdef OOMPH_HAS_TRILINOS
oomph_info << "We have Trilinos" << endl;
#else
oomph_info << "Built without Trilinos" << endl;
#endif
oomph_info << "\n" << std::endl;

 // Store command line arguments
 CommandLineArgs::setup(argc,argv);

 // Set up doc info
 DocInfo doc_info;
 doc_info.number()=0;

 // Do Taylor-Hood elements
 //------------------------
 {

 // Output the problem parameters before solve
 oomph_info << "\n" << std::endl;
 oomph_info << "Solving with ... \n" << std::endl;
 oomph_info << "Max number of (initial) adaptations: " <<
Mesh_Parameters::max_adapt << std::endl;
 oomph_info << "Max error target: " <<
Mesh_Parameters::emax << std::endl;
 oomph_info << "Min error target: " <<
Mesh_Parameters::emin << std::endl;
```

```
 oomph_info << "Files will be written to: " <<
Solve_Parameters::directory << " with '" <<
Solve_Parameters::file_title << "' as the title. \n" <<
std::endl;

 oomph_info << "Re = " << Global_Physical_Variables::Re <<
"\n" << std::endl;
 oomph_info << "ReSt = " << Global_Physical_Variables::ReSt
<< "\n" << std::endl;

 oomph_info << "Using direct solver" << std::endl;
#ifdef OOMPH_HAS_MPI
 if (Solve_Parameters::use_load_balance) {
 oomph_info << "Using load balancing " <<
std::endl;  }
 else {
 oomph_info << "Not using load balancing \n" <<
std::endl;
 }
#endif

 if (Solve_Parameters::checkRestart){oomph_info << "IC from
restart file" << std::endl;}
 else {oomph_info << "IC set as stagnant flow: (u,v,w) =
(0,0,0)" << std::endl;}



 /// Check the inlet condition if necessary:
 if (Solve_Parameters::check_inlet) {

 unsigned ts = 0;

 for (double t=0.0; t<=Global_Physical_Variables::T ;
t=t+Global_Physical_Variables::T/100.0)
 {

 ofstream some_file;
 char filename[200];
 sprintf(filename,"Ur_t%03i.dat",ts);
 some_file.open(filename);
```

```
 for (double r = 0.0; r <=1.00; r = r+0.01) {

 double Y = 0.0;
 double u_axial;

 unsteady_boundary_conditions::get_inlet_bc(t ,
r, Y, u_axial);

 some_file << t << " " << r << " " << u_axial
<< " " << std::endl;

 }
 some_file.close();
 ts++;
 }
 }


  // Set output directory:
  doc_info.set_directory(Solve_Parameters::directory);

 // Intitalise spline and write some output:
 Geometry::init_spline();

 double s0, sf;

 Geometry::return_arclength(Global_Physical_Variables::t0,
s0);
 Geometry::return_arclength(Global_Physical_Variables::tf,
sf);

 oomph_info << " start = (" <<
Global_Physical_Variables::t0 << ", " << s0 << ")" << endl;
 oomph_info << " end = (" << Global_Physical_Variables::tf
<< ", " << sf << ")" << endl;

 // Alter nlayer so that we have 0.6 layers per
arclength

 Global_Physical_Variables::Length = sf;
```

```
 Mesh_Parameters::nlayer = unsigned(sf*0.7);

 oomph_info << " nlayer = " << Mesh_Parameters::nlayer <<
endl;


  // Build problem:
  UnsteadyTubeProblem<CustomisedRefineableQTaylorHoodElement,
BDF<2> > problem;

#ifdef OOMPH_HAS_MPI
 problem.distribute();
#endif

  // Perform self-test:
  oomph_info << "Performing self-test\n" << std::endl;
  problem.self_test();

  oomph_info << "Starting unsteady run...\n" << std::endl;
  // Run the unsteady simulation
  problem.unsteady_run(doc_info);

 }

// Finalize MPI
#ifdef OOMPH_HAS_MPI
oomph_info << "Finalising MPI " << std::endl;
MPI_Helpers::finalize();
#endif

} // end_of_main
```

Appendix D

Pressure and flow indices

D.1 Empirical comparison

The error associated with the empirical formula from Liu and Masliyah (1993) at $Re = 100$ is included in table D.1 for the regularly coiled cords.

D.2 umbili-calc

The matlab script for the calculation of PX and QX is below. This script uses Liu and Masliyah (1993) without reference to the additional numerical data computed using oomph-lib. The script generates the indices in addition to a plot of the pressure and flow ratios as well as a schematic model of the input arteries and vein.

```
function [QX PX] = umbilicalc(w,lhP,N,ls,out)

% Created by D.Wilke 2014

% This function takes the cord width (w) in cm, cord (helical)
% pitch length (lhP) in cm, straight lengths (ls) in cm and
% number of coils (N) and computes the pressure and flow
% indices, PX, QX, from Liu and Masliyah (1993). The signifier
% 'out' controls whether the output is displayed on screen.

if out == 1
   disp([' '])
   disp([' '])
   disp(['------------------------------------------------ '])
```

	$e(\%)$	Dn	γ
U_{t1}	0.98	152.55	0.0395
U_{t2}	1.16	121.2403	0.0509
U_{t3}	0.55	111.8427	0.0366
U_{t4}	1.19	79.6241	0.0921
U_{t5}	0.51	107.6141	0.0213
U_{t6}	1.42	83.4769	0.0683
U_{c1}	55.3	58.6454	0.2895
U_{c2}	6.87	88.8054	0.1425
U_{c3}	1.06	115.0113	0.0536
U_{c4}	0.64	109.9109	0.0340
U_{c5}	0.75	101.0881	0.0238
U_{c6}	1.34	85.6131	0.0140
U_{c7}	2.11	69.4809	0.0079
U_{cN1}	62.23	41.7612	0.4880
U_{cN2}	43.22	71.0774	0.2124
U_{cN3}	22.82	80.8703	0.1700
U_{cN4}	1.15	110.3268	0.0794

Table D.1: Error in the empirical formula from Liu and Masliyah (1993) at $Re = 100$ for the regularly coiled cords.

```
   disp(['------------------------------------------------ '])
   disp(['                    Umbili-calc'])
   disp(['------------------------------------------------ '])
   disp(['------------------------------------------------ '])
end

% Vessel radius: [A V] cm:
R = [0.2 0.35];
%  Non-dimesional distance from vessel outer to cord outer:
F = [0 0];

% Reference Cord Parameters:
Re_ref = 100;
w_ref = 1.6; % cm
lhP_ref = 50.0; % cm
N_ref = 10;
ls_ref = 0.0; % cm

% For dimensional pressure:
% Blood flow-rate:
% Q = [2.3958e-6 4.42e-6]; % From Acharya et. al. (m^3/s)
% Blood density:
rho = 1060; % Guettouche et. al. (1992) (kg/m^3)
% Blood viscosity:
mu = 4e-3; %

% UCI
UCI = N/(lhP+ls);
if UCI > 0.3
    Class = 'O';
elseif UCI < 0.1
    Class = 'U';
else
    Class = 'N';
end

% Reference pressure calculation:
Rc_ref = 0.5*(w_ref./R)-1-F;
P_ref = lhP_ref./(R*N_ref);
tau_ref = (P_ref./(2*pi))./(Rc_ref.^2 + (P_ref./(2*pi)).^2);
kappa_ref = (Rc_ref)./(Rc_ref.^2 + (P_ref./(2*pi)).^2);
```

```
Dn_ref = 2*Re_ref*(kappa_ref.^0.5);
Lh_ref = 2*pi*(N_ref)*sqrt(Rc_ref.*Rc_ref+(P_ref./(2*pi)).^2);
fRe_ref = (16 + (0.378*((2*Re_ref).^(0.5)) + 12.1.*(...
    kappa_ref.^(-0.5)).*Dn_ref.^(-0.5)).*(tau_ref.^2)).*(1 ...
    + ((0.0908+0.0233*kappa_ref.^0.5).*Dn_ref.^0.5 ...
    -0.132*kappa_ref.^(0.5) + 0.37*kappa_ref - 0.2)./(1 ...
    +49./Dn_ref));

dP_h_ref = (fRe_ref./2).*Lh_ref;

% Straight section non-dim:
Ls=ls./R;
dP_s = 8*Ls;

Rc = 0.5*(w./R)-1-F;
P = lhP./(R*N);
tau = (P./(2*pi))./(Rc.^2 + (P./(2*pi)).^2);
kappa = (Rc)./(Rc.^2 + (P./(2*pi)).^2);
Lh = 2*pi*(N)*sqrt(Rc.*Rc+(P./(2*pi)).^2);
Re_c = (tau.^2)./(0.02*kappa.^(3/2));


count= 1;
% initialise
QX = [nan nan];
gammaQ = [nan nan];
Re = 0;
QX = [0 0];
while Re < 6.0*Re_ref

Re = Re+1;

    % Helical section:
    if lhP ~= 0 || N ~= 0
        gamma_parameter = tau./(kappa.^(3/4)).*(1./sqrt...
            (2*Re));
        Dn = 2*Re*(kappa.^0.5);
        fRe = (16 + (0.378*((2*Re).^(0.5)) + 12.1.*(...
            kappa.^(-0.5)).*Dn.^(-0.5)).*(tau.^2)).*(1 ...
            + ((0.0908+0.0233*kappa.^0.5).*Dn.^0.5 - ...
            0.132*kappa.^(0.5) + 0.37*kappa - 0.2)./(...
```

```
            1+49./Dn));
        dP_h = (fRe./2).*Lh;
        dPdZ_h = (-fRe./2);
    else
        fRe = [8 8];
        Lh = 0;
        dP_h = 0;
    end

    % Total length
    L = Ls+Lh;
    % Total pressure drop
    dP = (dP_s + dP_h);

    P_rat(count,:) = (Re/Re_ref)*(dP./dP_h_ref);
    Q_rat(count,:) = Re/Re_ref;

    % Flow Index (QX)
    if P_rat(count,1) == 1
        QX(1) = Q_rat(count,1);
        P_rat_des(1) = P_rat(count,1);
        Re_des(1) = Re;
        QXe(1) = (P_rat_des(1)-1)*100;
        if lhP ~= 0 || N ~= 0
            gammaQ(1) = gamma_parameter(1);
        end
        dPQ(1) = dP(1);
        dP_dimQ(1) = ((mu^2)./(rho*(R(1)/100).^2))...
            *Re.*dP(1)*0.0075;
        dPdZQ(1) = dPdZ_h(1);
    elseif QX(1) ==0 && P_rat(count,1) > 0.98 && ...
            P_rat(count,1) < 1.02
        QX(1) = Q_rat(count,1);
        P_rat_des(1) = P_rat(count,1);
        Re_des(1) = Re;
        QXe(1) = (P_rat_des(1)-1)*100;
        if lhP ~= 0 || N ~= 0
            gammaQ(1) = gamma_parameter(1);
        end
        dPQ(1) = dP(1);
        dP_dimQ(1) = ((mu^2)./(rho*(R(1)/100).^2))...
```

```
        .*Re.*dP(1)*0.0075;
    dPdZQ(1) = dPdZ_h(1);
end

if P_rat(count,2) == 1
    QX(2) = Q_rat(count,1);
    P_rat_des(2) = P_rat(count,2);
    Re_des(2) = Re;
    QXe(2) = (P_rat_des(2)-1)*100;
    if lhP ~= 0 || N ~= 0
        gammaQ(2) = gamma_parameter(2);
    end
    dPQ(2) = dP(2);
    dP_dimQ(2) = ((mu^2)./(rho*(R(2)/100).^2))...
        .*Re.*dP(2)*0.0075;
    dPdZQ(2) = dPdZ_h(2);

 elseif QX(2) == 0 && P_rat(count,2) > 0.98 ...
         && P_rat(count,2) < 1.02
    QX(2) = Q_rat(count,1);
    P_rat_des(2) = P_rat(count,2);
    Re_des(2) = Re;
    QXe(2) = (P_rat_des(2)-1)*100;
    if lhP ~= 0 || N ~= 0
        gammaQ(2) = gamma_parameter(2);
    end
    dPQ(2) = dP(2);
    dP_dimQ(2) = ((mu^2)./(rho*(R(2)/100).^2))....
        *Re.*dP(2)*0.0075;
    dPdZQ(2) = dPdZ_h(2);
end


% Pressure Index (QX)
if Q_rat(count,1) == 1
    PX(1) = P_rat(count,1);
    PX(2) = P_rat(count,2);
    fReQ = fRe;
    if lhP ~= 0 || N ~= 0
        gammaP = gamma_parameter;
    end
```

```
        dPP = dP;
        dP_dimP = ((mu^2)./(rho*(R/100).^2)).*...
            Re.*dP.*0.0075;
        dPdZP = dPdZ_h;
    end

    count = count+1;
end

Final = (Re/Re_ref)*(dP./dP_h_ref);




if out == 1
    % Output results:
    disp([' '])
    disp(['             Arterial                 Venous'])
    disp([' '])
    if Final(1) < 1 || Final(2) < 1
        disp(['     NOTE: NO FLOW INDEX FOUND BELOW Re = ' ...
            num2str(Re,'%3g')])
        disp([' '])
    end
    if lhP ~= 0 || N ~= 0
    disp(['         Rc = ' num2str(Rc(1),'%08.3f') ...
            '; |           Rc = ' num2str(Rc(2),'%08.3f') ])
    disp(['          P = ' num2str(P(1),'%08.3f') ...
            '; |            P = ' num2str(P(2),'%08.3f') ])
    disp(['        tau = ' num2str(tau(1),'%08.3f') ...
            '; |          tau = ' num2str(tau(2),'%08.3f')])
    disp(['      kappa = ' num2str(kappa(1),'%08.3f') ...
            '; |        kappa = ' num2str(kappa(2),'%08.3f')])
    disp(['-----------------------------------------------'])
    disp(['     gammaQ = ' num2str(gammaQ(1),'%08.3f')  ...
            '; |       gammaQ = ' num2str(gammaQ(2),'%08.3f')])
    disp(['     gammaP = ' num2str(gammaP(1),'%08.3f')   ...
            '; |       gammaP = ' num2str(gammaP(2),'%08.3f')])
    disp(['Re Critical = ' num2str(Re_c(1),'%08.3f')   ...
            '; |  Re Critical = ' num2str(Re_c(2),'%08.3f')])
```

```
   end
   disp(['-------------------------------------------------'])

   disp(['      dPdZP = ' num2str(dPdZP(1),'%08.3f') ...
       '; |        dPdZQ = ' num2str(dPdZP(2),'%08.3f')])
   disp(['      dPdZQ = ' num2str(dPdZQ(1),'%08.3f')   ...
       '; |        dPdZQ = ' num2str(dPdZQ(2),'%08.3f')])
   disp(['        dPP = ' num2str(dPP(1),'%08.3f')   ...
     '; |          dPP = ' num2str(dPP(2),'%08.3f')])
if Final(1) > 1 || Final(2) > 1
     disp(['        dPQ = ' num2str(dPQ(1),'%08.3f') ...
      '; |          dPQ = ' num2str(dPQ(2),'%08.3f')])
end
 disp([' dPP (mmHg) = ' num2str(dP_dimP(1),'%08.3f') ...
   '; |   dPQ (mmHg) = ' num2str(dP_dimP(2),'%08.3f') ])
if Final(1) > 1 || Final(2) > 1
 disp([' dPQ (mmHg) = ' num2str(dP_dimQ(1),'%08.3f') ...
    '; |   dPQ (mmHg) = ' num2str(dP_dimQ(2),'%08.3f') ])
 disp(['-------------------------------------------------'])
 disp(['         QX = ' num2str(QX(1),'%08.3f') ...
      '; |           QX = ' num2str(QX(2),'%08.3f')])
  end
 disp(['------------------------------------------------ '])
 disp(['         PX = ' num2str(PX(1),'%08.3f')     ...
       '; |           PX = ' num2str(PX(2),'%08.3f')])
 disp(['------------------------------------------------ '])
 if Final(1) > 1 || Final(2) > 1
  disp(['      PX/QX = ' num2str(PX(1)/(QX(1)),'%08.3f') ...
    '; |        PX/QX = ' num2str(PX(2)/(QX(2)),'%08.3f')])
  disp(['------------------------------------------------ '])
  end

   if lhP ~= 0 || N ~= 0
       if max([gammaQ(1) gammaQ(2) gammaP(1) gammaP(2)]) > 0.1
           disp([' '])
           disp(['                  GAMMA WARNING'])
       end
   end
```

```
% Plot tube:

tableview=0;

if lhP ~= 0 && N ~= 0
    t=linspace(0,2*pi*N,100*N);
    artery1 = [Rc(1)*R(1)*cos(t);Rc(1)*R(1)*sin(t);((...
     P(1)*R(1))/(2*pi))*t];
    vein = [Rc(2)*R(2)*cos(t+(2*pi)/3);Rc(2)*R(2...
     )*sin(t+(2*pi...
        )/3);((P(2)*R(2))/(2*pi))*t];
    artery2 = [Rc(1)*R(1)*cos(t+2*(2*pi)/3);Rc(1...
     )*R(1)*sin(t+...
        2*(2*pi)/3);((P(1)*R(1))/(2*pi))*t];

    [zA1,yA1,xA1]=tubeplot(artery1,R(1),40);
    [zA2,yA2,xA2]=tubeplot(artery2,R(1),40);
    [zV,yV,xV]=tubeplot(vein,R(2),70);


    h=figure;
    set(h, 'Position', [500 500 750 600]);
    hold on
    hSurfaceA1=surf(xA1,yA1,zA1);
    set(hSurfaceA1,'FaceColor',[0.7 0 0]);
    hSurfaceA2=surf(xA2,yA2,zA2);
    set(hSurfaceA2,'FaceColor',[0.7 0 0]);
    hSurfaceV=surf(xV,yV,zV);
    set(hSurfaceV,'FaceColor',[0 0 0.7]);
    axis([0 N*P(1)*R(1) -1 1 -1 1])
    set(hSurfaceA1, 'EdgeColor','none')
    set(hSurfaceA2, 'EdgeColor','none')
    set(hSurfaceV, 'EdgeColor','none')
    view([0 0]);

    axis equal
    axis([0 76 -1 1 -1 1])
    hold off

    h=figure;
    set(h, 'Position', [500 500 750 600]);
```

```
hold on
hSurfaceA1=surf(xA1,yA1,zA1);
set(hSurfaceA1,'FaceColor',[0.7 0 0]);
hSurfaceA2=surf(xA2,yA2,zA2);
set(hSurfaceA2,'FaceColor',[0.7 0 0]);
hSurfaceV=surf(xV,yV,zV);
set(hSurfaceV,'FaceColor',[0 0 0.7]);
axis equal
axis([5 10 -1 1 -1 1])
view([0 0]);
hold off
if Final(1) > 1 || Final(2) > 1
h=figure;
set(h, 'Position', [500 500 750 600]);
hold on
plot(Q_rat(:,1),P_rat(:,1),'r', 'markersize',20)
plot(Q_rat(:,1),P_rat(:,2),'b','markersize',20)

plot([0 QX(1)],[P_rat_des(1) P_rat_des(1)],'k--', ...
    'markersize',15)
plot([QX(1) QX(1)],[0 P_rat_des(1)],'k--', ...
    'markersize',15)
plot([0 QX(2)],[P_rat_des(2) P_rat_des(2)],'k--', ...
    'markersize',15)
plot([QX(2) QX(2)],[0 P_rat_des(2)],'k--', ...
    'markersize',15)
plot([0 1],[PX(1) PX(1)],'k--', 'markersize',15)
plot([1 1],[0 PX(1)],'k--', 'markersize',15)
plot([0 QX(2)],[P_rat_des(2) P_rat_des(2)],'k--', ...
    'markersize',15)
plot([QX(2) QX(2)],[0 P_rat_des(2)],'k--', ...
    'markersize',15)
hold off

axis equal
axis([max(Re_c/Re_ref) 2*max([1,QX(1),QX(2)]) ...
    0.1*min([1,PX(1),...
    PX(2)]) 2*max([1,PX(1),PX(2)])])
xlabel('$QR$','fontsize',20,'Interpreter','latex')
ylabel('$PR$','fontsize',20,'Interpreter','latex')
```

```
        end

        if tableview == 1
            data = rand(3);
            colnames = {'X-Data', 'Y-Data', 'Z-Data'};
            t = uitable(figure(1), 'Data', data, ...
                'ColumnName', colnames...
                , 'Position', [100 270 550 100]);
        end

    else
        if Final(1) > 1 || Final(2) > 1
        disp([' '])
        disp(['         Not plotting straight tube'])
        disp([' '])
        h=figure;
        set(h, 'Position', [500 500 750 600]);
        hold on
        plot(Q_rat(:,1),P_rat(:,1),'r', 'markersize',20)
        plot(Q_rat(:,1),P_rat(:,2),'b','markersize',20)
        plot([0 QX(1)],[P_rat_des(1) P_rat_des(1)],'k--',...
            'markersize',15)
        plot([QX(1) QX(1)],[0 P_rat_des(1)],'k--', ...
            'markersize',15)
        plot([0 QX(2)],[P_rat_des(2) P_rat_des(2)],'k--',...
            'markersize',15)
        plot([QX(2) QX(2)],[0 P_rat_des(2)],'k--', ...
            'markersize',15)
        plot([0 1],[PX(1) PX(1)],'k--', 'markersize',15)
        plot([1 1],[0 PX(1)],'k--', 'markersize',15)
        plot([0 QX(2)],[P_rat_des(2) P_rat_des(2)],'k--',...
            'markersize',15)
        plot([QX(2) QX(2)],[0 P_rat_des(2)],'k--',...
            'markersize',15)
        hold off
        axis equal
        axis([max(Re_c/Re_ref) 2*max([1,QX(1),QX(2)])...
            0.1*min([1,PX(1),...
            PX(2)]) 2*max([1,PX(1),PX(2)])])
```

```
        xlabel('QR','fontsize',20)
        ylabel('PR','fontsize',20)
        end
    end

end
end
```

D.3 Index sensitivity

For increasing UCI, the error associated with $\hat{w}$ and $\hat{L}_p$ increases similarly for both PX and QX and typically remain within 10%. The sensitivity of QX and PX to $\hat{L}_p$ is reduced for increasing UCI and as the cord width increases, the effect of incorrect measurements in the length become less apparent. For increasing width, the N and $\hat{L}_p$ sensitivity follow the same trends as at the nominal width, however the sensitivity to N increases with $\hat{w}$, while the sensitivity to $\hat{L}$ reduces. Changes in cord width have a more complex effect on the width sensitivity. As $\hat{w}$ increases, the sensitivity of PX to $\hat{w}$ tends to increase for low UCI cords, and decrease for high UCI cords. The sensitivity of QX to both $\hat{w}$ and $\hat{N}$ increases with increasing $\hat{w}$ for most cords, expect for those with high UCI and low length. The length sensitivity, however, tends to reduce with width. Relatively, errors in certain measurements are more important for different cords. The indices are typically more sensitive to the width at higher UCI, while lower UCI cords have higher sensitivity to the length. Cords with a UCI in the normal range at the nominal width will exhibit higher sensitivity to N. As width increases, however, cords become more sensitive in general to width measurement errors and the effect of N will be relatively less pronounced.

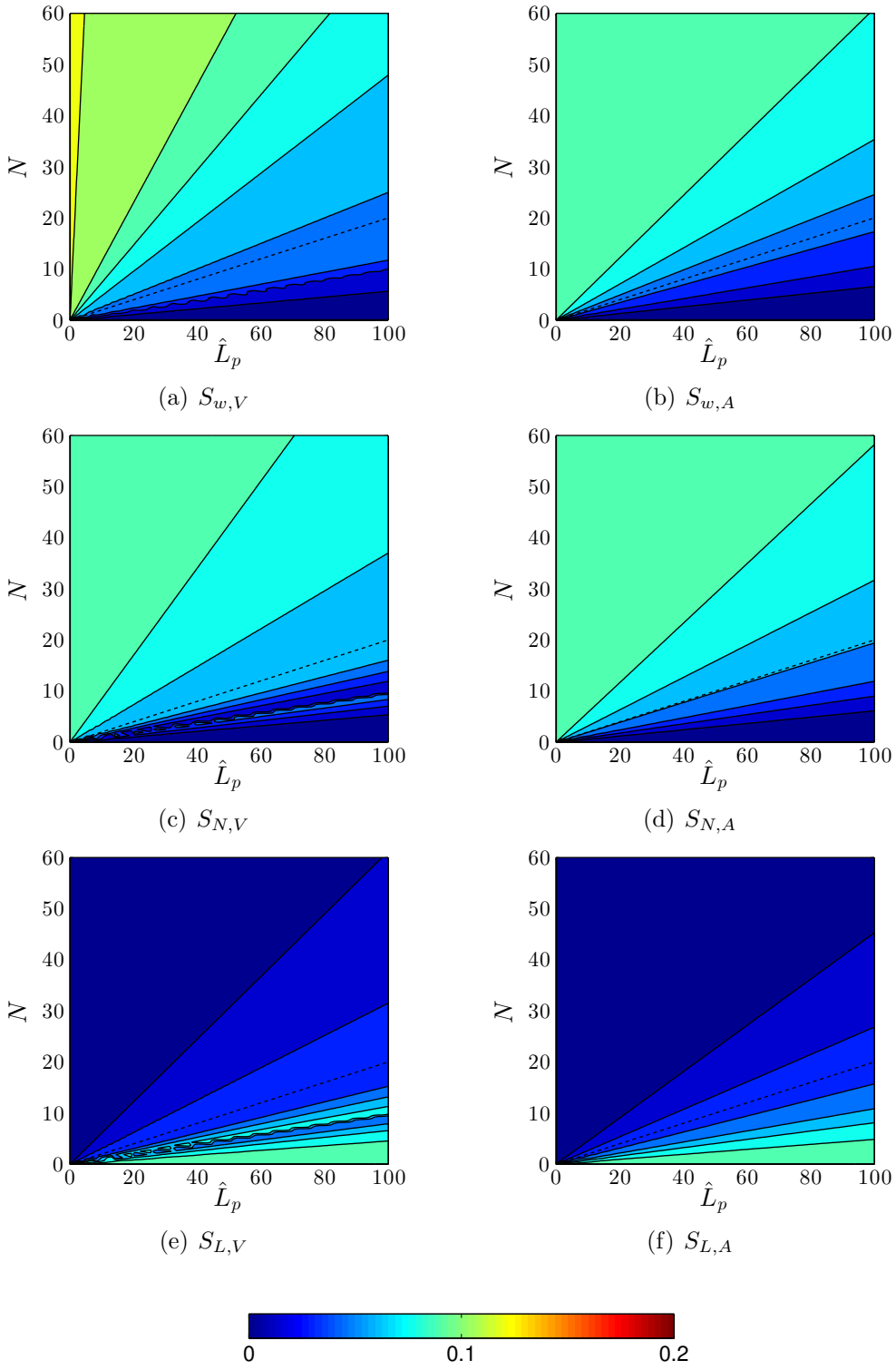

(a) $S_{w,V}$ (b) $S_{w,A}$

(c) $S_{N,V}$ (d) $S_{N,A}$

(e) $S_{L,V}$ (f) $S_{L,A}$

Figure D.1: Contours of the venous (left) and arterial (right) pressure index, PX, sensitivity over a range of $N, \hat{L}_p$ at $\hat{w} = 1.6$ cm to measurements in width, $\hat{w}$, (top), number of coils, N, (middle) and length, $\hat{L}_p$, (bottom).

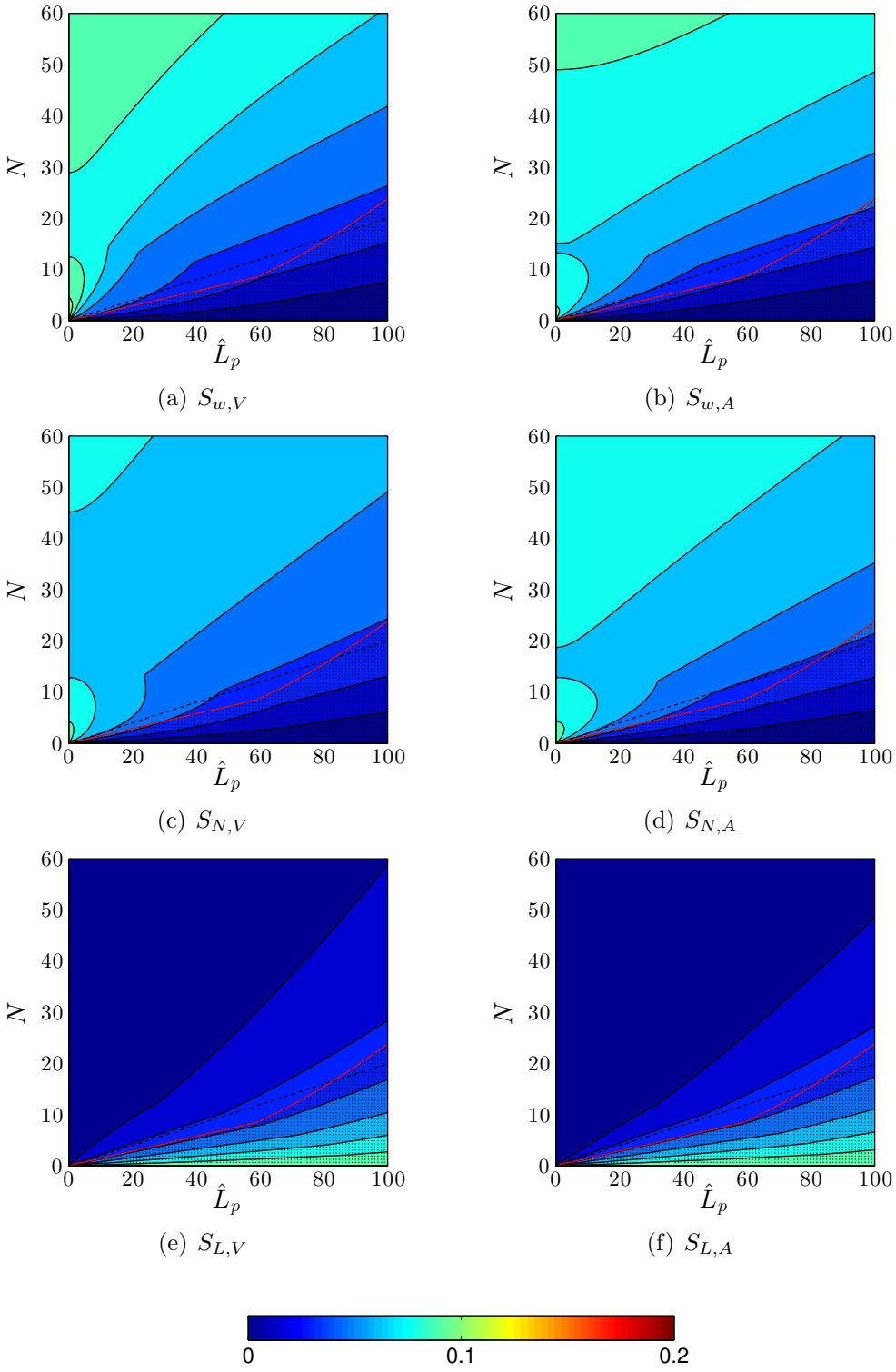

(a) $S_{w,V}$ (b) $S_{w,A}$

(c) $S_{N,V}$ (d) $S_{N,A}$

(e) $S_{L,V}$ (f) $S_{L,A}$

Figure D.2: Contours of the venous (left) and arterial (right) flow index, QX, sensitivity over a range of $N, \hat{L}_p$ at $\hat{w} = 1.6$ cm to measurements in width, $\hat{w}$, (top), number of coils, N, (middle) and length, $\hat{L}_p$, (bottom). The red line indicates cords for which $\gamma = 0.1$ with the shaded region marking those vessels outside correlation.

e_w	e_L	e_N	ΔPX_A	ΔPX_V	ΔQX_A	ΔQX_V	ΔUCI
0.1	0.0	0.0	0.051	0.051	0.040	0.038	0.000
0.0	0.1	0.0	0.042	0.042	0.033	0.032	0.101
0.0	0.0	0.1	0.058	0.058	0.045	0.044	0.100
0.1	0.1	0.0	0.094	0.093	0.074	0.071	0.101
0.1	0.0	0.1	0.109	0.104	0.085	0.078	0.100
0.0	0.1	0.1	0.100	0.100	0.079	0.077	0.202
0.1	0.1	0.1	0.151	0.151	0.120	0.116	0.202

Table D.2: Error variation for the reference cord. The quantity e is the error in a particular measurement.

e_w	e_L	e_N	ΔPX_A	ΔPX_V	ΔQX_A	ΔQX_V	ΔUCI
0.1	0.0	0.0	0.064	0.059	0.052	0.037	0.000
0.0	0.1	0.0	0.030	0.032	0.027	0.028	0.101
0.0	0.0	0.1	0.070	0.068	0.053	0.049	0.100
0.1	0.1	0.0	0.094	0.090	0.079	0.073	0.101
0.1	0.0	0.1	0.134	0.128	0.104	0.081	0.100
0.0	0.1	0.1	0.100	0.100	0.080	0.077	0.202
0.1	0.1	0.1	0.164	0.159	0.132	0.120	0.202

Table D.3: Index error variation for Cord I. The quantity e is the error in a particular measurement.

e_w	e_L	e_N	ΔPX_A	ΔPX_V	ΔQX_A	ΔQX_V	ΔUCI
0.1	0.0	0.0	0.081	0.049	0.062	0.036	0.000
0.0	0.1	0.0	0.017	0.021	0.013	0.016	0.101
0.0	0.0	0.1	0.083	0.079	0.062	0.056	0.100
0.1	0.1	0.0	0.098	0.068	0.075	0.051	0.101
0.1	0.0	0.1	0.165	0.130	0.123	0.094	0.100
0.0	0.1	0.1	0.100	0.100	0.075	0.071	0.202
0.1	0.1	0.1	0.181	0.149	0.137	0.108	0.202

Table D.4: Index error variation for Cord II. The quantity e is the error in a particular measurement.

e_w	e_L	e_N	ΔPX_A	ΔPX_V	ΔQX_A	ΔQX_V	ΔUCI
0.1	0.0	0.0	0.095	0.029	0.075	0.028	0.000
0.0	0.1	0.0	0.008	0.022	0.006	0.015	0.101
0.0	0.0	0.1	0.092	0.078	0.069	0.056	0.100
0.1	0.1	0.0	0.103	0.050	0.082	0.042	0.101
0.1	0.0	0.1	0.187	0.112	0.144	0.085	0.100
0.0	0.1	0.1	0.100	0.100	0.076	0.071	0.202
0.1	0.1	0.1	0.195	0.131	0.151	0.098	0.202

Table D.5: Index error variation for Cord III. The quantity e is the error in a particular measurement.

Bibliography

Acharya, G., Wilsgaard, T., Berntsen, G. K. R., Maltau, J. M. and Kiserud, T. (2005*a*), 'Reference ranges for serial measurements of blood velocity and pulsatility index at the intra-abdominal portion, and fetal and placental ends of the umbilical artery', *Ultrasound in Obstetrics and Gynecology* **26**, 162–169.

Acharya, G., Wilsgaard, T., Berntsen, G. K. R., Maltau, J. M. and Kiserud, T. (2005*b*), 'Reference ranges for umbilical vein blood flow in the second half of pregnancy based on longitudinal data', *Prenatal Diagnosis* **25**, 99–111.

Ali, S. (2001), 'Pressure drop correlations for flow through regular helical coil tubes', *Fluid Dynamics Research* **28**(4), 295–310.

Baergen, R. N. (2005), *Manual of Benirschke and Kaufmanns Pathology of the Human Placenta*, Springer-Verlag.

Barbieri, C., Cecatti, J. G., Surita, F. G., Costa, M. L., Marussi, E. F. and Costa, J. V. (2011), 'Area of Wharton's jelly as an estimate of the thickness of the umbilical cord and its relationship with estimated fetal weight', *Reproductive Health* **8**, 32.

Barbieri, C., Cecatti, J. G., Surita, F. G., Marussi, E. F. and Costa, J. V. (2012), 'Sonographic measurement of the umbilical cord area and the diameters of its vessels during pregnancy', *Journal of Obstetrics and Gynaecology* **32**, 230–236.

Batchelor, G. K. (1967), *An Introduction to Fluid Dynamics*, Cambridge University Press.

Benirschke, K., Kaufmann, P. and Baergen, R. (2006), Anatomy and pathology of the umbilical cord, *in* 'Pathology of the Human Placenta', Springer, chapter 12, pp. 380–451.

Boito, S., Struijk, P. C., Ursem, N. T. C., Stijnen, T. and Wladimiroff, J. W. (2002), 'Umbilical venous volume flow in the normally developing and growth-restricted human fetus', *Ultrasound in Obstetrics and Gynecology* **19**, 344– 349.

Bovendeerd, P. H. M., Van Steenhoven, A. A., Van de Vosse, F. N. and Vossers, G. (1987), 'Steady entry flow in a curved pipe', *Journal of Fluid Mechanics* **177**, 233–246.

Caro, C. G., Pedley, T. J., Schroter, C. W. and Seed, W. A. (1978), *The mechanics of the circulation*, Oxford University Press.

Cunningham, F., Leveno, K., Bloom, S., Hauth, J., Rouse, D. and Spong, C. (2009), *Williams Obstetrics*, 23rd edn, McGraw-Hill.

Cunningham, K. S. and Gotlieb, A. I. (2005), 'The role of shear stress in the pathogenesis of atherosclerosis.', *Laboratory investigation* **85**(1), 9–23.

de Laat, M. W. M., Franx, A., Bots, M. L., Visser, G. H. A. and Nikkels, P. G. J. (2006), 'Umbilical coiling index in normal and complicated pregnancies.', *Obstetrics and Gynecology* **107**(5), 1049–1055.

de Laat, M. W. M., Franx, A., van Alderen, E. D., Nikkels, P. G. J. and Visser, G. H. A. (2005), 'The umbilical coiling index, a review of the literature.', *Journal of Maternal-Fetal & Neonatal Medicine* **17**(2), 93–100.

Dean, W. (1927), 'Note on the motion of fluid in a curved pipe', *Philosophical Magazine* **4**, 208–223.

Dean, W. (1928), 'The stream-line motion of fluid in a curved pipe.', *Philosophical Magazine* **5**, 673–695.

Degani, S., Lewinsky, R. M., Berger, H. and Spiegel, D. (1995), 'Sonographic Estimation of Umbilical Coiling Index and Correlation With Doppler Flow Characteristics', *Obstetrics and Gynecology* **86**(6).

Denne, E., Diao, Y. and Sullivan, J. M. (2006), 'Quadrisecants give new lower bounds for the ropelength of a knot', *Geometry & Topology* **10**(1), 1–26.

Di Naro, E., Raio, L., Ghezzi, F., Franchi, M., Romano, F. and D'Addario, V. (2002), 'Longitudinal umbilical vein blood flow changes in normal and growth-retarded fetuses', *Acta Obstetricia et Gynecologica Scandinavica* **81**(9), 527–533.

Doorly, D. and Sherwin, S. (2009), Geometry and Flow, *in* L. Formaggia, A. Quarteroni and A. Veneziani, eds, 'Cardiovascular Mathematics', Springer-Verlag, chapter 5, pp. 177–209.

Dudiak, C., Salomon, C., Posniak, H., Olson, M. and Flisak, M. (1995), 'Sonography of the umbilical cord', *RadioGraphics* **15**, 1035–1050.

Edwards, H. (1954), 'The spiral twist of the normal umbilical cord in twins and in singletons', *American Journal of Obstetrics and Gynecology* **67**, 102–120.

Ferguson, V. L. and Dodson, R. B. (2009), 'Bioengineering aspects of the umbilical cord.', *European Journal of Obstetrics & Gynecology and Reproductive Biology* **144S**, S108–S113.

Fletcher, C. (1991), *Computational techniques for fluid dynamics*, second edn, Springer.

Flo, K., Wilsgaard, T. and Acharya, G. (2010), 'Longitudinal reference ranges for umbilical vein blood flow at a free loop of the umbilical cord', *Ultrasound in Obstetrics and Gynecology* **36**, 567–572.

Formaggia, L., Perktold, K. and Quarteroni, A. (2009), Basic mathematical models and motivations, *in* L. Formaggia, A. Quarteroni and A. Veneziani, eds, 'Cardiovascular Mathematics', Springer-Verlag, chapter 2, pp. 47–75.

Fung, Y. C. (1997), *Biomechanics Circulation*, second edn, Springer.

Gammack, D. and Hydon, P. (2001), 'Flow in pipes with non-uniform curvature and torsion', *Journal of Fluid Mechanics* **433**, 357–382.

Geipel, A. and Gembruch, U. (2009), Evaluation of fetal and uteroplacental blood flow, *in* 'Ultrasound in Obstetrics and Gynaecology', 1 edn, Elsevier Ltd, chapter 11, pp. 209–227.

Germano, M. (1982), 'On the effect of torsion on a helical pipe flow', *Journal of Fluid Mechanics* **125**, 1–8.

Germano, M. (1989), 'The Dean equations extended to a helical pipe flow', *Journal of Fluid Mechanics* **203**, 289–305.

Gordon, Z., Eytan, O., Jaffa, A. J. and Elad, D. (2007), 'Hemodynamic analysis of Hyrtl anastomosis in human placenta.', *American Journal of Physiology - Regulatory, Integrative and Comparative Physiology* **292**(2), R977–R982.

Guettouche, A., Challier, J., Ito, Y., Papapanayotou, C., Cherruault, Y. and Azancot-Benisty, A. (1992), 'Mathematical modeling of the human fetal arterial blood circulation', *International Journal of Biomedical Computing* **31**, 127–139.

Hagen, G. (1839), *Poggendorff's Annalen d. Physik u. Chemie* **46**(2), 423.

Hasson, D. (1955), 'Streamline flow resistance in coils', *Res. Corresp.* **1**, S1.

Heil, M., Hazel, A. and Boyle, J. (2008), 'Solvers for large-displacement fluid-structure interaction problems: segregated versus monolithic approaches', *Computational Mechanics* **43**(1), 91–101.
URL: *http://www.oomph-lib.org*

Hellevik, L. R., Stergiopulos, N., Kiserud, T., Rabben, S. I., Eik-Nes, S. H. and Irgens, F. (2000), 'A mathematical model of umbilical venous pulsation.', *Journal of Biomechanics* **33**(9), 1123–30.

Hobbins, J. C. (2008), *Obstetric Ultrasound Artistry in Practice*, Chicester : Wiley.

Jouppila, P., Kirkinen, P. and Puukka, R. (1986), 'Correlation between umbilical vein blood flow and umbilical blood viscosity in normal and complicated pregnancies', *Archives of Gynecology* **237**, 191–197.

Kao, H. C. (1987), 'Torsion effect on fully developed flow in a helical pipe', *Journal of Fluid Mechanics* **184**, 335–356.

Kaplan, A. D., Jaffa, A. J., Timor, I. E. and Elad, D. (2010), 'Hemodynamic analysis of arterial blood flow in the coiled umbilical cord.', *Reproductive Sciences* **17**(3), 258–268.

Kaplan, C. (2007), Umbilical cord, *in* 'Color atlas of gross placental pathology', Springer Science+Business Media, LLC., chapter 3.

Khong, T. Y. (2010), 'Evidence-based pathology: umbilical cord coiling', *Pathology* **42**(7), 618–622.

Kiserud, T. (2005), 'Physiology of the fetal circulation', *Seminars in Fetal & Neonatal Medicine* **10**, 493–503.

Kleiner-assaf, A., Jaffa, A. J. and Elad, D. (1999), 'Hemodynamic model for analysis of Doppler ultrasound indexes of umbilical blood flow arteries', *American Journal of Physiology - Heart and Circulatory Physiology* **276**, H2204–H2214.

Lees, C., Albaiges, G., Deane, C., Parra, M. and Nicolaides, K. H. (1999), 'Assessment of umbilical arterial and venous flow using color Doppler', *Ultrasound in Obstetrics and Gynecology* **14**, 250–255.

Liao, A. W., Snijders, R., Geerts, L., Spencer, K. and Nicolaides, K. H. (2000), 'Fetal heart rate in chromosomally abnormal fetuses', *Ultrasound in Obstetrics and Gynecology* **16**(7), 610–613.

Liu, S. and Masliyah, J. H. (1993), 'Axially invariant laminar flow in helical pipes with a finite pitch', *Journal of Fluid Mechanics* **251**, 315–353.

Machin, G. A., Ackerman, J. and Gilbert-Barness, E. (2000), 'Abnormal umbilical cord coiling is associated with adverse perinatal outcomes', *Pediatric and Developmental Pathology* **3**(5), 462–471.

Manlapaz, R. and Churchill, S. (1980), 'Fully developed laminal flow in a helically coiled tube of finite pitch', *Chemical Engineering Communications* **7**, 57.

Mazumdar, J. N. (1992), *Biofluid mechanics*, World Scientific Publishing Co. Pty. Ltd.

Mishra, P. and Gupta, S. (1979), 'Momentum transfer in curved pipes', *Industrial and engineering chemisty process design and development* **18**, 130–142.

Pedley, T. J. (1980), *The Fluid Mechanics of Large Blood Vessels*, Cambridge University Press.

Pildner von Steinburg, S., Boulesteix, A.-L., Lederer, C., Grunow, S., Schiermeier, S., Hatzmann, W., Schneider, K.-T. M. and Daumer, M. (2013), 'What is the"normal" fetal heart rate?', *PeerJ* **1**, e82.

Poiseuille, J. (1840), *Comptes Rendus* **11**, 961 – 1041.

Quarteroni, A., Formaggia, L. and Veneziani, A. (2009), *Cardiovascular Mathematics*, Springer-Verlag.

Raio, L., Ghezzi, F., Di Naro, E., Gomez, R., Franchi, M., Mazor, M. and Brühwiler, H. (1999), 'Sonographic measurement of the umbilical cord and fetal anthropometric parameters', *European Journal of Obstetrics, Gynecology, and Reproductive Biology* **83**(2), 131–5.

Reddy, J. and Gartling, D. (1994), *The finite element method in heat transfer and fluid dynamics*, CRC Press.

Reynolds, S. (1978), 'Mechanisms of placentofetal blood flow', *Obstetrics and Gynecology* **51**(2), 245–249.

Sherwin, S. and Blackburn, H. (2005), 'Three-dimensional instabilities and transition of steady and pulsatile axisymmetric stenotic flows', *Journal of Fluid Mechanics* **533**, 297–327.

Strong, T., Jarles, D., Vega, J. and Feldman, D. (1994), 'The umbilical coiling index', *American Journal of Obstetrics and Gynecology* **170**, 29–32.

Tahmasebi, M. and Alighanbari, R. (2011), 'Evaluation of umbilical cord thickness, cross-sectional area, and coiling index as predictors of pregnancy outcome', *Indian Journal of Radiology and Imaging* **21**(3), 195–198.

Tejada-Martínez, A. E., Borberg, C. J., Venugopal, R., Carballo, C., Moreno, W. A. and Quintero, R. A. (2011), 'Computational fluid dynamic analysis of flow velocity waveform notching in umbilical arteries.', *American Journal of Physiology - Regulatory, Integrative and Comparative Physiology* **300**(1), R76–84.

Thompson, R. S. and Trudinger, B. J. (1990), 'Doppler waveform pulsatility index and resistance, pressure and flow in the umbilical placental circulation: an investigation using a mathematical model', *Ultrasound in Medicine and Biology* **16**(5), 449–458.

Togni, F. A., Júnior, E. A., Vasques, F. A. P., Moron, A. F., Torloni, M. R. and Nardozza, L. M. M. (2007), 'The cross-sectional area of umbilical cord components in normal pregnancy', *Journal of Gynecology and Obstetrics* **96**, 156–161.

Tuttle, E. R. (1990), 'Laminar flow in twisted pipes', *Journal of Fluid Mechanics* **219**, 545–570.

Van de Vosse, F. N., Van Steenhoven, A. A., Segal, A. and Janssen, J. D. (1989), 'A finite element analysis of the steady laminar entrance flow in a 90 degree curved tube', *International Journal for Numerical Methods in Fluids* **9**, 275–287.

Van Dyke, M. (1978), 'Extended Stokes series laminar flow through a loosely coiled pipe', *Journal of Fluid Mechanics* **86**, 129–145.

Wang, C. Y. (1981), 'On the low-Reynolds-number flow in a helical pipe', *Journal of Fluid Mechanics* **108**, 185–194.

Ward-Smith, A. J. (1980), *Internal fluid flow*, Oxford University Press.

Waters, S. L. and Guiot, C. (2001), 'Flow in an Elastic Tube Subject to Prescribed Forcing: A Model of Umbilical Venous Flow', *Journal of Theoretical Medicine* **3**(4), 287–298.

Whitmore, R. L. (1968), *Rheology of the Circulation*, Pergamon Press, Oxford.

Womersley, J. R. (1955), 'Method for the calculation of velocity, rate of flow and viscous drag in arteries when the pressure gradient is known', *Journal of Physiology* **127**(2), 553–563.

Yamamoto, K., Aribowo, A., Hayamizu, Y., Hirose, T. and Kawahara, K. (2002), 'Visualization of the flow in a helical pipe', *Fluid Dynamics Research* **30**(4), 251–267.

Youngson, R. M. (1992), *Collins Dictionary of Medicine*, Harper Collins.

Zabielski, L. and Mestel, A. J. (1998*a*), 'Steady flow in a helically symmetric pipe', *Journal of Fluid Mechanics* **370**, 297–320.

Zabielski, L. and Mestel, A. J. (1998*b*), 'Unsteady blood flow in a helically symmetric pipe', *Journal of Fluid Mechanics* **370**, 321–345.